CUKUROVA UNIVERSITY
INSTITUTE OF NATURAL AND APPLIED SCIENCES

PhD THESIS

A Comprehensive Study on Indirect Evaporative Coolers: CFD-Based Performance Analysis, Geometric Optimization and Machine Learning Models

Yunus Emre GÜZELEL

Department of Mechanical Engineering

December, 2025

CUKUROVA UNIVERSITY
INSTITUTE OF NATURAL AND APPLIED SCIENCES

PhD THESIS APPROVAL

A Comprehensive Study on Indirect Evaporative Coolers: CFD-Based Performance Analysis, Geometric Optimization and Machine Learning Models

Yunus Emre GÜZELEL

Department of Mechanical Engineering

This Doctorate Thesis was evaluated by the following Jury Members on 22/12/2025 and was approved by unanimity.

Jury	: Prof. Dr. Orhan BÜYÜKALACA (Advisor)	…………
	: Prof. Dr. Ertaç HÜRDOĞAN	…………
	: Prof. Dr. Arif ÖZBEK	…………
	: Assoc. Prof. Dr. Göktürk Memduh ÖZKAN	…………
	: Asst. Prof. Dr. Kamil Neyfel ÇERÇİ	…………

This Thesis was written in the Department of Mechanical Engineering, Institute of Natural and Applied Sciences.
Thesis Number:

Prof. Dr. Sadık DİNÇER
Director
Institute of Natural and Applied Sciences

This work was supported by the Scientific Research Project Unit of Çukurova University.
Project ID: FDK-2023-15552

CONTENTS

CUKUROVA UNIVERSITY
INSTITUTE OF NATURAL AND APPLIED SCIENCES

PhD THESIS

A Comprehensive Study on Indirect Evaporative Coolers: CFD-Based Performance Analysis, Geometric Optimization and Machine Learning Models

Yunus Emre GÜZELEL

Advisor: Prof. Dr. Orhan BÜYÜKALACA

Department of Mechanical Engineering

ABSTRACT

This thesis presents a comprehensive three-phase investigation into the performance and optimization of dew-point indirect evaporative coolers by combining computational fluid dynamics (CFD), geometric optimization and advanced predictive modeling. In the first phase, five cooler configurations (Type 0 to Type 4) with varying structural and fixed geometrical features were developed and systematically analyzed under a wide range of psychrometric and operating conditions. Key independent variables, including process air inlet temperature, humidity, velocity and working-to-intake air ratio, were varied to assess their influence on four primary performance indicators: dew-point effectiveness, cooling capacity, water consumption and cooling coefficient of performance (COP). Among the tested designs, multi-perforated Type 2 configuration demonstrated superior overall performance. Building upon these findings, the second phase of the thesis focused on the geometric optimization of the Type 2 cooler. Using the desirability function method, a total of 4,200 CFD simulations were performed, of which 2,225 valid cases (excluding reverse flow conditions) were used for optimization. Optimal design parameters, such as channel length, channel gap, aperture number, aperture diameter and working-to-intake air ratio were identified. The multi-objective optimization of the cooler was conducted across five different scenarios, each designed for a specific objective. In the final phase, predictor models were developed to reproduce CFD-level results at reduced computational cost. A total of 20,480 CFD simulations were conducted, and after excluding reverse flow cases, 17,525 valid results were used for model training and testing. Seven multiple linear regression (MLR) models and 32 machine learning (ML) models, including decision trees (DT), support vector machines (SVM) and multilayer perceptrons (MLP), were developed to predict performance parameters. Model accuracy was assessed through coefficient of determination (R^2), root mean square error (RMSE) and relative error (RE) distributions. While MLR models offered practicality and ease of use, machine learning models, particularly the models coded as DT-7 and MLP-4, exhibited superior predictive accuracy across most performance parameters. This thesis demonstrates that the systematic integration of CFD analysis, optimization and predictive modeling provides a robust pathway for designing efficient dew-point indirect evaporative coolers and enabling fast, reliable performance predictions for real-world applications.

Keywords: Dew-point evaporative cooler, CFD modeling, Geometric optimization, Machine learning

ÇUKUROVA ÜNİVERSİTESİ
FEN BİLİMLERİ ENSTİTÜSÜ

DOKTORA TEZİ

Dolaylı Buharlaştırıcı Soğutucular Üzerine Kapsamlı Bir Çalışma: HAD Tabanlı Performans Analizi, Geometrik Optimizasyon ve Makine Öğrenmesi Modelleri

Yunus Emre GÜZELEL

Danışman: Prof. Dr. Orhan BÜYÜKALACA

Makine Mühendisliği Anabilim Dalı

ÖZ

Bu tez, hesaplamalı akışkanlar dinamiği (HAD), geometrik optimizasyon ve gelişmiş tahmin edici modeller üretmeyi bir araya getirerek, çiğ noktası dolaylı buharlaştırıcı soğutucuların performansı ve optimizasyonu üzerine kapsamlı üç aşamalı bir araştırma sunmaktadır. İlk aşamada, farklı yapısal tasarıma ve sabit geometrik özelliklere sahip beş soğutucu konfigürasyonu (Tip 0'dan Tip 4'e kadar) geliştirilmiş ve geniş bir psikrometrik ve çalışma koşulları aralığında sistematik olarak analiz edilmiştir. İşlem havası giriş sıcaklığı, nemi, hızı ve çalışma-giriş havası oranı gibi temel bağımsız değişkenler; çiğ noktası etkinliği, soğutma kapasitesi, su tüketimi ve soğutma performans katsayısı (COP) olmak üzere dört performans göstergesi üzerindeki etkilerini değerlendirmek amacıyla geniş bir aralıkta değiştirilmiştir. Test edilen tasarımlar arasında, çok açıklıklı Tip 2 konfigürasyonu sürekli olarak üstün performans göstermiştir. Bu bulgulara dayanarak, tezin ikinci aşaması Tip 2 soğutucunun geometrik optimizasyonuna odaklanmıştır. İstenilebilirlik fonksiyonu yöntemi kullanılarak toplam 4.200 HAD simülasyonu gerçekleştirilmiş ve bunlardan 2.225 geçerli durum (ters akış koşullarının oluşmadığı) optimizasyon için kullanılmıştır. Kanal uzunluğu, kanal genişliği, açıklık sayısı, açıklık çapı ve çalışma-giriş havası oranı için optimum tasarım parametreleri belirlenmiştir. Soğutucunun çok amaçlı optimizasyonu, her biri belirli bir amaç için tasarlanmış beş farklı senaryoda gerçekleştirilmiştir. Üçüncü ve son aşamada, HAD düzeyinde sonuçları daha düşük hesaplama maliyetiyle yeniden üretmek için tahmin edici modeller geliştirilmiştir. Toplam 20.480 HAD simülasyonu oluşturulmuş ve ters akışın oluştuğu durumlar hariç tutulduktan sonra, model eğitimi ve testi için 17.525 geçerli sonuç kullanılmıştır. Karar ağaçları (DT), destek vektör makineleri (SVM) ve çok katmanlı algılayıcılar (MLP) dahil olmak üzere otuz iki makine öğrenimi modeli ve yedi çoklu doğrusal regresyon modeli, performans parametrelerini tahmin etmek için geliştirilmiştir. Model doğruluğu determinasyon katsayısı (R^2), kök ortalama kare hatası (RMSE) ve bağıl hata (RE) dağılımları ile değerlendirilmiştir. Çoklu doğrusal regresyon modelleri pratiklik ve kullanım kolaylığı sağlarken, özellikle DT-7 ve MLP-4 kodlu modeller olmak üzere makine öğrenimi modelleri üstün tahmin doğruluğu sergilemiştir. Bu tez, çiğ noktası dolaylı buharlaştırıcı soğutucunun hesaplamalı akışkanlar dinamiği analizi, optimizasyonu ve performans parametreleri tahmin modellemesinin sistematik olarak bütünleştirilmesinin, verimli çiğ noktası dolaylı buharlaştırıcı soğutucular tasarlamak ve gerçek uygulamalara yönelik hızlı, güvenilir performans tahminleri yapmak için sağlam bir yol sağladığını göstermektedir.

Anahtar Kelimeler: Çiğ noktası buharlaştırıcı soğutma, HAD modelleme, Geometrik optimizasyon, Makine öğrenmesi

GENİŞLETİLMİŞ ÖZET

Günümüzde iklimlendirme ve soğutma teknolojileri, küresel enerji tüketiminin ve sera gazı emisyonlarının önemli bir bölümünden sorumludur. Artan nüfus, şehirleşme ve konfor beklentisi, soğutma sistemlerine olan talebi hızla yükseltmektedir. Özellikle yaz aylarında soğutma yüklerinin artması, elektrik tüketiminde zirve değerlerin görülmesine yol açmaktadır. Konvansiyonel buhar sıkıştırmalı soğutma sistemleri yüksek enerji tüketimleri, yüksek maliyetleri ve çevresel etkileri nedeniyle sürdürülebilirlik açısından tartışmalıdır. Dolayısıyla, daha düşük enerjiyle çalışan, çevreye daha duyarlı ve yenilikçi soğutma teknolojilerine ihtiyaç artmıştır. Özellikle, dolaylı buharlaşmalı soğutucular, düşük enerji tüketimleri ve çevre dostu yapılarıyla öne çıkmaktadır. Ancak bu sistemlerin performanslarının tam olarak anlaşılması, farklı geometrik tasarımlar ve çalışma koşulları altında davranışlarının optimize edilmesi ve son kullanıcıya uygun, hızlı uygulanabilir performans tahmin modellerinin geliştirilmesi için kapsamlı araştırmalara ihtiyaç vardır. Bu açığı gidermesi beklenen bu tez çalışmasında, üç aşamalı bir metodoloji izlenmiştir. Birinci aşamada, farklı konfigürasyonların (Tip 0, Tip 1, Tip 2, Tip 3 ve Tip 4) karşılaştırmalı incelenmesi yapılmış, ikinci aşamada, üstün performans gösteren Tip 2 çiğ noktası dolaylı buharlaştırıcı soğutucunun geometrik optimizasyonu gerçekleştirilmiş, üçüncü aşamada ise hesaplamalı akışkanlar dinamiği simülasyonlarının yüksek hesaplama maliyetlerini ortadan kaldırmak amacıyla doğrusal regresyon ve makine öğrenmesi tabanlı tahmin modelleri geliştirilmiştir.

Tezin ilk aşamasında (Faz 1), literatürde daha önce birçok çalışmaya konu olan (Tip 0, Tip 1, Tip 2 ve Tip 3) soğutucular incelenmiş; buna ek olarak, bu çalışma kapsamında ilk kez ele alınan (Tip 4) ve yine ilk defa hesaplamalı akışkanlar dinamiği yöntemi ile modellenen (Tip 2) dahil olmak üzere beş farklı dolaylı buharlaşmalı soğutucu geliştirilerek karşılaştırmalı analizleri gerçekleştirilmiştir. Bu konfigürasyonlar Tip 0’dan Tip 4’e kadar sınıflandırılmıştır. Tip 0, işlem ve çalışma havası kanallarının tamamen ayrıldığı konvansiyonel dolaylı buharlaşmalı soğutma tasarımını temsil ederken, Tip 1 ve Tip 3 tek açıklıklı, Tip 2 ve Tip 4 ise çoklu açıklıklı yapılarıyla, işlem ve çalışma kanalları arasındaki hava geçişine izin veren yapılarıyla dikkat çekmektedir. Tip 3 ve Tip 4 ayrıca ilave yardımcı bir çalışma kanalı kullanımı ile diğerlerinden ayrılmaktadır. Çalışmada bağımsız değişkenler olarak işlem havası giriş sıcaklığı ($T_{p,i}$), işlem havası özgül nemi ($\omega_{p,i}$), işlem havası giriş hızı ($u_{p,i}$) ve çalışma-giriş havası oranı (β) ele alınmıştır. Bu değişkenlerin etkileri, kapsamlı bir performans değerlendirmesi için belirlenen başlıca performans parametreleri üzerinden incelenmiştir. Bu parametreler; işlem havası sıcaklığındaki düşüşü temsil eden ΔT_p, çalışma havasının nem artışını gösteren $\Delta\omega_w$, yaş termometre etkinliği (ε_{wb}), çiğ noktası etkinliği (ε_{dp}), soğutma kapasitesi (CC), birim alan başına soğutma kapasitesi (CC_a), su tüketimi (WC), soğutma kapasitesi başına su tüketimi (WC_c), fan güç tüketimi (W_f) ve soğutma performans katsayısı (COP) olarak belirlenmiştir.

Faz 1 kapsamında toplam 420 hesaplamalı akışkanlar dinamiği (HAD) simülasyonu gerçekleştirilmiş ve elde edilen sonuçlara göre, çoklu açıklıklı tasarıma sahip Tip 2 konfigürasyonu, farklı giriş koşulları altında diğer tasarımlara kıyasla daha üstün bir performans sergilemiştir. Özellikle çiğ noktası etkinliği ve COP değerlerinde sağladığı avantaj, bu konfigürasyonun sonraki fazlarda daha detaylı incelenmesini gerekli kılmıştır. Birinci fazda yapılan karşılaştırmalı analizler sonucunda, çoklu açıklıklı yapısı sayesinde hem yüksek soğutma etkinliği hem de düşük su tüketimi sağlayan Tip 2 konfigürasyonu, genel anlamda en üstün performansı göstermiştir. Bu nedenle bu çalışmanın ikinci fazında, bu konfigürasyonun geometrik optimizasyonu gerçekleştirilmiştir. Tip 2'nin çoklu açıklıklı yapısı, işlem havasının belirli bölgelerden çalışma kanalına geçişine imkan tanıyarak buharlaşmalı soğutma etkinliğini artırsa da sistemin genel performansının geometrik yapıya yüksek derecede bağımlı olduğu görülmüştür. Dolayısıyla bu faz, tamamen Tip 2'nin geliştirilmesine ve en uygun geometrik parametrelerin belirlenmesine ayrılmıştır. Bu fazda hem geometrik hem de operasyonel olmak üzere beş temel değişken sistematik olarak incelenmiştir: açıklık sayısı (apN), açıklık çapı (apD), kanal uzunluğu (L), kanal genişliği (h) ve çalışma-giriş havası oranı (β). Bu değişkenler, sistem içerisindeki akış yapısını, basınç kaybını ve buharlaşma dağılımını doğrudan etkileyerek, dolaylı olarak soğutucunun ısıl ve hidrolojik performansını belirlemektedir.

Optimizasyon yöntemi iki ana aşamadan oluşmuştur. İlk aşamada, belirli kombinasyonlarda çalışma kanalında ters akış (reverse flow) oluştuğu tespit edilmiştir. Ters akış, çalışma havasının kanal boyunca ilerlemesi gereken tasarım yönünün aksine geri yönde hareket etmesi ve işlem havasına karışması sonucu ortaya çıkan durumdur. Dolaylı buharlaşmalı soğutmanın temel prensiplerine aykırı olan bu davranış, hem ısı ve kütle transfer mekanizmasını bozmakta hem de işlem havasının nemini artırarak soğutulan havanın temel özelliklerini olumsuz yönde etkilemektedir. Bu nedenle ters akış oluşumu, fiziksel olarak kabul edilemez bir çalışma senaryosu olarak değerlendirilmektedir. Bu koşulların sistematik bir şekilde tespit edilebilmesi için lojistik regresyon tabanlı bir sınıflandırma modeli geliştirilmiş ve çalışma kanalında ters akış görülen tüm durumlar geçersiz olarak etiketlenmiştir. Dolayısıyla bu tür durumlar analiz ve optimizasyon çalışmaları kapsamının dışında bırakılmıştır. İkinci aşamada ise yalnızca ters akışın oluşmadığı geçerli koşullar kullanılarak, yanıt yüzeyi metodolojisi (RSM) tabanlı yeni bir regresyon modeli oluşturulmuştur. Bu model, dört temel performans göstergesi olan çiğ noktası etkinliği (ε_{dp}), soğutma kapasitesi (CC), su tüketimi (WC) ve soğutma performans katsayısı (COP) üzerine kurulmuş; her bir performans çıktısı için farklı geometrik parametrelerin etkisini tahmin eden çok boyutlu yüzeyler elde edilmiştir. Bu yanıt yüzeyleri, çok hedefli optimizasyon çalışmalarının temelini oluşturmuştur.

Faz 2 kapsamında toplam 4.200 HAD simülasyonu gerçekleştirilmiş ve bu simülasyonlardan 2.225 adedi, ters akış içermeyen geçerli durumlar olarak değerlendirmeye alınmıştır. Bu geçerli veri kümesi kullanılarak, sistemin performansını maksimize etmeye yönelik beş farklı optimizasyon senaryosu kurgulanmıştır. Her bir senaryo, soğutucu tasarımında farklı bir önceliği temsil etmektedir:

- Temel senaryo (Senaryo 0): Tüm performans göstergelerinin eşit ağırlıkta değerlendirildiği durum,
- Düşük çıkış sıcaklığı (Senaryo 1): İşlem havası çıkış sıcaklığının minimize edilmesi hedeflenmiştir,
- Yüksek kapasite (Senaryo 2): Soğutma kapasitesinin maksimize edilmesi hedeflenmiştir,
- Düşük su tüketimi (Senaryo 3): Su tüketiminin en aza indirilmesi hedeflenmiştir,
- Yüksek COP (Senaryo 4): Performans katsayısının maksimize edilmesi hedeflenmiştir.

Her bir senaryo sonucunda elde edilen optimum geometrik parametreler ve buna karşılık gelen performans değerleri karşılaştırılmış, sistemin hangi tasarım parametreleri ile hangi performans önceliklerinin sağlanabileceği ortaya konmuştur. Örneğin, kanal uzunluğunun (L) artışı çiğ noktası etkinliğini artırırken, aynı anda basınç kaybını da yükselttiği ve dolayısıyla COP üzerinde ters bir etki yarattığı gözlemlenmiştir. Benzer şekilde, açıklık sayısının (apN) artırılması, buharlaşmanın daha homojen dağılmasını sağlarken, açıklık çapının (apD) büyütülmesi, işlem kanalından çalışma kanalına aşırı hava transferine neden olarak su tüketimini artırmıştır. Sonuç olarak, Tip 2 konfigürasyonunun performansı tek bir optimum geometrik tasarımla sınırlı değildir. Dolaylı buharlaşmalı soğutucu tasarımı, sistemden beklenen performans önceliklerine göre şekillendirilmelidir. Bu durum, tek bir "en iyi tasarım" kavramının gerçekte mümkün olmadığını; bunun yerine iklim koşulları, uygulama senaryosu ve enerji-su dengesi gibi kriterler doğrultusunda tasarımın yeniden yapılandırılması gerektiğini ortaya koymaktadır. Bu fazın sonunda elde edilen bulgular, Tip 2 konfigürasyonunun geliştirilmeye en uygun temel tasarım olduğunu bir kez daha doğrulamış ve üçüncü fazda gerçekleştirilecek modelleme çalışmaları için güçlü bir zemin oluşturmuştur. Böylece, HAD analizleriyle belirlenen bu kapsamlı veri seti, sonraki aşamada genişletilerek regresyon ve makine öğrenmesi tabanlı tahmin modellerinin eğitiminde kullanılmıştır.

Tezin üçüncü ve son fazında, Tip 2 çiğ noktası dolaylı buharlaştırıcı soğutucunun performansını tahmin edebilecek öngörü (tahmin) modellerinin geliştirilmesine odaklanılmıştır. Bu aşamada amaç, hesaplamalı akışkanlar dinamiği analizlerinden elde edilen yüksek doğrulukta sonuçları, çok daha düşük hesaplama maliyetiyle yeniden üretebilen matematiksel modeller oluşturmaktır. HAD analizleri, detaylı fiziksel süreçleri doğru şekilde temsil etmesine karşın hem uzun hesaplama süresi gerektirmesi hem de çok sayıda simülasyonun yapılmasının zor olması nedeniyle, gerçek zamanlı kontrol, sistem optimizasyonu veya bina enerji simülasyonu gibi uygulamalarda pratik değildir. Bu kısıtlamayı aşmak amacıyla, üçüncü fazda HAD verilerinden faydalanarak hızlı, pratik ve yüksek doğrulukta çalışan tahmin modelleri oluşturulmuştur.

Bu amaçla, modelleme fazında üretilen toplam 20.480 HAD simülasyonu kullanılmış, ancak ikinci fazda olduğu gibi ters akış gözlemlenen fiziksel olarak geçersiz durumlar elenmiştir. Geriye kalan 17.525 geçerli simülasyon verisi, modellerin eğitilmesi ve test edilmesi için kullanılmıştır. Bu veri seti, sistemin çok geniş bir çalışma aralığını temsil edecek şekilde oluşturulmuştur. Model giriş parametreleri olarak işlem havası giriş sıcaklığı ($T_{p,i}$), işlem havası özgül nemi ($\omega_{p,i}$), işlem havası hızı ($v_{p,i}$), açıklık sayısı (apN), kanal uzunluğu (L), kanal genişliği (h) ve çalışma-giriş havası oranı (β) seçilmiştir. Bu parametreler, sistemin hem psikrometrik hem de geometrik özelliklerini temsil etmekte olup, modelin farklı iklim koşullarında ve farklı tasarım senaryolarında geçerliliğini korumasını sağlamaktadır. Tüm modeller, beş temel çıktı değişkeninin tahmini üzerine yapılandırılmıştır: çiğ noktası etkinliği (ε_{dp}), soğutma kapasitesi (CC), su tüketimi (WC) ve soğutma performans katsayısı (COP). Buna ek olarak, işlem havası çıkış sıcaklığı ($T_{p,o}$), mühendislik uygulamalarında doğrudan kullanılabilir pratik bir parametre olarak ek bir çıktı değişkeni şeklinde modellenmiştir. Bu fazda, iki ana modelleme yaklaşımı kullanılmıştır: Çoklu Doğrusal Regresyon (Multiple Linear Regression, MLR) ve Makine Öğrenmesi (Machine Learning, ML).

- MLR modelleri, matematiksel olarak açık, kolay uygulanabilir ve herhangi bir yazılıma ihtiyaç duymadan kullanılabilecek deterministik denklemler oluşturmak amacıyla geliştirilmiştir. Bu kapsamda, farklı denklem derecelerine ve çapraz terim yapılarına sahip 7 farklı MLR modeli (MLR-1'den MLR-7'ye kadar) üretilmiştir.
- Makine öğrenmesi (ML) modelleri ise daha karmaşık veri örüntülerini yakalayabilen, doğrusal olmayan ilişkileri daha yüksek hassasiyetle çözebilen yöntemleri içermektedir. ML yaklaşımı Karar Ağaçları (Decision Tree, DT), Destek Vektör Makineleri (Support Vector Machine, SVM) ve Çok Katmanlı Algılayıcı Sinir Ağları (Multilayer Perceptron, MLP) olmak üzere üç alt kategoriye ayrılmıştır.

Her bir makine öğrenmesi algoritması, farklı öğrenme fonksiyonları, ağaç sayıları, çekirdek (kernel) türleri veya katman-nöron yapılarına göre optimize edilerek test edilmiştir. Bu kapsamda toplam 32 farklı ML modeli geliştirilmiştir: 10 adet karar ağacı modeli (DT), 6 adet destek vektör makinesi modeli (SVM) ve 16 adet çok katmanlı algılayıcı modeli (MLP). Model performanslarının değerlendirilmesinde determinasyon katsayısı (R^2), kök ortalama kare hatası (RMSE) ve bağıl hata (RE) gibi istatistiksel başarı ölçütleri kullanılmıştır. Determinasyon katsayısı, modelin gerçek veriyi ne ölçüde temsil ettiğini gösterirken, kök ortalama kare hatası tahmin değerlerinin sapma miktarını ifade etmektedir. Bağıl hata analizleri ise modellerin sadece ortalama doğruluğunu değil, aynı zamanda farklı çalışma koşulları altındaki tutarlılığını da değerlendirmek amacıyla kullanılmıştır.

Yapılan analizler sonucunda, MLR modellerinin uygulanabilirlik ve şeffaflık açısından avantajlı, ML modellerinin ise yüksek doğruluk ve genelleme kabiliyeti bakımından üstün olduğu belirlenmiştir. Özellikle DT-7 ve MLP-4 konfigürasyonlarının, HAD tabanlı sonuçlara en yakın tahminleri sunduğu görülmüştür. Sonuç olarak, bu fazda geliştirilen modeller, dolaylı buharlaşmalı soğutucuların performansını HAD çözümüne gerek kalmadan, saniyeler mertebesinde tahmin edebilecek güvenilir bir altyapı sunmaktadır. Bu modellerin hem tasarım optimizasyonlarında hem de gerçek zamanlı kontrol veya enerji simülasyonu uygulamalarında kolayca entegre edilebileceği ortaya konmuştur. Böylece, üçüncü fazın sonunda oluşturulan modelleme çerçevesi, HAD analizlerinin getirdiği yüksek hesaplama maliyetini ortadan kaldıran, hızlı, esnek ve kullanıcı dostu bir alternatif olarak tez kapsamında önerilmiştir.

ACKNOWLEDGEMENTS

I would like to begin by expressing my sincere gratitude to my supervisor, Prof. Dr. Orhan BÜYÜKALACA, for his guidance, encouragement and support throughout the preparation of this thesis. His insight and experience have shaped both the academic depth of this work and my overall research approach, and I am truly grateful for his mentorship.

I also thank the members of my thesis committee, Prof. Dr. Ertaç HÜRDOĞAN, Prof. Dr. Arif ÖZBEK, Assoc. Prof. Dr. Göktürk Memduh ÖZKAN, and Assist. Prof. Dr. Kamil Neyfel ÇERÇİ, for their valuable comments, suggestions and for taking the time to contribute to the refinement of this study. I would also like to extend my appreciation to our department head, Prof. Dr. Hüseyin AKILLI, for his support.

During this period, I was fortunate to receive support from my colleagues. I would like to extend my special thanks to Res. Asst. Umutcan OLMUŞ, whose help and dedication played a significant role in the progress of my thesis. I am also grateful to Res. Asst. Alperen Burak GÜRÜK and Res. Asst. İbrahim DİKER for their collaboration whenever I needed support. Additionally, I would like to thank Assist. Prof. Mustafa DAĞDELEN and Res. Asst. Muhammet Batuhan KÜLTÜR for their contributions throughout this journey. I also thank the Çukurova University Scientific Research Projects (BAP) unit for financial support under contract no: FDK-2023-15552.

At this point, I would like to express my heartfelt gratitude to my dear late mother-in-law, Saadet, whose memory continues to give me strength and courage in every step of my academic life. I am deeply thankful to my siblings, Osman, Seda, Tunahan and Alper, for their continuous support and for always standing by me. I also owe my sincerest thanks to my mother Havva GÜZELEL and my father Galip GÜZELEL for raising me with love, patience and a strong sense of determination. Everything I have achieved is built upon the foundation they have given me.

Finally, I want to express my deepest gratitude to my dear wife, Dr. Bilge GÜZELEL and my dear son, Yiğit Emre GÜZELEL. This journey was long, intense and sometimes overwhelming. There were moments when I could not give them the time they deserved, yet I always felt their love, understanding and constant support with me. Knowing they were there for me, sometimes quietly, sometimes with a simple smile or a kind word, gave me the strength to keep going when the going got tough and reminded me that I was never alone. They are not only a part of my life but also the reason I can overcome challenges and keep moving forward. Their presence has been my greatest source of motivation, courage and peace.

LIST OF TABLES

LIST OF FIGURES

SYMBOLS AND ABBREVIATIONS

Symbols

A	: area (m^2)
apN	: aperture number
apD	: aperture diameter (mm)
c	: regression coefficient
h	: channel gap (mm)
L	: channel length (mm)
$\dot{m}$	: mass flow rate (kg/s)
P	: pressure (Pa)
T	: temperature (˚C)
u	: velocity (m/s)
$\dot{V}$	: volume flow rate (m^3/s)
$\dot{W}_f$	: fanning power (W)

Greek letters

β	: working-to-intake air ratio
ε	: effectiveness
Κ	: predictor function
ρ	: density (kg/m^3)
ω	: humidity ratio (g/kg)

Subscripts

dp	: dew-point
i	: inlet
p	: process
o	: outlet
w	: working
wb	: wet-bulb

Abbreviations

CC	: cooling capacity
CC_a	: cooling capacity per unit area
CFD	: computational fluid dynamics
COP	: cooling coefficient of performance
DT	: decision tree
DPIEC	: dew-point indirect evaporative cooler
FEM	: finite element method
ML	: machine learning
MLP	: multilayer perceptron
MLR	: multiple linear regression
SVM	: support vector machine
WC	: water consumption
WC_c	: water consumption per cooling capacity

1. INTRODUCTION

Global demand for space cooling is rapidly increasing due to economic growth, rising living standards and the accelerating effects of global warming (Güzelel et al., 2025). In residential and commercial buildings, air-conditioning systems account for approximately 35-40% of total electricity consumption, while on a global scale, around 15% of all electricity produced is consumed by these systems (Olmuş et al., 2023). The global stock of air-conditioning units, currently estimated at about two billion, is expected to nearly triple by 2050, driven by growing incomes and warmer climates. This exponential growth poses serious energy and environmental challenges; if no efficiency improvements are made, energy use for cooling could more than double by 2050, straining electricity grids and undermining climate targets (IEA, 2025; Oh et al., 2019).

The modern cooling sector is dominated by mechanical vapor-compression systems, which account for nearly 95% of the market (Wu et al., 2024). However, these systems suffer from well-known limitations. First, their energy density is quite high; even the most efficient models create significant electricity demand during hot summer periods. It is also estimated that at least half of active systems operate at less than 50% the efficiency of the best available technologies (IEA, 2025; Liu et al., 2025). Secondly, conventional air conditioners rely on refrigerants with high global warming potential (GWP). Leakage of these substances contribute significantly to greenhouse gas emissions and ozone layer depletion (Duan et al., 2019). Consequently, the operational cost and environmental impact of compressor-based cooling are becoming increasingly unsustainable. This growing dependency on air conditioning has created a vicious cycle that, as temperatures rise, cooling demand increases, leading to higher fossil fuel consumption and, in turn, further warming. Hence, there is an urgent need for alternative, sustainable cooling technologies, such as evaporative cooling, that can provide thermal comfort while decoupling cooling from excessive energy use and harmful refrigerants (Chua et al., 2013).

Evaporative cooling offers a fundamentally different and passive cooling mechanism that eliminates both refrigerants and high electrical loads (Cuce and Riffat, 2016). By utilizing the latent heat of water evaporation, evaporative cooling systems can reduce air temperature using only a fan and a water circulation pump, thus requiring no energy-intensive compressor (Xuan et al., 2012). This principle has been applied since ancient times and has regained attention in recent years with the advancement of modern heat and mass exchangers (Watt, 1963). Moreover, evaporative cooling technologies can be integrated with renewable energy sources (e.g., solar PV) to achieve near zero-carbon operation (Porumb et al., 2016).

Evaporative coolers are traditionally categorized into two types: Direct Evaporative Cooling (DEC) and Indirect Evaporative Cooling (IEC). In DEC systems, air is cooled by direct contact with water. Hot and dry air is either passed through a wetted medium or sprayed with water. Because the latent heat required for evaporation is absorbed from the air, its dry-bulb temperature decreases while its humidity increases. Although DEC systems are extremely energy-efficient, their cooling capacity is limited by the ambient wet-bulb temperature, which is the lowest achievable temperature under adiabatic saturation (Heidarinejad et al., 2009). Figure 1.1 illustrates the schematic representation and psychrometric process of a DEC system. The performance of a direct evaporative cooler is quantified using wet-bulb effectiveness (ε_{wb}), defined as the ratio of the actual dry-bulb temperature drop to the difference between the inlet dry-bulb and wet-bulb temperatures, as given in Equation 1.1. Furthermore, the increase in air humidity can cause discomfort or even be intolerable in enclosed environments, which restricts the application of DEC systems mainly to open or extremely arid climates (Bom, 1999).

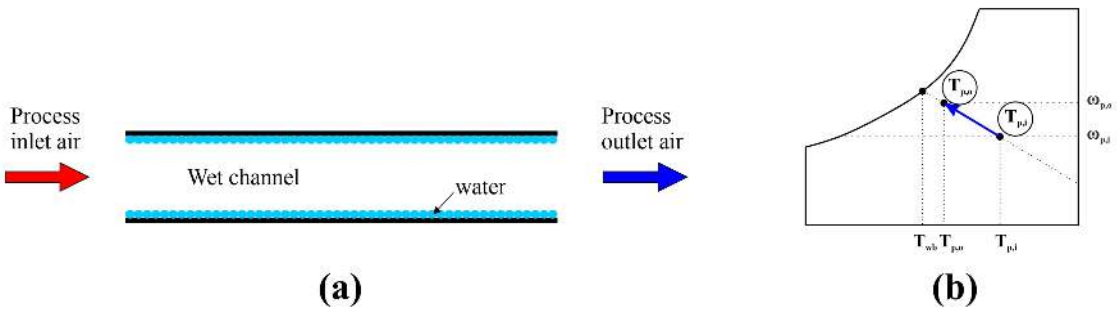

Figure 1.1. Schematic representation (a) and psychrometric diagram (b) of direct evaporative cooler

$$\varepsilon_{wb} = \frac{T_{p,i} - T_{p,o}}{T_{p,i} - T_{wb,i}} \tag{1.1}$$

where;

ε_{wb}: wet-bulb effectiveness (-)
$T_{p,i}$: process air inlet dry-bulb temperature (°C)
$T_{p,o}$: process air outlet dry-bulb temperature (°C)
$T_{wb,i}$: process air inlet wet-bulb temperature (°C)

The main disadvantage of Direct Evaporative Cooling (DEC) is its tendency to increase air humidity during cooling. This limitation has been effectively overcome through the implementation of Indirect Evaporative Cooling (IEC) systems (Caruana et al., 2023). IEC employs a secondary airstream to provide cooling without adding moisture to the supply air. In this process, the supply (or process) air is sensibly cooled along a heat-exchange wall separating it from a secondary working air stream. The working air gains moisture as it passes through the wetted channels and is then exhausted to the ambient environment. As a result, IEC systems deliver cool and dry air to the conditioned space, completely eliminating the humidity issue associated with DEC (Hasan, 2010). However, conventional IEC systems still have fundamental limitations. The lowest achievable temperature in an IEC unit is restricted to the inlet air wet-bulb temperature, and therefore, its performance (similar to that of DEC) is evaluated by the wet-bulb effectiveness, as given by Equation 1.1. In practice, IEC effectiveness typically ranges between 60% and 80%, and the outlet air temperature remains above the dew-point temperature (Hasan, 2012). A schematic representation and a sample psychrometric process of a conventional IEC system are presented in Figure 1.2.

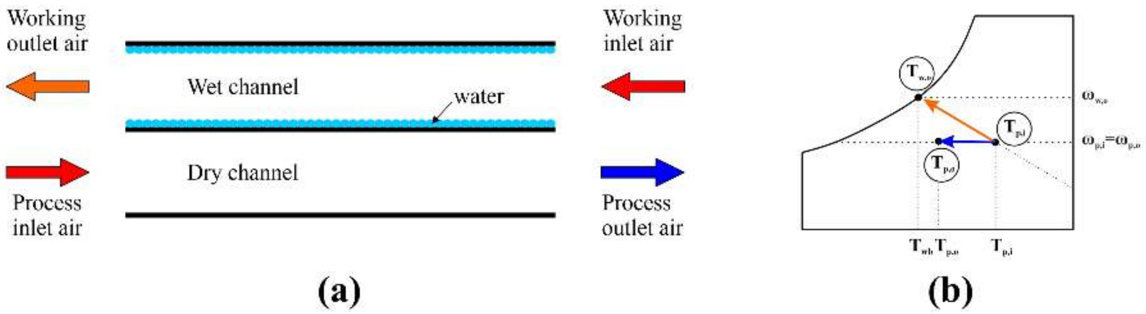

Figure 1.2. Schematic representation (a) and psychrometric diagram (b) of indirect evaporative cooler

Despite their advantages, the humidity increase of DEC and the limited cooling capacity of IEC have restricted their applications to specific climates and operating conditions. To overcome these drawbacks, extensive research efforts have been devoted to enhancing the cooling potential of evaporative systems. As a result of these investigations, a breakthrough concept was introduced by Valeriy Maisotsenko, known as the Dew-Point Indirect Evaporative Cooler (DPIEC) (Maisotsenko et al., 2003). The DPIEC represents an advanced form of indirect evaporative cooling capable of cooling air below the ambient wet-bulb temperature, approaching the dew-point limit. This is achieved through a modified heat and mass exchange configuration, often referred to as the Maisotsenko cycle, in which part of the air is used as a regenerative stream to enhance evaporation and heat transfer. Consequently, DPIEC can deliver air temperatures significantly lower than those attainable by conventional IEC systems (Anisimov et al., 2014). The basic operating principle of a counter-flow DPIEC and its corresponding psychrometric representation are illustrated in Figure 1.3.

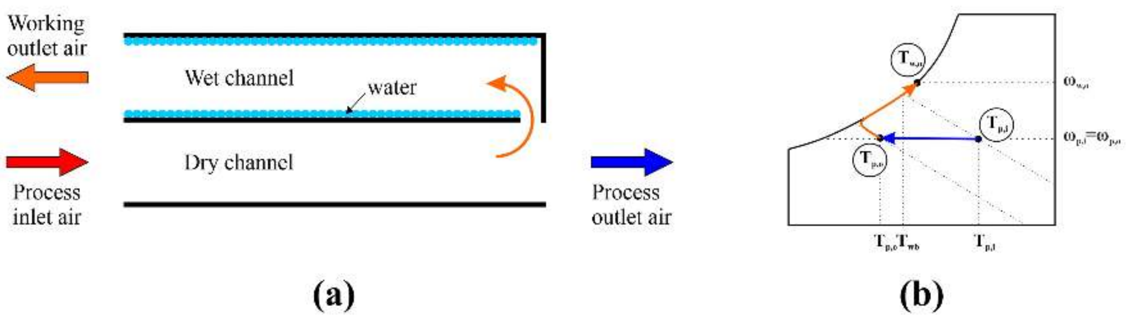

Figure 1.3. Schematic representation (a) and psychrometric diagram (b) of dew-point indirect evaporative cooler

In a Dew-Point Indirect Evaporative Cooler (DPIEC), a portion of the incoming process air, referred to as the working air, is directed through wet channels, where it is cooled by direct evaporation. This moisture-loaded, cooled air subsequently acts as a heat sink, transferring its cooling potential through thin plate heat exchangers to the adjacent dry channels, through which the primary air flows. As a result, the primary air can be cooled below its inlet wet-bulb temperature, since the evaporative medium (the working air) has already been pre-cooled before evaporation occurs. This arrangement establishes a regenerative evaporative cycle in which the evaporation process is staged to utilize the latent cooling potential of air more efficiently than in conventional IEC systems. Theoretically, the outlet air temperature of a DPIEC can approach the dew-point temperature of the incoming air, hence the term "dew-point cooling" (Pacak and Worek, 2021). In practice, studies have demonstrated that in counter-flow DPIEC configurations, the outlet air temperature can be up to 4 °C below the inlet wet-bulb temperature, corresponding to a wet-bulb effectiveness of 114% and a dew-point effectiveness of 84% (Riangvilaikul and Kumar, 2010a).

Two main DPIEC configurations are commonly employed (Cui et al., 2021):

- Counter-flow designs (Figure 1.4a), which achieve cooling closer to the dew-point limit but are more complex to manufacture.
- Cross-flow designs (Figure 1.4b), which are simpler and typically employ perforated plates or multi-stage arrangements.

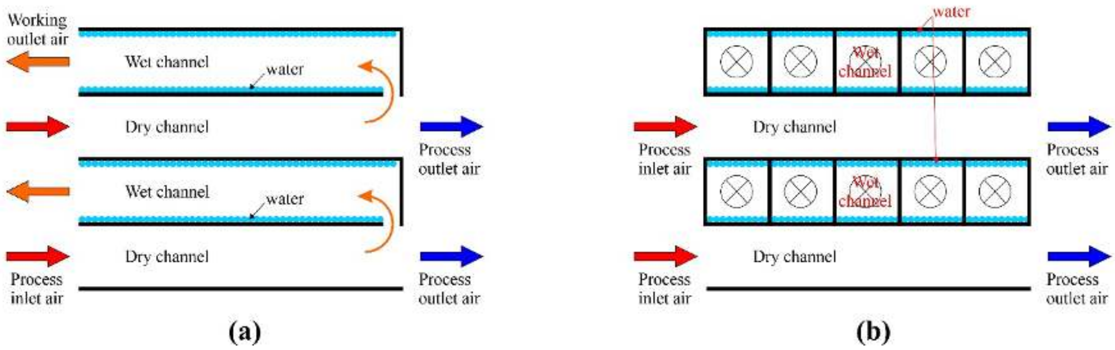

Figure 1.4. Types of dew-point evaporative cooler, counter-flow (a) and cross-flow (b)

Early commercial implementations of DPIEC systems, such as the Coolerado and Climate Wizard units (Coolerado, 2025), validated the concept by demonstrating the ability to deliver air temperatures 15–20 °C lower than the ambient dry-bulb temperature, using only water and low fan power, without adding humidity to the supply air (Caliskan et al., 2011). This technological breakthrough significantly expanded the climatic applicability of evaporative cooling beyond hot and arid regions. Modern DPIEC typologies now encompass a wide range of heat exchanger geometries, including counter-flow, cross-flow and multi-stage hybrid configurations. These units frequently employ polymer or coated paper materials to maximize wetted surface area while minimizing flow resistance. Researchers continue to explore enhancements in heat and mass transfer by incorporating fins, microchannels, perforations and other innovative evaporative surface designs. For instance, introducing small transverse protrusions within wet channels has been shown to improve wet-bulb effectiveness by 10–20% at high air velocities. Similarly, porous or wick-type surfaces promote more uniform water film distribution, resulting in higher overall cooling efficiency (Bruno, 2011; Kabeel and Abdelgaied, 2016; Lee and Lee, 2013; Liu et al., 2025; Wan et al., 2024).

The literature reveals a clear evolution from simple, single-stage designs toward sophisticated regenerative cycles that aim for higher effectiveness and lower pressure losses. Overall, DPIEC systems represent a promising, energy-efficient and refrigerant-free alternative to conventional air-conditioning. By approaching the dew-point temperature, they can achieve far greater temperature reductions than traditional IEC units, making evaporative cooling feasible even in moderately humid climates, including demanding applications such as data centers, where supply air close to the ambient wet-bulb temperature is required (Xiao and Liu, 2024).

The performance of dew-point evaporative coolers, like their predecessors, can be expressed in terms of wet-bulb effectiveness. However, since a dew-point cooler is ideally capable of reducing the process air temperature to its dew-point temperature, its performance is more suitably characterized using dew-point effectiveness (ε_{dp}), as defined in Equation 1.2 (Güzelel et al., 2022a). This parameter indicates the temperature drop achieved by the process air. Additionally, various performance indicators have been proposed in the literature, depending on the intended application. One of the most common is the cooling capacity (CC), which measures the total amount of cooling achieved by the air discharged from the cooler, as given in Equation 1.3 (Cui et al., 2021). Another important parameter is water consumption (WC), which shows the rate at which water is evaporated in the working channel (Equation 1.4) (Kashyap et al., 2021). Finally, the overall energy efficiency of the system can be expressed by the cooling coefficient of performance (COP), defined as the ratio of cooling capacity to the total power consumed by the fans and the pump, if the working water is circulated (Equation 1.5) (Zhao et al., 2008).

$$\varepsilon_{dp} = \frac{T_{p,i} - T_{p,o}}{T_{p,i} - T_{dp,p,i}} \tag{1.2}$$

where;

ε_{dp} : dew-point effectiveness (-)

$T_{p,i}$: process air inlet dry-bulb temperature (°C)

$T_{p,o}$: process air outlet dry-bulb temperature (°C)

$T_{dp,i}$: process air inlet dew-point temperature (°C)

$$CC = \dot{m}_{p,o}(h_{p,o} - h_{p,i}) \tag{1.3}$$

where;

CC: cooling capacity (W)

$\dot{m}_{p,o}$: mass flow rate of process air (kg/s)

$h_{p,o}$: process air outlet enthalpy (kJ/kg)

$h_{p,i}$: process air inlet enthalpy (kJ/kg)

$$WC = \dot{m}_{w,o}(\omega_{w,o} - \omega_{w,i}) \tag{1.4}$$

where;

WC: water consumption (kg/s)

$\dot{m}_{w,o}$: mass flow rate of working air (kg/s)

$\omega_{w,o}$: humidity ratio of working air at outlet (kg/kg)

$\omega_{w,i}$: humidity ratio of working air at inlet (kg/kg)

$$COP = \frac{CC}{\dot{W}_f} \tag{1.5}$$

where;

COP: cooling coefficient of performance (-)

CC: cooling capacity (W)

$\dot{W}_f$: fanning power (W)

Both operational and geometric parameters strongly influence the performance of a dew-point evaporative cooler. Among the operational parameters, the psychrometric properties of the inlet air (temperature and humidity) play a crucial role, along with air velocity and the working-to-intake air ratio (β). From a design perspective, several geometric factors also affect performance, including the channel length (L), channel gap (h), the number and arrangement of apertures (apN), and the aperture diameter (apD). Each of these parameters governs internal flow distribution, heat and mass transfer area, and evaporation intensity, thereby determining the overall cooling efficiency and water usage characteristics of the system (Güzelel et al., 2024; Güzelel et al., 2025).

2. LITERATURE REVIEW

Over recent decades, the growing demand for effective, energy-efficient and environmentally sustainable cooling solutions has stimulated considerable interest in evaporative cooling technologies. Unlike conventional mechanical vapor-compression systems, which are energy-intensive and rely on refrigerants with high global warming potential, evaporative systems exploit the natural process of water evaporation to reduce air temperature, offering a potentially more sustainable alternative for air conditioning. Among these, direct evaporative coolers represent the most basic form of technology, with evidence suggesting that similar principles have been applied, albeit indirectly, since ancient times (Duan et al., 2012).

One of the earliest documented modern works is attributed to Watt (1963), which is not an experimental study but provided a psychrometric design framework and analytical guidelines that laid the groundwork for subsequent developments. With advancements in experimental capabilities during the 1990s, research shifted towards empirical investigations, accompanied by the emergence of mathematical models, often validated against experimental data, to predict system performance (Halasz, 1998). Following these early contributions, numerous studies have been conducted up to the present day. In recent years, particular attention has been devoted to enhancing the efficiency and sustainability of direct evaporative cooling. For example, the study, conducted by Dhamneya et al. (2018), analyzed the thermodynamic performance of cooling pad configurations to increase the heat and mass transfer area in direct evaporative cooling systems. Different geometric pad shapes (triangular, square, pentagonal, hexagonal and octagonal) made of aspen fiber were compared. The findings revealed that the triangle top-flow configuration provided saturation efficiencies of up to 97%. The study demonstrates that pad geometry can significantly improve cooling capacity and efficiency by increasing wetted surface area. Ndukwu et al. (2022) developed a simple direct evaporative cooler suitable for Nigerian conditions, which is low-cost and easy to manufacture. The system used local biomass waste such as jute fiber, palm fruit mesocarp fiber, and charcoal as humectant materials. Experimental results indicate that these systems, with their low cost and sustainability advantages, can be used for short-term storage by farmers, especially during low humidity seasons. Another study examined the effects of air velocity, water flow and multi-stage pad placement on direct evaporative cooler performance under controlled environmental conditions. Biodegradable pads were used, and single, dual and triple stage configurations were compared. The results showed that the three-stage system achieved the highest system efficiency of 65%. These findings highlight the potential of multi-stage DEC systems to increase energy efficiency (Kassie et al., 2025).

Although research is ongoing nowadays, the fundamental limitation of direct evaporative cooling, that lowers air temperature while increasing humidity, has long been recognized. This makes it suitable for hot and arid regions but presents challenges in humid regions, ultimately leading to the development of indirect evaporative coolers.

The fundamental limitation of direct evaporative cooling in terms of increasing humidity has led to the development of systems capable of cooling without adding moisture to the process air. Conventional indirect evaporative cooling (IEC) systems achieve this by separating the process and working air streams with a solid heat transfer surface. On the working side, the air is humidified adiabatically and cooled, while the process air undergoes only sensible cooling and exits at a lower temperature without any change in humidity ratio. This enables indirect evaporative systems to operate effectively in more humid climates, where direct evaporative coolers are less effective, making them suitable for applications where humidity control is critical, such as data centers, industrial processes and certain comfort cooling scenarios (Mahmood et al., 2016; Zhao et al., 2009).

Early conceptual and engineering-based studies on conventional IEC began in the 1980s. Scofield and DesChamps (1984) experimentally examined cross-flow and counter-flow configurations. By the 1990s, Halasz (1998)investigated the effects of wetting rate, air velocity and plate material on IEC performance, providing empirical correlations for design purposes. From the late 1990s to the early 2000s, mathematical modeling gained popularity. Tulsidasani et al. (1997) developed an ε–NTU based model for the performance of plate-type IECs and with this model, the researcher optimized the COP of the cooler. Saman and Alizadeh (2001) proposed a model, incorporating cross-flow geometry and wetting rate. Yang et al. (2011) developed an analytical solution for a counter-flow IEC by simultaneously solving heat and mass transfer equations.

In the following years, subsequent experimental work of Rey Martínez et al. (2004) compared various heat exchanger configurations in conventional IECs. In experiments, parallel and cross-flow arrangements were tested, with measurements of thermal performance and pressure drop. Findings indicated that cross-flow systems achieved higher effectiveness than parallel-flow ones, though at the expense of higher pressure loss. The study emphasized the importance of performance–pressure balance in design optimization. Velasco Gómez et al. (2005) examined the use of IEC systems in agricultural storage applications, measuring performance under several air conditions. Results showed higher cooling effectiveness at lower air velocities; however, insufficient air circulation could compromise storage conditions, supporting the suitability of IECs for agricultural cooling.

Some researchers conducted experimental studies and developed numerical models that they validated with these experimental results. Heidarinejad et al. (2009) investigated the performance of an indirect evaporative cooler using mathematical modeling and experimental validation. Simulations under various climatic conditions and operating parameters were compared with experimental results. The model was found to predict the system's outlet temperature and efficiency with high accuracy. The study also emphasized the significance of water distribution uniformity for system optimization. Zhao (2010), also validating their numerical results experimentally, compared different cooler designs, examining the effects of plate and surface coating material on performance. They concluded that the best channel material under those conditions was wick aluminum because it was less expensive than copper. De Antonellis et al. (2017) tested and modeled an indirect evaporative cooler based on a cross-flow heat exchanger. Numerous experiments were conducted for typical data center conditions, varying the input parameters. The model was extensively validated, and the simulation results were shown to be in very good agreement with the experimental data. Wan et al. (2017) performed a CFD-based analysis of heat and mass transfer characteristics in IECs, considering and calculating variations in local Nusselt and Sherwood numbers. Li et al. (2018) presented a comparative study of a counter–cross-flow plate heat recovery exchanger operating as an IEC under cooling conditions, numerically simulating thermal performance in both vertical and horizontal orientations based on an original mathematical model. Prototypes of both orientations were fabricated and tested for validation. Results showed that, under constant conditions, the vertically oriented exchanger achieved outlet air temperatures 1.5–2 °C lower than the horizontally oriented one, while delivering 24–44% greater cooling capacity.

In recent years, there has been limited research focusing on the performance of conventional IECs. This is because, much like the humidity increase in direct evaporative coolers, indirect evaporative coolers have the natural limitation of cooling only down to the wet-bulb temperature. These limitations have driven researchers to push beyond these limits leading to new research. As a result of these searches, Maisotsenko et al. (2003) invented dew-point evaporative cooler (M-cycle) that can cool the air below the wet-bulb temperature, or rather, ideally, to the dew-point temperature. Beyond the patented design, since the 2010s, numerous alternative configurations have been proposed and investigated through a variety of methods.

Although the dew-point indirect evaporative cooler (DPIEC) initially emerged as a theoretical concept, the most reliable demonstration of its performance can only be achieved through experimental setups. In this context, various experimental studies have been carried out in literature to provide a deeper understanding of the operating principles and performance characteristics of DPIEC systems. One of the first experiments on the new dew-point indirect evaporative cooling (DPIEC) system for sensible cooling applications was performed by Riangvilaikul and Kumar (2010a). The study analyzed the performance of the cooling system in relation to influencing parameters, including inlet air temperature, humidity, and air velocity. The results showed that the system's wet-bulb effectiveness ranged from 92% to 114%, and its dew-point effectiveness ranged from 58% to 84%. The work, being one of the first experimental studies in the field of dew-point evaporative coolers (Figure 2.1), often served other researchers as a kind of validation of their modeling studies. The authors provided an equation (Equation 2.1) that correlated the conditions of the inlet air to predict the outlet air temperature. The inclusion of easily measurable parameters, such as temperature and humidity, allowed this equation to provide a practical yet sufficiently accurate approximation of system performance; therefore, it was highly valued during the development and optimization of various cooling systems. In fact, the DPIEC systems were found to be much more effective at bringing outlet air temperatures below the ambient wet-bulb temperature with no added humidity than conventional evaporative cooling systems.

$$T_{p,o} = 7.65 + 0.152 * T_{p,i} + 681 * \omega_{p,i} \tag{2.1}$$

where $T_{p,o}$ is the outlet air temperature (°C), $T_{p,i}$ is the inlet air temperature (°C), and $\omega_{p,i}$ is the inlet air humidity ratio (kg/kg).

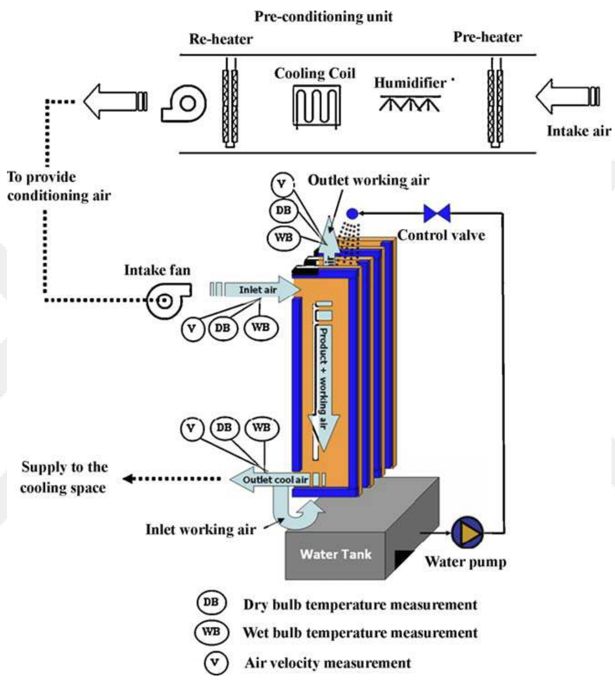

Figure 2.1. The schematic representation of the experimental setup (Riangvilaikul and Kumar, 2010a)

Duan et al. (2016) conducted one of the first systematic experimental investigations of a counter-flow dew-point evaporative cooler, aiming to validate the theoretical potential of DPIECs under real operating conditions (Figure 2.2a). Their results demonstrated that outlet air temperatures could be reduced significantly, often 4–8 °C below the inlet values and in many cases below the ambient wet-bulb temperature, without added humidity. On the other hand, it was concluded that the inlet temperature of the evaporating water has minimal effect on the cooler performance. Performance was strongly dependent on working-to-intake air ratio, inlet temperature and humidity, with wet-bulb effectiveness exceeding 100% under favorable conditions. Building directly on these findings, Duan et al. (2017) advanced research by designing, fabricating, and experimentally testing a compact regenerative evaporative cooler intended for building applications (Figure 2.2b). Unlike the laboratory-scale setup of the previous year, this work emphasized practicality, manufacturability and integration into HVAC systems, showing that high cooling capacity could be achieved with remarkably low energy consumption. The originality of the 2017 study lies in its transition from validation to application, demonstrating dew-point evaporative cooling as a viable low-energy alternative to conventional air conditioning, particularly in hot and dry climates. Taken together, these two works by Duan et al. represent a critical progression: from experimental credibility in 2016 to applied innovation in 2017, thereby enriching the literature on dew-point evaporative coolers and serving as a promising sustainable solution for the built environment.

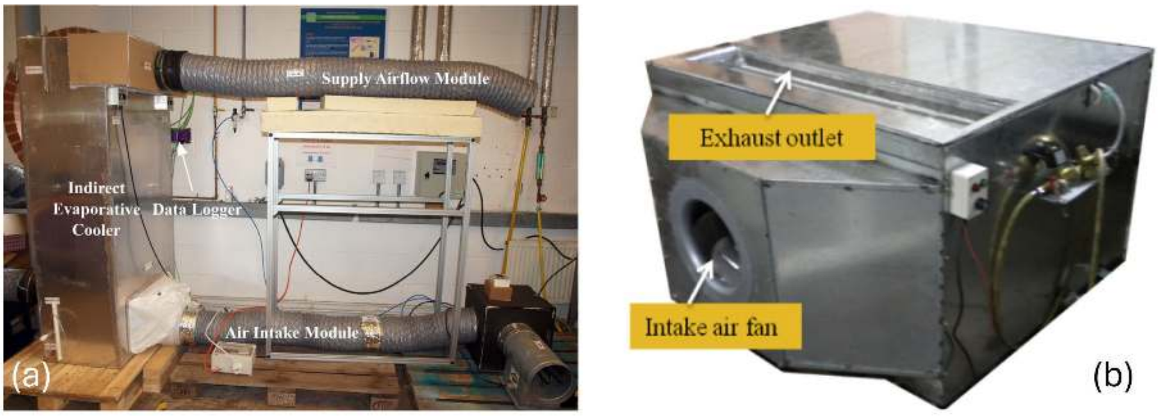

Figure 2.2. Photograph of (a) laboratory scale experimental setup (Duan et al., 2016) (b) compact fabrication (Duan et al., 2017) of dew-point evaporative cooler

Xu et al. (2017) carried out a detailed experimental study on a novel dew-point evaporative cooler configuration, aiming to assess its cooling potential under controlled laboratory conditions. Their results showed that the system could reduce outlet air temperature below the wet-bulb temperature, with wet-bulb effectiveness values ranging from 0.8 to 1.15, depending on operating conditions. Importantly, they observed that system performance was sensitive to inlet air velocity and working-to-intake air ratio, where an optimal balance was required: too low an air ratio resulted in insufficient cooling, while excessively high values led to diminished energy efficiency. Identified an optimum working-to-intake air ratio of 0.364, at which the prototype achieved wet-bulb effectiveness of approximately 1.14, dew-point effectiveness of approximately 0.75 and COP up to 52.5 under the standard test condition (T_{db}=37.8 °C, T_{wb}=21.1 °C). They further showed that lower inlet humidity increases cooling effectiveness and that reducing process outlet temperature slightly raises both effectiveness and COP; in warm and humid climates, they recommend pre-dehumidification ahead of the cooler. This result shows that in very high humidity regions, rather than using dew-point indirect evaporative coolers alone, coupling them to a desiccant air-conditioning system will provide a much more effective cooling solution.

Jia et al. (2019) conducted an experimental investigation in which two counter–crossflow dew-point evaporative coolers with identical flow configurations but different materials were designed, fabricated and tested. One prototype employed aluminum foil (ALF), while the other was made of a polystyrene structure with its wet channel coated by electrostatically flocked nylon fibers

(PS+NL) (Figure 2.3). Both consisted of alternating wet and dry channels arranged in a counter-cross flow pattern, where each pair of channels comprised two crossflow triangular ducts and one counter-flow rectangular duct. Under identical operating conditions, the PS+NL core consistently outperformed the ALF design, delivering process air outlet temperatures that were 0.8–1.2 °C lower and dew-point effectiveness values 0.03-0.075 higher. The measured cooling capacity of the PS+NL unit was also higher, with outlet air temperatures reduced by 4.4–9.2 °C depending on the ambient conditions. This superior performance was attributed to the nylon fiber coating, which enhanced water retention and capillarity on the wetted surface, thereby improving heat and mass transfer. Overall, the PS+NL core achieved a dew-point effectiveness range of 0.47-0.79, bringing its performance close to that of counter-flow IECs and significantly above typical crossflow designs. While the working-to-intake air ratio was fixed at 0.4 in line with established literature rather than optimized experimentally, the study provided strong evidence that material innovation (particularly enhanced wettability of the wet channels) can be as critical as geometric configuration in advancing the cooling performance of counter-crossflow dew-point evaporative coolers.

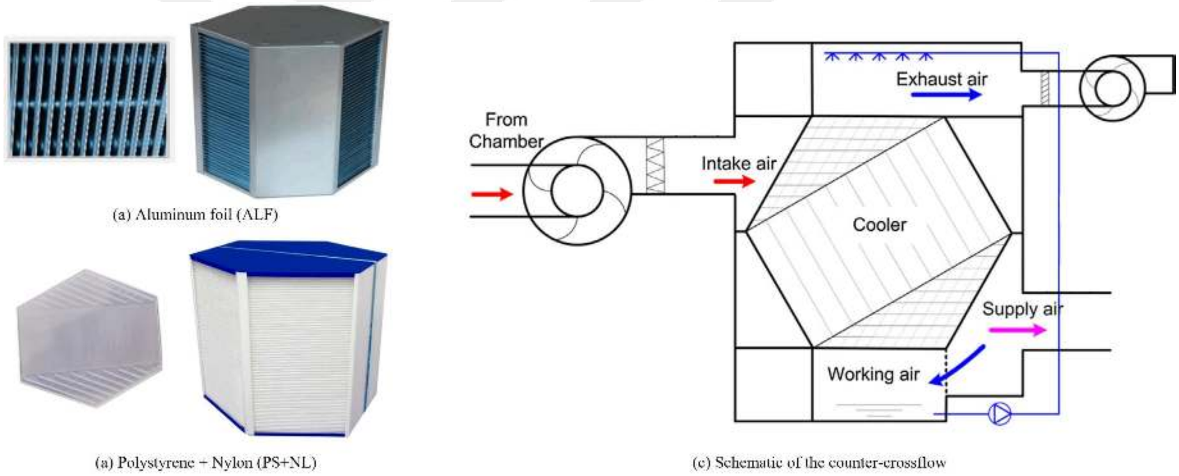

Figure 2.3. Fabricated dew-point evaporative coolers (a) ALF (b) PS+NL (c) schematic of the flow configuration (Jia et al., 2019)

Chu et al. (2021)carried out an experimental evaluation of a counter-flow dew-point evaporative cooler in which five representative conditions were reproduced in the laboratory. Three of these corresponded directly to real climatic conditions of Chinese cities (Jiuquan, Urumqi and Xi'an), while the remaining two were standardized catalog values representing a typical dry region and a typical high-humidity region. The device was fabricated from a polymer plant-fibre composite and tested. Performance metrics were examined by varying the working-to-intake air ratio (β) from 0.41 to 0.66, under standard dry conditions at a constant working-to-intake air ratio of 0.55, the cooler achieved a wet-bulb effectiveness of 1.06, a dew-point effectiveness of 0.76 and a temperature drop of 15.2 °C. More broadly, wet-bulb effectiveness remained about 0.9-1.25 and dew-point effectiveness 0.6-0.9, depending on air psychrometric conditions and β. While increasing the β up to

0.66 further reduced process air temperature and raised effectiveness, it simultaneously decreased useful process outlet air volume, so capacity peaked near β=0.55, which the authors recommended as the most practical operating point. Across all scenarios, the observed temperature drop was 8–18 °C, and the degree of approach to inlet dew-point was 1.2–7.4 °C (average=4.1 °C), confirming close approximation to dew-point cooling. Overall, the study underscored the potential of this configuration to deliver high efficiency in hot-dry climates, while suggesting further refinement for applications in humid regions.

Ali et al. (2021) fabricated a modified cross-flow DPIEC configuration in which the heat and mass transfer surfaces were corrugated rather than flat, aiming to enhance air mixing and prolong the contact path between air and water films. The study systematically compared the conventional flat-plate cross-flow arrangement against several corrugated surface designs with different corrugation angles. Results revealed that the corrugated configuration significantly improved wet-bulb and dew-point effectiveness, with the highest gains observed at larger corrugation angles where the turbulence was more pronounced. At the same time, the pressure drop increased, indicating a trade-off between enhanced cooling performance and fan power consumption. The authors reported that the maximum dew-point effectiveness reached values above 0.8, while wet-bulb effectiveness exceeded 1.0 under certain operating conditions. Importantly, they demonstrated that by optimizing the corrugation angle, the overall cooling coefficient of performance (COP) of the cooler could be improved without a proportionally large increase in pressure drop, making the design highly promising for low-energy building cooling.

Castillo-González et al. (2023) advanced the field by manufacturing testing a cross-flow dew-point evaporative cooler produced entirely via additive manufacturing. The distinctive feature of this study lies in the use of two different composite materials: PLA combined with bronze to form the hydrophobic dry channels, and PVA combined with felt to form the hydrophilic wet channels. After printing, the PVA component was dissolved to expose the porous felt structure, thereby ensuring efficient water absorption and evaporation. The resulting geometry and fabrication concept are depicted in Figure 2.4, which illustrates the three-dimensional scheme of the cooler, a two-dimensional section, and a photograph of the final printed device, respectively. Experimental results demonstrated that cooling effectiveness improved with increasing inlet air temperature and working-to-intake air ratio, while pressure drops became more pronounced at higher airflow rates. The system achieved a dew-point effectiveness approaching 0.9, which is competitive with conventionally fabricated devices of similar scale, and the cooling capacity reached its maximum under the hottest inlet conditions. However, energy efficiency was highest at lower airflow rates, indicating a trade-off between cooling power and fan energy consumption.

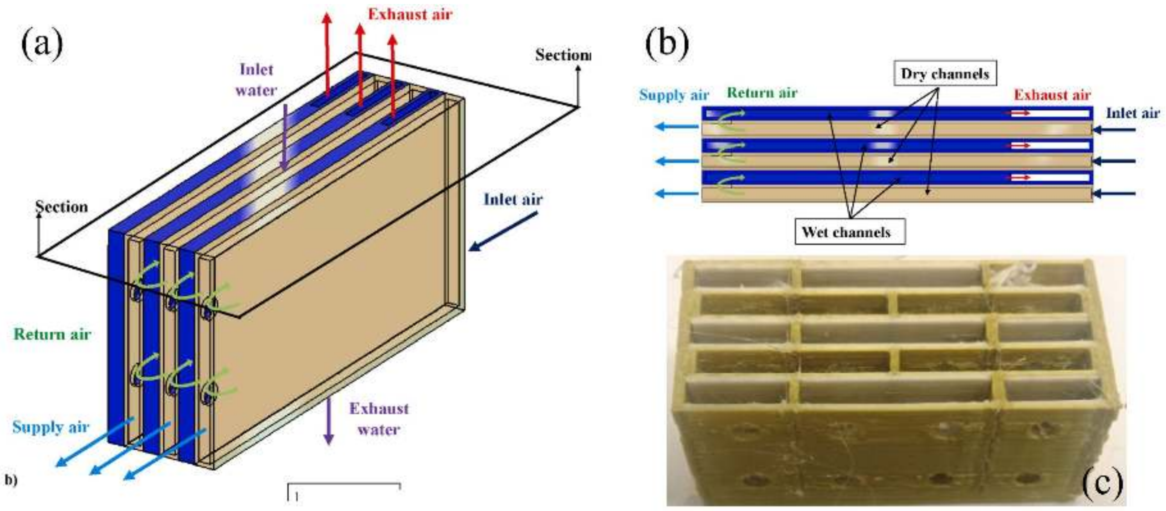

Figure 2.4. Schematic representation of cooler with (a) 3D view, (b) 2D view and (c) photograph of final printed cooler (Castillo-González et al., 2023)

Urso et al. (2024) carried out a comprehensive experimental investigation on a dew-point evaporative cooler specifically designed for application in Mediterranean climates, where high summer temperatures and moderate humidity levels demand efficient cooling solutions. Their study focused on a counter-cross-flow configuration, aiming to balance cooling effectiveness with practical feasibility for building integration. A key feature of this work was the development of an experimental setup that reproduced realistic outdoor operating conditions, with inlet air temperatures ranging from 26 °C to 36 °C and relative humidity spanning 30–60%. Results demonstrated that the cooler achieved dew-point effectiveness between 0.7 and 0.85, while wet-bulb effectiveness values exceeded 1.1 under favorable conditions. The authors also highlighted the significant impact of working-to-intake air ratio, identifying an optimal operating range around 0.3–0.4 that maximized cooling performance without imposing excessive pressure drops. Importantly, the study not only confirmed the robustness of DPIEC technology under Mediterranean climatic conditions but also emphasized its potential for reducing energy demand in residential and commercial buildings.

As one of the most recent experimental studies in the field, Chen et al. (2025) introduce a two-stage dew-point evaporative cooler that departs fundamentally from conventional DPIECs by splitting the cooling duty into sequential stages and redirecting only 10-12% of the process air as working air (thus preserving 88-90% supply). The operating principle of the cooler and the fabricated prototype are shown in Figure 2.5. Tested under subtropical conditions, the system consistently cooled product air below the wet-bulb and near the dew-point, achieving wet-bulb effectiveness up to 1.29, dew-point effectiveness up to 0.99, and a COP of 10.6–14.2 with the laboratory axial-fan setup; in outdoor operation, the COP reached 15-17. Compared with single-stage DPIECs that typically divert 30-50% of product air to the wet side (limiting useful supply volume), this configuration delivers 30-40% more product air at comparable effectiveness. Thus, the cooling capacity is significantly higher than that of conventional DPIECs.

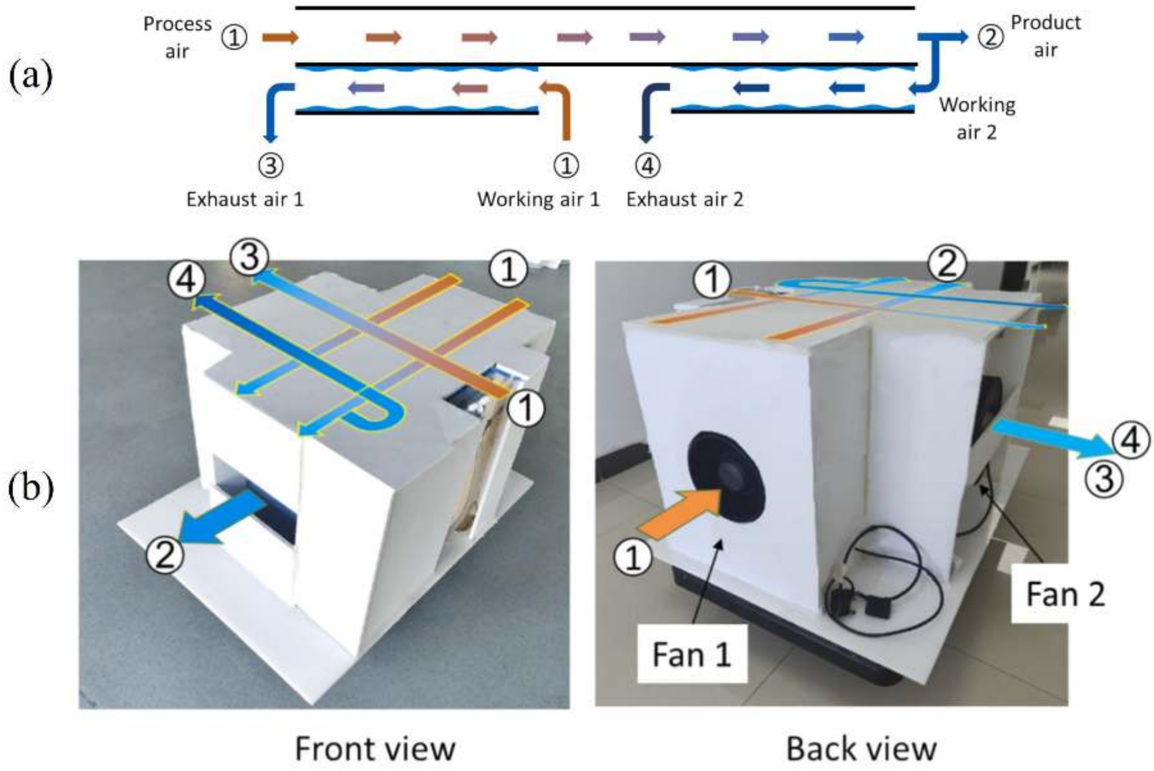

Figure 2.5. (a) Schematic representation of operating principle and (b) photograph of the fabricated cooler (Chen et al., 2025)

As summarized in Table 2.1, experimental investigations have been crucial in validating the feasibility of dew-point indirect evaporative cooling systems. These efforts demonstrate that once a conceptual design is manufactured, its geometry remains fixed, and performance assessment can only be carried out by varying psychrometric parameters such as inlet temperature, humidity, or working-to-intake air ratio. While this provides valuable insights into the practical potential of DPIECs, it inherently limits the scope of exploration. In contrast, numerical simulations offer full flexibility for parametric studies, where both geometrical characteristics (e.g., channel length, width, gap) and operational conditions can be systematically modified. This freedom enables a deeper understanding of the physical phenomena and facilitates the optimization of cooler designs beyond the limitations of experimental prototypes. Therefore, the next section will focus on numerical studies, beginning with the earliest modeling approaches and gradually progressing toward advanced CFD-based analyses.

Table 2.1. Experimental conditions of studies conducted on dew-point indirect evaporative coolers in literature

Reference	**Flow arrangement**	**Channel length (mm)**	**Channel width (mm)**	**Plate thickness (mm)**	**Channel gap (mm)**	**Working-to-intake air ratio**	**Air inlet temperature (°C)**	**Air inlet humidity (g/kg)**	**Air inlet velocity (m/s) or flow rate (m^3/h)**
Riangvilaikul and Kumar (2010a)	Counter	1200	80	0.5	5	0.33	25.0-45.0	6.9-26.4	1.50-6.00
Duan et al. (2016)	Counter	900	314	0.25	6	0.10-0.70	22.7-38.9	9.3-9.4	1.58-2.83
Duan et al. (2017)	Counter	860	458	0.375	3	0.35-0.58	35.9-40.1	11.0	3.60
Xu et al. (2017)	Counter	1000	358	0.2	2.8	0.27-0.45	26.0-37.8	7.9-20.0	1350 (m^3/h)
Jia et al. (2019)	Counter-cross	866 ; 366	-	0.1 ; 0.35	5 ; 3	0.34-0.48	29.5-35.5	13.0-19.0	35-85 (m^3/h)
Chu et al. (2021)	Counter	1000	300	-	5	0.41-0.66	30.4-38.0	6.8-19.9	4.00
Ali et al. (2021)	Cross	900	480	0.115	5	0.30-0.70	30.0-45.0	10.0-12.0	2.00-6.00
Castillo-González et al. (2023)	Cross	400	138	0.8	3	0.40-0.60	30.0-45.0	6.4-17.3	90-120 (m^3/h)
Urso et al. (2024)	Counter-cross	300	300	0.5	9	0.40-0.80	30.0-40.0	5.0-23.0	5.00
Chen et al. (2025)	Counter	500	400	0.32	3	0.09-0.12	29.0-36.0	12.0-17.0	0.30-4.75

Riangvilaikul and Kumar (2010b) developed control volume-based model for a counter-flow dew-point indirect evaporative cooler to predict outlet conditions and effectiveness under a wide range of inlet climates (dry, moderate, humid) and operating parameters (inlet velocity, channel dimensions, working-to-intake air ratio). The model was validated against their experimental data and subsequently applied for parametric optimization. The formulation included one-dimensional balances for sensible energy in the dry channel and coupled heat and mass transfer in the wet channel; assumptions include fully wetted surfaces, laminar flows and negligible wall resistance. The governing equations were discretized using finite differences and solved with a Newton iteration scheme. In their experimental study, several parameters could not be varied; this numerical model was therefore used to investigate their influence. The results showed that smaller channel gaps produced higher effectiveness. For achieving a wet-bulb effectiveness greater than 1.0, channel gaps of 5 mm or smaller were recommended, while gaps of 3 mm or smaller were required to obtain dew-point effectiveness close to 1.0. In addition, as expected, extending the channel length increased the contact surface and time, which led to proportional improvements in both wet-bulb and dew-point effectiveness.

Anisimov and Pandelidis (2014) built a numerical model for a cross-flow dew-point indirect evaporative cooler. The model covered how working air bleeds through apertures into the wet channels and mixes there, and it includes heat transfer on fins. The model results aligned well with published measurements. It showed that denser apertures smooth the temperature–humidity distribution in the wet channel and improve stability. They also found that, with fin rich geometries, most heat and mass transfer can occur on the fins, not the flat plates. Predicted performance was strong: wet-bulb effectiveness was often over 1.0 and dew-point effectiveness up to 0.9. The main design advice was to increase the aperture number to keep the wet working section short and add fins to enhance the heat transfer.

Pandelidis et al. (2015a) numerically compared two counter-flow dew-point indirect evaporative cooler designs: a typical unit (referred to in this thesis as Type 1) and a perforated unit that bleeds working air into the wet side (this thesis Type 2). They used a validated, modified ε–NTU model; they varied channel length and height, channel shape (rectangular, square, triangular, flat), air velocity, and the working-to-intake air ratio. The results showed that the longer channels and smaller channel gap increased both wet-bulb and dew-point effectiveness. Triangular channels provided the highest effectiveness, but flat plates performed nearly as well and are easier to manufacture. Lower air velocity reduced the process air outlet temperature but also lowered cooling capacity. For operation, a practical working-to-intake air ratio band is 0.30–0.45, within which Type 1 is generally preferable. When the ratio rises to 0.47–0.50 or higher, the Type 2 (apertured) design delivered a lower process air outlet temperature and higher effectiveness. Thus, Type 1 suits low-to-moderate air ratios, whereas Type 2 is recommended for higher ratios, subject to acceptable pressure drop and manufacturability. In another study in the same year, Pandelidis et al. (2015b) numerically compared several counter-flow dew-point indirect evaporative cooler arrangements using a validated 1D ε–NTU model that considered heat and mass transfer at finned surfaces and, where relevant, perforated mixing. The comparison set included a typical counter-flow unit (Type 0), a regenerative unit (Type 1), a perforated regenerative unit (Type 2), a counter-flow unit using heat recovery with a cooling coil, a desiccant-assisted regenerative option and a new modified counter-flow design that recirculates a small portion of the process air to the wet side. According to results, when both operated with ambient air, Type 1 achieved a lower process air outlet temperature but at the expense of lower cooling capacity (because a portion of the main air becomes working air); when the Type 0 used exhaust air, it generally exhibited higher efficiency and significantly higher capacity, especially at RH ≥50%. The modified counter-flow configuration outperformed others in many cases, achieving 0.5-5 ℃ lower process air temperatures while maintaining high capacity by adjusting the working-to-intake air ratio. Aperture placement was important in Type 2. At low working-to-intake ratios, apertures near the wet-channel inlet performed best, at higher ratios, a more even distribution yields lower outlet temperatures.

Lin et al. (2016) proposed an improved numerical model for a single-stage, counter-flow dew-point evaporative cooler that includes longitudinal heat conduction and mass diffusion in both air streams, the separating plate and the water film, and allows a temperature difference between plate and film. The model was validated against multiple experimental study from literature with around 4% error in product-air temperature. A key finding was that the working air reaches saturation at a nearly fixed axial location (0.68 m in a 1 m channel), largely independent of inlet state; this point shifts mainly with working-to-intake air ratio and channel length. Another interesting result was that evaporation was not efficient before 0.2 m of the channel inlet section. Parametric results confirmed that the lower inlet velocity, higher working-to-intake air ratio, longer channels and smaller gaps reduced process air outlet temperature and raised effectiveness. Wet-bulb effectiveness varied between 0.42 and 1.47 under different geometric and operating conditions. It was also determined to be greater than 1.0 when the working-to-intake air ratio was greater than 0.5, the channel length was longer than 1.8 m, and the channel gap was less than 5 mm. Consistent with prior studies, longer channels and narrower channel gaps improved cooler effectiveness; this trend was also evident by Pandelidis and Anisimov (2016). In their study, a numerical model of a cross-flow dew-point indirect evaporative cooler was developed to test how design parameters affect performance, and the parametric analysis identified an optimal working-to-intake air ratio of about 0.3-0.4, which balances effectiveness, cooling capacity and COP under moderate climatic conditions.

Baakeem et al. (2021) developed and validated a heat and mass transfer model for a counter-flow dew-point evaporative cooler, then used it to study how geometry and operating conditions affect performance. They compared concentric circular, triangular cases, and stacked plates in the rectangular cases (in total six shape; a circle, rectangles with aspect ratios 6, 8 and ∞, and triangles with 30° and 60°). The analysis varied the intake temperature, humidity, air velocity, hydraulic diameter and channel length. Performance improved with longer channels and declined with larger hydraulic diameter or higher intake velocity; a 2-3 m/s inlet velocity was preferable across all cases. Among shapes, the 60° triangular channel produced the best overall effectiveness, followed by the circular duct, while the rectangular geometry with aspect ratio 6 performed worst; the “infinite” rectangle offered high capacity but with higher water and fan demands. The study reported results in terms of dew-point and wet-bulb effectiveness, COP, cooling capacity and water consumption, and noted practical wetting challenges for non-rectangular ducts, suggesting porous media or fine perforations to improve water distribution.

The increase in computer capacities with technology has made CFD studies popular, which is another numerical solution method. Cui et al. (2015) presented the first CFD-based analysis of a dew-point indirect evaporative cooler (DPIEC), using Comsol Multiphysics software. They built a 2D conjugate heat-and-mass transfer model that permits condensation on the product channel and uses room exhaust air as the working stream, which is critical for hot–humid climates. They investigated two DPIEC configurations, a conventional counter-flow dew-point indirect evaporative cooler (coded as Type 0 in this thesis) and a single apertured, multi-channel counter-flow dew-point indirect evaporative cooler (coded as Type 3 in this thesis). The model was validated against literature data and then used to compare the two designs under Singapore climate. Type 3 provided a lower outlet temperature than Type 0, with wet-bulb effectiveness ranging from 0.38 to 0.68 and 0.41 to 0.72, respectively. While Type 0 required lower fan power, it could only meet 35-47% of the cooling load. In contrast, Type 3 resulted in a higher pressure drop, but still provided higher cooling capacity. The results demonstrated that using Type 3 over the conventional Type 0 was significantly more effective and robust.

Jafarian et al. (2017b) built a CFD model for a counter-flow dew-point evaporative cooler that is closer to physics than earlier 2D/3D models with OpenFoam software. The key step involved a modified wall boundary condition, where momentum, heat and mass balances were solved simultaneously on the separating plate, including entrance region effects. The model was validated with Riangvilaikul and Kumar (2010a) measurements with a maximum error of ±3.53%. A 3D run was only slightly more accurate than 2D but required 14 times more computer processing time, making 2D acceptable for design scans. Parametric results were consistent and practical, showing that lower inlet velocity and higher working-to-intake air ratio reduced process air outlet temperature and raised dew-point effectiveness, but reduced cooling capacity. A channel gap of around 4–5 mm produced a good balance between effectiveness and pressure drop. While the optimum channel length was found to be around 1 m, the optimum working-to-intake ratio was found to be around 0.35.

In another CFD study, Liu et al. (2019) constructed a two-dimensional CFD model with Comsol Multiphysics software for counter-flow dew-point evaporative cooler. In the study, the effects of parameters such as channel dimensions, inlet air velocity and working-to-intake air ratio on cooler effectiveness were evaluated. Also, the saturation distribution and flow field characteristics occurring on wet channel surfaces were analyzed. The results showed that increasing channel length increased effectiveness, while increasing channel gap decreased cooling performance. Furthermore, increasing the process air velocity increased cooling capacity but also increased the process air outlet temperature. The process air outlet temperature was most strongly influenced by the inlet air wet-bulb temperature, so the desired air temperature and cooling capacity of the dew-point evaporative cooler can be obtained by controlling the inlet air wet-bulb temperature.

Gao et al. (2023) numerically examined a counter-flow tubular dew-point evaporative cooler and compared it against a conventional plate design using an axisymmetric model with Comsol Multiphysics software (Figure 2.6). Across inlet temperature ranges of 30–38 °C and inlet humidity ranges of 12–20 g/kg, the tubular unit produced cooler process outlet air by 1.6–3.0 °C and raised dew-point effectiveness by about 0.18 relative to the plate type. The tubular wet channel maintained stronger moisture transport and a longer active cooling region, explaining the observed gains. A base case reported process air outlet temperature 20.1 °C and dew-point effectiveness of 0.86 for the tubular design versus 21.7 °C and 0.72 for the plate. The process occurred with a lower dry side pressure drop (45.6 Pa vs 52.2 Pa) but a higher wet side drop (56.1 Pa vs 20.7 Pa) for the tubular unit. The study presented the tubular geometry as a promising alternative when lower outlet temperatures and higher dew-point effectiveness are required, while it needs improvement for pressure drop and other operational parameters.

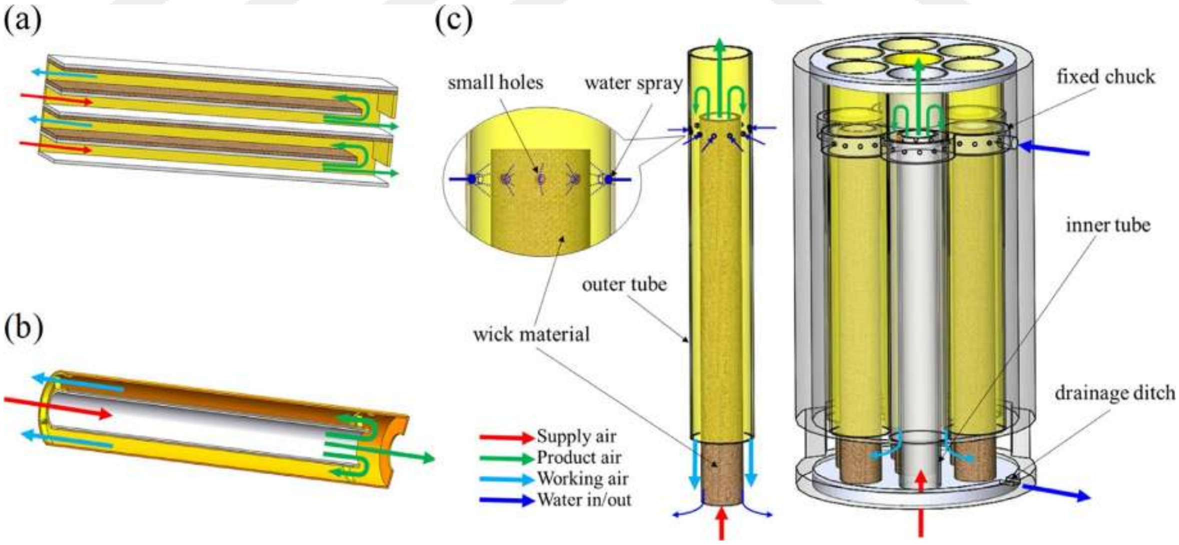

Figure 2.6. Counter-flow DPIEC structure. (a) Plate structure. (b) Tube structure. (c) DPIEC system of tube-type (Gao et al., 2023)

Zhu et al. (2023) developed a three-dimensional numerical model for a counter-flow dew-point evaporative cooler that explicitly accounted for non-uniform water-film distribution and allowed evaporation/condensation boundary conditions with Comsol Multiphysics software. The model agreed with published experimental data with small errors and was more accurate than a conventional two-dimensional model. Parametric results showed clear trends: higher inlet temperature increased cooling capacity and slightly raised dew-point effectiveness; higher inlet humidity reduced cooling capacity but increased dew-point effectiveness; higher inlet velocity increased cooling capacity but lowered dew-point effectiveness; and an optimal working-to-intake ratio around 0.33 maximized cooling capacity. Most importantly, dry (non-wetted) patches in the wet channel negatively affected performance, with the largest penalties occurring when these patches were near the entrance or outlet. These findings highlighted the need to control water distribution to achieve reliable dew-point evaporative cooler performance.

Wang et al. (2024) developed a three-dimensional Comsol model for a counter-flow dew-point evaporative cooler that eliminates the working air separation, cutting flow resistance in the wet side and improving fan efficiency (Figure 2.7). The simulation validated with experimental data within 3% for process air outlet temperature and 8% for pressure drop. Parametric results showed that raising the working-to-intake air ratio lowers the process air outlet temperature, while higher inlet air velocity increases cooling capacity but warms the process air; wet-bulb effectiveness exceeded 100% and dew-point effectiveness approached 99% when velocity was modest, with COP peaking at a working-to-intake air ratio of 0.5–0.6. Channel gap set a clear trade-off: narrower channels produced colder air and higher effectiveness but at higher pressure drop; wider channels improved COP.

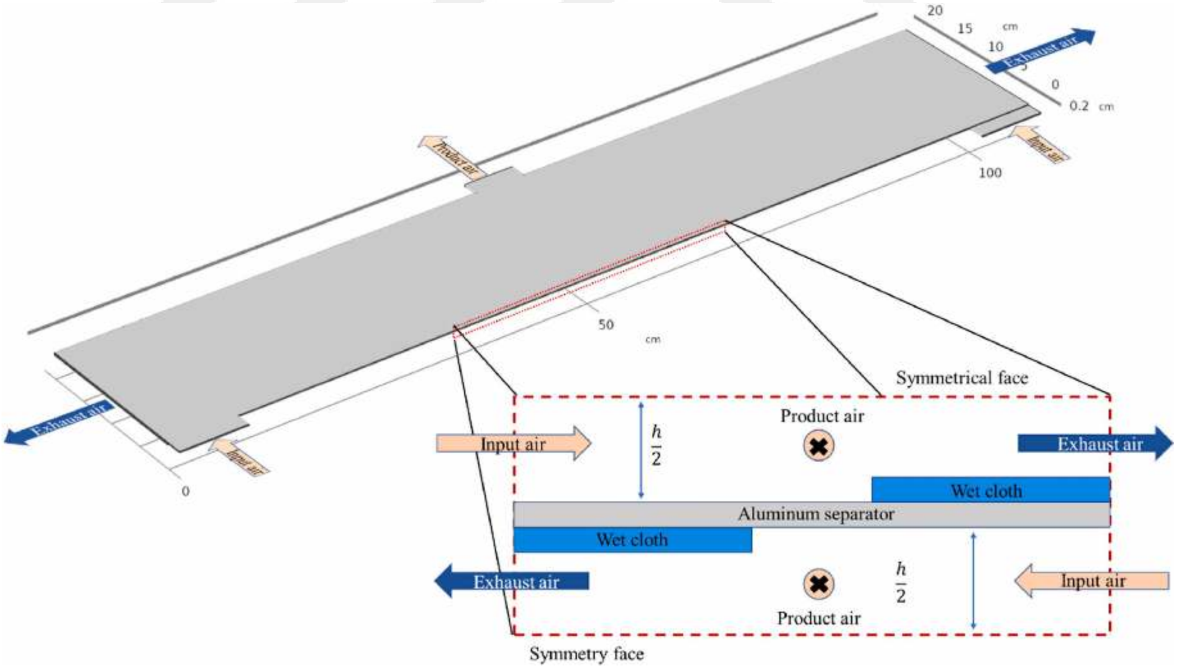

Figure 2.7. Geometry of the simulation model in the study conducted by (Wang et al., 2024)

As summarized in Table 2.2, the numerical studies included broad parameter ranges and tested geometries and operating conditions beyond what the laboratory allowed. Purely experimental work reported the actual performance of a fixed design under real psychrometric inputs. Purely numerical work revealed theoretical limits and sensitivities, but it relied on modeling assumptions.

Studies that combined experiments and simulations bridged this gap that built prototypes, developed models, and then validated those models with measured data. These hybrid studies guided our understanding of the cooler's internal processes and enabled reliable performance assessment and optimization. The next section reviews such combined experimental–numerical studies in chronological order.

Jradi and Riffat (2014) presented a combined numerical and experimental study of a cross-flow, perforated dew-point evaporative cooler for building applications. They built a 2D finite-difference model that coupled heat and mass transfer in the dry and wet channels and validated it against their own laboratory rig. Under a base case condition (inlet 30 °C, 50% RH, working-to-intake 0.33, gap 5 mm, length 500 mm), the optimized design achieved wet-bulb effectiveness of 1.12 and dew-point effectiveness of 0.78. Experiments across several parameters confirmed the main trends that higher intake velocity and larger channel gap reduced effectiveness and raised process air outlet temperature, whereas longer channels and higher inlet temperature improved effectiveness, and COP decreased as air velocity increased.

Lin et al. (2017) combined modeling and experiments to assess a cross-flow dew-point evaporative cooler with and without pre-dehumidification. They developed a 2D finite-volume model that coupled heat and mass transfer in the dry/wet channels and water film, which was validated against prototype and system tests with less than 3% error. Prototype results under moderate humidity showed wet-bulb effectiveness of 1.25 and dew-point effectiveness of 0.85, comparable to counter-flow devices. However, under humid ambient air (30 °C, 18 g/kg), the system achieved only wet-bulb effectiveness of 0.83-0.86, with 2.2 kW cooling capacity and COP of 4.6. To overcome this humidity constraint, they proposed pre-dehumidification. Reducing inlet humidity by 4.7–8.7 g/kg lowered the process air outlet temperature by 5.2–8.5 °C, lifted cooling capacity to 5.2 kW, and increased COP to 10.8.

Wan et al. (2018) proposed a validated numerical framework for a counter-flow dew-point evaporative cooler that first derives heat and mass transfer coefficients with NTU-Le-R formulation and then validates those with a 2D CFD model and laboratory data. The CFD model reproduced the process air outlet temperatures within about ±0.4 °C of measurements, and the NTU-Le-R outputs matched the CFD working-air outlet temperature within about ±0.3 °C, confirmin g consistency. The effects of varying climatic, operating and geometric conditions on the average heat and mass transfer coefficients were investigated. The results showed that wet side heat and mass transfer coefficients rise with higher inlet temperature and humidity, while the dry side coefficient stays nearly constant. Higher inlet velocity increases both heat and mass coefficients, while increasing the working-to-intake air ratio lowers the wet side coefficient and produces a minimum in mass transfer coefficient. Larger channel gap strongly reduces both coefficients, and longer channels decrease average coefficients by shifting more of the flow to fully developed regions.

Table 2.2. Some numerical studies on dew-point indirect evaporative coolers in literature

Reference	**Mathematical model**	**Software**	**Flow arrang.**	**Channel geometry**	**Channel length (mm)**	**Channel gap (mm)**	**Working-to-intake air ratio**	**Air inlet temperature (℃)**	**Air inlet humidty (g/kg)**	**Air inlet velocity (m/s)**
Riangvilaikul and Kumar (2010b)	1D finite-difference	-	Counter	Plate	300-1200	1.0-10.0	0.05-0.95	25.0-45.0	6.9-26.4	1.50-6.00
Anisimov and Pandelidis (2014)	1D ε-NTU	-	Cross	Rectangle, Square and Triangle	250-1250	2.5-20.0	0.20-0.75	25.0-45.0	20-90% (RH)	1.80-7.00
Cui et al. (2015)	2D finite-element	Comsol	Counter	Plate	500	5.0	-	30.0-37.5	18.8-37.8	1.50-2.50
Pandelidis et al. (2015a)	1D ε-NTU	-	Counter	Rectangle, Square and Triangle	200-1500	2.0-10.0	0.30-0.70	-	-	2.00-6.00
Pandelidis et al. (2015b)	1D ε-NTU	-	Counter	Plate	700	3	0.30-0.70	25.0-35.0	42-72% (RH)	3.00
Lin et al. (2016)	1D finite-difference	Matlab	Counter	Plate	600-2000	3.0-8.0	0.10-0.90	25.0-45.0	3.0-18.0	0.50-3.50
Jafarian et al. (2017b)	3D finite-volume	OpenFOAM	Counter	Plate	300-1800	2.0-7.0	0.20-0.65	35.0	8.57	1.50-6.00
Liu et al. (2019)	2D finite-element	Comsol	Counter	Corrugated plate	1000	4.3	0.10-0.90	38.0	8.28	0.60-3.00
Baakeem et al. (2021)	1D finite-volume	Matlab	Counter	Circle, Rectangle and Triangle	300-1300	8.0-19.0 (hydraulic diameter)	0.33	24.0-44.0	20-70% (RH)	1.40-6.40
Gao et al. (2023)	2D finite-element	Comsol	Counter	Tubular	500-1000	1.0-6.0 (radius)	0.10-0.80	30.0-38.0	12.0-20.0	0.50-4.50
Zhu et al. (2023)	3D finite-element	Comsol	Counter	Plate	1200	5.00	0.10-0.70	30.0-45.0	6.0-26.0	1.00-6.00
Wang et al. (2024)	3D finite-element	Comsol	Counter	Plate	1080	2.00-7.00	0.10-0.90	30.0-46.0	10-80% (RH)	-

Pakari and Ghani (2019a) examined a counter-flow dew-point evaporative cooler using both a simplified 1D model and a detailed 3D CFD model and validated against a laboratory prototype. Experiments reached wet-bulb effectiveness up to 1.25. The 1D and 3D models reproduced temperature profiles along both channels with good agreement; on average, the 1D model predicted a 1.86% lower process air outlet temperature than the 3D model. Relative to measurements, the 3D and 1D prediction errors were within 8.5% and 10%, respectively, while the 3D runs required much more CPU time.

Lv et al. (2020) fabricated a dew-point evaporative cooler (coded as Type 3 in this thesis) as a laboratory prototype and developed a CFD model with ANSYS Fluent software. The CFD model reproduced dry and wet side outlet temperatures to within 10% error of measurements. The sizing of the cooler was also carried out with simulations. With the same inlet air parameters, the small-sized model can cool the air with higher effectiveness.

Comino et al. (2022) combined laboratory testing with a detailed ε–NTU model to design a counter-flow dew-point evaporative cooler for different buildings. The prototype (polymer plates with a hydrophilic coating) was tested over wide inlet air condition ranges and working-to-intake air ratio (0.2–0.8), achieving dew-point effectiveness up to 0.87. The model, segmented into 100 sub-exchangers, closely matched experiments (ΔT deviation ≤ 0.7 °C). Results of the model were clear: COP peaked at low air ratio (0.2), reaching 50.26, 44.19, and 37.14 for office, restaurant, and auditorium, respectively, whereas cooling capacity per unit cooler volume was maximized at an air ratio of approximately 0.6. Operating intersection points that balance COP and cooling capacity were clustered near the working-to-intake ratio of 0.35 for offices, 0.30 for restaurants, and 0.31 for auditoriums.

Wu et al. (2024) presented a validated 2D CFD model to study a counter-flow dew-point evaporative cooler in which dry channels were macro-roughened with staggered ribs (Figure 2.8). The prototype was tested over a wide range of inlet temperatures, humidities, air velocities and working-to-intake air ratios. The key mechanism was the formation of detached vortices near the ribs, which disrupted boundary layers and boosted convective transfer: average Nusselt numbers rose up to 4 times in the dry channel and 1.1 times in the wet channel, and Sherwood numbers in the wet channel rose by 1.1 times compared with flat channels. As a result, at higher inlet velocities, the roughened surface limited performance reduction, delivering 2.3–3.0 °C lower process air outlet temperature and 0.14–0.18 °C higher dew-point effectiveness than a flat channel of the same size. The roughened channel also reached over 0.8 of dew-point effectiveness at a working-to-intake air ratio of 0.5, which would otherwise require 0.8 for a flat plate.

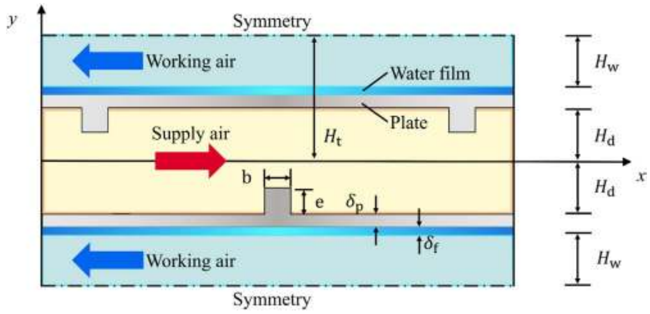

Figure 2.8. Model geometry of roughened channels in the study conducted by (Wu et al., 2024)

Liu et al. (2025) presented a numerical study of an apertured counter-flow dew-point IEC, developing a one-dimensional finite-difference model with Fortran programming and validating it both on their own test rig and against literature data. The results showed that the apertures improved performance only at low working-to-intake air ratios (<0.5), with the single-apertured cooler performing best at higher air ratios; the non-perforated cooler underperformed the perforated variants at almost all working-to-intake air ratios. At a working-to-intake air ratio of 0.1, the multi-perforated model reduced the outlet air temperature by 4 °C and increased effectiveness (wet-bulb from 0.98 to 1.35, dew-point from 0.64 to 0.89) and cooling capacity (from 3.9 to 5.4 W) relative to the non-apertured design.

Sulaiman et al. (2025) proposed and tested a shell-and-tube dew-point evaporative cooler and benchmarked it against a flat-plate design. A 1D finite-difference model was solved with EES software and then validated on a laboratory prototype across 25–50 °C air temperature, 5.2–16.7 g/kg air humidity and 0.2–0.8 working-to-intake air ratio. Model and experiment deviations for process air outlet temperature, effectiveness and cooling capacity stayed within a few percent. The prototype reached wet-bulb effectiveness of 1.35 and dew-point effectiveness up to 0.99, including an extreme test that dropped 53 °C to 18.9 °C (5.2 g/kg air humidity). Trends were consistent that a higher air ratio lowered process air outlet temperature but reduced cooling capacity, a higher inlet velocity raised cooling capacity but warmed the process air. In a fair numerical comparison at equal volume and channel areas, the shell-and-tube cooler delivered 3.1 °C colder outlet process air on average, higher dew-point effectiveness and 12% higher COP than the flat plate configuration.

Table 2.3 listed the configurations, modeling methods and boundary conditions for the hybrid (experimental–numerical) studies given above. The next section turns to alternative modeling methods that include analytical formulations, regression-based correlations and machine learning models for prediction, and multi-objective optimization.

Table 2.3. Some hybrid (experimental-numerical) studies on dew-point indirect evaporative coolers in literature

					Channel length (mm)		Channel gap (mm)		Working-to-intake air ratio		Air inlet temperature (°C)		Air inlet humidity (g/kg)		Air inlet velocity (m/s)	
Reference	**Mathematical model**	**Software**	**Flow arrangement**	**Channel geometry**	*Experiment (or base)*	*Numeric (or parametric)*	*Experiment (or base)*	*Numeric (or parametric)*	*Experiment (or base)*	*Numeric (or parametric)*	*Experiment (or base)*	*Numeric (or parametric)*	*Experiment (or base)*	*Numeric (or parametric)*	*Experiment (or base)*	*Numeric (or parametric)*
Jradi and Riffat (2014)	2D finite-difference	Matlab	Cross	Plate	500	100-800	5.0	1.0-15.0	0.33	0.10-0.90	30.0	25.0-43.0	50% (RH)	50% (RH)	2.00	0.50-6.00
Lin et al. (2017)	2D	Matlab	Cross	Plate	-	-	3.0	-	0.45	-	30.0	-	18.0	6.0-18.0	1.50	-
Wan et al. (2018)	2D finite-element	Comsol	Counter	Plate	600	200-1000	4.5	1.0-7.0	0.33	0.10-0.90	30.0	25.0-45.0	13.3	5.0-21.0	2.00	0.50-3.50
Pakari and Ghani (2019a)	1D ε-NTU 3D finite-element	Comsol	Counter	Plate	500	200-2000	2.0	2.0-10.0	0.35	0.10-0.90	29.2-44.2	30.0-45.0	8.0-17.5	6.0-20.0	0.04-0.07 kg/s (m)	0.03-0.07 kg/s (m)
Lv et al. (2020)	Finite-volume	Ansys	Counter	Plate	1200	-	5.0	-	0.25	-	35	15.0-35.0	10.0	-	2.00	-
Comino et al. (2022)	ε-NTU	EES	Counter	Plate	1200	1200	3.4	3.4	0.20-0.80	0.20-0.80	32.0-43.0	40.0	6.0-13.0	9.00	3000-4500 m^3/h (V)	288-5040 m^3/h (V)
Wu et al. (2024)	2D finite-element	Comsol	Counter	Roughened plate	600	-	4.0	-	0.20-0.80	0.20-0.90	30.0-38.0	30.0-44.0	12.0-24.0	12.0-26.0	2.00-4.00	2.00-5.50
Liu et al. (2025)	1D finite-difference	Fortran	Counter	Apertured plate	1000	200-1000	5.0	4.0-12.0		0.10-0.70	20.1-49.9	28.0-36.0	9.6	9.0-17.0	2.00	1.00-9.00
Sulaiman et al. (2025)	1D finite-difference	EES	Counter	Shell and tube	850	400-2400	5.0	-	0.20-0.80	-	25.0-50.0	25.0-45.0	5.2-16.7	2.0-20.0	1.00-2.20	-

Cui et al. (2016) developed a regression-type performance correlation (Equation 2.2) for a counter-flow dew-point evaporative cooler (coded as Type 3 in this thesis) by reducing the governing heat-mass equations to three dimensionless groups and fitting the dimensionless outlet temperature as;

$$T_{p,o} = \xi \pi_1^a \pi_2^b \pi_3^c \tag{2.2}$$

where ξ is dimensionless coefficient-dependent humidity ratio, π is dimensionless group, and a, b, c are regression constants. π_1 combines the process side Stanton number with the length and gap of the channel (L/h), so longer channels, narrower gaps improve performance. π_2 links working-to-intake air ratio and flow rate, so more working flow lowers outlet temperature but may reduce capacity. Finally, π_3 represents inlet air psychrometric features. The correlation was validated with experimental data from literature with maximum 12% error. Regression-based equations were used not only to predict the outlet conditions but also for optimization of the cooler.

Pandelidis and Anisimov (2016) optimized a commercial-scale cross-flow dew-point evaporative cooler using response surface regression. With fixed external dimensions (length 0.5 m, total height 0.5 m, channel height 3 mm), they defined three objectives (dew-point effectiveness, volume specific cooling capacity and COP) and five factors from air specification. Single objective optimization led to conflicting optimum points, so they offered a multi-objective optimization for dew-point evaporative coolers.

Another tool that researchers use is machine learning to predict performance of the dew-point evaporative coolers. Jafarian et al. (2017a) developed a neural network model for a counter-flow dew-point evaporative cooler, trained on data generated by a validated numerical model solved with OpenFoam software. The model predicted process air outlet temperature within ±1 °C, then enabled multi-objective optimization to maximize dew-point effectiveness, cooling capacity and COP and minimize process air outlet temperature, pressure drop and specific area. The study showed that machine learning models, once grounded in a trusted physics model, can deliver fast and accurate design optimization for dew-point coolers.

Another study that collected data from a validated numerical model to train machine learning models was conducted by Zhu et al. (2017). The artificial neural network (ANN) model reproduced experimental trends with an average error of about 4%. Using the model, the authors performed parametric studies and optimization. They reported that the optimal working-to-intake air ratio falls as ambient temperature or relative humidity increases and typically lies in the range 0.30–0.36.

Dizaji et al. (2018) developed an analytical model for an apertured dew-point evaporative cooler (coded as Type 2 in this thesis), for the first in the literature, enabling the air temperature and humidity to be solved. The model was based on the "spray-water" assumption (the working channel surface is completely wet and the wet plate temperature is assumed constant) and was validated with numerical results. Furthermore, Dizaji et al. (2020) also presented a new analytical framework based on the "wet surface theory," where the wet plate temperature varies along the channel and evaporation is determined by airflow rather than water flow. This model reproduces not only the outlet states but also the temperature and humidity distributions along the dry channel and wet channel. It was experimentally validated in a unique test setup, and sensitivity analysis was performed for several psychrometric and operational parameters. Thus, the second study expands on the first “spray-water” limited approach, providing both physical insight and experimental support at the dispersion level, while also clarifying that the theoretical upper limit of apertured dew-point evaporative cooler performance is the wet surface regime.

Akhlaghi et al. (2019) developed a fast multiple polynomial regression model to predict dew-point evaporative cooler performance without solving heat and mass transfer equations. Using thousands of numerical and experimental data, they predicted five outputs (wet-bulb effectiveness, dew-point effectiveness, cooling capacity, COP and pressure drop) against four operating inputs (inlet air temperature, relative humidity, velocity and working-to-intake air ratio) and three geometric descriptors (channel height, channel gap and number of layers). An 8th-degree global polynomial, produced with 7857 data, yielded maximum relative errors of 2.53% for wet-bulb effectiveness, 3.54% for dew-point effectiveness, 6.1% for cooling capacity, 7.54% for COP and 0.07% for pressure drop. In a follow-up study, Akhlaghi et al. (2020) built another model using a feedforward neural network trained on a larger dataset, input and output parameters, and combined this model with a constraint multi-objective genetic algorithm. Optimization was performed on four Köppen-Geiger climate classifications (Miami, Doha, Rome, Beijing). The proposed settings were around 2 m/s inlet velocity, 0.21-0.25 working-to-intake air ratio, 800-840 mm channel length, 5-6 mm channel gap, and approximately 160 layers. Achieved annual COP gains of up to 70%, surface area reductions of 24% and power savings of approximately 49% compared to the base case, with virtually no change in cooling capacity. As a continuation of the first two works, Akhlaghi et al. (2021) used machine learning models to forecast the hourly performance of the same dew-point evaporative cooler through year 2050. They trained a deep neural network on the dataset used in the previous study and applied several methods to forecast the base and optimized cooler. Using hourly weather data for Beijing, Doha, Miami and Rome, the optimized cooler outperformed the base design and achieved large power savings despite more operating hours from 2020 to 2050.

Pakari and Ghani (2019b) built second order regression models for a counter-flow dew-point evaporative cooler using response surface methodology on data from a validated numerical model and a laboratory prototype. Inputs were inlet air temperature, relative humidity, velocity, working-to-intake ratio, channel length and gap, while outputs were outlet temperature, outlet relative humidity and wet-bulb effectiveness. The regressions matched the numerical model and experiments within 4% and 10%, respectively.

Lin et al. (2020) coupled a 2D CFD model of the dew-point evaporative cooler that was produced with Comsol Multiphysics software with a genetic algorithm optimization method. The multi-objective and single-objective optimizations were compared, and desirability-based multi-objective route was recommended for the complex internal structure of the dew-point evaporative cooler.

Gupta et al. (2022) conducted an experimental study on a dew-point evaporative cooler and then built a machine learning predictor of its energy and exergy performance from the test data. Six operating inputs were used, inlet air temperature, flow rate, humidity, water flow rate, inlet water temperature and working-to-intake air ratio, to predict dew-point effectiveness, cooling capacity, COP and exergy efficiency. Linear and polynomial models were tested; the linear model performed best with a training R^2 of 0.997 and a testing R^2 of 0.991.

Hua et al. (2024) built a machine learning model for a dew-point evaporative cooler by training a 4^{th}-degree polynomial regression on 625 cases drawn from an analytical model that was experimentally validated. The inputs covered process inlet air temperature 18–58 ℃, inlet air relative humidity 9–49% and working-to-intake air ratio 0.2–0.6; the model achieved R^2 of 0.999 for outlet temperature and was cross-checked on the test rig. Using the model to generate 3600 additional points, they mapped interactions and identified a distinct optimum working-to-intake air ratio of 0.45 for maximizing total cooling capacity. Dizaji et al. (2025) used the same data set employed by Hua et al. (2024) for model training to examine the impact of geometric features on the performance of a dew-point evaporative cooler. The results showed strong and correlated trends: longer channels and narrower gaps lowered the process air outlet temperature and increased wet-bulb efficiency, while also increasing pressure drop. Table 2.4 compiles the modeling and prediction studies that use analytical formulations, regression correlations and machine learning algorithms.

Table 2.4. Some modeling studies on dew-point indirect evaporative coolers in literature

Reference	Modeling method	Software	Flow arrang.	Channel geometry	Channel length (mm)	Channel gap (mm)	Working-to-intake air ratio	Air inlet temperature (°C)	Air inlet humidity (g/kg)	Air inlet velocity (m/s)	Predicted parameter
Cui et al. (2016)	Correlation regression	-	Counter	Plate	400-1400	6.0-12.0	0.10-0.80	22.0-38.0	8.0-12.0	0.70-3.50	$T_{p,o}$
Pandelidis and Anisimov (2016)	Response surface optimization	-	Cross	Plate	500	3.0	0.37-0.58	25.0-40.0	30-70% (RH)	0.10-0.26 kg/s (m)	ε_{dp}; CC; COP
Jafarian et al. (2017a)	Machine learning optimization	Matlab	Counter	Plate	400-600	2.0-6.5	0.15-0.35	31.0-45.0	3.8-17.5	2.00-3.50	$T_{p,o}$; ε_{dp}; CC; COP; ΔP; A_s
Zhu et al. (2017)	Machine learning regression	Matlab	Counter	Plate	500	5.0	0.20-0.50	22.0-36.0	20-70% (RH)	0.60-3.00	$T_{p,o}$; ε_{dp}
Dizaji et al. (2018)	Analytical	Matlab	Counter	Apertured plate	700	-	-	40.0	6.0	3.00	$T_{p,o}$; $T_{w,o}$
Akhlaghi et al. (2019)	Correlation regression	R	Counter	Corrugated plate	1000-3000	4.0-8.0	0.10-0.90	25.0-45.0	12.5-50.0% (RH)	0.30-3.00	ε_{wb}; ε_{dp}; CC; COP; ΔP
Pakari and Ghani (2019b)	Correlation regression	-	Counter	Plate	500-1000	2.0-5.0	0.15-0.50	26.0-45.0	10-50% (RH)	0.50-1.50	$T_{p,}$; $RH_{p,o}$; ε_{wb}
Akhlaghi et al. (2020)	Machine learning optimization	-	Counter	Corrugated plate	800-3000	4.0-8.0	0.10-0.80	25.0-45.0	10-80% (RH)	0.30-3.30	ε_{wb}; ε_{dp}; CC; COP; A_s
Dizaji et al. (2020)	Analytical	Maple	Counter	Apertured plate	400-1200	1.0-5.0	0.10-0.70	25.0-55.0	5.0-15.0	0.01-0.09 kg/s (m)	$T_{p,o}$; $T_{w,o}$; $\omega_{w,o}$; ε_{wb}; ε_{dp}
Lin et al. (2020)	Machine learning optimization	Matlab	Counter	Plate	500-2000	1.0-10.0	0.01-0.99	-	-	0.50-6.00	ε_{dp}; CC; COP
Akhlaghi et al. (2021)	Machine learning regression	-	Counter	Corrugated plate	800-3000	4.0-8.0	0.10-0.90	25.0-45.0	10-80% (RH)	0.30-3.30	ε_{wb}; ε_{dp}; CC; COP; ΔP; A_s
Gupta et al. (2022)	Machine learning regression	Python	-	Plate	900	5.00	0.30-0.75	27.5-45.0	18.0-24.0	0.50-2.25	ε_{dp}; CC; COP; η_{exergy}
Hua et al. (2024)	Machine learning regression	Python	Counter	Plate	100	1.00	0.20-0.60	-	-	0.8-4.8 L/s (V)	$T_{p,o}$; ε_{wb}; CC
Dizaji et al. (2025)	Machine learning regression	Python	Counter	Plate	5-250	0.5-4.5	0.20-0.60	-	-	0.8-4.8 L/s (V)	$T_{p,o}$; ε_{wb}; CC; ΔP

From the reviewed literature, it is evident that a wide spectrum of studies has been conducted on dew-point evaporative coolers. Building upon this foundation, the present thesis introduces a three-stage framework of comparison, optimization, and prediction, which extends the state-of-the-art by offering broader scope and greater depth within the family of indirect dew-point evaporative coolers.

- First, five different flow configurations (Type 0–4) were fairly compared under identical geometric specifications (L = 1000 mm, h = 5 mm, δ = 0.5 mm), and a total of 420 independent CFD runs were performed in this phase, thereby eliminating design bias and isolating the effect of configuration on performance only.
- While the existing literature has predominantly focused on Type 1 (conventional dew-point evaporative cooler), a detailed CFD analysis of the multi-aperture configuration (Type 2) has, for the first time in the open literature, been carried out within this thesis.
- In addition, a completely new configuration (Type 4) combining the channel architecture of Type 3 with the multi-aperture approach of Type 2 has been proposed.
- In the second phase, for the best-performing configuration of the first phase, Type 2, all combinations of input conditions were conducted over aperture number (apN), aperture diameter (apD), channel length (L), channel gap (h) and working-to-intake air ratio (β).
- Within the 4200-case design space, the “reverse-flow” scenario, which was addressed for the first time in the literature, was automatically identified and eliminated using two logistic regression models. In this study, treating the aperture diameter (apD) as an independent design variable is also a first in the literature, and the mapping of reverse-flow conditions across the design space has been quantitatively demonstrated.
- Multi-objective optimization based on response surface/desirability was performed on 2225 valid cases where no reverse flow occurs out of 4200 cases. This optimization was performed across different scenarios, each targeting specific performance goals, such as minimizing the outlet air temperature, maximizing cooling capacity, minimizing water consumption, and maximizing the COP.
- In the third phase, again for Type 2, a comprehensive dataset consisting of 20,480 cases covering geometric, operational (working-to-intake air ratio, process air velocity, aperture number, aperture diameter, channel length and channel gap) and psychrometric parameters (process air inlet temperature and humidity) was established. Using this dataset, 7 different multiple linear regression (MLR) structures and a total of 32 machine learning models (10 Decision Trees, 6 Support Vector Machines, 16 MultiLayer Perceptrons) were trained to develop fast and reliable predictors for process outlet temperature, dew-point effectiveness, cooling capacity, water consumption and COP.

- When the three phases are considered together, with a total of 25,100 CFD solutions, one of the most comprehensive dataset in the field has been established. The multi-configuration comparison, geometrical optimization and data-driven performance prediction have been integrated on a single methodological framework.

3. METHODOLOGY

The indirect evaporative cooling technology investigated in this study is based on the principle of transferring sensible and latent heat between two air streams flowing through adjacent dry and wet channels. These channels are typically separated by thin aluminum plates, and the cooling mechanism relies on the evaporation of water in the wet channels to reduce the temperature of the air flowing through the dry side without adding moisture to it.

The study presented in this thesis was structured in three progressive stages, each building upon the findings of the previous. In the first stage, five distinct cooler configurations (referred to as Type 0 through Type 4) were developed to evaluate the effect of structural differences on indirect evaporative cooling performance (Figure 3.1). Type 0 represents a conventional dew-point indirect evaporative cooler design in which no apertures are present; the process and working air streams remain completely separated along their entire path. Similarly, Type 1 and Type 3 also contain single apertures at the end but differ in how the airflow pathways are arranged. Type 1 features a conventional dew-point channel arrangement, while Type 3 includes an auxiliary channel that directs the working air first through the dry and then through the wet side, offering a more complex airflow routing. In contrast, Type 2 and Type 4 include multi-apertures that allow a portion of the dry process air to enter the wet channel through small gaps placed along the separating plate. This internal air redistribution promotes enhanced evaporation and improved cooling performance. Among the five configurations, Type 1 and Type 2 share a common overall layout but differ in the presence of apertures, with Type 2 offering an advanced version of Type 1. Likewise, Type 3 and Type 4 have similar auxiliary channel geometries, but only Type 4 includes air transfer openings, combining the structural complexity of Type 3 with the internal mixing approach of Type 2. While Type 0, Type 1, and Type 3 follow traditional design logic with no cross-channel air exchange, Type 2 and Type 4 feature multi-aperture arrangements that enable partial redirection of dry air into the wet channel. This comparative structure allowed for the isolated analysis of geometric and functional modifications, providing a fair and systematic basis for identifying the most effective configuration.

Among these, Type 2, which incorporates a multi-aperture internal structure, was numerically modeled using CFD for the first time in the literature. More notably, Type 4, which integrates the internal airflow features of Type 2 with the complex channel layout of Type 3, represents a completely novel configuration that has not been previously studied. These two designs constitute original contributions to the geometric advancement of dew-point indirect evaporative cooling systems. The first phase of the study revealed the best type among the five types examined when considering the cooler performance parameters.

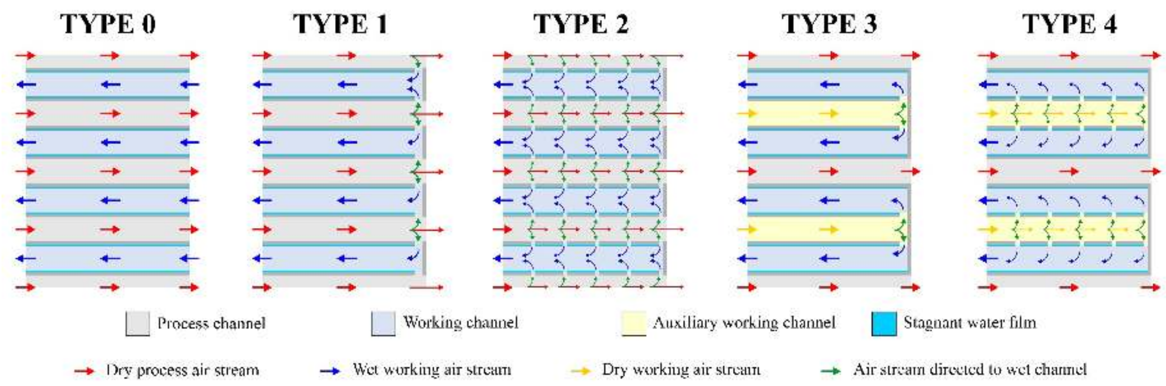

Figure 3.1. Flow arrangements of investigated indirect evaporative coolers

In the second phase of the study, a detailed geometric optimization process was carried out for the most efficient configuration identified in the first phase. The objective of this stage was to investigate how variations in the physical dimensions of the cooler and the arrangement of airflow apertures influence overall performance. In the context of this study, the channels refer to the narrow, parallel passages through which the process and working air streams flow, separated by thin aluminum plates. The channel length (L) denotes the longitudinal extent of these passages, while the channel gap (h) indicates the vertical spacing between adjacent aluminum plates, directly affecting the cross-sectional flow area and pressure drop characteristics. The apertures are small openings located along the separating plate that allow a portion of the dry process air to transfer into the wet working channel. Two primary aperture parameters were considered in the analysis: the aperture number (apN), which specifies the total number of openings distributed along the flow path, and the aperture diameter (apD), which defines the size of each individual opening. The number of apertures was varied from 1 to 9. A configuration with a single aperture corresponds to a traditional dew-point evaporative cooler (Type 1), while higher aperture counts represent advanced multi-perforated designs (Type 2 and 4), where the openings were evenly distributed along the channel length.

Notably, this study is the first in the literature to treat aperture diameter as an independent design variable, enabling a detailed investigation of its influence on the mass flow of air entering the working channel and the intensity of evaporation within the wet surface. This allowed for a deeper understanding of how local geometric refinements affect the thermal and mass transfer performance of the system. All geometric features were assessed under consistent boundary conditions, including a process air inlet temperature of 35 °C, a humidity ratio of 16 g/kg, and an inlet velocity of 3 m/s. This phase of the study demonstrated that reverse flow could occur under certain conditions and established some useful limits for design purposes on the geometric parameters of the Type 2 cooler.

Finally, in the third stage of the research, the geometrically examined cooler configuration (Type 2) was analyzed in more detail. By changing both the geometric (aperture number, aperture diameter, channel length and gap) and operational parameters (air temperature, humidity, speed and working-to-intake air ratio) of the cooler, the cooler performance was obtained in a very wide range.

Moreover, using the obtained dataset, different Multiple Linear Regression (MLR) and Machine Learning (ML) models were obtained to predict the cooler performance. The goal was to develop predictive models capable of estimating cooler performance parameters, such as outlet temperature, cooling capacity, and effectiveness, based on the input geometric features and operating conditions. This approach enabled rapid evaluation of new configurations and supported data-driven optimization strategies, complementing the computational fluid dynamics (CFD) methods used in the earlier stages.

By organizing the thesis in these three integrated stages, configuration comparison, geometric optimization, and AI-assisted modeling, a comprehensive understanding of the dew-point indirect evaporative cooler design was achieved. This multi-layered approach ensured that both the physical phenomena and the design parameters were thoroughly explored and optimized for real-world applications. The entire methodology of this thesis is visually summarized in Figure 3.2.

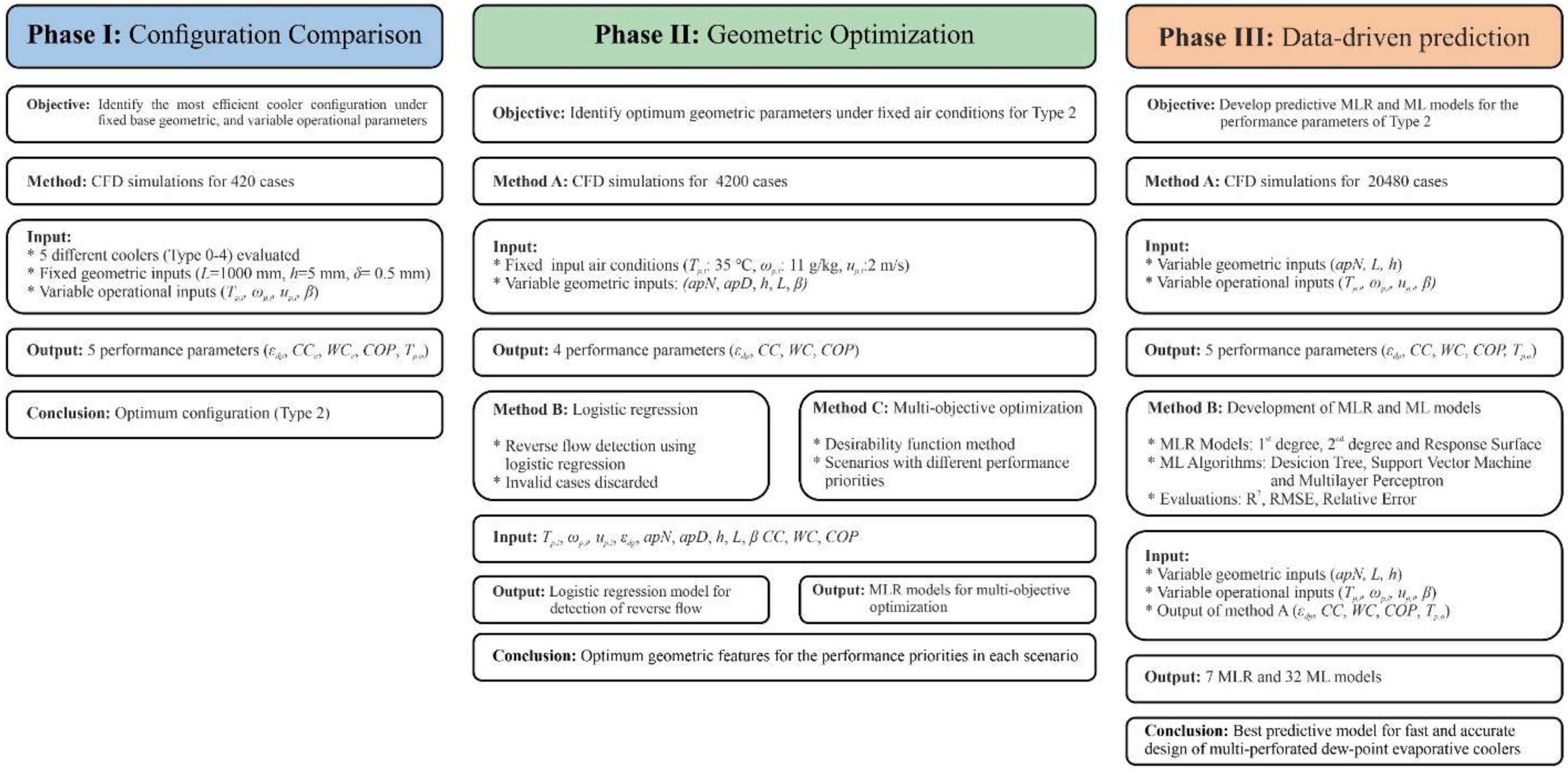

Figure 3.2. Methodological workflow of the thesis study, showing the structure of the three-phase approach involving configuration comparison, geometric optimization and data-driven prediction

3.1. Configurations of Coolers

All types of coolers examined consist of dry and wet channels, a very thin layer of water film and a channel plate. The coolers are typically designed with a dry channel positioned between every two wet channels and the channels are separated from each other by aluminum channel plates. These configurations, coded as Type 0 through Type 4, were differentiated based on their internal airflow arrangements and the use of apertures to redirect air between channels (Figure 3.1). Type 0 served as the base configuration, representing a conventional indirect evaporative cooler in which the process air and the working air follow completely separate flow paths. This configuration reflects the classical counter-flow principle where no mixing occurs between the dry and wet channels. In contrast, Type 1 and Type 2 introduced one or more apertures along the dry channel, enabling partial redirection of the process air into the adjacent wet channels. In Type 1, a single aperture is placed at the end of the dry channel, whereas Type 2 includes multiple evenly spaced apertures distributed along the flow direction. These designs were intended to enhance cooling effectiveness by allowing a controlled fraction of the process air to participate in the evaporation process. Specifically, the multi-aperture configuration aims to introduce unsaturated air into the wet channel at multiple points along its length, thereby renewing the local evaporation potential at each section. This approach helps to delay saturation of the wet channel environment and maximizes the benefit derived from the latent heat of evaporation at each aperture location, sustaining high cooling performance throughout the entire channel.

The comparison between the five types of coolers involved designs with the same geometric features to facilitate a fair evaluation. As shown in Table 3.1, the channel gaps for all coolers were set to 5 mm, and 0.5 mm thick aluminum plates were selected. Likewise, the channel lengths were standardized at 1000 mm. These specific values were selected considering the results of previous studies on the subject (Alam et al., 2024; Badiei et al., 2020; Chu et al., 2021; Kashyap et al., 2021; Xu et al., 2024) to investigate the effect of various geometric and operational parameters.

Table 3.1. Geometric properties of the coolers

Description	Symbol	Dimension	Unit
Channel length	L	1000	mm
Channel gap	h	5	mm
Aluminum plate thickness	δ	0.5	mm

3.2. Numerical Procedure

The numerical modeling process employed in this study was carried out using Comsol Multiphysics (version 6.2), which provides an integrated environment for solving coupled fluid flow, heat transfer, and mass transfer problems. The cooling configurations were modeled in a two-dimensional (2D) domain representing a vertical cross-section of the dry and wet channel pairs. This approach provided an optimal balance between computational cost and accuracy, while sufficiently capturing the dominant physical phenomena occurring within the cooler (Pakari and Ghani, 2019a).

Given the nature of indirect evaporative cooling, the problem formulation involved the simultaneous resolution of three primary physical processes: airflow dynamics, heat transfer in moist air, and water vapor diffusion. Accordingly, the modeling domain was constructed using the following physics modules available in Comsol Multiphysics software:

- *Laminar Flow*, to simulate the air movement within the channels under the assumption of steady-state, incompressible, and laminar conditions,
- *Heat Transfer in Moist Air*, which accounted for both sensible and latent heat exchange between the airflow and the wet surfaces,
- *Moisture Transport in Air*, to represent water vapor diffusion governed by Fick's Law.

Rather than solving each physical field in isolation, Comsol Multiphysics coupling capabilities were used to fully integrate the governing equations. Specifically, the *Non-Isothermal Flow* interface was utilized to couple fluid flow with air thermophysical properties, while *Moisture Flow* interface enabled the simulation of coupled humidity and velocity fields. Additionally, the *Heat and Moisture Transfer* interface captured the interdependence of thermal and mass diffusion effects, particularly in the wet channels (Figure 3.3).

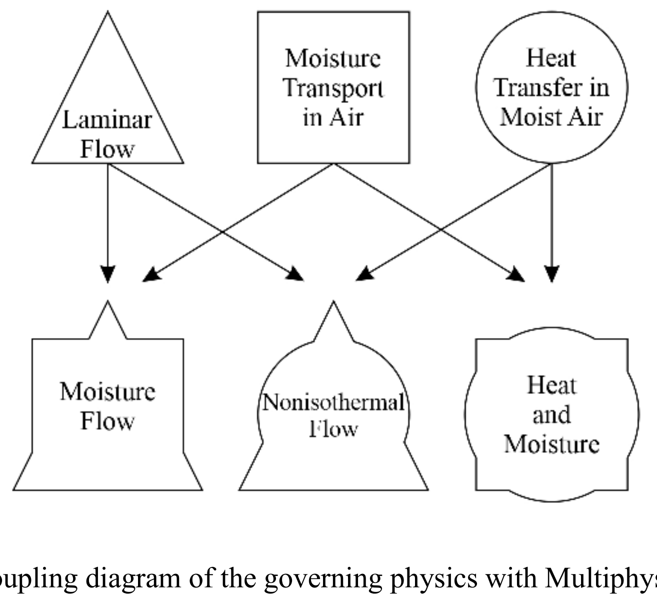

Figure 3.3. Coupling diagram of the governing physics with Multiphysics interfaces

The numerical analyses carried out in this study were based on the following assumptions (Lin et al., 2021a; Yan et al., 2024):

- Steady-state conditions were considered for all simulations, assuming that the system had reached thermal and flow equilibrium.
- The airflow inside both dry and wet channels was assumed to be incompressible and laminar, in accordance with the low Reynolds number regime typically observed in such systems.
- The wet channel surfaces were covered by a stagnant film of water, enabling evaporative cooling via phase change.
- The thickness of the water film was neglected, as it was considered extremely thin and had a negligible effect on both flow dynamics and heat transfer fields.
- The outer channel walls were assumed to be thermally insulated from the external environment to isolate the internal energy balance and eliminate external heat gain or loss.

The Finite Element Method (FEM) was adopted for numerical discretization, and the convergence criterion was defined as 10^{-5} for all governing equations. To optimize the computational efficiency and stability of the solution, a segregated solver scheme was adopted. Within this iterative framework, the governing equations were solved sequentially in separate substeps. The linear system for the fluid flow (velocity and pressure fields) was resolved using the GMRES (Generalized Minimal Residual) iterative solver, preconditioned with an Algebraic Multigrid (AMG) method. This choice was specifically made to handle the high degrees of freedom in the flow domain with manageable memory consumption. Conversely, the transport equations for Heat Transfer and Moisture Transport were solved using the PARDISO parallel sparse direct solver. This hybrid configuration combines the computational speed of iterative methods for hydrodynamics with the robustness of direct solvers for scalar transport variables, ensuring stable convergence even in the presence of strong source terms derived from the phase change phenomena.

The overall modeling process, from geometry creation to result extraction, followed a consistent sequence: geometry generation, material assignment, physics setup, mesh construction, boundary condition implementation, solver configuration, and finally post-processing and validation. This structured framework was consistently applied across all configuration types and geometric variants analyzed throughout the study.

3.2.1. Governing Equations

The physical behavior of the indirect evaporative cooler was governed by a set of coupled differential equations representing the conservation of mass, momentum, energy, and species concentration. These equations were implemented in the Comsol Multiphysics environment through the selected physics interfaces and solved in a steady-state regime. All governing equations are solved in two dimensions (x-y), where vector quantities are denoted in bold and the velocity vector is defined as $\boldsymbol{u} = (u_x, u_y)$.

In *Laminar Flow* physic the airflow within the channels was modeled using the incompressible form of the Navier–Stokes equations along with the continuity equation. These equations describe the conservation of momentum and mass in laminar flow conditions (Zhou et al., 2023):

$$\rho(\boldsymbol{u} \cdot \nabla)\boldsymbol{u} = \nabla \cdot [-p\boldsymbol{I} + \mu(\nabla\boldsymbol{u} + (\nabla\boldsymbol{u})^T)] + \boldsymbol{F} \tag{3.1}$$

$$\rho\nabla \cdot \boldsymbol{u} = 0 \tag{3.2}$$

where;

ρ: density

$\boldsymbol{u}$: velocity vector (u_x, u_y)

$\boldsymbol{I}$: identity tensor

p: pressure

μ: dynamic viscosity

$\boldsymbol{F}$: volume force vector

For modeling *Moisture Transport in Air*, the variation in moist air density is accounted for using a concentrated species formulation. This approach accurately represents changes in moisture content by incorporating the density of moisture into the process. Variation of moisture content can be expressed as (Wang et al., 2024):

$$\rho_g \boldsymbol{u} \cdot \nabla\omega_v + \nabla\boldsymbol{g}_w = G \tag{3.3}$$

$$\boldsymbol{g}_w = -\rho_g D \nabla\omega_v \tag{3.4}$$

$$\omega_v = \frac{M_v c_v}{\rho_g} \tag{3.5}$$

where;

D: vapor diffusion coefficient

$\boldsymbol{g}_w$: diffusive mass flux vector of water vapor

G: water vapor source

M_v: molar mass of water vapor

The relation between relative humidity, vapor concentration and saturated concentration is expressed as (Güzelel et al., 2025):

$$c_v = \varphi_w c_{sat} \tag{3.6}$$

where;

φ: relative humidity

c_v and c_{sat}: water vapor concentration and saturated water vapor concentration

The relationship expressed in Equation 3.6, which links relative humidity to vapor concentration via the saturation concentration, is essential for coupling moisture content with temperature.

The energy equation for heat transfer in moist air accounts for both sensible and latent heat effects. Convective heat transfer in *Heat Transfer in Moist Air* physics can be solved as (Zhou et al., 2023):

$$\rho c_p \boldsymbol{u} \cdot \nabla T + \nabla \cdot \boldsymbol{q} = Q \tag{3.7}$$

$$\boldsymbol{q} = -k\nabla T \tag{3.8}$$

where;

T: temperature

c_p: specific heat of air

k: thermal conductivity

$\boldsymbol{q}$: heat flux vector

Q: heat source or sink

These three physics are solved in a fully coupled form through Comsol's Multiphysics interfaces. The *Non-Isothermal Flow* module couples Equations 3.1 and 3.7 while the *Heat and Moisture Transfer* module couples Equations 3.3 and 3.7. The *Moisture Flow* interface handles the interaction between Equations 3.1 and 3.3, ensuring that air movement, temperature, and humidity interact dynamically within the domain.

3.2.2. Boundary Conditions

In numerical simulations, appropriate boundary conditions were applied to ensure accurate representation of the thermal and fluid dynamics within the indirect evaporative cooler. Although the configurations differ geometrically, particularly in the presence or absence of apertures, the same fundamental boundary condition definitions were employed across all cases. The distinction in behavior emerges not from the boundary conditions themselves, but from the variation in geometry and the resulting natural flow development within the domain. In both single-pass and multi-pass models, process air enters the computational domain with predefined velocity, temperature and humidity ratio, corresponding to the ambient air conditions. The process air inlet boundary conditions are presented in Equation 3.9. At the outlets, zero-gauge pressure is applied to allow natural outflow without introducing backpressure.

$$u_x = u_{p,i},\ \ u_y = 0,\ \ T = T_{p,i},\ \ \omega = \omega_{p,i} \tag{3.9}$$

The process air outlet boundary condition is defined as a pressure outlet:

$$P_o=0 \tag{3.10}$$

Likewise, the working air inlet is defined with constant boundary values, modulated by the working-to-intake ratio β. The working air inlet boundary conditions are presented in Equation 3.11.

$$T = T_{p,o},\ \ \omega = \omega_{p,o} \tag{3.11}$$

The working air outlet boundary conditions are presented in Equation 3.12. These outlet boundaries are non-reflective and permit full development of the flow field before exit.

$$u_x = \beta * u_{p,i},\ \ u_y = 0 \tag{3.12}$$

The wet surfaces adjacent to the channel plate are assumed to be fully saturated and are modeled as constant-temperature, constant-humidity boundaries. The thin water film is treated as stagnant, and its thickness is neglected, given its negligible effect on the flow dynamics. The channel walls are assumed to be adiabatic, meaning that no heat transfer occurs through these external boundaries. No-slip conditions are applied at all solid-fluid interfaces, ensuring zero velocity at the wall boundaries. The channel plate inlet (x=0) and outlet (x=L) boundary conditions are presented in Equation 3.13.

$$\frac{\partial T_{pl}}{\partial x} = 0 \tag{3.13}$$

Additionally, symmetry boundary conditions were imposed along both the vertical and horizontal midlines of the geometry to minimize computational effort and exploit the structural symmetry of the system. The symmetry boundary conditions are presented in Equation 3.14.

$$\frac{\partial u_x}{\partial y} = 0, \quad \frac{\partial T}{\partial y} = 0, \quad \frac{\partial \omega}{\partial y} = 0, \quad \frac{\partial P}{\partial y} = 0 \tag{3.14}$$

While these boundary definitions are consistent in both configurations, the presence of apertures in the multi-pass geometry introduces significant changes in the airflow path. In the multi-pass model, air naturally redistributes between the process and working channels due to local pressure gradients formed around the apertures. This passive flow interaction, enabled by the geometric design rather than imposed boundary conditions, is what differentiates the multi-pass model behavior from the single-pass case. In other words, the solution's uniqueness is not a result of changing boundary conditions, but rather of how the geometry influences the natural behavior of the internal flow fields. The boundary conditions of a sample case of single-pass (Type 1) and multi-pass (Type 2) are presented in Figures 3.4 and 3.5, respectively.

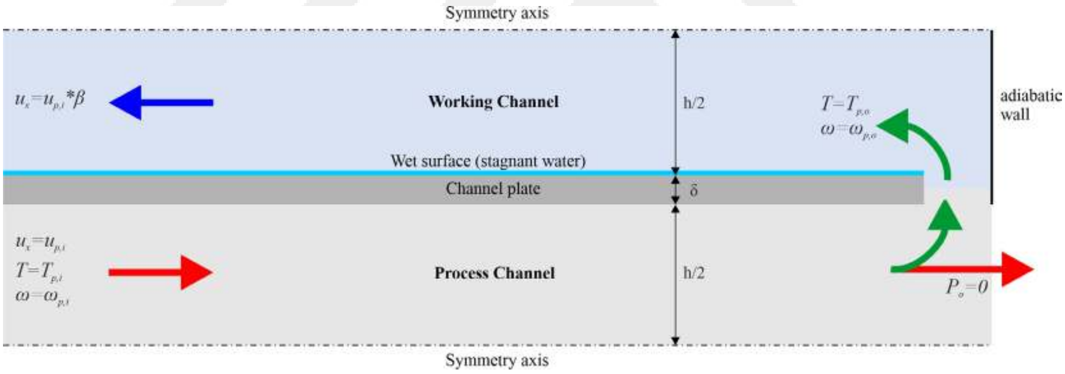

Figure 3.4. Boundary conditions for the single-pass indirect evaporative cooler configuration

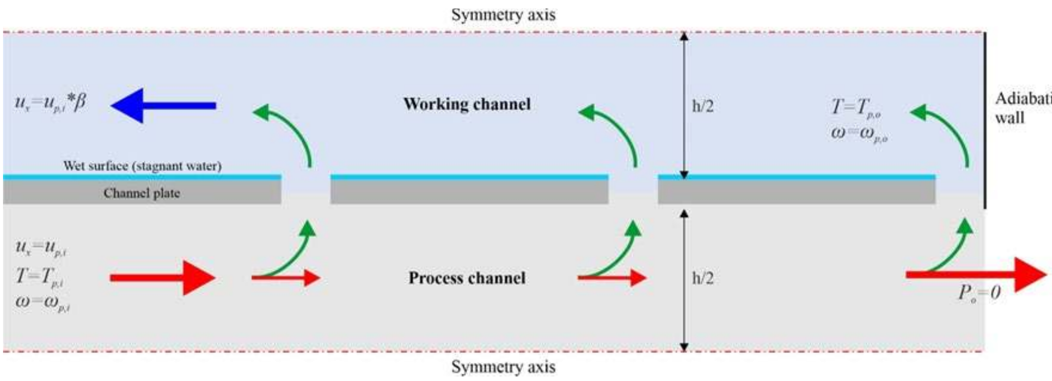

Figure 3.5. Boundary conditions for the multi-pass indirect evaporative cooler configuration

3.2.3. Mesh Structure

To ensure the reliability and accuracy of the numerical simulations, a detailed mesh independency analysis was performed for both the configuration comparison and the geometric optimization phases. All models were discretized using the finite element method (FEM), and the computational domain was meshed using triangular elements. The triangular elements allowed for better resolution around curved and irregular features, offering greater flexibility in controlling local refinement near high-gradient zones such as aperture edges and channel junctions. Moreover, this approach aligned well with the capabilities of the FEM-based solver (Wang et al., 2024; Zhou et al., 2023), which handles triangular elements efficiently, especially in laminar and multi-physics applications.

The geometric aspect ratio of the modeled cooler is exceptionally low due to the long and narrow nature of the channels. For this reason, it was not practical to present the entire mesh structure in a single visual. Instead, representative mesh views from three critical sections of the Type 3 cooler (the inlet, middle and outlet) were extracted and are shown in Figure 3.6. The mesh generation was physics-controlled and refined in regions where steep gradients in velocity, temperature, and humidity were anticipated, particularly near the channel walls and around the apertures. These regions experience intense momentum and heat/mass transfer interactions, making local mesh refinement essential for capturing the behavior accurately. In contrast, the central regions of the channels where the flow tends to be more uniform were assigned coarser elements to reduce computational cost without sacrificing solution quality.

A mesh independency study was conducted by systematically increasing the number of elements in the domain and observing the change in a key output parameter: the process air outlet temperature. When the relative change in this temperature fell below 0.1%, the solution was considered independent of the mesh size. Figure 3.7 illustrates the numerical results of exit temperature obtained using different mesh configurations for different types of coolers studied. To ensure a fair and consistent comparison across all five configurations, the same geometric and operational conditions were applied in all simulations presented in Figure 3.7. Specifically, the channel length was fixed at 1000 mm, and the channel gap was set to 5 mm for each case. Additionally, the operational parameters were taken as the base values defined in Table 3.2, including a process air inlet temperature of 35 °C, humidity ratio of 16 g/kg, air velocity of 3 m/s, and a working-to-intake air ratio (β) of 0.5. These standardized inputs ensured that differences observed in the simulation results could be attributed solely to the internal airflow configuration of each cooler type, not to variations in geometry or boundary conditions. For the configuration comparison phase, the models typically converged with approximately 350,000 to 450,000 elements, depending on the complexity of the geometry. Type 0 and Type 1 models, which involved simpler geometries, required fewer elements, while Type 3 and Type 4, which incorporated additional airflow paths and internal apertures, required denser meshing for accurate resolution.

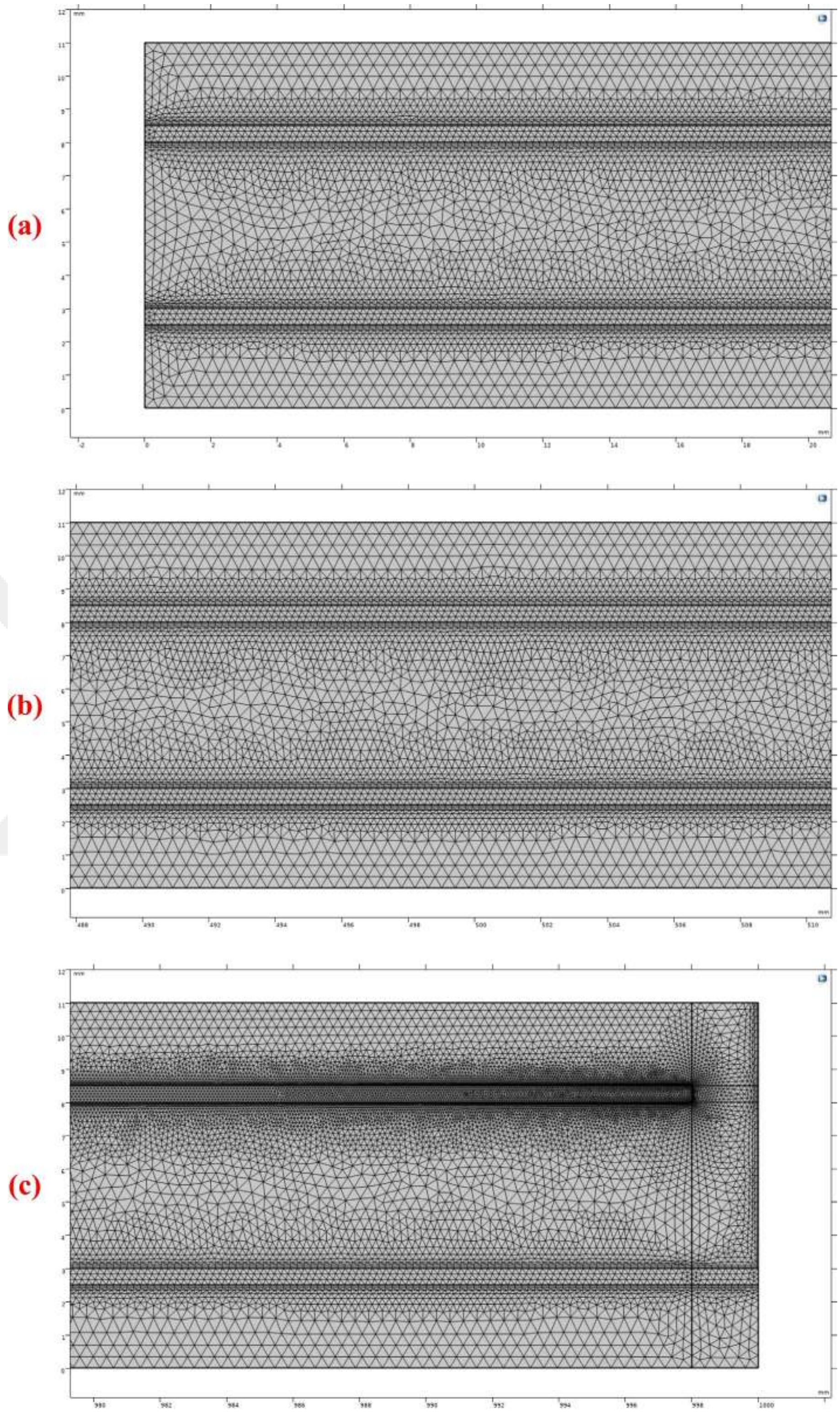

Figure 3.6. The schematic view of the mesh structure of inlet (a), middle (b) and exit (c) part of Type 3 cooler

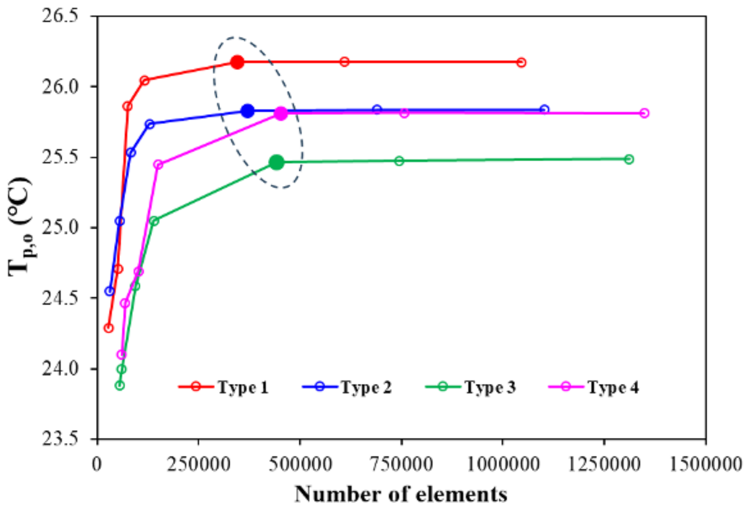

Figure 3.7. Mesh independency test of the various types of coolers

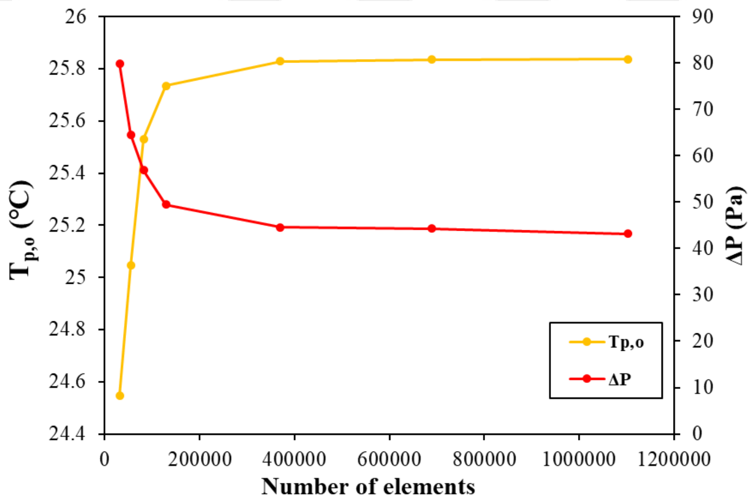

Figure 3.8. Mesh independency test of Type 2 cooler

In the geometric optimization phase, which involved the geometric optimization of the Type 2 configuration, a new mesh independency analysis was conducted. A base geometry with five apertures, channel length of 1000 mm, and aperture diameter of 0.2 mm was used to conduct the mesh sensitivity test. The working-to-intake air ratio was set to 0.5, and the inlet air conditions were fixed at 35 °C, 16 g/kg humidity, and 3 m/s velocity (Table 3.3). While the outlet temperature was again used as a convergence metric, a second indicator pressure drop across the cooler was included to account for hydraulic behavior, which can be more sensitive to mesh density, especially in narrow channels and aperture regions. As shown in Figure 3.8, the pressure drop showed significant variation with mesh size up to a threshold value. After approximately 370,000 elements, further refinement yielded minimal changes, indicating that both thermal and pressure-driven behaviors were reliably captured. The mesh structure of the Type 2 cooler is shown in Figure 3.9, with the critical parts shown separately as in the previous mesh figure.

In the final part of the study, a comprehensive set of CFD simulations was conducted to generate a large-scale dataset for data-driven modeling. Unlike the previous phases, in this stage, both geometric and operational parameters were varied simultaneously across a wide range of values, resulting in 20,480 unique simulation cases. These simulations were based on the validated numerical model of the Type 2 cooler and covered realistic variations in aperture configuration, channel dimensions, airflow ratios and psychrometric and operational conditions (Table 3.4). The outcome of this extensive parametric sweep was a detailed performance dataset, including outputs such as dew-point effectiveness, cooling capacity, water consumption and cooling coefficient of performance for each configuration. This dataset served as the foundation for training a series of machine learning models aimed at enabling the rapid and accurate prediction of cooler performance without the need for further CFD simulations. Although this phase involved thousands of individual simulations, no additional mesh independency analysis was performed. Several considerations justified this approach. First, all the simulations used in this phase were based on the same geometric and physical framework that had already been rigorously validated during the first and second phases of the study. Second, the operational parameter space explored during the machine learning phase remained well within the physical bounds of the configurations and flow conditions previously analyzed. Finally, the mesh structure established and verified during the geometric optimization process had already demonstrated sufficient convergence and robustness across a wide range of geometries. Therefore, the mesh design and validation work conducted in the earlier phases was deemed adequate to ensure the accuracy, consistency, and generalizability of the dataset used for developing and training machine learning models.

In addition to mesh resolution, numerical stability was ensured through careful solver settings. The simulations employed segregated solvers with appropriate under-relaxation factors to stabilize the coupled solution of momentum, energy, and species equations. Convergence was considered achieved when the relative residual for all governing equations fell below 10^{-5}. No significant divergence or oscillatory behavior was observed, even in models with complex recirculating flows, indicating robust numerical performance.

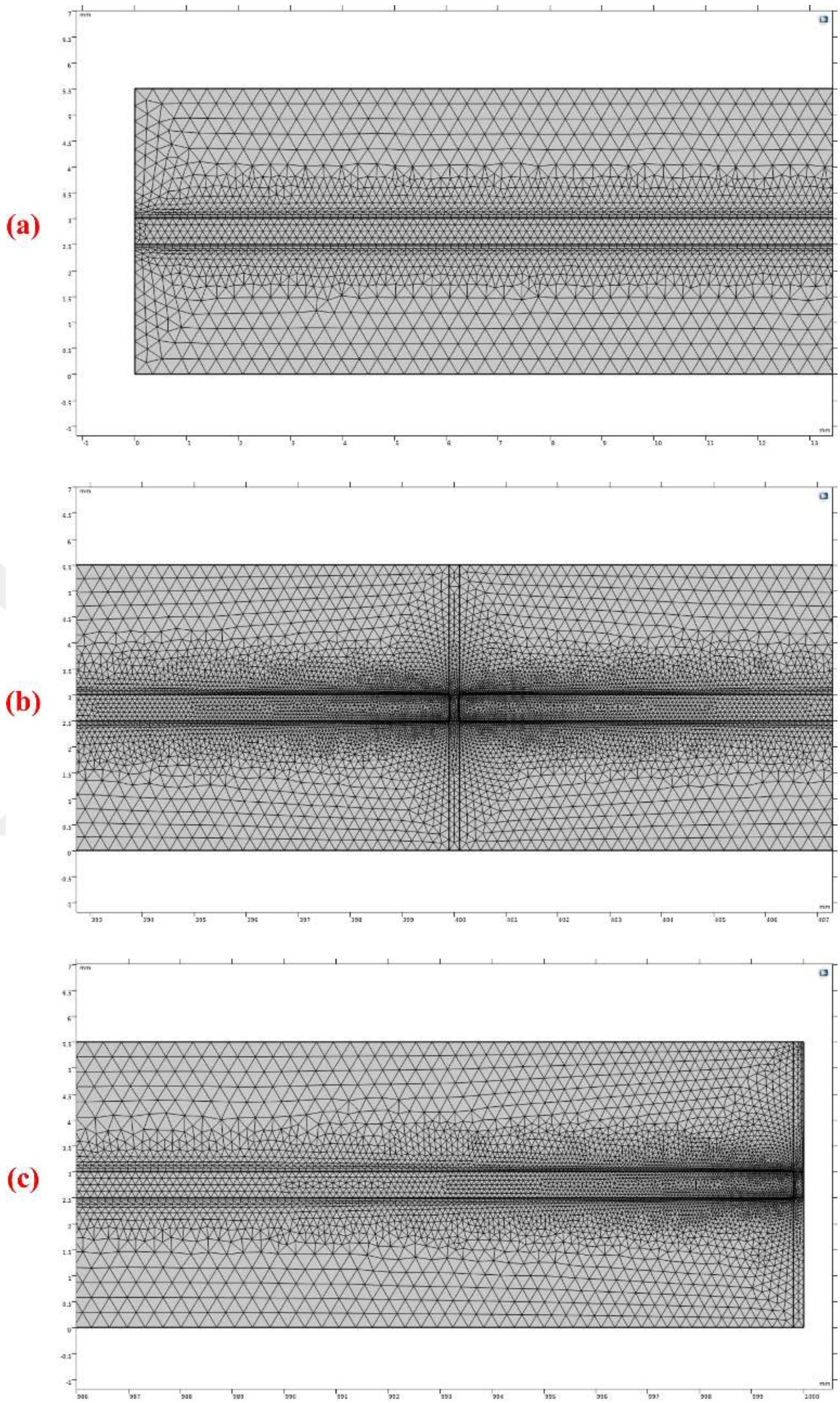

Figure 3.9. The schematic view of the mesh structure of inlet (a), middle (b) and exit (c) part of Type 2 cooler

3.3. Validation with Experimental Data

The accuracy of the developed numerical model was validated using two experimental datasets from the literature, both widely recognized in the field of dew-point evaporative cooling. In each case, simulations were conducted using geometric parameters identical to those reported in the experimental setups, ensuring that the comparisons would reflect model performance under realistic and consistent conditions. Moreover, each validation study included multiple test conditions, allowing the evaluation of the model under varying thermal and airflow scenarios.

The first validation was based on the work of Riangvilaikul and Kumar (2010a), whose experimental cooler featured a channel length of 1200 mm, a channel gap of 5 mm, and an aluminum plate thickness of 0.5 mm. The numerical domain was configured accordingly, using a single-aperture representation of the Type 2 cooler to match the experimental conditions. In the validation process, two sets of simulations were performed: one where the air velocity was fixed at 2.4 m/s and the inlet temperature and humidity were varied across a wide range, and another where the temperature was held constant at 34 °C, while the air velocity and humidity ratio were changed. In both sets of simulations, the model produced results that were in strong agreement with the experimental data, with an average relative error of 2.4% and a maximum deviation of 5.0%, primarily at the extremes of the tested range. The results of these comparisons are presented in Figure 3.10.

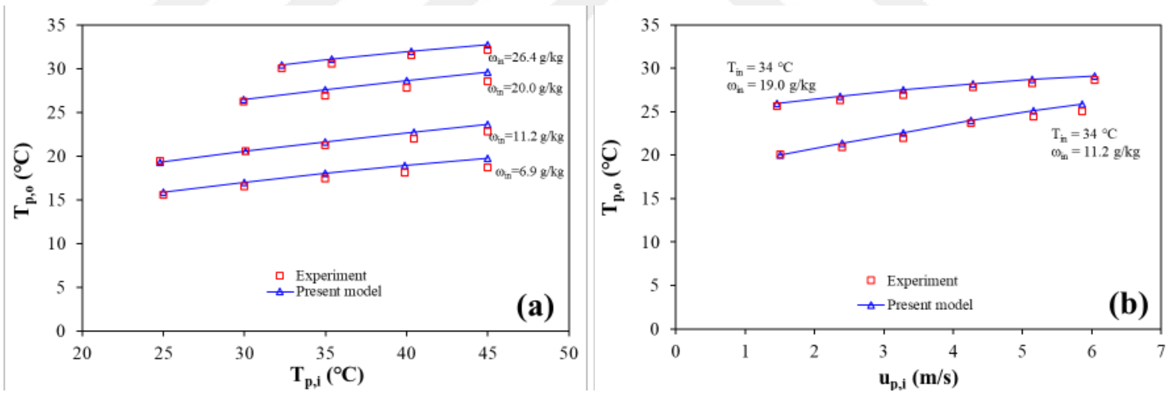

Figure 3.10. Comparison of numerical results with experimental data of Riangvilaikul and Kumar (2010a) at various temperatures (a) and velocities (b)

The second validation employed the experimental dataset from Lin et al. (2018), using a cooler with a channel length of 600 mm, a gap of 3 mm, and a plate thickness of 0.4 mm. The same geometry was implemented in the numerical domain. Two sets of experiments were again considered: one in which the air velocity and humidity were fixed at 2.0 m/s and 11 g/kg, respectively, while the inlet air temperature varied between 30 and 40 °C, and another where the temperature and humidity were kept constant at 35 °C and 11 g/kg, respectively, while the velocity varied between 1.1 m/s and 2.0 m/s. The numerical results closely followed the experimental trends in both scenarios, yielding an average error of 3% and a maximum error below 6%. These comparisons are shown in Figure 3.11.

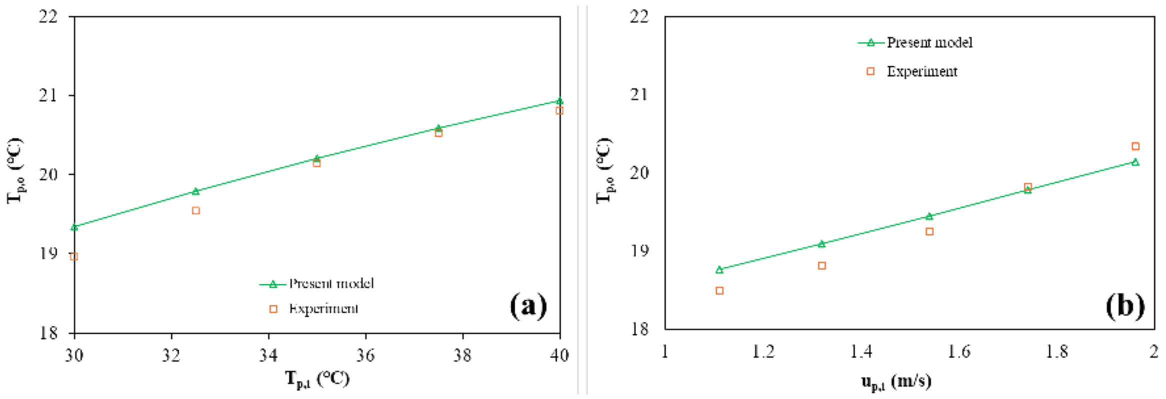

Figure 3.11. Comparison of numerical results with experimental data of Lin et al. (2018) at various temperatures (a) and velocities (b)

The consistency observed across different thermal and flow conditions, as well as the close numerical-experimental agreement for both geometries, demonstrated the robustness and general applicability of the numerical model developed in this study.

3.4. Parametric Study

The current study employed a systematic exploration of both operational and geometric variables to assess and optimize the performance of dew-point indirect evaporative coolers. The investigation was structured in three distinct stages: a parametric study of five different cooler configurations under varying psychrometric conditions, a geometric optimization of the best-performing configuration and an extended parametric sweep covering both geometric and environmental variables, used to generate a dataset for machine learning model development. In total, 25,100 individual CFD simulations were performed across these three phases.

3.4.1. Parametric Study of Cooler Configurations

In the first phase of the study, five different cooler types (Type 0–4) were analyzed under varying operating conditions to identify the most effective configuration. In order to ensure a fair comparison across different configurations, all geometric parameters were kept constant (Table 3.1), thereby eliminating any geometric bias in the performance evaluation. The fixed geometric dimensions were as follows: channel length L=1000 mm, channel gap h=5 mm and aluminum plate thickness δ=0.5 mm.

The study investigated the influence of four key operational parameters: process air inlet temperature $T_{p,i}$, humidity ratio $\omega_{p,i}$, air velocity $u_{p,i}$ and the working-to-intake air ratio β. Each parameter was varied systematically within defined ranges, while all other parameters were held at their base values to isolate the effect of the variable under study. The ranges and step sizes for the parametric sweep are summarized in Table 3.2. Each simulation run involved modifying only one parameter while the others were fixed at base values. This approach enabled the clear identification of performance trends and sensitivities associated with each variable. The performance outputs, including dew-point effectiveness, cooling capacity, and water consumption, were recorded for each case and used to compare the relative efficiency of the five cooler configurations.

Table 3.2. Operating parameters used in parametric study

Symbol	Description	Unit	Range	Increment	Base Value
Type 0, 1, 2, 3, 4	Cooler configuration	-	-	-	-
$T_{p,i}$	Temperature	°C	25-45	1	35
$\omega_{p,i}$	Humidity ratio	g/kg	6-26	1	16
$u_{p,i}$	Velocity	m/s	1-5	0.2	3
β	Working-to-intake air ratio	-	0.2-0.8	0.03	0.5
Number of the simulations				420	

3.4.2. Parametric Study of Geometric Optimization for Type 2 Cooler

Based on the results of the first phase, Type 2 was selected as the best-performing configuration. In the second phase, a geometric optimization study was conducted to enhance its performance under a fixed set of environmental conditions: inlet air temperature of 35 °C, humidity ratio of 11 g/kg, and air velocity of 2 m/s. These conditions were selected to represent a typical hot-dry climate where indirect evaporative cooling is highly relevant. Unlike the previous phase, in this stage, the psychrometric conditions were held constant, and the effects of changing geometric parameters were investigated. The variables considered in geometric optimization included the number of apertures apN, aperture diameter apD, channel length L, channel gap h and working-to-intake ratio β. All combinations of the parameter values within the ranges shown in Table 3.3 were simulated, resulting in a total of 4,200 unique CFD runs.

Table 3.3. Geometric parameters used in the optimization study for Type 2 cooler

Symbol	Description	Unit	Range	Increment
apN	Aperture number	-	1-9	2
apD	Aperture diameter	mm	0.2-0.5	0.05
L	Channel length	mm	600-1400	200
h	Channel gap	mm	3-6	1
β	Working-to-intake air ratio	-	0.2-0.7	0.1
Number of the simulations			4,200	

Unlike the previous phase, no variable was held constant in this stage; instead, all possible combinations of the parameter values were explored. The objective was to identify optimal geometries that maximize cooling effectiveness while minimizing pressure loss and water consumption.

3.4.3. Full-Range Parametric Coverage for Machine Learning Dataset

In the final stage of the study, an extensive set of simulations was carried out to support the development of machine learning models. In contrast to the earlier phases, where either geometric or operational parameters were varied in isolation, this phase considered all parameters, both operational and geometric, simultaneously. The parameter values were selected to represent a realistic and comprehensive range, as shown in Table 3.4.

Table 3.4. Full parameter ranges used for machine learning dataset for Type 2 cooler

Symbol	Description	Unit	Range	Increment
apN	Aperture number	-	1-5	1
L	Channel length	mm	800-1400	200
h	Channel gap	mm	3-6	1
β	Working-to-intake air ratio	-	0.25, 0.33, 0.50, 0.67	
$u_{p,i}$	Velocity	m/s	1-4	1
$\omega_{p,i}$	Humidity ratio	g/kg	6-18	4
$T_{p,i}$	Temperature	°C	25-40	5
Number of the simulations			20,480	

A total of 20,480 combinations were generated and solved, forming the input dataset for the machine learning models. This comprehensive dataset captures the full response surface of the cooler's behavior, allowing data-driven prediction models to interpolate performance metrics for arbitrary input combinations.

3.5. Performance Parameters for Coolers

To quantify and compare the thermal, hydraulic, and water-use performance of the studied cooler configurations and geometries, a set of key evaluation parameters was adopted. These performance metrics were computed for each numerical solution and subsequently used as target outputs in the machine learning modeling phase.

Conventional indirect evaporative coolers can cool air at most to the inlet wet-bulb temperature; accordingly, their performance is typically expressed as wet-bulb effectiveness (ε_{wb}) (Equation 3.15). However, the outlet temperature of the modeled indirect evaporative coolers ideally can be cooled below the inlet wet-bulb temperature. Therefore, it would be more appropriate to establish a performance parameter based on dew-point temperature. Dew-point effectiveness (ε_{dp}) quantifies how closely the process air outlet temperature approaches the process air inlet dew-point temperature (Equation 3.16). The wet-bulb and dew-point effectiveness was described as (Lin et al., 2021b; Pandelidis et al., 2018);

$$\varepsilon_{wb} = \frac{T_{p,i} - T_{p,o}}{T_{p,i} - T_{wb,p,i}} \tag{3.15}$$

$$\varepsilon_{dp} = \frac{T_{p,i} - T_{p,o}}{T_{p,i} - T_{dp,p,i}} \tag{3.16}$$

where;

ε_{wb} : wet-bulb effectiveness (-)

ε_{dp} : dew-point effectiveness (-)

$T_{p,i}$: process air dry-bulb inlet temperature (°C)

$T_{p,o}$: process air dry-bulb outlet temperature (°C)

$T_{wb,i}$: process air inlet wet-bulb temperature (°C)

$T_{dp,i}$: process air inlet dew-point temperature (°C)

A higher ε_{dp} indicates better cooling performance, with values typically ranging from 0.5 to 1.0 depending on design and operating conditions.

Cooling capacity (CC) represents the actual rate of thermal energy extraction from the process air stream. It reflects the net cooling potential delivered to a conditioned space or downstream process. This parameter is essential for sizing and comparing systems based on thermal demand (Zhan et al., 2011).

$$CC = \dot{m}_{p,o}(h_{p,o} - h_{p,i}) \tag{3.17}$$

where;

CC: cooling capacity (W)

$\dot{m}_{p,o}$: mass flow rate of process air (kg/s)

$h_{p,o}$: process air outlet enthalpy (kJ/kg)

$h_{p,i}$: process air inlet enthalpy (kJ/kg)

While examining the cooling capacities of the five different cooler types examined, the concept of cooling capacity per unit area (CC_a) was introduced in order to ensure a fair comparison. This was necessary due to variations in the total number of channels employed for cooling the process air, consequently leading to differences in channel surface areas. This metric indicates the cooling capacity generated per square meter of dry and wet channel heat exchange area (Zhou et al., 2024).

$$CC_a = \frac{CC}{A} \tag{3.18}$$

where;

CC_a: cooling capacity per area (W/m^2)

A: area (m^2)

Water is one of the working fluids in evaporative cooling, and its consumption is a crucial operational and sustainability metric. The total water consumption represents the actual mass of water evaporated during the cooling process (Kashyap et al., 2021).

$$WC = \dot{m}_{w,o}(\omega_{w,o} - \omega_{w,i}) \tag{3.19}$$

where;

WC: water consumption (kg/s)

$\dot{m}_{w,o}$: mass flow rate of working air (kg/s)

$\omega_{w,o}$: humidity ratio of working air at outlet (kg/kg)

$\omega_{w,i}$: humidity ratio of working air at inlet (kg/kg)

While water consumption represents the absolute usage, the specific water consumption metric (WC_c) indicates the amount of water required to produce a unit of cooling. This is particularly important in arid regions where water scarcity makes efficient usage essential (Güzelel et al., 2024).

$$WC_c = \frac{WC}{CC} \tag{3.20}$$

where;

WC_c: water consumption per unit cooling ((kg/s)/W)

Cooling coefficient of performance (*COP*) was defined as the ratio of cooling capacity to the total power consumption of the fans ($\dot{W}_f$) on both the process and working side (Zhao et al., 2008). When defining COP (Equation 3.21), pumping power was neglected due to the small amount of water consumption and therefore low pumping power requirement, as well as the comparative nature of this study, as it would cause a similar effect in all types of coolers studied (Tariq et al., 2018).

$$COP = \frac{CC}{\dot{W}_f} \tag{3.21}$$

$$\dot{W}_f = \dot{V}_{p,i}\Delta P_p + \dot{V}_{w,o}\Delta P_w \tag{3.22}$$

where;

$\dot{W}_f$: fanning power (W)

$\dot{V}$: volume flow rate of air (m^3/s)

ΔP_p: pressure drop of process channel (Pa)

ΔP_w: pressure drop of working channel (Pa)

3.6. Optimization Methodology

This section outlines the methods employed during the geometric optimization of the multi-perforated indirect evaporative cooler configuration (Type 2). The optimization process was based on two core procedures, first reverse flow checking and second desirability function method. These methods ensured that the selected designs were both functionally viable and thermally efficient.

3.6.1. Detection and Elimination of Reverse Airflow

In contrast to conventional indirect evaporative coolers, a fundamental design principle of dew-point indirect evaporative coolers is that a portion of the process air is transferred to the working channels through the apertures, without returning. However, under certain combinations of aperture size, number, and channel length, an undesirable reverse flow may develop within the working channel. This phenomenon results in moist air returning to the process channel, leading to a significant increase in outlet humidity and a decline in cooling effectiveness. To detect this condition, computational velocity vector fields and humidity contours were evaluated for each geometric case. Figure 3.12 demonstrates a typical desired normal flow profile, whereas Figure 3.13 shows the undesired reverse flow case.

Figure 3.12 not only displays the airflow vectors but also illustrates the relative humidity of the air within the cooler, as indicated by the contours and the color scale at the bottom. In normal flow conditions, the relative humidity gradually increases towards the exit of the process channel due to the decrease in dry-bulb temperature. The process air moves smoothly through the cooler, with a designated portion splitting off into the working channels at each aperture. This arrangement ensures that the process air continues towards the discharge end without any reverse flow, thus maintaining optimal operational performance by keeping the process air dry.

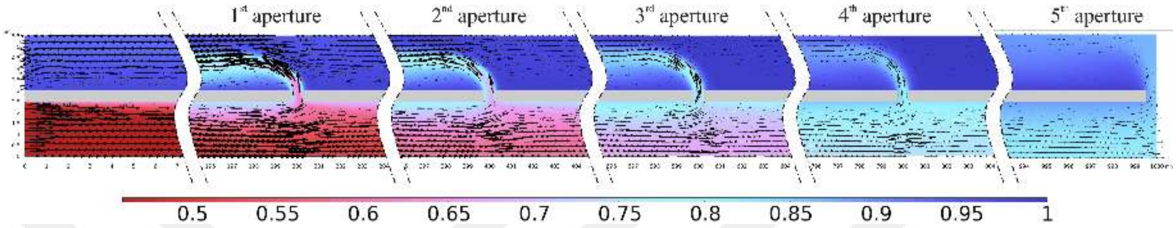

Figure 3.12. Velocity vectors and relative humidity gradients of normal airflow condition

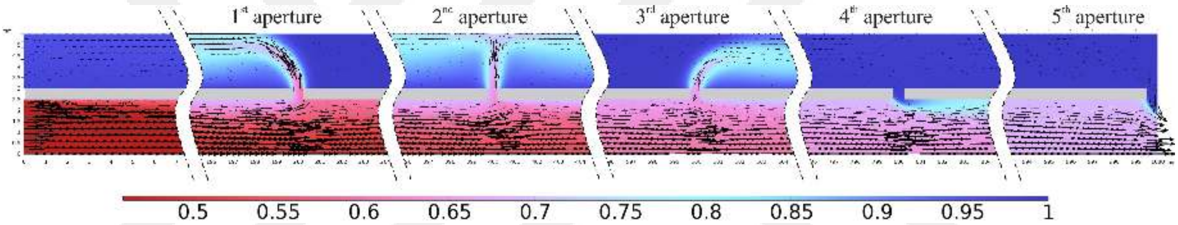

Figure 3.13. Velocity vectors and relative humidity gradients of reverse airflow condition

However, under certain geometric and operational conditions, an unintended reverse airflow can occur, as illustrated in Figure 3.13. In this scenario, instead of being directed towards the working channel discharge end, the air exhibits reverse flow behavior within the working channel. This reverse airflow can move back towards the process channel through the apertures, increasing the moisture content of the outlet process air, which is contrary to the operating principle of the dew-point evaporative cooler. Figure 3.13 illustrates a rare case of reverse flow starting from the second aperture onwards, selected specifically to effectively visualize this phenomenon. In this example, evaporation occurring over more than half the total length of the wet channel transports moisture to the process channel, leading to a significant increase in the outlet humidity of the process air. In some cases, reverse flow was observed to occur near the last apertures of the channel. Although this does not significantly increase the humidity of the process air, it renders the final section of the working channel ineffective, reducing cooling efficiency. To avoid the adverse effects described in these examples, it is essential to design and operate the cooler to eliminate reverse airflow.

Figure 3.13 also shows the effect of reverse flow conditions on relative humidity. Unlike the normal flow scenario, the increase in relative humidity is not only due to the temperature drop but also because the moistened working air mixes with the process air. This mixing further elevates the humidity, which can significantly compromise the working principle of the cooler by increasing the moisture content of the air intended for cooling. Therefore, it is crucial to carefully consider and control the reverse airflow phenomenon during the design, modeling, and operation of dew-point indirect evaporative coolers to prevent a decline in performance and ensure that the system operates as intended.

Reverse airflow was checked with the logistic regression method, which assesses the relationship between a binary dependent variable and one or more independent variables. In the logistic regression model, the probability of the dependent variable belonging to a specific category is determined based on the values of independent variables. These probabilities are calculated using the predictor function, which follows a sigmoid curve. In this analysis, the presence of reverse airflow was coded as 0, while its absence was coded as 1. The probabilities associated with these two scenarios are expressed as follows (Agresti and Kateri, 2011):

$$Prob[1] = \frac{1}{(1 + e^{(-\text{К}[1])})} \tag{3.23}$$

$$Prob[0] = \frac{1}{(1 + e^{(\text{К}[1])})} \tag{3.24}$$

where, К[1] denotes the predictor function, which is defined as a combination of geometric variables apN, apD, L, h and β.

In this study, both the first-degree polynomial (Equation 3.25) and the response surface (Equation 3.26) regression models were employed not only at this stage to define the predictor function К[1], but also in subsequent analyses to model the performance of the cooler. These general formulations incorporate the following terms (Güzelel et al., 2021):

$$y = c_0 + \sum_{i=1}^{p} c_i\, x_i \tag{3.25}$$

$$y = c_0 + \sum_{i=1}^{p} c_i x_i + \sum_{i=1}^{p} c_{ii} x_i^2 + \sum_{i=1}^{p-1} \sum_{j=i+1}^{p} c_{ij} x_i x_j \tag{3.26}$$

where;

y: dependent variable

x: independent variable

c: coefficient from logistic regression

p: number of variables

After calculating K[1] using Equations 3.25 or 3.26 with coefficients from Table 4.1 and 4.2, respectively, the probability values derived from the K[1] functions were compared using the "ifmax" function, as presented in Equation 3.27. If the obtained *Prob*[1] value is greater than the *Prob*[0] value, it is concluded that reverse airflow will not occur. Conversely, if the *Prob*[0] value is greater than the *Prob*[1] value, it is concluded that reverse airflow will occur (Agresti and Kateri, 2011).

$$IfMax \begin{pmatrix} Prob[1] \rightarrow 1 \\ Prob[0] \rightarrow 0 \end{pmatrix} \tag{3.27}$$

The procedure adopted for checking the reverse airflow probability is schematically illustrated in Figure 3.14.

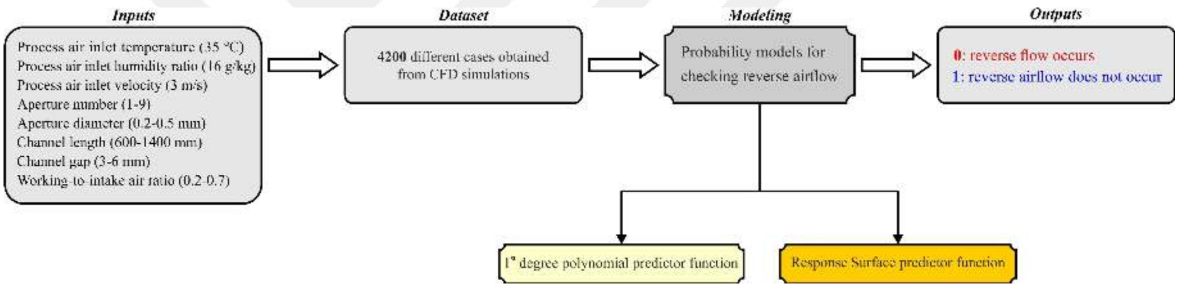

Figure 3.14. Procedure followed for checking reverse airflow probability

3.6.2. Desirability Function-Based Optimization

Out of 4,200 simulated operating conditions, reverse flow was detected in 1975 cases, leaving 2225 valid scenarios to be evaluated using the Desirability Function Method. This approach enables multi-objective optimization by converting each performance parameter into a normalized scale (0 to 1), referred to as the desirability score. Each performance indicator, such as dew-point effectiveness, cooling capacity per area, water consumption per cooling coefficient of performance, was associated with a desirability function, depending on whether the goal was to maximize or minimize the parameter. Each scenario, numbered from 1 to 4, represents a condition where one performance parameter is given more weight than the others. Additionally, *Scenario 0* represents a condition where all performance parameters are considered equally important (Figure 3.15).

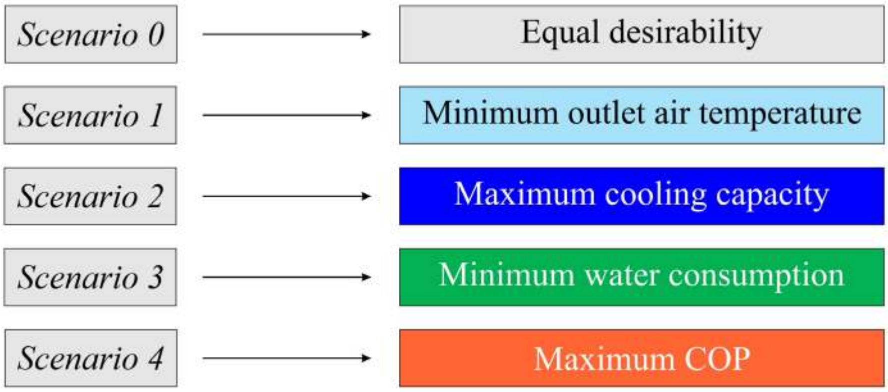

Figure 3.15. Schematic representation for different scenarios

The response surface models (Table 4.3) to predict the performance parameters given in results section were obtained using the general form of the equation (Equation 3.26), within the working ranges shown in Table 3.3. The developed models are function of independent variables expressed as:

$$pp_i = f\,(apN, apD, L, h, \beta) \tag{3.28}$$

where;

pp_i : performance parameters

apN: aperture number

apD: aperture diameter

L: channel length

h: channel gap

β: working-to-intake air ratio

The desirability values for the defined functions were determined linearly. For each parameter to be maximized or minimized according to the operating conditions, the representation is as follows (Boudjabi et al., 2021):

$$d_{max} = \left\{ \begin{array}{cc} 0 & pp_i \leq L_i \\ \dfrac{pp_i - L_i}{U_i - L_i} & L_i < pp_i < U_i \\ 1 & U_i \leq pp_i \end{array} \right\} \tag{3.29}$$

$$d_{min} = \left\{ \begin{array}{cc} 0 & U_i \leq pp_i \\ \dfrac{U_i - pp_i}{U_i - L_i} & L_i < pp_i < U_i \\ 1 & pp_i \leq L_i \end{array} \right\} \tag{3.30}$$

where;

L_i: lower limits of parameter

U_i: upper limits of parameter

d: desirability score for that parameter

For each performance parameter, the desirability values were individually obtained and then combined using the weighted geometric mean to determine the overall desirability value (D), as shown in Equation 3.31, and then maximized. The weights (w_1, w_2,…, w_n) in the equations were adjusted based on the importance of each performance parameter. To combine all desirability scores into a single indicator, a weighted geometric mean was used (Boudjabi et al., 2021):

$$D = (d_1^{w1} * d_2^{w2} * \ldots * d_n^{wn})^{\frac{1}{w1 + w2 + \cdots + wn}} \tag{3.31}$$

where;

D: overall desirability index to be maximized

d_i: individual desirability score for each performance metric

w_i: assigned weight for each parameter (based on scenario)

3.7. Model Development for Predicting Performance of Type 2 Cooler

In the final phase of this thesis, predictive models were developed to estimate the thermal and hydraulic performance of the optimized dew-point indirect evaporative cooler (Type 2) across a wide range of input conditions. The primary motivation for this modeling effort was to provide a fast, practical, and reliable alternative to computational fluid dynamics (CFD) simulations, which, although accurate, are computationally expensive and time-consuming, particularly in high-volume design studies or control-oriented applications.

The modeling approach was structured under two main categories: Multiple Linear Regression (MLR) and Machine Learning (ML). Within the MLR category, seven different regression structures were developed to explore both the linear and non-linear relationships between input and output variables. These include; first-degree regression, second-degree regression, third-degree regression, each of the above with added cross-product terms to account for interactions between variables and a final, compact model derived using the Response Surface Methodology (RSM), which offers lower model complexity and ease of use for practical applications.

The Machine Learning (ML) category was further divided into three commonly used model structures: Multilayer Perceptron (MLP), a feedforward artificial neural network capable of learning complex non-linear relationships, Support Vector Machine (SVM), which utilizes kernel functions to find optimal hyperplanes for regression tasks and Decision Tree (DT), which splits the dataset based on input features to minimize prediction error across hierarchical branches.

The dataset for model training and testing was obtained from the high-accuracy CFD simulations, comprising a total of 20,480 cases (Table 3.4). As previously discussed, simulation results exhibiting reverse flow were considered physically invalid and removed from the dataset. After this filtering process, a total of 17,525 valid cases were retained and used to train and evaluate all models. Each simulation case includes a unique combination of input variables, covering

- Geometric parameters
  - aperture number
  - channel length
  - channel gap
- Operational parameters
  - working-to-intake air ratio
  - inlet air velocity
- Psychrometric parameters
  - inlet air humidity ratio
  - inlet air temperature

For each case, five key performance indicators were calculated:

- Dew-point effectiveness (ε_{dp})
- Cooling capacity (CC)
- Water consumption (WC)
- Cooling coefficient of performance (COP)
- Outlet temperature of the process air ($T_{p,o}$)

In addition to the conventional performance metrics ε_{dp}, CC, WC and COP, the outlet temperature of the process air ($T_{p,o}$) was also included as a fifth model target, motivated by its practical relevance in real-world applications, where users typically seek direct temperature predictions. A schematic representation of the procedure developed to obtain predictive models is given in Figure 3.16.

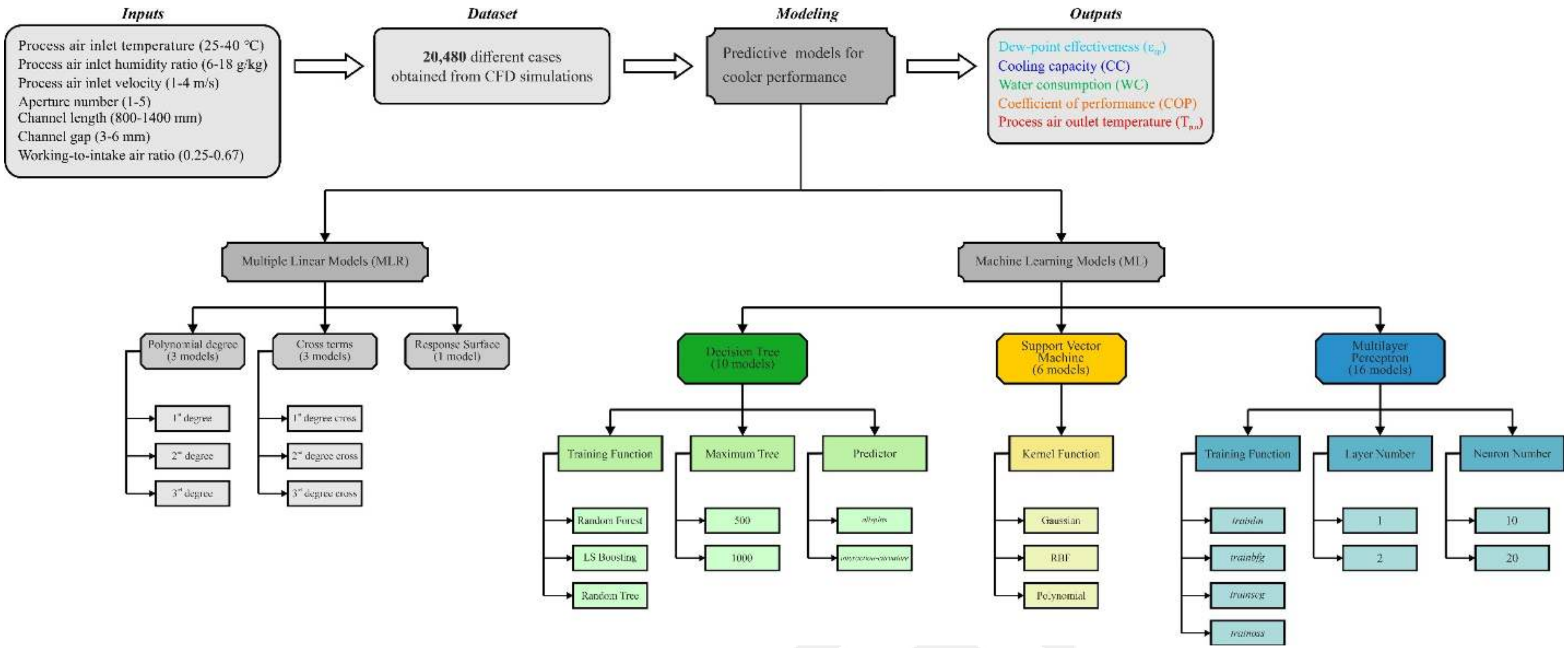

Figure 3.16. Schematic representation for predictive modeling procedure

3.7.1. Multiple Linear Regression Models

To explore the relationship between input variables and performance indicators, a series of multiple linear regression (MLR) models was developed and tested. These models offer ease of reproduction and can be easily implemented or tested without the need for specialized software. Due to their explicit mathematical structure, they can be directly integrated into any equation solver or simulation environment for practical use. Initially, six different polynomial regression structures were employed: 1st degree, 1st degree cross, 2nd degree, 2nd degree cross, 3rd degree and 3rd degree cross. Additionally, a seventh model was developed using Response Surface Methodology (RSM). This model was included due to its favorable balance between a reduced number of coefficients and predictive power, especially for practical implementations.

In models involving higher-order and interaction terms, polynomial and cross-product expressions are included. The complete set of formulations used in this study is listed below (Güzelel et al., 2022b):

1st degree model (Eq. 3.33):

$$y = \alpha_0 + \sum_{i=1}^{p} \alpha_i x_i \tag{3.32}$$

1st degree cross model (Eq. 3.34):

$$y = \alpha_0 + \sum_{i=1}^{p} \alpha_i x_i + \sum_{i=1}^{p-1} \sum_{j=i+1}^{p} \alpha_{ij} x_i x_j \tag{3.33}$$

2nd degree model (Eq. 3.35):

$$y = \alpha_0 + \sum_{i=1}^{p} \alpha_i x_i + \sum_{i=1}^{p} \alpha_{ii} x_i^2 \tag{3.34}$$

2nd degree cross model (Eq. 3.36):

$$y = \alpha_0 + \sum_{i=1}^{p} \alpha_i x_i + \sum_{i=1}^{p} \alpha_{ii} x_i^2 + \sum_{i=1}^{p-1} \sum_{j=i+1}^{p} \alpha_{ij} x_i x_j + \sum_{i=1}^{p-1} \sum_{j=i+1}^{p} \alpha_{iij} x_i^2 x_j + \sum_{i=1}^{p-1} \sum_{j=i+1}^{p} \alpha_{ijj} x_i x_j^2 \tag{3.35}$$

3rd degree model (Eq. 3.37):

$$y = \alpha_0 + \sum_{i=1}^{p} \alpha_i x_i + \sum_{i=1}^{p} \alpha_{ii} x_i^2 + \sum_{i=1}^{p} \alpha_{iii} x_i^3 \tag{3.36}$$

3rd degree cross model (Eq. 3.38):

$$\begin{aligned} y = \alpha_0 &+ \sum_{i=1}^{p} \alpha_i x_i + \sum_{i=1}^{p} \alpha_{ii} x_i^2 + \sum_{i=1}^{p} \alpha_{iii} x_i^3 \\ &+ \sum_{i=1}^{p-1} \sum_{j=i+1}^{p} \alpha_{ij} x_i x_j + \sum_{i=1}^{p-1} \sum_{j=i+1}^{p} \alpha_{iij} x_i^2 x_j + \sum_{i=1}^{p-1} \sum_{j=i+1}^{p} \alpha_{ijj} x_i x_j^2 \\ &+ \sum_{i=1}^{p-1} \sum_{j=i+1}^{p} \alpha_{iiij} x_i^3 x_j + \sum_{i=1}^{p-1} \sum_{j=i+1}^{p} \alpha_{ijjj} x_i x_j^3 \end{aligned} \tag{3.37}$$

Response surface model (Eq. 3.39):

$$y = \alpha_0 + \sum_{i=1}^{p} \alpha_i x_i + \sum_{i=1}^{p} \alpha_{ii} x_i^2 + \sum_{i=1}^{p-1} \sum_{j=i+1}^{p} \alpha_{ij} x_i x_j \tag{3.38}$$

where;

y: dependent variable

α_0: constant regression coefficient

p: total number of input features

α_i: regression coefficients

x_i: independent input variables.

3.7.2. Machine Learning Models

Beyond multiple linear regression methods, three categories of machine learning algorithms were employed to develop predictive models: *Decision Tree* (DT), *Support Vector Machines* (SVM) and *Multilayer Perceptron* (MLP) neural networks. All machine learning models were implemented and evaluated using the machine learning toolbox of Matlab software. The same dataset and cooler performance indicators utilized in the MLR modeling stage were also used here, ensuring consistency across all modeling approaches. To prevent overfitting and ensure accuracy, the data split technique was applied during training and testing. Each algorithm group was further investigated under multiple architectures and parameter combinations to evaluate the influence of model complexity, particularly in terms of tree depth, kernel type and neural network layer structure, on predictive accuracy.

3.7.2.1. Decision Tree

Decision trees are supervised learning algorithms that iteratively split the input data into smaller subsets based on the value of input features, aiming to reduce prediction error at each step. The structure of a typical decision tree consists of nodes, branches and leaves (Figure 3.17). The tree starts from a root node, which contains the entire dataset. Based on a decision rule involving one of the input variables, the data is split into two or more branches, leading to internal nodes that repeat the splitting process. Eventually, this structure ends at leaf nodes, which represent the final prediction output, either a class label or a continuous value, depending on whether the task is classification or regression (Loh, 2011).

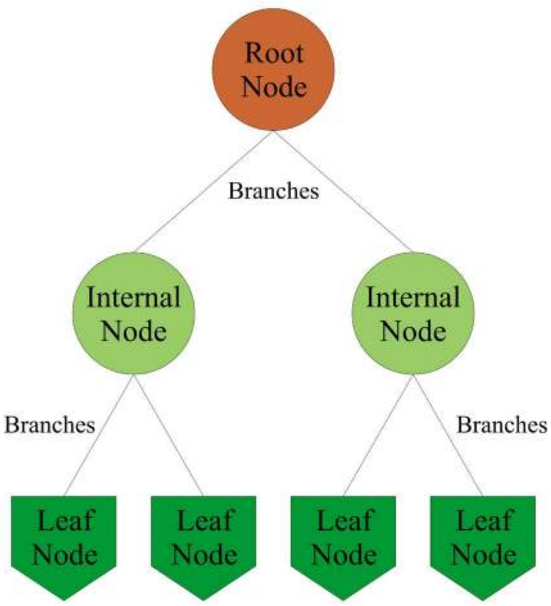

Figure 3.17. Typical decision tree structure (Loh, 2011)

While a single decision tree can capture non-linear relationships and provide significant results, its performance may be limited due to overfitting or underfitting. To overcome these limitations, three types of algorithms were explored: Random Forest, Least Squares Boosting (LSBoosting) and Random Tree (Single Tree) methods. Each approach leverages the basic structure of decision trees but differs in how trees are constructed and combined to make final predictions (Loh, 2011).

In the Random Forest method (Figure 3.18a), multiple independent decision trees are trained in parallel using randomly selected subsets of the training data and features. The final prediction is calculated by averaging the outputs of all individual trees, which helps to reduce overfitting and improve generalization. In contrast, LSBoosting (Least Squares Boosting) employs a sequential training strategy (Figure 3.18b), where each new decision tree focuses on correcting the errors of the previous ensemble. This additive approach builds a strong predictive model by combining many weak learners, resulting in increased accuracy, especially in capturing complex, non-linear relationships. Finally, the Random Tree model creates a single tree using randomly selected predictors and split criteria, serving as a lightweight, fast baseline for comparison (Figure 3.18c) (Kowalek et al., 2019).

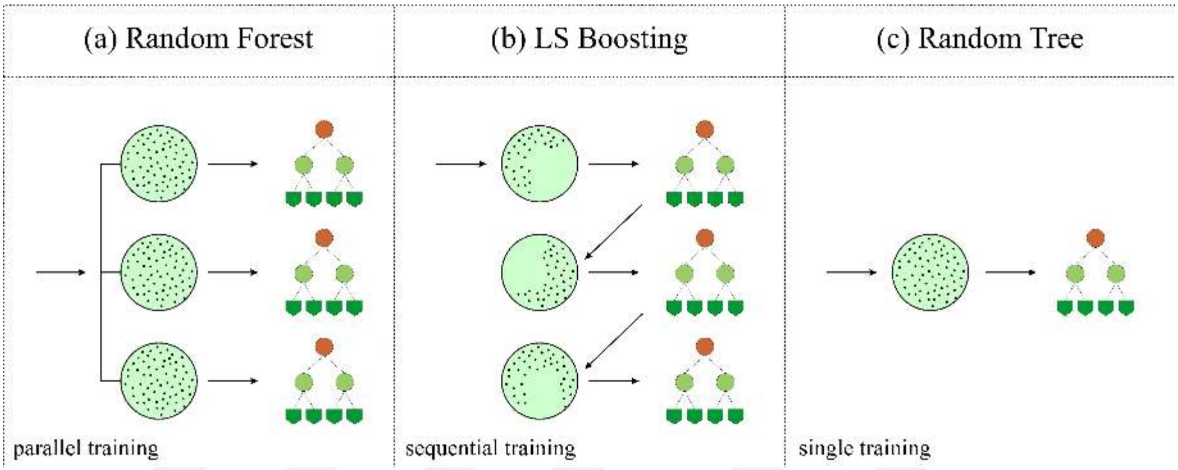

Figure 3.18. Structure of the decision tree models (a) Random Forest, (b) LS Boosting and (c) Random Tree (Kowalek et al., 2019)

As shown in Table 3.5, a total of 10 model configurations were tested. These variations included different combinations of training algorithms, maximum tree depths and predictor selection methods (such as allsplits and interaction-curvature). For instance, models DT-1 to DT-4 utilized the Random Forest algorithm with 500 or 1000 trees, while DT-5 to DT-8 employed LSBoosting with similar parameters. DT-9 and DT-10 represented simpler Random Tree models. These diversified setups enabled a comprehensive comparison of decision tree approaches under varying complexity levels.

Table 3.5. Configuration details of decision tree models

Code	Training Function	Max Tree	Max Split	Predictor
DT-1	Random Forest	500	500	allsplits
DT-2	Random Forest	500	500	interaction-curvature
DT-3	Random Forest	1000	500	allsplits
DT-4	Random Forest	1000	500	interaction-curvature
DT-5	LSBoosting	500	500	allsplits
DT-6	LSBoosting	500	500	interaction-curvature
DT-7	LSBoosting	1000	500	allsplits
DT-8	LSBoosting	1000	500	interaction-curvature
DT-9	Random Tree	-	500	allsplits
DT-10	Random Tree	-	500	interaction-curvature

3.7.2.2. Support Vector Machine

The Support Vector Machine (SVM) method is a supervised learning technique that can be used for both classification and regression tasks. In this study, the regression variant (Support Vector Regression (SVR)) was employed to model the thermal and hydraulic performance of the Type 2 cooler. As illustrated in Figure 3.19, SVR aims to find an optimal hyperplane that best fits the data within a defined margin of tolerance. The algorithm minimizes prediction error by focusing on a subset of critical data points known as support vectors, which lie closest to the margin and significantly influence the position and orientation of the hyperplane (Ergun et al., 2010). In total, six SVM models were developed by varying the kernel functions and, in the case of the polynomial kernel, the polynomial degree. All models used the Iterative Single Data Algorithm (ISDA) as the solver. Model configurations are summarized in Table 3.6.

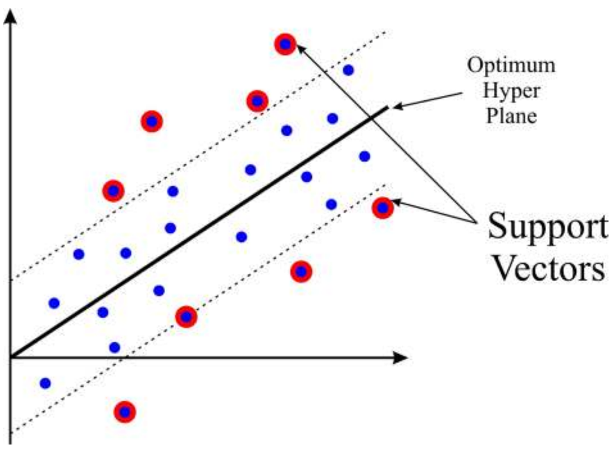

Figure 3.19. Typical Support Vector Machine structure (Ergun et al., 2010)

Table 3.6. Configuration details of the support vector machine models

Code	Kernel Function	Degree	Solver
SVM-1	Gaussian	-	ISDA
SVM-2	RBF	-	ISDA
SVM-3	Polynomial	1	ISDA
SVM-4	Polynomial	2	ISDA
SVM-5	Polynomial	3	ISDA
SVM-6	Polynomial	4	ISDA

3.7.2.3. Multilayer Perceptron

Multilayer Perceptron (MLP) is a type of artificial neural network commonly used for regression and classification tasks. A MLP model is composed of three main layers: the input layer, one or more hidden layers and the output layer. As illustrated in Figure 3.20, the input layer receives multiple input parameters (such as geometrical, operational and psychrometric properties) and transmits them to the hidden layers. Within the hidden layers, each neuron applies weighted summation and activation functions to transform the data. These transformations capture nonlinear relationships between inputs and outputs (Gürük et al., 2025). Finally, the output layer delivers predictions corresponding to performance metrics such as dew-point effectiveness, cooling capacity, water consumption, COP and process air outlet temperature.

MLP models are typically trained using backpropagation. In this method, data flows forward through the network, while the prediction error is propagated backward to update the weights using optimization algorithms. Different training functions are available, each with trade-offs in terms of training speed, convergence stability, and computational cost (Büyükalaca et al., 2023; Çerçi and Hürdoğan, 2020). In this study, four widely used algorithms were explored:

- Levenberg–Marquardt (trainlm): Fast and suitable for small to medium-sized datasets.
- Scaled Conjugate Gradient (trainscg): Memory-efficient, suitable for larger networks.
- BFGS Quasi-Newton (trainbfg): Accurate but slower, preferred in precise modeling.
- One Step Secant (trainoss): Hybrid approach balancing speed and memory usage.

To investigate the effect of network structure and training strategy, a total of 16 MLP models were developed using different combinations of hidden layer count, neuron numbers, activation functions and training algorithms. The model configurations are summarized in Table 3.7.

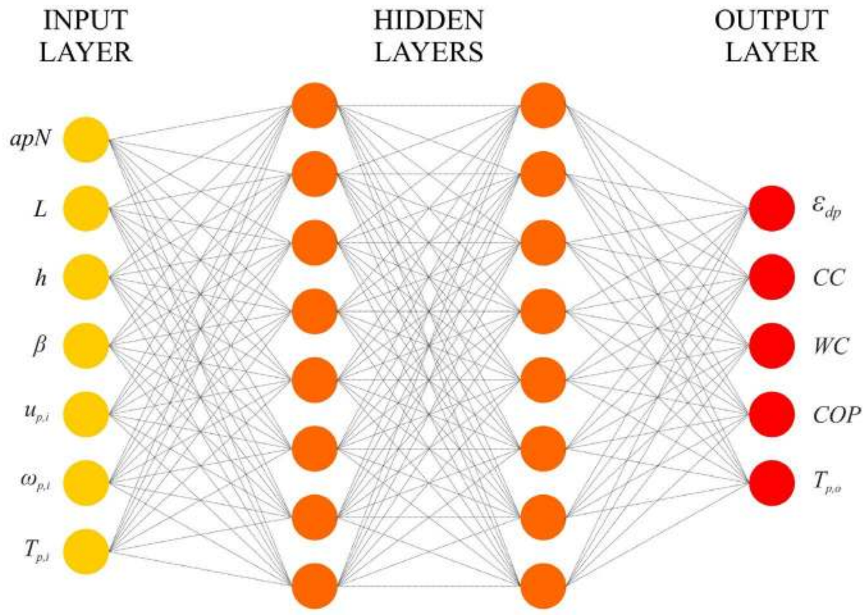

Figure 3.20. Schematic representation of the Multilayer Perceptron (MLP) network architecture (Asfahan et al., 2021)

Table 3.7. Configuration details of the multilayer perceptron models

Code	Training Function	Layer Number	Neuron Numbers	Activation Function
MLP-1	trainlm	1	10	tansig
MLP-2	trainlm	1	20	tansig
MLP-3	trainlm	2	10/10	tansig/tansig
MLP-4	trainlm	2	20/20	tansig/tansig
MLP-5	trainbfg	1	10	tansig
MLP-6	trainbfg	1	20	tansig
MLP-7	trainbfg	2	10/10	tansig/tansig
MLP-8	trainbfg	2	20/20	tansig/tansig
MLP-9	trainscg	1	10	tansig
MLP-10	trainscg	1	20	tansig
MLP-11	trainscg	2	10/10	tansig/tansig
MLP-12	trainscg	2	20/20	tansig/tansig
MLP-13	trainoss	1	10	tansig
MLP-14	trainoss	1	20	tansig
MLP-15	trainoss	2	10/10	tansig/tansig
MLP-16	trainoss	2	20/20	tansig/tansig

3.7.3. Statistical Indicators of Models

Model performance was assessed using three commonly adopted statistical metrics: the coefficient of determination (R^2), root mean squared error (RMSE) and relative error (RE) distributions. These metrics offer comprehensive insights into both the overall predictive accuracy and the consistency of the models across varying operating conditions.

The R^2 value ranges from 0 to 1, with values closer to 1 indicating a strong agreement between the predicted and actual outputs, which signifies high model accuracy. The RMSE quantifies the average magnitude of the prediction error, calculated as the square root of the mean of squared differences between predicted and observed values. A lower RMSE reflects better predictive performance. In addition, the relative error distribution helps identify localized deviations and anomalies, providing further clarity on model reliability at specific input conditions. Ideally, a well-performing model should yield high R^2, low RMSE, and narrow RE distributions. The formulations of these statistical indicators are provided in Equations 3.39 through 3.41 (Moore et al., 2009).

$$R^2 = 1 - \frac{\sum_{i=1}^{n} (Y_i - \hat{Y}_i)^2}{\sum_{i=1}^{n} (Y_i - \bar{Y})^2} \tag{3.39}$$

$$RMSE = \sqrt{\sum_{i=1}^{n} \frac{\left(Y_i - \hat{Y}_i\right)^2}{n}} \tag{3.40}$$

$$RE = \frac{Y_i - \hat{Y}_i}{Y_i} \tag{3.41}$$

where;

R^2: determination coefficient

n: number of data points

Y_i: actual dependent variable

$\hat{Y}_i$: predicted value

$\bar{Y}$: mean of Y_i values

RMSE: root mean square error

RE: relative error

4. RESULTS AND DISCUSSION

The results obtained from this study are presented in three structured phases, each focusing on a specific research objective while building upon the findings of the previous stage. This tiered methodology enabled a comprehensive understanding of the performance of indirect evaporative coolers and their optimization under realistic climatic and design constraints.

In the first phase, five different indirect evaporative cooler configurations (Type 0 through Type 4) were numerically analyzed under varying psychrometric conditions to evaluate the impact of airflow arrangement and internal mixing mechanisms on cooling performance. All geometric parameters were kept constant across configurations to ensure a fair comparison, with simulations exploring the effects of key operational inputs such as inlet temperature, humidity ratio, air velocity and the working-to-intake air ratio. A total of 420 CFD simulations were conducted to systematically evaluate the performance of each cooler configuration using a validated numerical model. For every case, four key performance parameters were calculated: dew-point effectiveness, area-normalized cooling capacity, specific water consumption and cooling coefficient of performance (COP). These metrics enabled a multi-dimensional comparison of thermal efficiency, energy performance and water usage across the five configurations.

In the second phase, the best-performing configuration (Type 2) from the first phase was selected for an in-depth geometric optimization study. Unlike the configuration comparison phase, the operational conditions were fixed to reflect a representative hot-humid climate, while key geometric parameters, aperture number, aperture diameter, channel length, channel gap, and working-to-intake air ratio, ere varied in full combination. This resulted in 4,200 unique CFD runs, each of which was evaluated for its effectiveness, cooling capacity, water consumption and COP characteristics. Additionally, geometric constraints such as reverse flow behavior were identified and filtered out using logistic regression analysis, and the remaining cases were analyzed using the desirability function method to determine optimal geometries under different performance priorities.

In the third and final phase, a comprehensive full-range parametric sweep was conducted, varying both geometric and operational parameters simultaneously. A total of 20,480 simulation cases were solved for the optimized Type 2 configuration, covering the full range of geometric and operational input combinations. The resulting dataset was used to develop a series of multi-linear regression (MLR) models, each designed to predict one of the key performance parameters: process air outlet temperature, cooling capacity, water consumption, and COP. In addition to the regression-based models, a diverse set of machine learning algorithms, including support vector machines (SVM), multilayer perceptrons (MLP) and decision tree (DT) models, were trained and evaluated to enable rapid and accurate estimation of cooler performance across all conditions. The aim was to create fast and accurate surrogate models capable of estimating cooler performance metrics without the need for further CFD computations.

In total, 25,100 CFD simulations were performed across all three phases. This makes the current research one of the most extensive numerical investigations in the field of dew-point indirect evaporative cooling, offering a robust foundation for both physical understanding and data-driven model development.

4.1. Configuration Performance Analysis

To identify the most effective internal flow configuration for dew-point indirect evaporative cooling, five distinct cooler designs, referred to as Type 0 through Type 4, were developed and numerically analyzed. These configurations included both conventional designs and novel multi-aperture variants introduced for the first time in this thesis. In order to ensure a fair and systematic comparison, all geometric parameters were kept constant across the simulations, including a fixed channel length of 1000 mm and a channel gap of 5 mm. The coolers were tested under a range of realistic psychrometric conditions, where key operational variables such as inlet air temperature, humidity ratio, air velocity and working-to-intake air ratio were varied according to the base values defined in Table 3.2.

To better understand the physical mechanisms that govern the performance differences between the five cooler configurations, velocity vectors, temperature contours and humidity distributions were extracted and analyzed for each design. These visualizations provide direct insight into airflow behavior, inter-channel mixing, evaporative cooling potential and saturation dynamics under identical boundary conditions. The results are discussed below in relation to Figures 4.1 to 4.10, which illustrates the representative distributions for each configuration.

Type 0 represents a conventional indirect evaporative cooler design, in which the process and working air streams are completely separated by an aluminum plate. There is no air transfer between the two channels, and as a result, the airflow remains uniform and undisturbed, exhibiting a nearly ideal laminar profile throughout the domain. As shown in the velocity vector plot (Figure 4.1), the absence of apertures or geometric intrusions leads to a streamlined flow. Regarding thermal behavior, the process air is cooled solely through heat exchange across the separating plate and even ideally, cannot be cooled beyond the wet-bulb temperature. As such, temperature reductions are lower when compared to other configurations. The humidity field confirms that the process air retains a constant humidity ratio, while the working channel air becomes increasingly humid due to continuous contact with the saturated wet surface, approaching saturation by the channel exit.

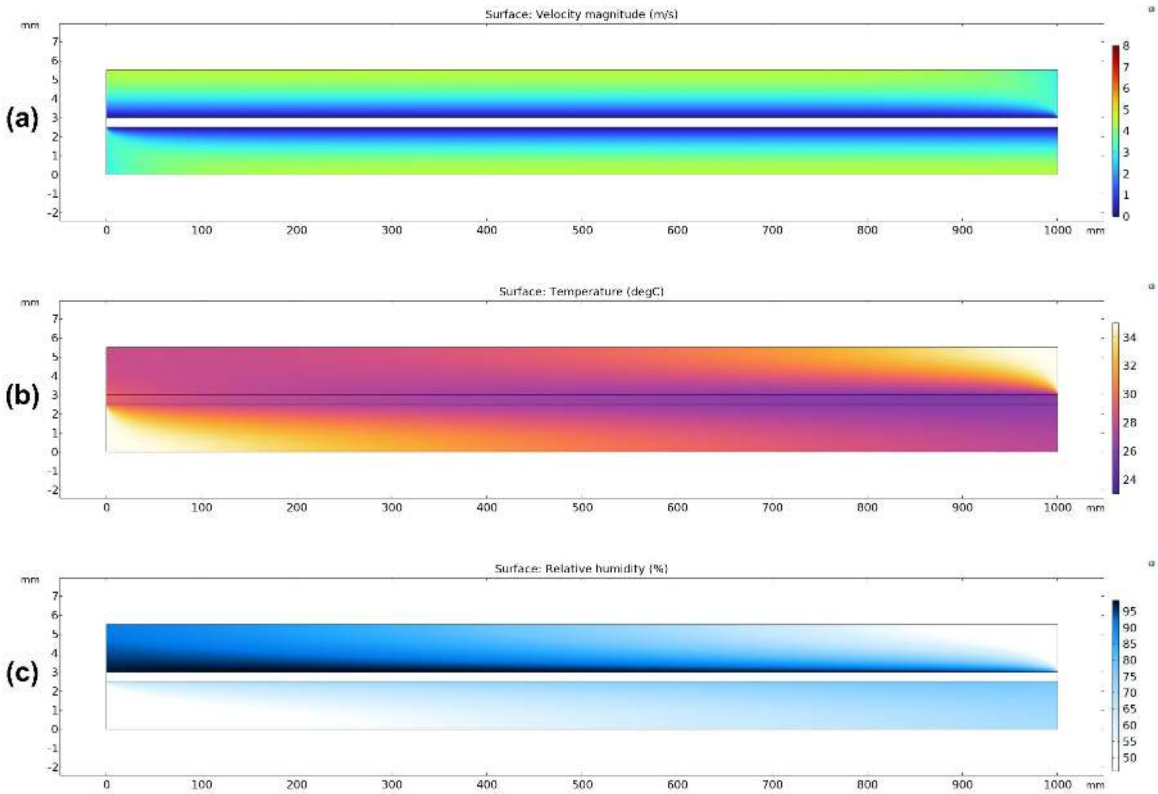

Figure 4.1. Velocity (a), temperature (b) and relative humidity (c) distributions for Type 0

In addition to the velocity, temperature, and humidity fields, the psychrometric chart presented in Figure 4.2 further clarifies the thermodynamic behavior of Type 0 under the given conditions. The blue squares trace the process air path, which follows a horizontal line at constant humidity ratio, confirming the absence of any mass transfer or moisture gain. The cooling process is purely sensible, resulting in a progressive temperature drop while maintaining the initial absolute humidity level. In contrast, the red markers show the working air path. This curve moves upward and slightly to the left, following an almost constant wet-bulb temperature line, at the early stages of the process. This indicates simultaneous cooling and humidification of the working air as it approaches saturation through continuous evaporation from the wetted surface. The final state of the working air moves closer to the saturation curve, highlighting the core principle of indirect evaporative cooling: enhancing process-side cooling via evaporation in the separate working channel, without direct moisture transfer.

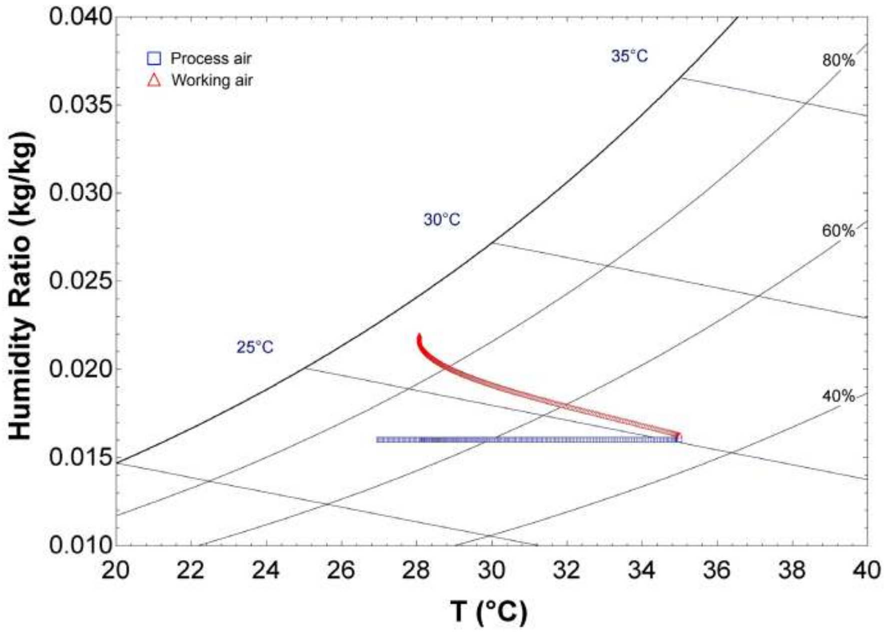

Figure 4.2. Representation of thermodynamic processes on psychrometric diagram for Type 0

Type 1 corresponds to a classical dew-point indirect evaporative cooler, widely studied in the literature. In this configuration, a single aperture is placed at end of the process channel, allowing a portion of the process air, defined by the working-to-intake air ratio, to enter the wet channel. This internal airflow redistribution enables cooling beyond the wet-bulb limit, theoretically approaching the dew-point temperature. As seen in the velocity vectors (Figure 4.3a), the airflow accelerates through the aperture, with noticeable changes in velocity gradients at the junction. The unhumidified process air, although partially cooled, retains its absolute humidity level prior to the aperture, while the redirected flow entering the wet channel experiences both relative and humidity ratio increases as it interacts with the wet surface (Figure 4.3c).

The psychrometric analysis of the Type 1 configuration (Figure 4.4) provides deeper insight into the thermodynamic behavior of both air streams and highlights the fundamental cooling mechanism of classical dew-point indirect evaporative coolers. While previous studies have illustrated schematic process paths on psychrometric charts, the diagrams presented in this section are, to the best of the author's knowledge, the first in the open literature to be generated directly from CFD-based simulation data. In this design, a single aperture positioned at the end of the process channel allows a portion of the already partially cooled process air to be redirected into the working channel, where it undergoes evaporative cooling. As reflected in the psychrometric chart, the process air, represented by blue markers, follows a nearly horizontal line of constant humidity ratio as it sensibly cools along the channel without any moisture addition. Upon reaching the aperture, the diverted process air enters the wet channel, triggering the onset of evaporative cooling. This is characterized by the working air (red markers) simultaneously decreasing in temperature and increasing in humidity ratio as it moves towards saturation.

Importantly, the working air in this configuration only begins evaporative cooling after the initial sensible cooling phase in the process channel. As evaporation progresses, the air approaches saturation and eventually continues downstream in a nearly saturated state. Once the air nears full saturation, further latent cooling potential is significantly limited, restricting the system's ability to exploit the full benefits of the evaporative process. This behavior illustrates a key limitation of conventional single-aperture dew-point coolers: the working air gradually loses its moisture-absorption capacity as it saturates, capping the achievable cooling performance. To overcome this thermodynamic bottleneck, multi-aperture configurations such as the Type 2 design have been proposed. By introducing fresh, dry process air through multiple apertures along the channel length, these systems maintain the driving force for continuous evaporation, thereby enhancing cooling effectiveness while preventing early saturation of the working air stream.

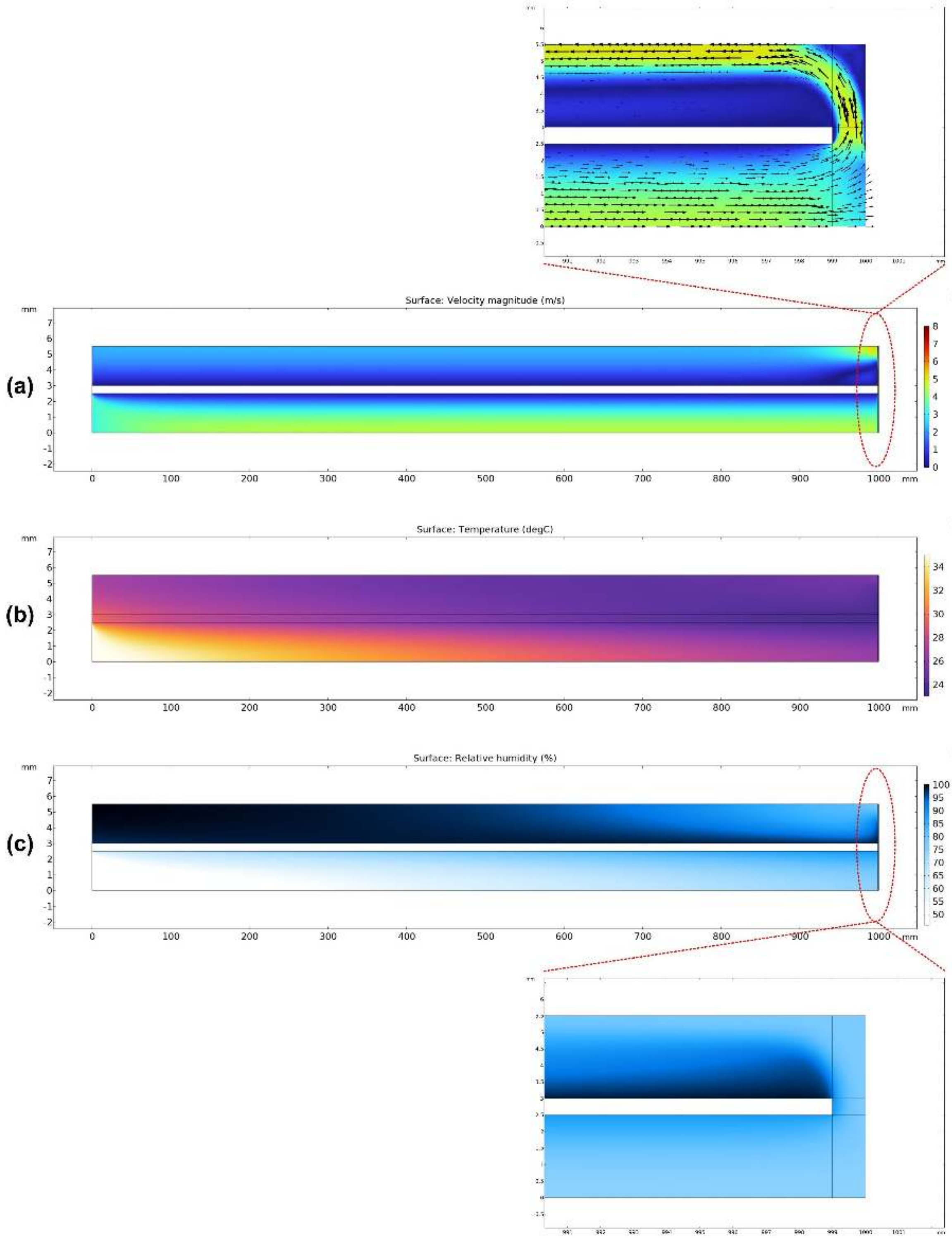

Figure 4.3. Velocity (a), temperature (b) and relative humidity (c) distributions for Type 1

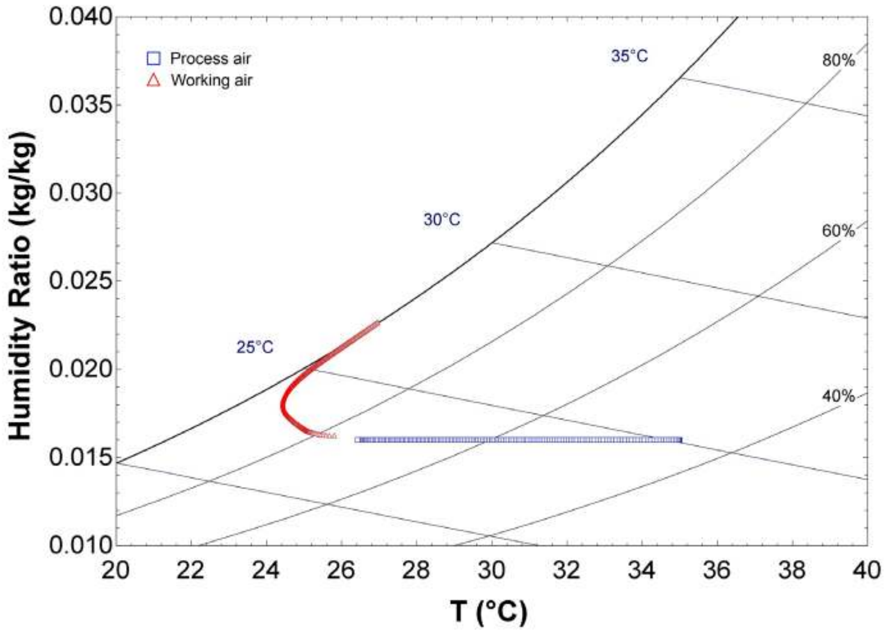

Figure 4.4. Representation of thermodynamic processes on psychrometric diagram for Type 1

Type 2 enhances the airflow strategy of Type 1 by incorporating multiple apertures spaced evenly along the length of the separating plate. This multi-aperture design addresses a critical limitation observed in Type 1, where the air entering from the single end aperture often reaches saturation too quickly, limiting further evaporative cooling. As illustrated in the velocity field (Figure 4.5a), the multi-point transfer of air from the process to the working channel ensures a more distributed and continuous introduction of relatively dry air, sustaining evaporation throughout the channel. Consequently, this design enables a greater approach toward the dew-point temperature and improves overall cooling efficiency. The humidity distribution reveals a repeated regeneration of evaporation zones, supported by unsaturated air entering at each aperture location (Figure 4.5c).

The psychrometric diagram of Type 2 (Figure 4.6) provides valuable insights into how the multi-aperture strategy fundamentally improves the evaporative cooling process compared to the single-aperture approach used in Type 1. In this configuration, the process air (blue squares) undergoes progressive sensible cooling along the length of the channel. At each of the five apertures, a portion of this partially cooled process air is redirected into the working channel. The psychrometric conditions of the air immediately after crossing each aperture are shown by the dotted red curves emerging from the process air flow. These dotted curves correspond to the localized evaporative cooling that the air begins to experience upon entering the wet working channel. Crucially, these air portions do not maintain their initial post-aperture conditions but rapidly mix with the working air that comes from upstream, which is represented by the connected red triangle markers.

A key observation is that the air extracted from the last aperture, depicted on the leftmost side of the psychrometric plot, originates from the most cooled section of the process channel, exhibiting lower temperatures and the lowest humidity ratios. Conversely, air from the first aperture (rightmost side of the diagram) has undergone minimal sensible cooling and thus appears at higher temperature and humidity values. The dashed lines connecting each aperture's exit point to the working channel trajectory visually demonstrate this rapid mixing process. Once inside the working channel, the incoming dry air refreshes the local evaporation potential, preventing the working air from reaching saturation too early. As a result, the working air evolves in a stepwise pattern, each injection point creates a new opportunity for further evaporative cooling. This staged regeneration mechanism allows Type 2 to maintain a stronger and more consistent cooling drive, ultimately enabling a closer approach to the dew-point temperature. The psychrometric illustration clearly highlights how the spatial distribution of apertures translates into thermodynamic advantages within the air streams, providing a comprehensive understanding of the superior performance of the multi-aperture concept.

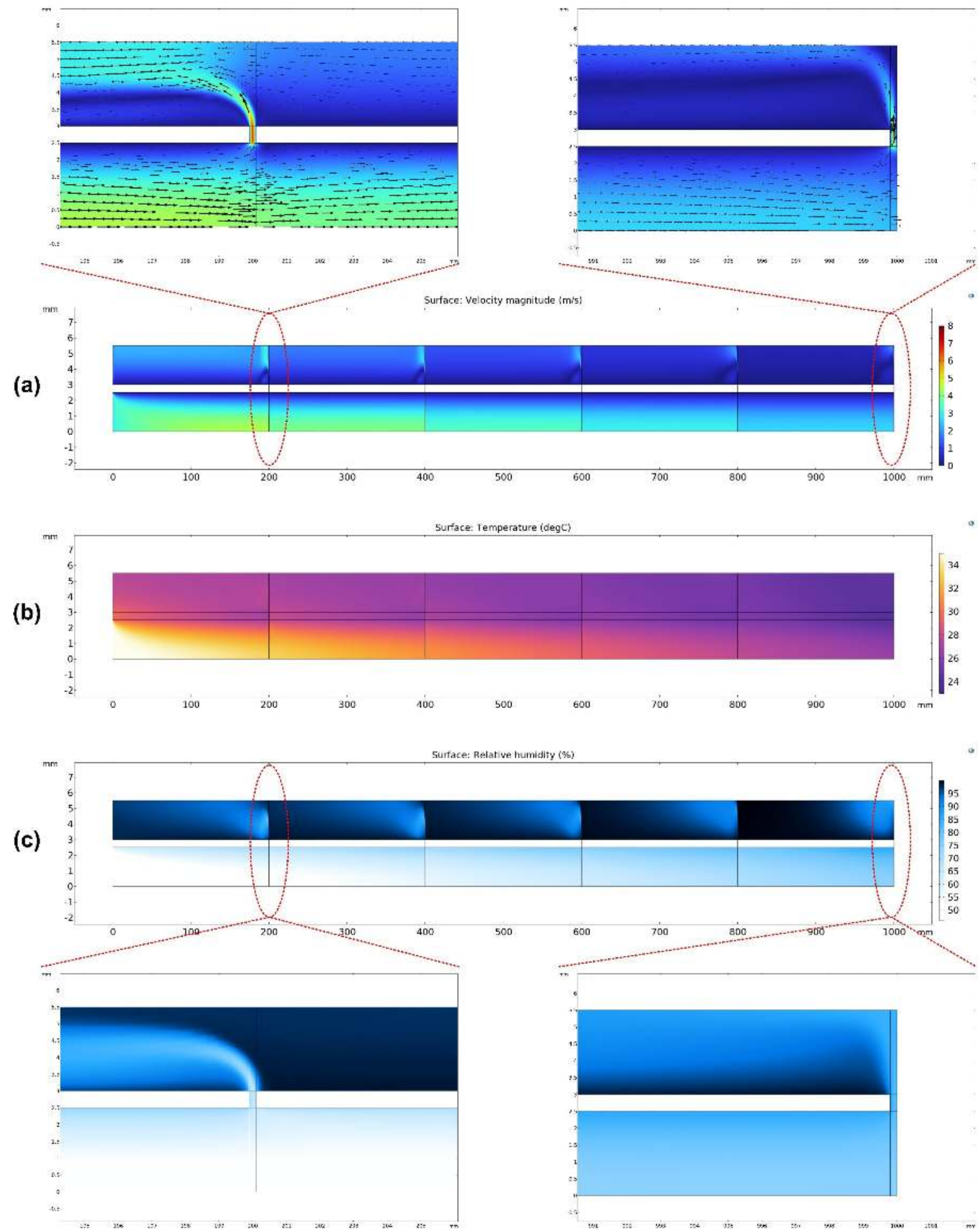

Figure 4.5. Velocity (a), temperature (b) and relative humidity (c) distributions for Type 2

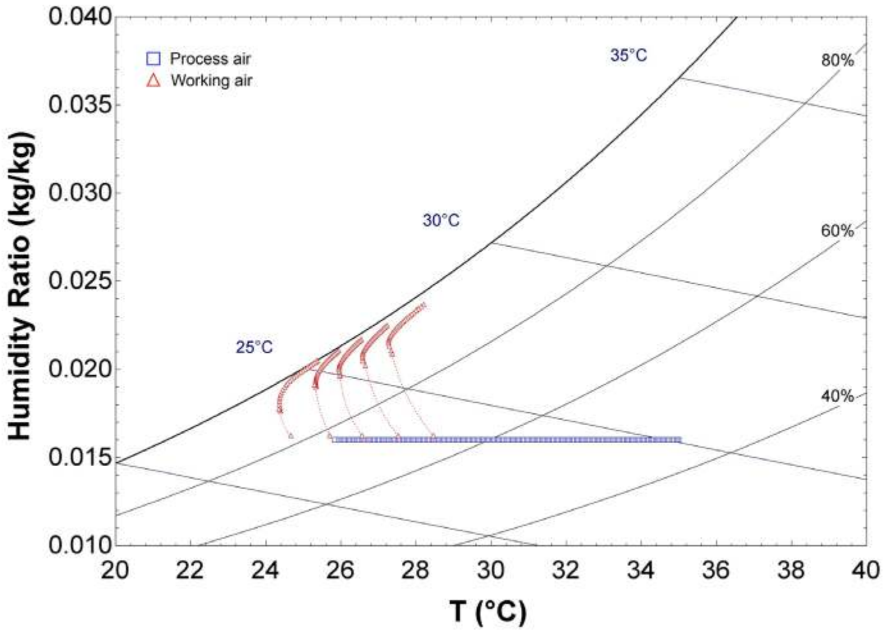

Figure 4.6. Representation of thermodynamic processes on psychrometric diagram for Type 2

Type 3 is an enhanced configuration of Type 1 that introduces a third airflow pathway by adding an auxiliary working air channel positioned above the primary working channel. In this design, the process air and working air streams are fully separated, eliminating the internal airflow mixing characteristic of Type 1. The working air is instead supplied exclusively by the auxiliary channel through a single aperture located near the outlet of the working channel. This auxiliary airflow, which remains dry and cooled throughout its passage, is injected into the wet channel where it undergoes evaporation and cooling upon contact with the wetted surfaces.

The presence of the auxiliary channel allows Type 3 to maintain the full process air stream without sacrificing any portion to the working channel, as observed in Type 1. Consequently, the process air volume is higher, leading to increased velocities in the process channel, as shown in the velocity contours (Figure 4.7a). To ensure fair performance comparisons, key metrics such as cooling capacity and water consumption are normalized per unit surface area, mitigating the influence of volumetric imbalances. The working air, after entering through the single aperture, quickly reaches saturation over a relatively short distance, which inherently limits the extent of evaporative cooling. This behavior is evident in the relative humidity distribution (Figure 4.7c), where the moistening effect diminishes once saturation is achieved.

The psychrometric diagram (Figure 4.8) further illustrates the distinct thermodynamic behavior of each air stream within Type 3. The process air follows a typical indirect evaporative cooling path, experiencing a temperature drop at constant humidity ratio. The auxiliary air remains entirely unchanged, maintaining its original dry state since it never comes into contact with wetted surfaces. In contrast, the working air initiates evaporative cooling after receiving the auxiliary flow from the aperture and gradually approaches saturation, initially following a constant wet-bulb trajectory. However, due to the single injection point, the working air cannot sustain prolonged evaporation, and the cooling potential is effectively capped by the early attainment of saturation. This phenomenon highlights the inherent limitation of single-aperture systems and motivates the transition to multi-aperture designs, such as that implemented in Type 4, where continuous regeneration of unsaturated air can significantly enhance cooling effectiveness.

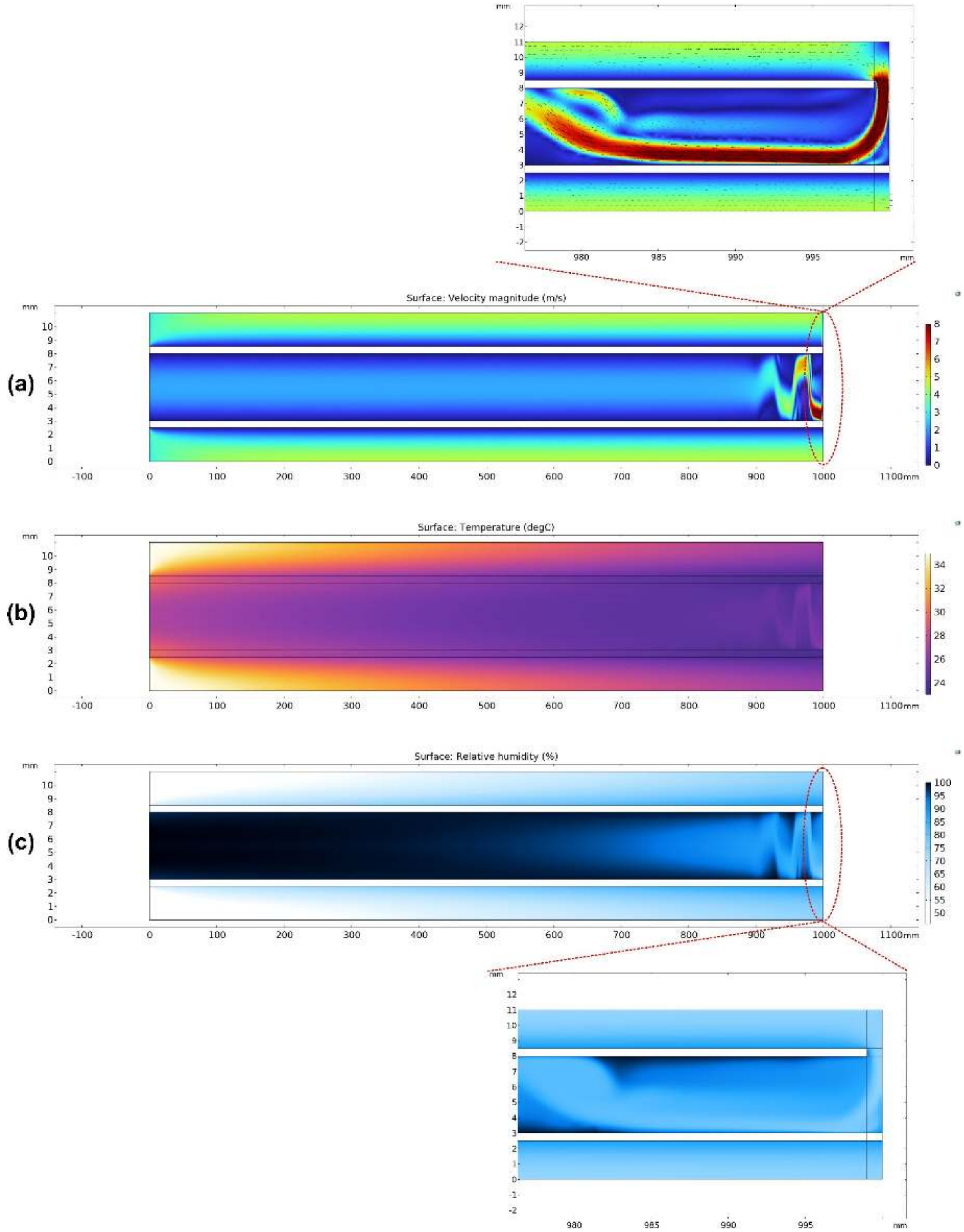

Figure 4.7. Velocity (a), temperature (b) and relative humidity (c) distributions for Type 3

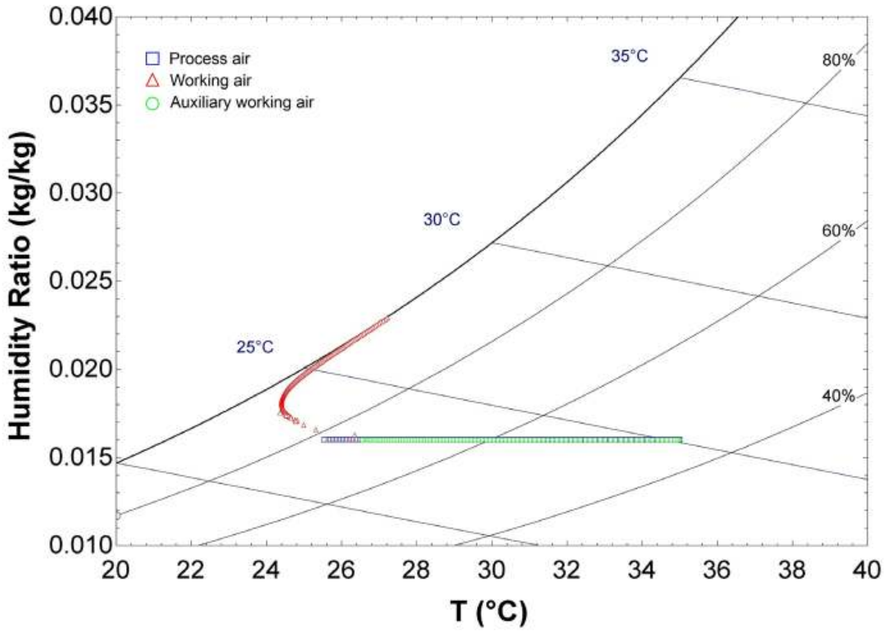

Figure 4.8. Representation of thermodynamic processes on psychrometric diagram for Type 3

Type 4 represents the most advanced configuration evaluated in this study, combining the complete air separation strategy of Type 3 with the multi-aperture concept introduced in Type 2. In this design, the process and working air channels are entirely independent, with the working air supplied exclusively through a dedicated auxiliary channel. This structural arrangement is clearly reflected in the velocity contours (Figure 4.9a), where the airflow remains steady and stable across the process channel, while the working channel receives distributed air injections at multiple aperture locations. The temperature distribution (Figure 4.9b) reveals that the multi-aperture approach successfully maintains active evaporation along the entire length of the wet channel. Unlike Type 3, where the wet surface quickly reaches saturation and evaporation ceases prematurely, Type 4 sustains effective cooling by continuously introducing relatively dry air at several points. The relative humidity contours (Figure 4.9c) further demonstrate this mechanism: rather than a single large humidification zone, multiple smaller evaporation fronts emerge, preventing full saturation until the very end of the channel.

The psychrometric diagram (Figure 4.10) provides deeper insight into this staged evaporation behavior. The process air (blue squares) moves horizontally without any moisture gain, confirming the strict separation of dry and wet channels. The auxiliary air (green circles), which feeds the working channel, also maintains its original dry state initially. Upon entering the working channel through each aperture, portions of this auxiliary air follow individual evaporative cooling paths (red triangles) before mixing with the upstream humidified working air. The distinctive curved trajectories demonstrate how each aperture introduces unsaturated air that momentarily supports evaporation before blending into the increasingly saturated bulk air. This multi-point regeneration prevents early saturation, maximizes the utilization of evaporation potential, and enables a closer approach to the dew-point temperature without incurring the performance penalties seen in single-aperture designs. By strategically distributing both airflow and evaporation demand, Type 4 achieves good cooling performance with improved flow stability and humidity control.

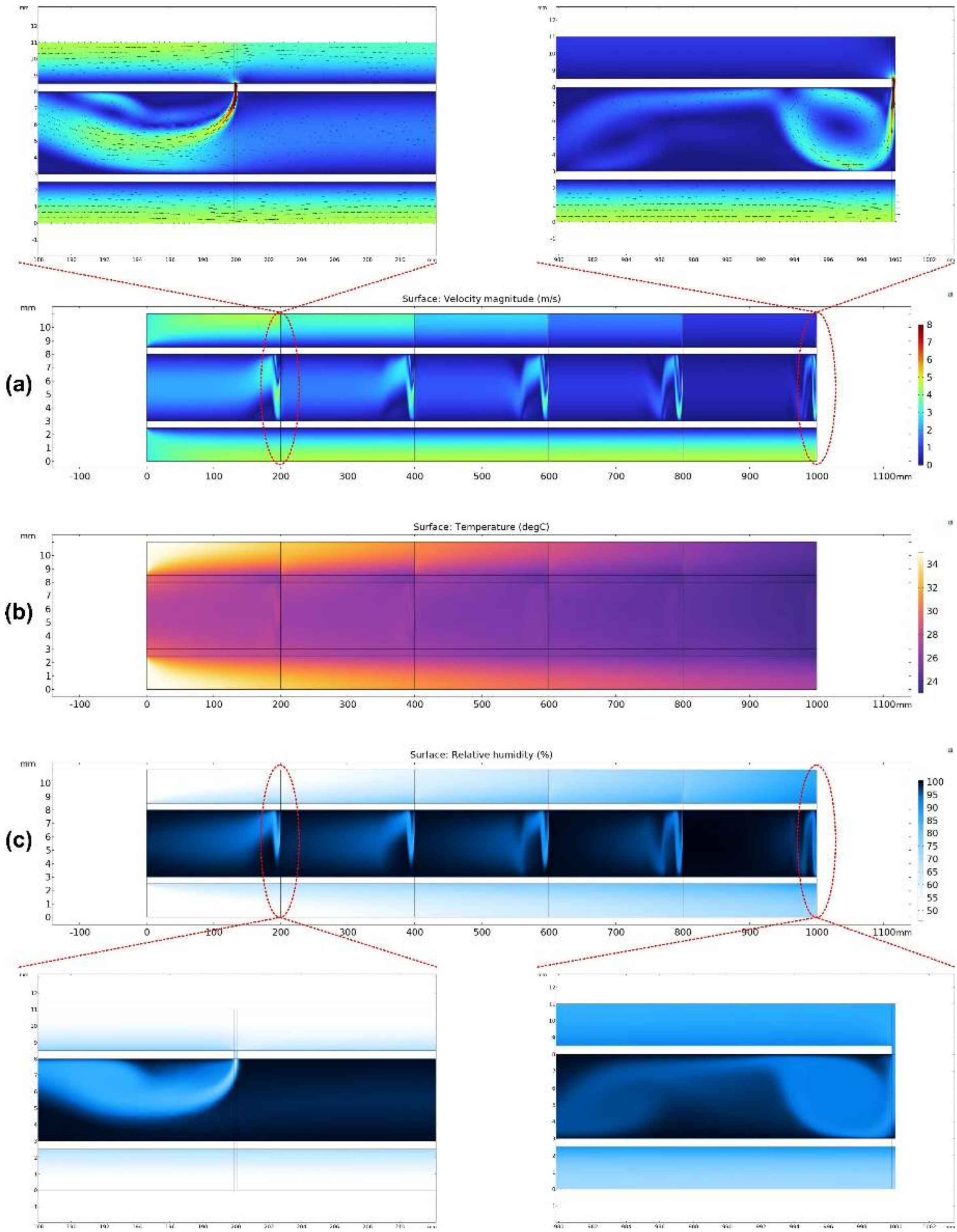

Figure 4.9. Velocity (a), temperature (b) and relative humidity (c) distributions for Type 4

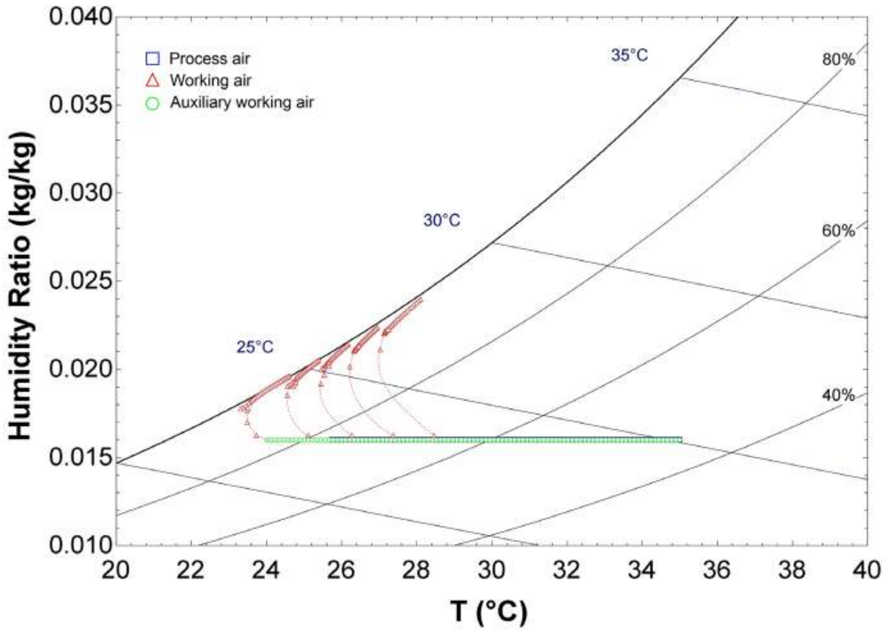

Figure 4.10. Representation of thermodynamic processes on psychrometric diagram for Type 4

4.1.1. Pressure Drops and In-Channel Air Property Distribution

An important aspect of cooler performance is the pressure drop across the cooler, as it directly influences the fan power requirement and thus the overall energy efficiency. Figure 4.11 compares the total pressure drop values (ΔP) observed for all configurations under base operating conditions. It is important to note that the presented ΔP values correspond to the total pressure losses encountered along all flow passages within each cooler, including both the process and working channels. While Type 0, Type 1, and Type 2 have two flow domains (process and working channels), Type 3 and Type 4 include an additional auxiliary working channel, bringing the total number of internal flow paths to three. This structural difference leads to a significant impact on pressure loss. As illustrated in Figure 4.11, Type 3 exhibits the highest pressure drop among all configurations, reaching approximately 80 Pa, which is attributed to its more complex internal geometry and extended airflow path through the auxiliary channel. Type 4, which shares the auxiliary channel concept but includes air mixing apertures, shows a moderately high pressure drop (65 Pa), lower than Type 3 yet higher than the dual-channel configurations. In contrast, Type 1 and Type 2 exhibit the lowest ΔP values, around 45 Pa and 42 Pa, respectively, indicating their relatively favorable aerodynamic design. Type 0, despite having only two channels, shows a higher pressure drop (60 Pa) than Type 1 and 2, likely due to the lack of apertures allowing internal air redistribution and the resulting higher resistance along the full-length channels.

These observations emphasize the aerodynamic advantage of aperture-based designs (especially Type 2), not only in enhancing thermal performance but also in reducing flow resistance. Minimizing pressure drop is essential for lowering fan consumption and maximizing system COP, which is discussed in later sections.

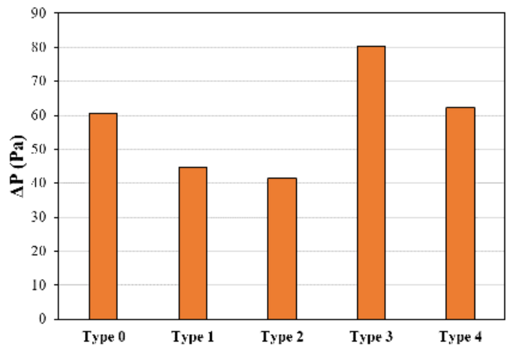

Figure 4.11. Comparison of pressure drops across various cooler types

To eliminate any potential ambiguity regarding the source of data presented in the upcoming figures, an additional visualization is provided in Figure 4.12, which illustrates the evolution of velocity profiles along a simplified 2D air channel. These results were directly obtained from Comsol simulations carried out in this thesis under representative flow conditions and demonstrate the development of the velocity field from the channel inlet to the fully developed region. As shown in Figure 4.12, the channel can be divided into three distinct flow regimes: the irrotational entrance region, the developing flow region, and the fully developed laminar region. At the inlet (left), a uniform velocity profile is imposed with a constant average velocity of 3 m/s. As the flow progresses downstream, the viscous effects from the channel walls gradually modify the profile, resulting in a parabolic distribution at the fully developed stage. At this point, the maximum velocity (u_{max}) at the symmetry axis reaches 4.5 m/s, consistent with the analytical relationship for laminar flow between parallel plates (White, 2011):

$$u_{max} = \frac{3}{2} u_{avg} \quad (4.1)$$

The observed increase from 3 m/s to 4.5 m/s at the centerline of velocity figure (Figure 4.12) is therefore a direct consequence of laminar flow development within the narrow channels of the cooler.

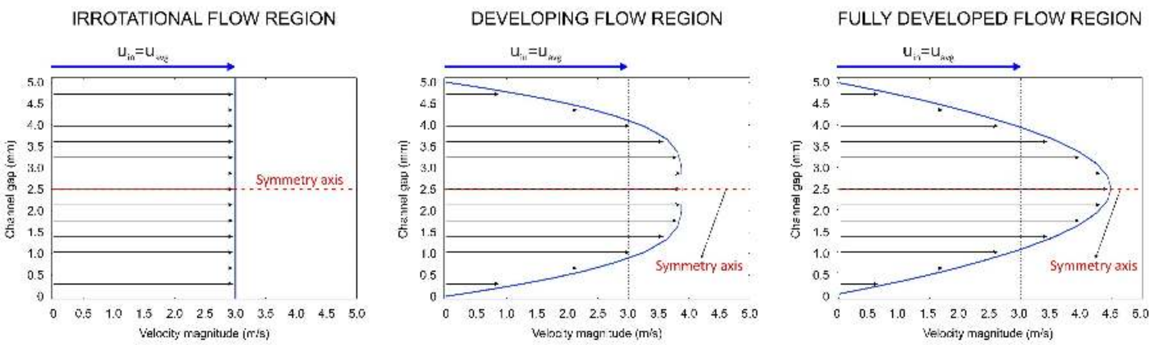

Figure 4.12. Velocity profile development along the air channel

All velocity, pressure, temperature and humidity distributions presented in the following sections (Figures. 4.13-4.15) are extracted along the central symmetry plane of the channel, as indicated by the red dashed lines in Figure 4.12. This plane was chosen to capture the most representative profiles while benefiting from reduced computational costs due to geometric symmetry.

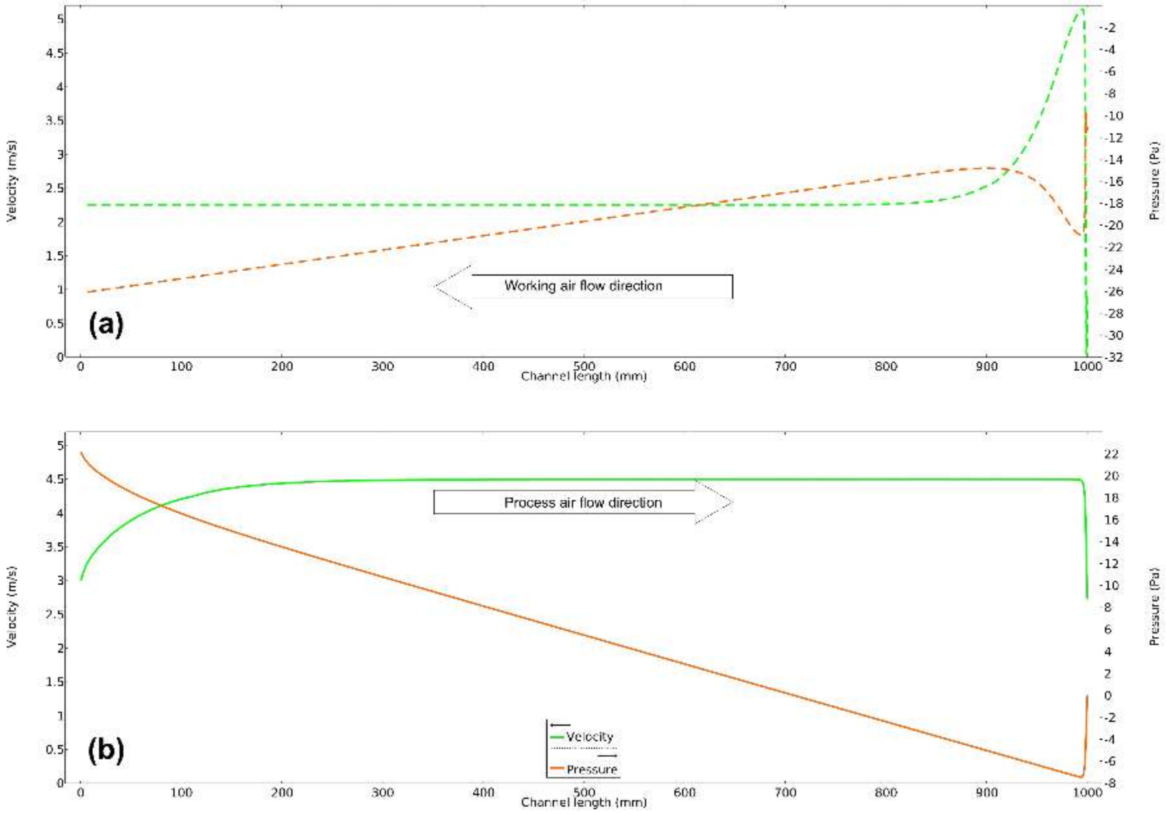

Figure 4.13. Velocity and pressure distributions along working channel (a) and process channel (b) for Type 1

Figure 4.13 displays the velocity magnitude and pressure along both channels of the cooler. In the working channel (Figure 4.13a), the airflow direction is from right to left, starting at x = 1000 mm and exiting at x = 0 mm. Since Type 1 features only a single aperture located at the very end of the channel, the working air enters only at that point. This configuration results in a nearly uniform velocity along most of the channel length, followed by a steep acceleration near the exit due to sudden inflow. The pressure decreases slightly across the channel, with a rapid drop at the aperture region, which indicates concentrated mixing and momentum gain at the aperture section. In the process channel (Figure 4.13b), air flows from left to right in a typical manner. Since there is no intermediate air diversion until the very end, the velocity is constant, while pressure drops continuously in a relatively smooth profile. The absence of multiple apertures yields a predictable and steady decline in pressure without any pronounced jumps.

Temperature and relative humidity profiles for Type 1 are presented in Figure 4.14. In the working channel (Figure 4.14a), fresh process air enters only at the final aperture. As a result, the evaporation-induced cooling is dominant along the initial and middle section of the working channel, causing the working air to simultaneously decrease in temperature and increase in relative humidity. However, as the working air approaches saturation, the rate of evaporation diminishes considerably. Beyond this point (typically observed near the latter half of the channel) the cooling potential of evaporation is nearly exhausted. Consequently, the process air flowing in the other channel begins to transfer heat back into the now-saturated working air, resulting in a slight temperature increase near the outlet of the working channel. This shift marks a transition from latent to primarily sensible heat exchange, illustrating the thermodynamic limit of evaporation-driven cooling in single aperture configurations. On the process side (Figure 4.14b), the typical indirect evaporative cooling pattern is evident. As the process air moves from left to right, its temperature steadily decreases while the relative humidity increases. Since no water is added to the process air, its humidity ratio remains constant, and the observed relative humidity rise is solely attributed to the drop in saturation vapor pressure, a classic psychrometric effect.

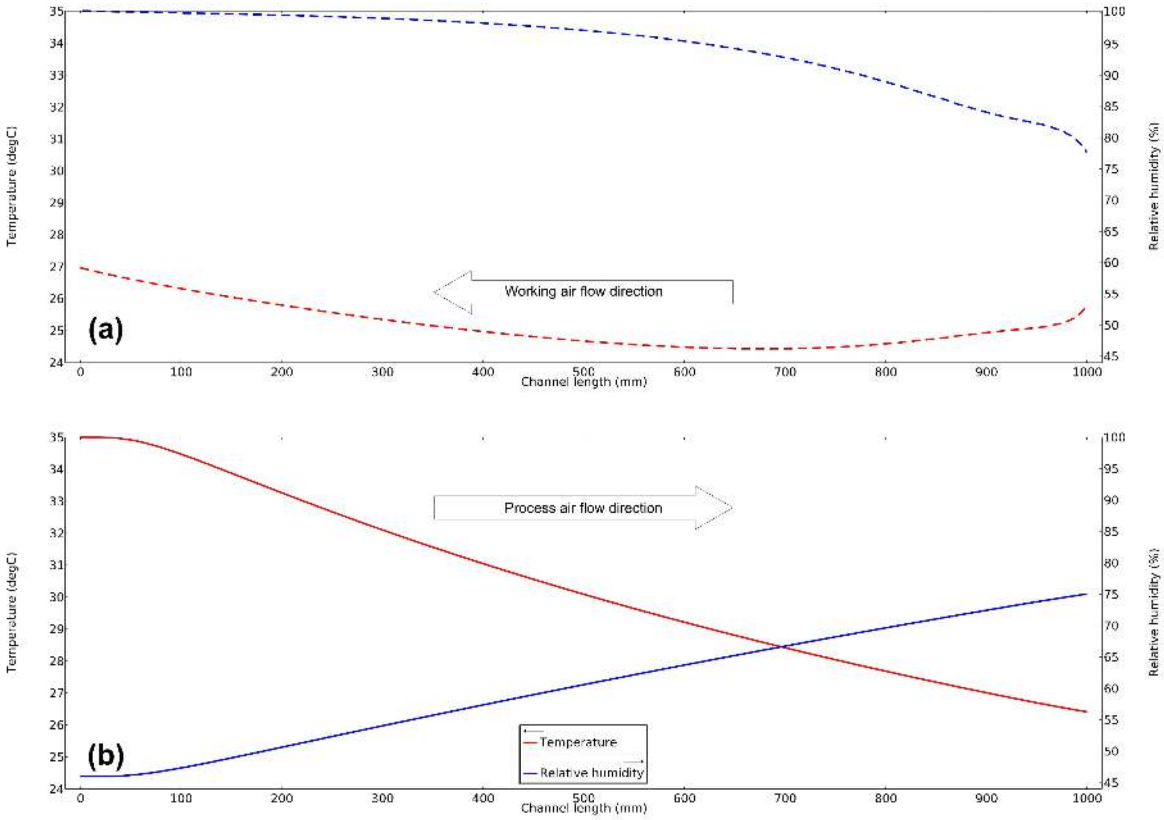

Figure 4.14. Temperature and relative humidity distributions along working channel (a) and process channel (b) for Type 1

Finally, Figure 4.15 presents the variation of humidity ratio along the channel length for both process and working air. As expected, the humidity ratio of the process air remains flat throughout its path, confirming that no moisture transfer occurs into the dry process air stream. In contrast, the working air exhibits a gradually increasing humidity ratio as it absorbs moisture from the wet surfaces. This monotonic trend is consistent with the evaporative cooling mechanism and indicates the continuous absorption of water vapor along the channel length.

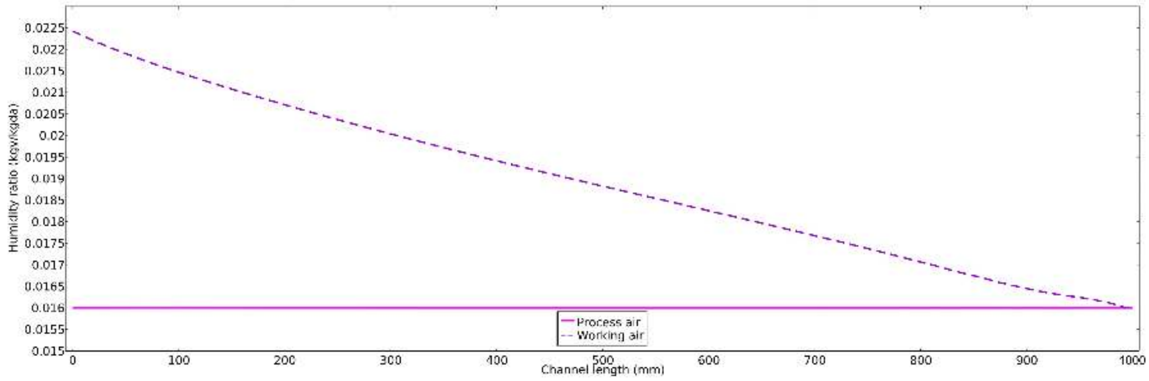

Figure 4.15. Humidity ratio distributions along the channels for Type 1

To further investigate the performance of Type 2, which utilizes a multi-aperture configuration for enhanced internal mixing, detailed analyses of velocity, pressure, temperature, relative humidity, and humidity ratio were conducted. All profiles presented in Figure 4.16, Figure 4.17 and Figure 4.18 were extracted from the centerline (symmetry axis) of the channels as modeled in Comsol Multiphysics software.

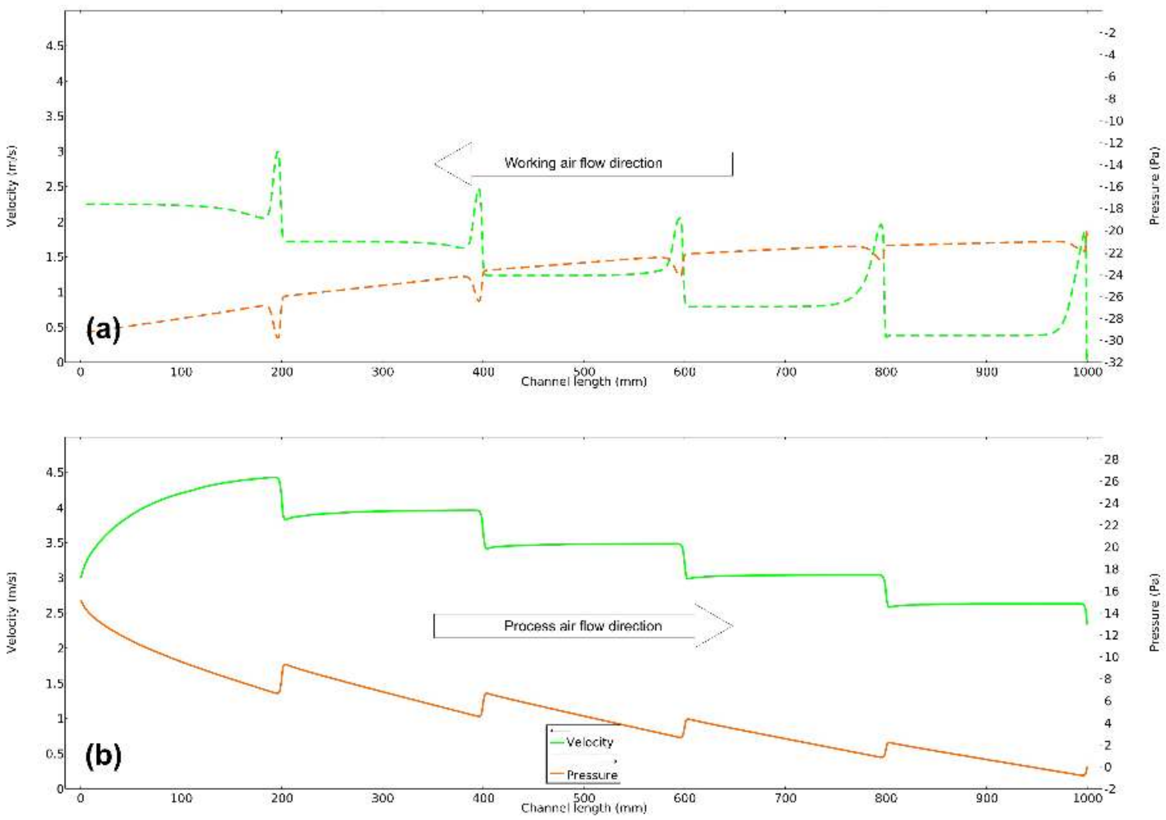

Figure 4.16. Velocity and pressure distributions along working channel (a) and process channel (b) for Type 2

Figure 4.16 presents the velocity and pressure distributions along the working channel (Figure 4.16a) and the process channel (Figure 4.16b). In the working channel, airflow proceeds from right to left, starting at x = 1000 mm and exiting at x = 0 mm. As air is introduced through five equally spaced apertures, the velocity experiences a series of sharp increases due to the momentum added by the incoming stream. Between each aperture, the flow stabilizes until the next injection occurs. The maximum velocity is reached near the outlet, where the total redirected air volume is the highest. Correspondingly, pressure in this channel gradually decreases along the direction of flow, though small localized drops occur after each aperture due to rapid mixing. These pressure drops directly correlate with the local velocity surges, revealing how aperture-induced disturbances shape the dynamic field. In the process channel (Figure 4.16b), air flows in the standard direction, from x = 0 mm to x = 1000 mm. Velocity decreases progressively due to mass loss through the apertures, while the pressure drops nearly linearly with only minor perturbations. These small fluctuations reflect localized changes in flow momentum and minor redistribution events, but overall, the aerodynamic profile remains smooth and predictable.

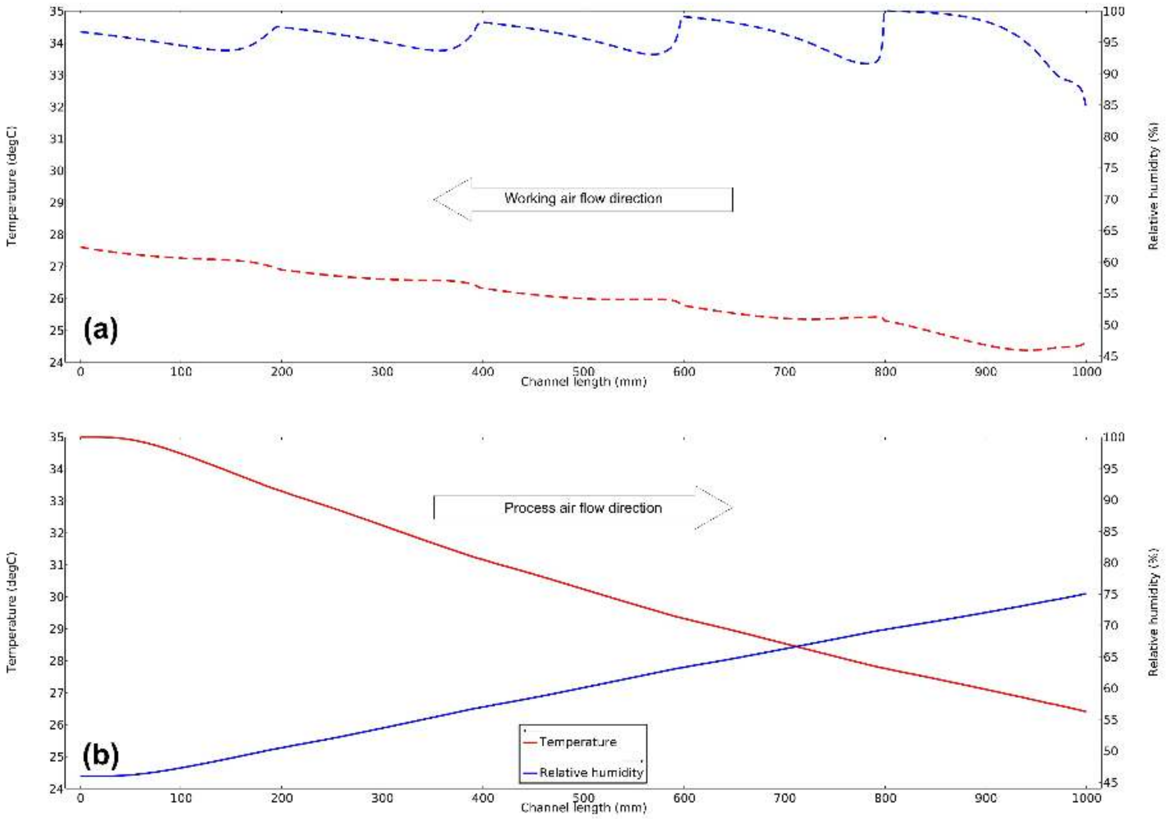

Figure 4.17. Temperature and relative humidity distributions along working channel (a) and process channel (b) for Type 2

Figure 4.17 displays the temperature and relative humidity trends within both channels. As before, the working channel (Figure 4.17a) should be read from right to left. Each aperture introduces relatively warmer and drier process air into the wet channel, causing local temperature increases and relative humidity drops. These are followed by gradual humidity recovery and temperature stabilization due to ongoing evaporation at the wet walls. This alternating pattern forms a distinctive sawtooth shape in both temperature and RH profiles. Meanwhile, the process channel (Figure 4.17b) exhibits a typical indirect evaporative cooling pattern: temperature steadily decreases along the flow direction, while relative humidity increases due to the psychrometric shift, even though there is no change in absolute moisture content.

Completing the thermodynamic picture, Figure 4.18 illustrates the humidity ratio distributions. In the process channel, the humidity ratio remains flat, confirming no mass transfer across the dry side boundary. However, in the working channel, the pattern is more dynamic. After each aperture, the dry process air dilutes the moist working stream, causing a sudden drop in humidity ratio. This is followed by a gradual climb as evaporation replenishes moisture. This cycle repeats with each aperture, revealing a consistent sequence of dilution and re-saturation, which exemplifies the role of geometric design in shaping moisture transport within the device.

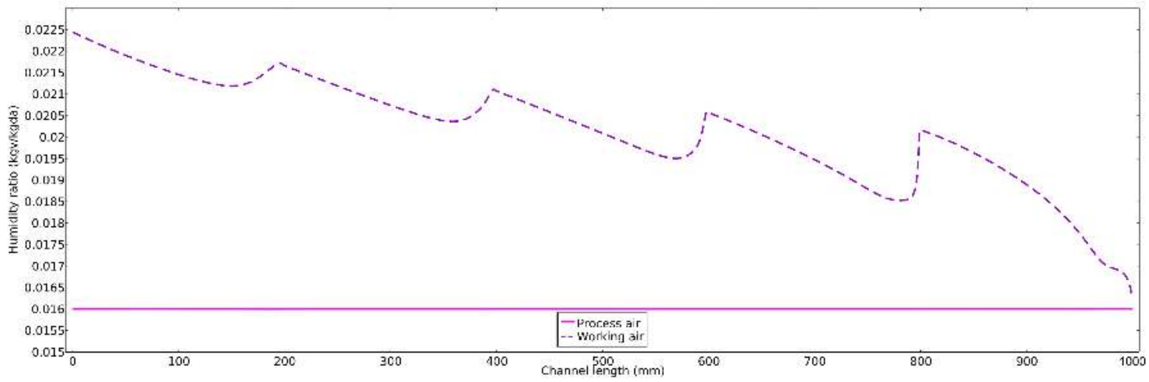

Figure 4.18. Humidity ratio distributions along the channels for Type 2

In contrast to the simpler two-channel designs of Type 1 and Type 2, Type 3 and Type 4 adopt a three-layer configuration comprising a process channel, a primary working channel, and an auxiliary working channel at the top. This structural complexity introduces additional interactions and requires special attention in data extraction. In this study, velocity, pressure, temperature, relative humidity, and humidity ratio distributions for Type 3 were obtained by referencing the symmetry axes of the process and auxiliary channels, while for the working channel, a virtual mid-plane was defined across its cross-section to ensure data was collected from the geometric center. This consistent mid-channel sampling across all layers allows fair comparisons among the three domains. It should be noted that the flow direction in the process and auxiliary working channels follows the standard convention, from x = 0 mm to x = 1000 mm (left to right), whereas the working channel data must be interpreted in reverse—from x = 1000 mm to x = 0 mm (right to left). This directional alignment ensures accurate reading and comparison of the profiles along each channel. Figures 4.19-21 illustrate the in-channel air property distributions for the Type 3 configuration. This layout features a three-layer design with an auxiliary working channel, a primary working channel, and a process channel, each contributing uniquely to the internal air behavior.

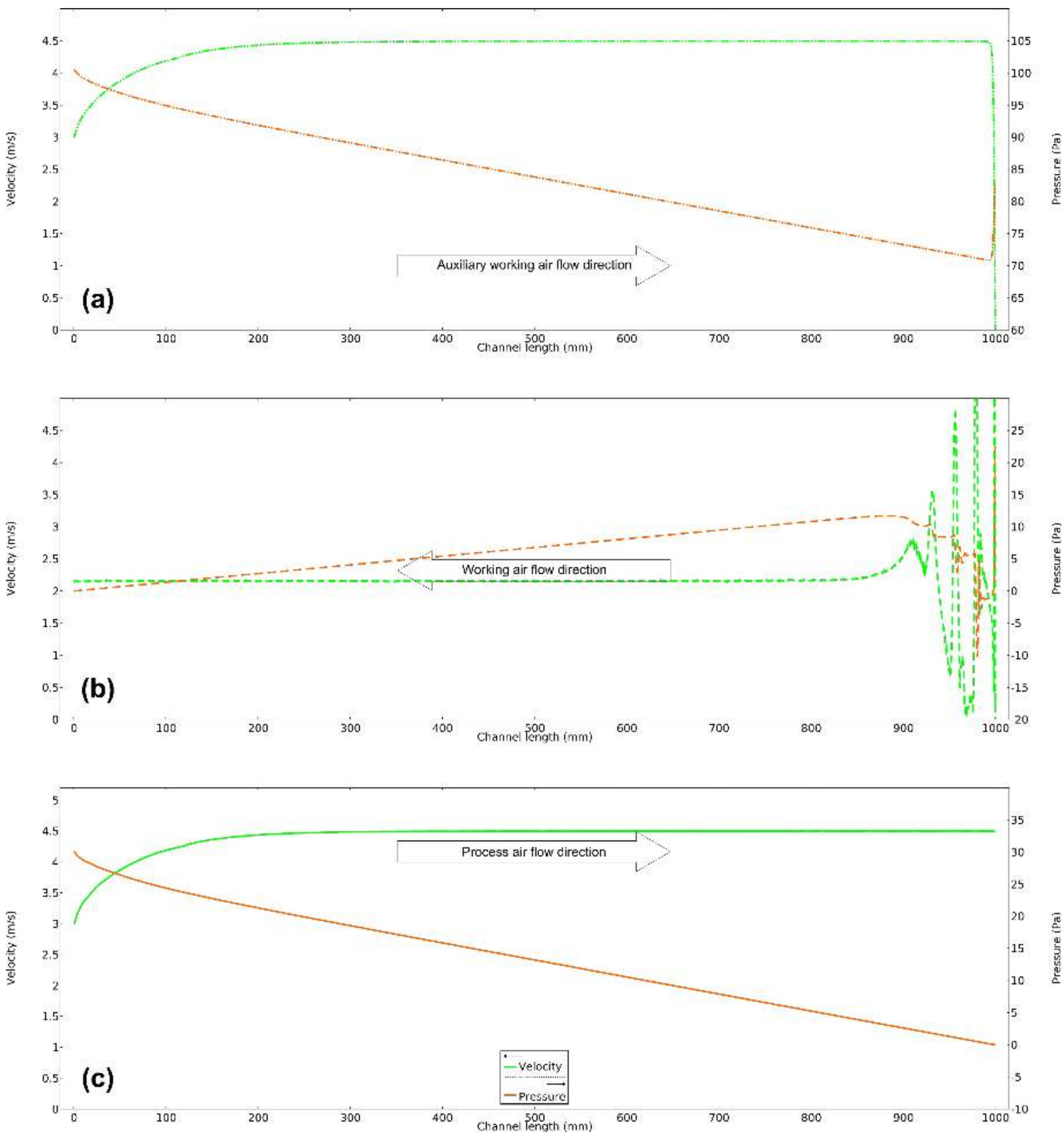

Figure 4.19. Velocity and pressure distributions along auxiliary working channel (a), working channel (b) process channel (c) for Type 3

In Figure 4.19, the pressure and velocity profiles for the auxiliary working (a), working (b) and process (c) channels are presented. The auxiliary working channel (Figure 4.19a) shows a smooth pressure drop, indicating stable flow through the topmost passage. In contrast, the working channel (Figure 4.19b), which receives redirected air from the auxiliary passage through the aperture exhibits irregular pressure oscillations and velocity spikes near the outlet region. These disturbances are caused by the injection of auxiliary air into the working stream, creating local turbulence and enhancing mixing but also increasing flow complexity. The process channel (Figure 4.19c) maintains a steady pressure gradient and consistent velocity profile, demonstrating minimal disruption and effective heat transfer.

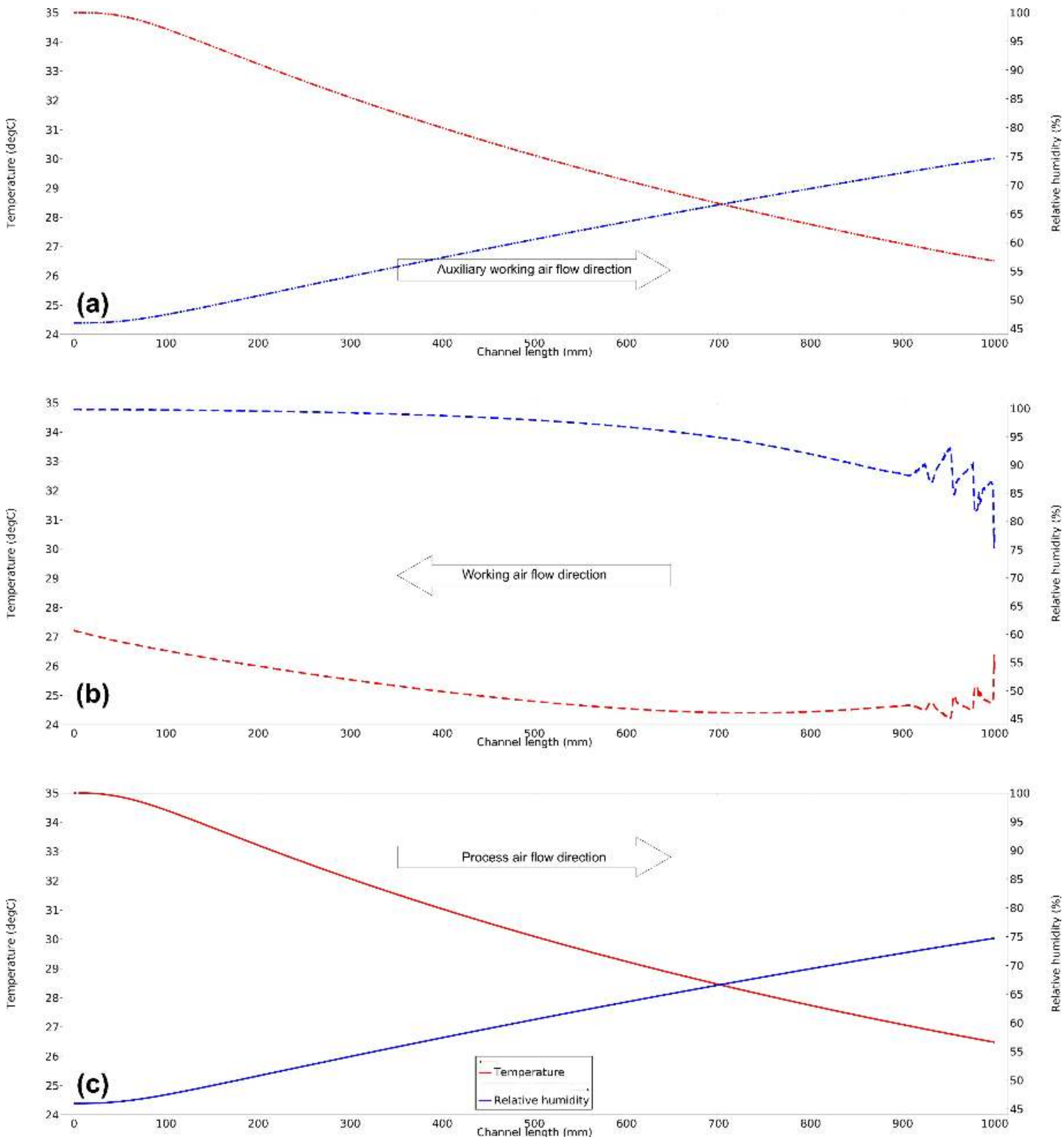

Figure 4.20. Temperature and relative humidity distributions along auxiliary working channel (a), working channel (b) process channel (c) for Type 3

Figure 4.20 displays the evolution of air temperature and relative humidity in the same three channels. In the auxiliary channel (Figure 4.20a), the air experiences continuous cooling as it flows. Unlike the primary working channel, this auxiliary passage does not feature wetted surfaces; therefore, no evaporation occurs within it. The observed increase in relative humidity is hence not a result of added moisture, but rather a psychrometric response to the decreasing air temperature. As the air cools due to indirect heat transfer from the evaporative activity occurring in the adjacent wet channels below, its capacity to hold moisture diminishes. Consequently, the saturation pressure drops while the moisture content (humidity ratio) remains constant, causing the relative humidity to increase. This behavior exemplifies a classic indirect evaporative cooling phenomenon, where sensible cooling is achieved without any mass transfer.

The working air (Figure 4.20b) shows a more irregular pattern, especially near the outlet of the process channel or the inlet of the working channel, where successive air injections disturb the temperature and humidity fields. The sawtooth-like pattern in the humidity profile indicates alternating phases of dilution by unsaturated air and recovery through evaporation. The process channel (Figure 4.20c) follows a typical indirect evaporative trend, where air cools down progressively and becomes more saturated, without a change in its absolute moisture content.

To complement these analyses, Figure 4.21 presents the variation in humidity ratio along all three channels. As previously noted, the process and auxiliary working channels do not involve any direct evaporation or moisture addition, and therefore, their humidity ratio values remain constant throughout the flow. This confirms the absence of mass exchange in these dry-air passages, consistent with the indirect cooling principle of the system. In contrast, the working channel (read from right to left) exhibits a markedly different trend. Along this wet channel, where evaporative cooling actively occurs, the humidity ratio steadily increases as water vapor is added to the air through phase change from the wetted surfaces. The highest humidity ratio is observed near the outlet (leftmost side), where the cumulative effect of evaporation is greatest. Additionally, in the inlet region (right side), the graph shows a distinct zigzag pattern, which reflects the mixing of relatively dry process air with the moist working stream after the aperture. This local dilution is then followed by gradual moisture recovery through evaporation, a repeating pattern that shapes the humidity ratio distribution along the channel.

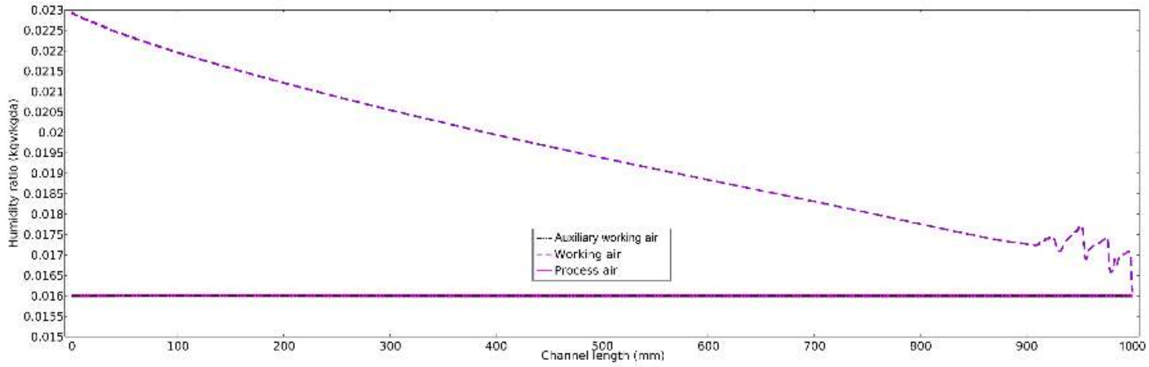

Figure 4.21. Humidity ratio distributions along the channels for Type 3

Figure 4.22, Figure 4.23 and Figure 4.24 illustrate the velocity–pressure, temperature–relative humidity, and humidity ratio distributions, respectively, for the Type 4 configuration. Similar to Type 3, this configuration features a three-layer structure composed of an auxiliary working channel, a primary working channel, and a process channel. While the auxiliary and process channels follow standard left-to-right flow direction (x = 0 mm to x = 1000 mm), the primary working channel operates in the reverse direction, with flow progressing from x = 1000 mm to x = 0 mm. For accurate and consistent analysis, the data for all channels were extracted along the symmetry plane and in the case of the working channel, a central virtual plane was used to ensure equivalent mid-channel representation across all layers.

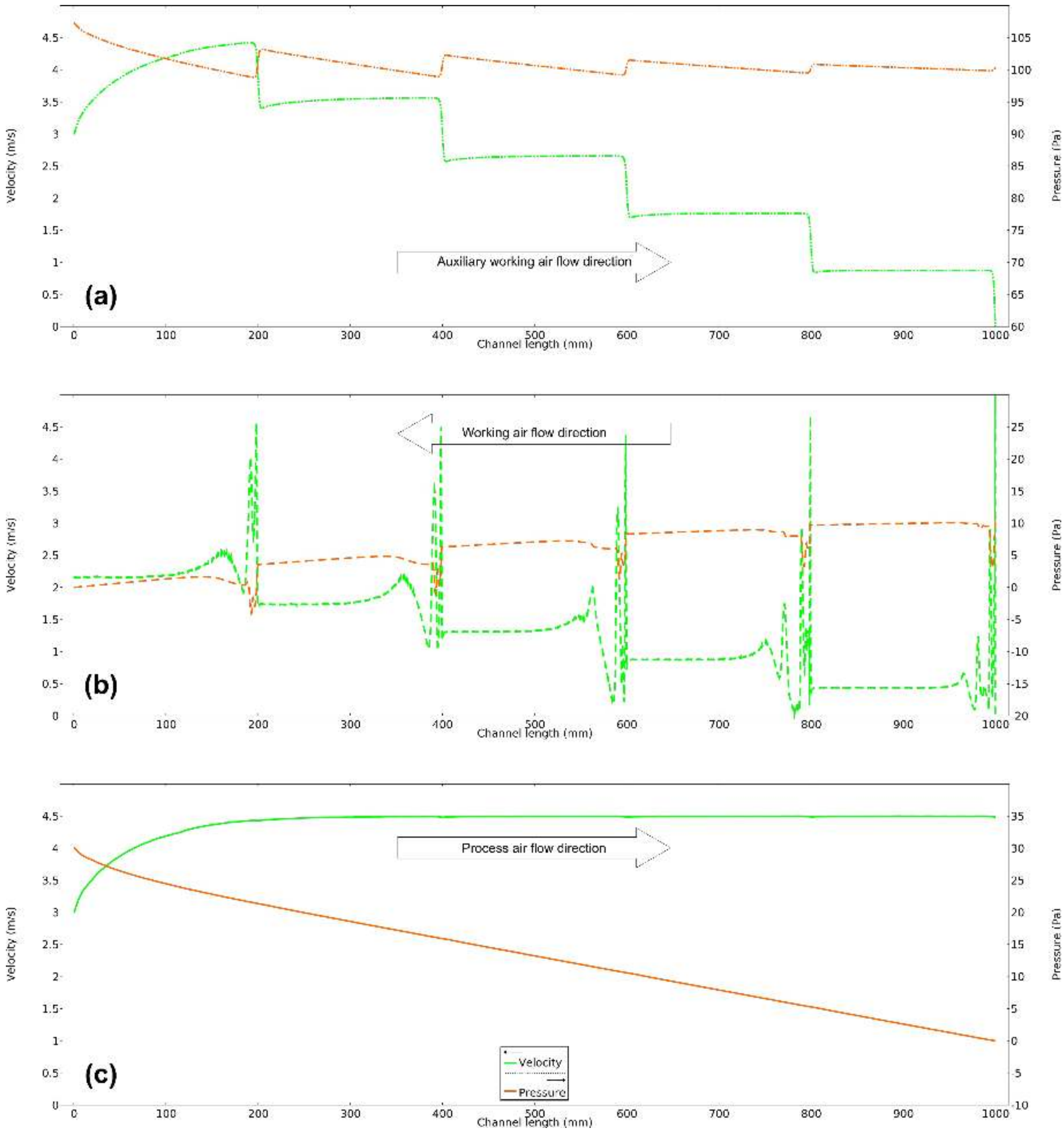

Figure 4.22. Velocity and pressure distributions along auxiliary working channel (a), working channel (b) process channel (c) for Type 4

Figure 4.22 presents the pressure and velocity profiles for the three channels. The auxiliary working channel (Figure 4.22a) demonstrates a stable decrease in pressure, indicating consistent and undisturbed airflow along the top passage. In contrast, the working channel (Figure 4.22b) exhibits multiple sharp pressure drops and velocity spikes along the flow direction, especially near the downstream region. These fluctuations correspond to the apertures through which the auxiliary air is injected, creating complex local flow fields characterized by sudden accelerations and turbulent mixing. The process channel (Figure 4.22c), similar to other configurations, shows a nearly linear pressure decline with minimal disturbance and a smooth velocity profile, reinforcing its role as a thermally efficient but hydrodynamically simple passage.

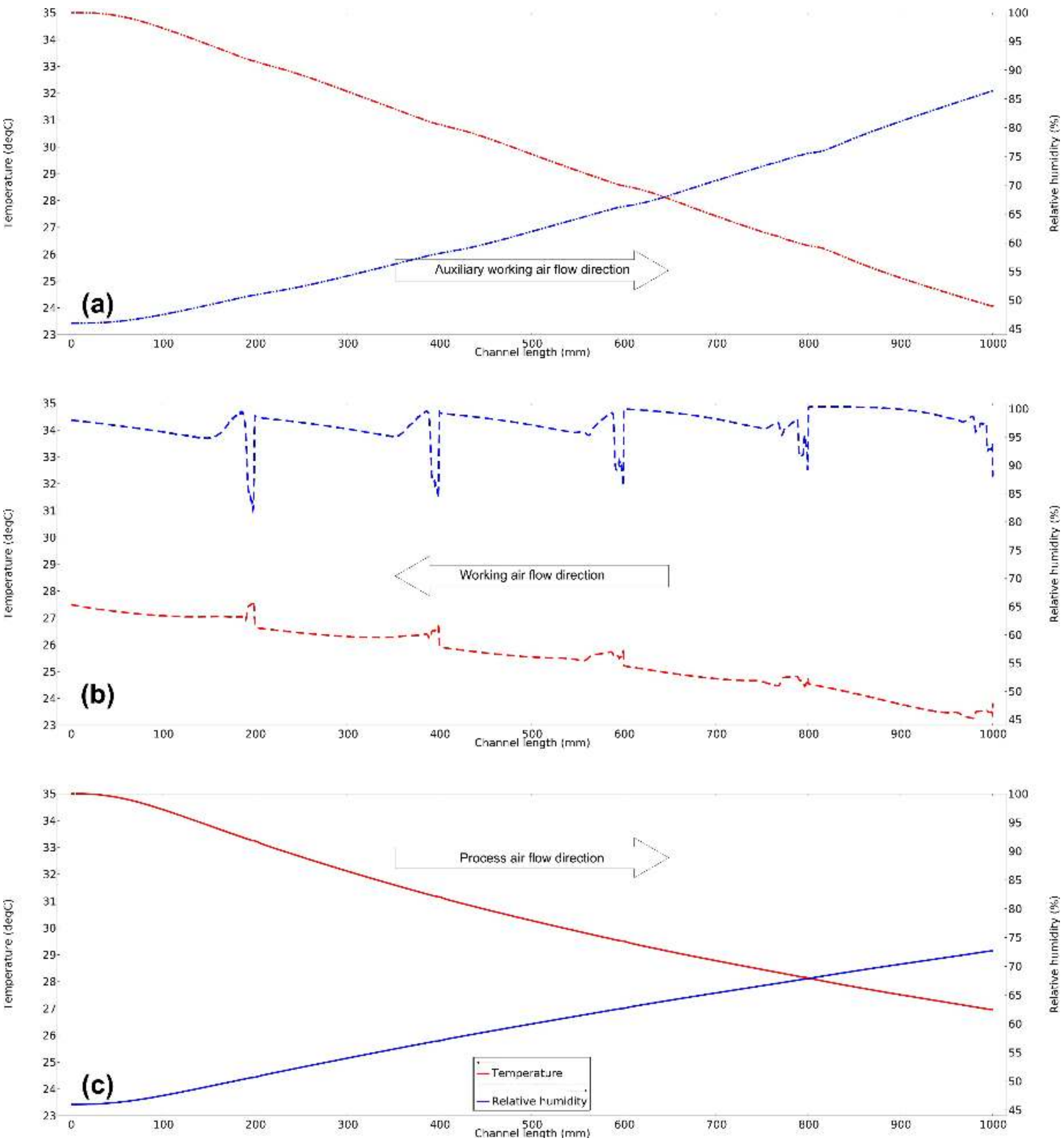

Figure 4.23. Temperature and relative humidity distributions along auxiliary working channel (a), working channel (b) process channel (c) for Type 4

Figure 4.23 provides a thermodynamic perspective by plotting temperature and relative humidity for each channel. In the auxiliary channel (Figure 4.23a), the air temperature decreases and relative humidity increases consistently along the flow. However, since no water evaporation occurs in this dry channel, the increase in relative humidity is a direct consequence of sensible cooling. As the temperature drops, the saturation vapor pressure decreases, leading to an increase in relative humidity without any change in actual moisture content, a classic psychrometric effect in indirect evaporative systems. In the primary working channel (Figure 4.23b), the combined effects of auxiliary air injection and surface evaporation generate a repeating pattern in both temperature and humidity. The temperature slightly rises after each aperture due to mixing with drier and warmer air, while relative humidity drops sharply and then recovers as evaporation resumes. This sawtooth behavior mirrors the spatial sequence of dilution and re-saturation. The process channel (Figure 4.23c) shows the typical indirect evaporative cooling profile: a steady drop in temperature and a corresponding rise in relative humidity as the air cools without gaining moisture.

Figure 4.24 complements the above results by presenting the humidity ratio distributions. As expected, the humidity ratio remains constant in both the auxiliary and process channels, confirming the absence of direct moisture addition. In the working channel, however, the humidity ratio progressively increases along the flow due to continuous evaporation from the wetted walls. Each aperture causes a localized dip in the humidity ratio, a result of mixing with unsaturated auxiliary air, followed by a recovery phase as evaporation re-establishes moisture levels.

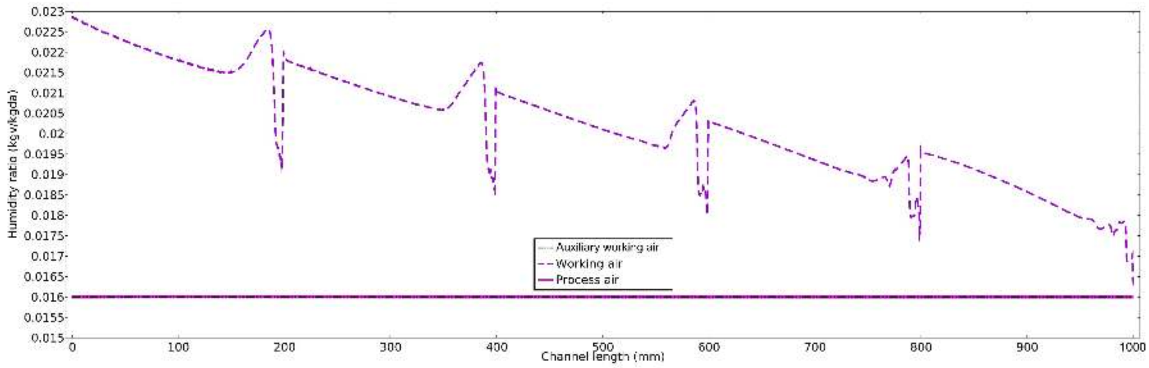

Figure 4.24. Humidity ratio distributions along the channels for Type 4

4.1.2. Parametric Performance Comparison

To further assess the behavior of each cooler configuration under realistic climatic variations, a series of parametric analyses were conducted. Four critical input parameters, inlet air temperature (T_i), inlet humidity ratio (ω_i), inlet air velocity (u_i), and working-to-intake air ratio (β), were systematically varied within practical operational ranges. These parameters were selected based on their direct influence on the underlying heat and mass transfer mechanisms that govern cooler performance.

Variations in inlet temperature affect the thermodynamic potential for cooling and represent different ambient conditions. Changes in humidity ratio impact the evaporation capacity of the wet channel and the approach to saturation. Modifying the air velocity alters residence time and convective heat transfer coefficients, while variations in β control the fraction of air diverted into the working channel, directly influencing internal flow dynamics. The impact of each parameter was evaluated across all five configurations using four key performance metrics: dew-point effectiveness (ε_{dp}), area-normalized cooling capacity (CC_a), specific water consumption (WC_c) and cooling coefficient of performance (COP). Several supplementary parameters were also examined to provide a more comprehensive understanding of cooler behavior. These include process air temperature reduction (ΔT_p), working air humidity increase ($\Delta\omega_w$), wet-bulb effectiveness (ε_{wb}), cooling capacity

(CC), water consumption (WC) and fan power consumption (W_f). Moreover, the results are presented and discussed in the following subsections, with a focus on identifying performance trends, configuration sensitivities and relative advantages.

4.1.2.1. Effect of inlet air temperature on cooler performance

The process air inlet temperature ($T_{p,i}$) is one of the most influential parameters in indirect evaporative cooling, as it directly determines the thermodynamic potential for heat exchange. Simulations were conducted for all five cooler configurations under varying inlet temperatures ranging from 25°C to 45°C, in 1°C increments, while keeping other operational parameters fixed at their base values (Table 3.2). To establish a comprehensive understanding of how varying process air inlet temperature impacts system behavior, two fundamental metrics were first examined: the process air temperature reduction (ΔT_p) and the working air humidity increase ($\Delta\omega_w$) (Equations 4.1 and 4.2). These parameters, presented in Figures 4.25a and 4.25b, respectively, provide direct insight into the thermodynamic driving forces underlying the evaporative cooling process.

$$\Delta T_p = T_{p,i} - T_{p,o} \tag{4.1}$$

$$\Delta\omega_w = \omega_{w,o} - \omega_{w,i} \tag{4.2}$$

As shown in Figure 4.25a, increasing the inlet air temperature enhances the ΔT_p across all cooler types, reflecting a greater potential for sensible cooling. This trend is thermodynamically expected since higher inlet temperatures increase the difference between the air's dry-bulb temperature and its saturation line, thereby expanding the cooling capacity. Similarly, the corresponding increase in $\Delta\omega_w$ (Figure 4.25b) demonstrates that more water vapor is absorbed into the working air at higher inlet temperatures, highlighting the intensified evaporation process. While all cooler types exhibit this trend, regenerative configurations (Types 1-4) consistently achieve larger ΔT_p and $\Delta\omega_w$ values than the conventional Type 0, underscoring the advantages of internal air recirculation in boosting both sensible and latent cooling effects.

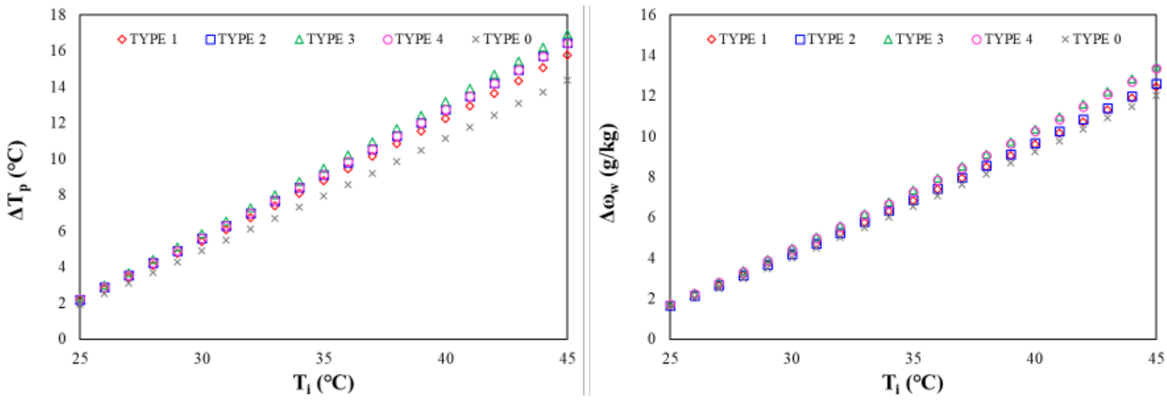

Figure 4.25. Variation of ΔT_p (a) and $\Delta\omega_w$ (b) with inlet air temperature.

Following this, the effect of inlet air temperature on coolers performance is examined through the wet-bulb effectiveness (ε_{wb}) parameter (Figure 4.26a). As introduced in Equation 3.15, this metric describes how closely the outlet process air approaches its own wet-bulb temperature. Traditionally, this performance indicator is used for conventional indirect evaporative coolers (Type 0), which are thermodynamically limited to cooling air down to its wet-bulb temperature. In contrast, more advanced systems, namely dew-point indirect evaporative coolers, are capable of sub-wet-bulb cooling, which can result in wet-bulb effectiveness values exceeding 1. For this reason, the dew-point effectiveness (ε_{dp}), defined in Equation 3.16, provides a more appropriate basis for performance evaluation in regenerative cooler designs. It represents how closely the outlet air approaches its dew-point temperature. The variation of this metric with inlet temperature is shown in Figure 4.26b for all five configurations.

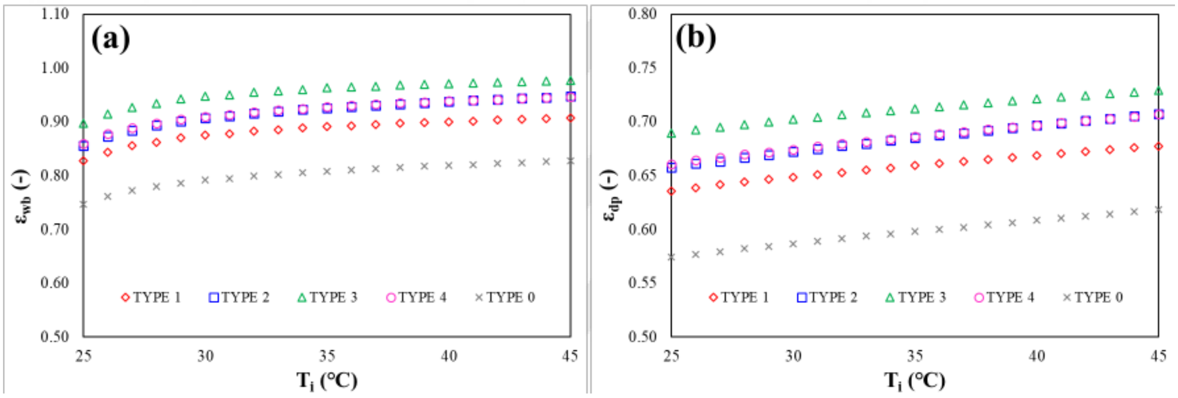

Figure 4.26. Variation of ε_{wb} (a) and ε_{dp} (b) with inlet air temperature

Both effectiveness values exhibit a slight upward trend with increasing inlet temperature across all cooler types. This is primarily due to the higher thermal gradient at elevated temperatures, which enhances heat transfer potential. In terms of wet-bulb effectiveness, Type 0 displays the lowest performance throughout the entire range, with values remaining around 0.75. Type 1 offers slightly better results, while Types 2 and 4 perform similarly and maintain higher effectiveness due to their regenerative airflow designs. Type 3, which employs a multi-layer airflow structure, achieves the highest wet-bulb effectiveness across all temperatures, approaching a value of nearly 1 at 45 °C.

A similar performance order is observed in dew-point effectiveness. Type 0 again ranks lowest due to the absence of any regeneration. Type 1 follows with moderate values, while Types 2 and 4 again show similar and improved performance. Notably, Type 3 outperforms all other configurations in this regard, delivering the highest dew-point effectiveness across the entire temperature range. This confirms the thermal superiority of the multi-layer structure, particularly in high-temperature conditions.

The third set of performance metrics evaluated in this section pertains to the cooling capacity, both in absolute terms and normalized by heat transfer surface area. The absolute cooling capacity

(CC), defined in Equation 3.17, represents the net amount of heat removed from the process air stream and is a direct indicator of the system cooling output. Figure 4.27a presents the variation of cooling capacity with inlet air temperature for each cooler configuration.

As expected, cooling capacity increases nearly linearly with inlet temperature for all types. This behavior is attributed to the larger temperature difference between the inlet air and the cooled surface at higher Ti values, which enhances sensible heat transfer. Among the configurations, Type 3 consistently delivers the highest cooling capacity values across the entire range, followed closely by Type 4. These results can be linked to their higher airflow rates and enhanced mixing characteristics, particularly in the working channel. Type 0 also shows relatively high cooling capacity despite its low effectiveness, primarily due to its unidirectional airflow structure that drives all the intake air through the process channel. In contrast, Types 1 and 2, which divert a portion of the process air into the working channel, exhibit lower absolute cooling capacity. Type 2, however, maintains its relative performance advantage through more efficient use of regenerative airflow.

To normalize this performance with respect to surface area, the cooling capacity per unit area (CC_a) is introduced in Equation 3.18. This metric enables a fair comparison among configurations with different physical layouts and space utilization. As shown in Figure 4.27b, Type 0 outperforms all others in CC_a due to its full utilization of the process channel area, effectively doubling the airflow through the cooling surface. This structural advantage significantly boosts its area-based output. All other configurations, Types 1 through 4, share nearly identical CC_a values, indicating that their structural differences do not translate into meaningful variations in surface efficiency. This observation highlights that while regenerative coolers may provide better thermal effectiveness, their geometric complexity can limit area-normalized cooling performance unless airflow rates are optimized accordingly.

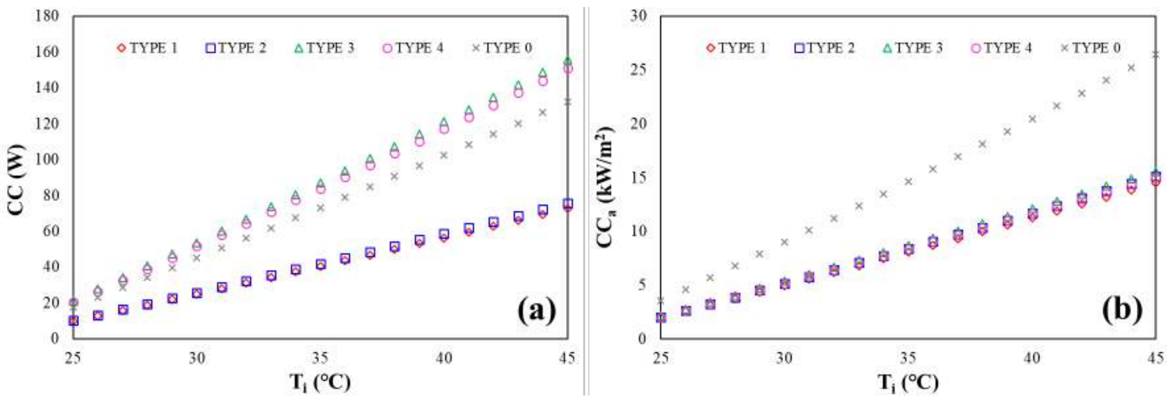

Figure 4.27. Variation of CC (a) and CC_a (b) with inlet air temperature

Another critical aspect of cooler performance, particularly in regions with limited water availability, is water consumption. This parameter is considered in both absolute terms and normalized with respect to the cooling output. The absolute water consumption (WC), defined in

Equation 3.19, represents the total mass flow rate of water, which is a direct consequence of latent heat exchange. Figure 4.28a illustrates the variation of water consumption with inlet air temperature for all configurations.

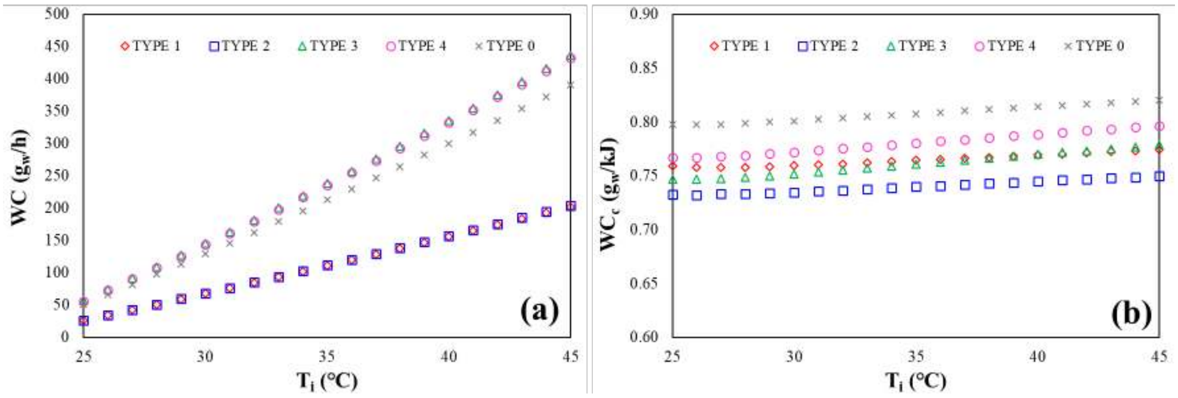

Figure 4.28. Variation of WC (a) and WC_c (b) with inlet air temperature

As shown in the figure, water consumption increases sharply with rising inlet temperature across all types, due to the enhanced evaporative potential at higher temperature levels. Type 3 and Type 4 consistently record the highest water usage, reflecting their higher heat and mass transfer areas. Type 0 also shows considerable consumption owing to its high airflow rate through the wet surface. In contrast, Type 2, followed closely by Type 1, maintains the lowest water consumption values. This outcome reflects their operational principle that restricts the working channel flow rate, thereby limiting the available surface area for evaporation.

However, absolute water consumption alone does not convey the efficiency of water use. For a more comprehensive assessment, the specific water consumption (WC_c), defined in Equation 3.20, is considered. This parameter expresses the amount of water used per unit of cooling energy delivered and is thus a critical indicator of water-use efficiency. Figure 4.28b presents the trends of WC_c for the five configurations.

Interestingly, while WC increases significantly with temperature, WC_c remains relatively stable across the temperature range. This suggests that higher water usage at elevated inlet temperature levels is accompanied by proportionally greater cooling. Type 2 exhibits the lowest WC_c throughout, confirming its superior water efficiency. In contrast, Type 0 demonstrates the weakest performance in this metric, as it consumes significantly more water relative to its cooling output, despite delivering high absolute cooling capacity.

Figure 4.29a illustrates the total fan power consumption (W_f), which accounts for the energy required to drive airflow through both the working and process channels (Equation 3.22). Since the inlet air temperature does not affect flow parameters under constant operating conditions, total fan consumption remains stable across the entire temperature range for all cooler types. The observed differences between configurations arise solely from their internal flow resistance characteristics.

Type 3, which involves a multi-layer channel system and an auxiliary airflow loop, exhibits the highest fan energy demand. Type 4, which has a similar channel layer and auxiliary airflow but an optimized geometry with multi-apertures, shows lower fan consumption. Notably, Type 2 consistently shows the lowest fan power demand among all configurations. This trend reveals an important advantage of the multi-aperture architecture employed in Types 2 and 4, with respect to their single aperture alternatives (Types 1 and 3). These configurations benefit from reduced airflow resistance due to their distributed injection design, leading to significantly lower pressure losses across the system. This design characteristic directly contributes to improved fan consumption and results in overall energy savings when compared to their single aperture counterparts, such as Types 1 and 3.

In Figure 4.29b, the cooling coefficient of performance (COP), defined in Equation 3.21, is presented as a function of inlet air temperature. As expected, COP increases steadily with temperature for all configurations. This trend occurs because the cooling capacity grows more rapidly than the required fan power, which remains constant. Among the designs, Type 2 offers the most favorable COP profile, combining efficient cooling performance with minimal fan energy consumption. Despite its high cooling output, Type 3 ranks lowest in terms of COP due to its elevated airflow resistance. Type 4, benefiting from both multi-aperture regeneration and moderate fan demand, achieves a well-balanced outcome. Types 0 and 1 display intermediate performances, with Type 1 slightly outperforming Type 0 due to better energy utilization.

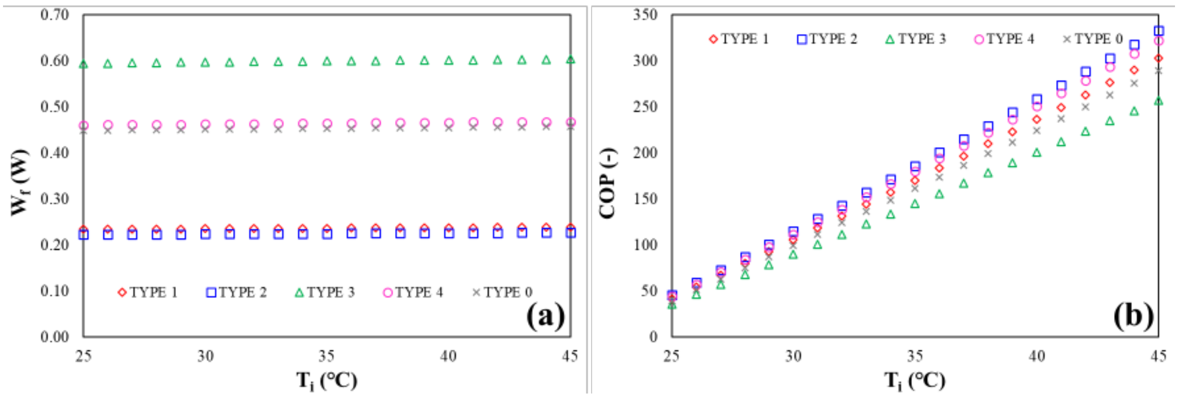

Figure 4.29. Variation of W_f (a) and COP (b) with inlet air temperature

4.1.2.2. Effect of inlet air humidity on cooler performance

The humidity ratio of the process air inlet (ω_i) is a critical parameter that influences both the dew-point temperature and the evaporative cooling potential. In this part of the study, inlet humidity was varied from 6 g/kg to 26 g/kg, while the other input variables were fixed at their base values (Table 3.2).

Figure 4.30a and Figure 4.30b illustrate the variation of wet-bulb effectiveness (ε_{wb}) and dew-point effectiveness (ε_{dp}), respectively, across different inlet humidity levels for all cooler configurations. As seen in Figure 4.30b, dew-point effectiveness consistently increases with increasing inlet humidity. This trend can be explained by the fact that, although the outlet air temperature also increases with higher inlet humidity, the increase in dew-point temperature is more pronounced. Consequently, the outlet temperature becomes relatively closer to the elevated dew-point temperature, leading to a higher dew-point effectiveness. This thermodynamic effect accounts for the consistent upward trend in the dew-point effectiveness across all configurations.

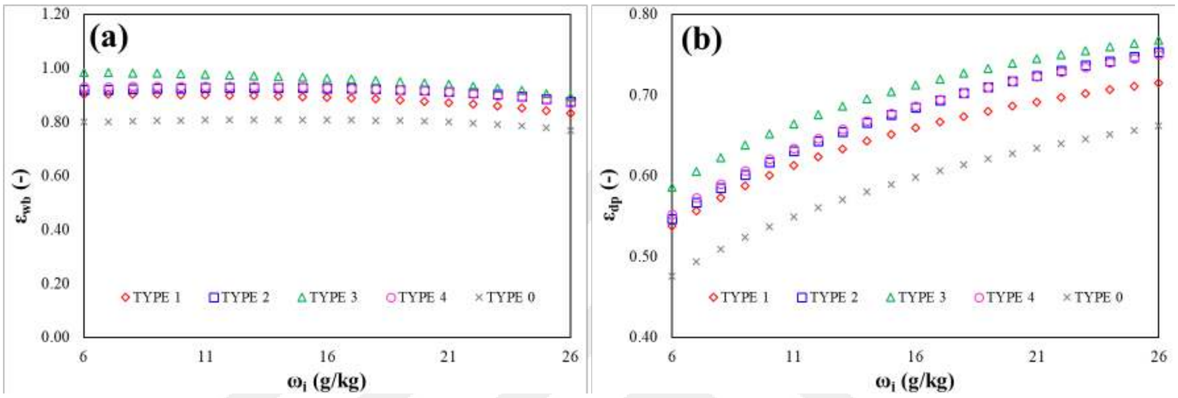

Figure 4.30. Variation of wet-bulb effectiveness (a) and dew-point effectiveness (b) with inlet air humidity

In contrast, wet-bulb effectiveness exhibits distinct behavior (Figure 4.30a). For lower and moderate humidity levels, wet-bulb effectiveness remains relatively stable. However, at higher humidity levels, particularly beyond 20 g/kg, a slight decline is observed for all configurations. This phenomenon can be explained through the psychrometric characteristics of moist air. As air becomes increasingly humid, its wet-bulb temperature converges toward the dry-bulb temperature, diminishing the available cooling potential. This convergence reduces the temperature differential that drives evaporative cooling and simultaneously compresses the denominator of the wet-bulb effectiveness expression. The overall result is a reduction in both the absolute cooling effect and the numerical value of wet-bulb effectiveness. Therefore, while dew-point effectiveness benefits from higher latent cooling capacity at elevated humidity, wet-bulb effectiveness is constrained by narrowing psychrometric margin in highly humid conditions.

Figure 4.31a illustrates the variation of water consumption per unit cooling capacity (WC_c) with respect to the inlet air humidity ratio. At first glance, one might expect that as ω_i increases, the total water evaporated in the working channel would decrease, given the reduced potential for moisture absorption by more humid air. Indeed, this is thermodynamically accurate, the amount of water that can be evaporated diminishes with increasing humidity. However, it is important to recognize that WC_c is not solely a function of water consumption, but rather the ratio between water use and delivered cooling effect (as defined in Equation 3.20). In humid conditions, although less water is consumed overall, the cooling capacity decreases even more sharply due to the reduced driving force for evaporation. This disproportionate drop in cooling output leads to an increase in WC_c, as each gram of water yields less thermal benefit. Therefore, the upward trend observed in all cooler types with rising ω_i is primarily driven by this imbalance: the reduction in absolute cooling capacity is more pronounced than the decline in water consumption, especially under higher humidity conditions.

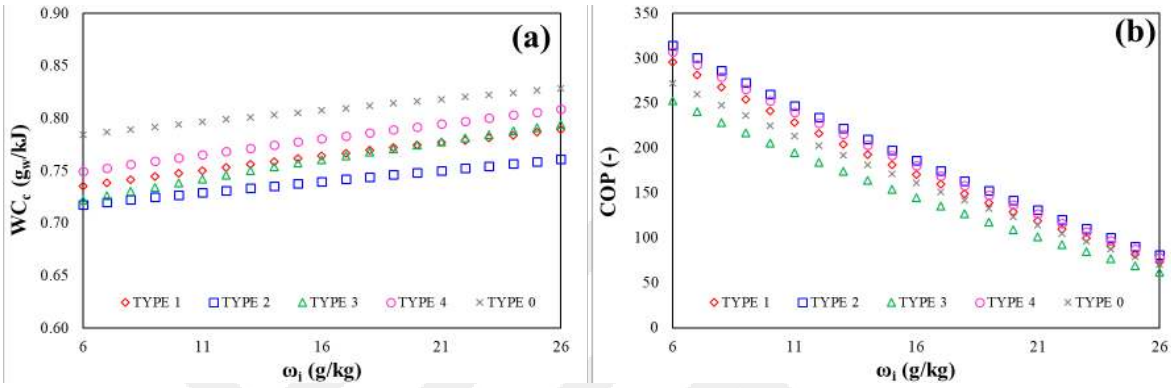

Figure 4.31. Variation of WC_c (a) and COP (b) with inlet air temperature

Among the configurations, Type 2 consistently maintains the lowest WC_c values across the full range of humidity conditions, indicating its superior water efficiency. In contrast, Type 0 exhibits higher WC_c values, with the latter being particularly susceptible at high humidity levels due to increased evaporation surface area but reduced cooling gain per unit water.

Turning to Figure 4.31b, COP shows a clearly declining trend with rising inlet humidity ratio for all cooler types. This behavior is in line with the general reduction in cooling capacity (also confirmed in the background analysis figures) while fan power remains mostly constant. Since COP is calculated as the ratio of cooling capacity to total fan power (Equation 3.21), a drop in cooling output, driven by limited evaporation potential, directly reduces system efficiency. It is important to note that while Type 2 consistently retains the highest COP values throughout the entire humidity range, Type 3 performs the worst under all conditions due to its elevated fan power requirement and limited thermal performance. Type 0, although basic in design, outperforms Type 3 at all humidity levels thanks to its lower hydraulic resistance and more efficient airflow structure. As humidity increases and COP declines, the performance differences among configurations become less pronounced.

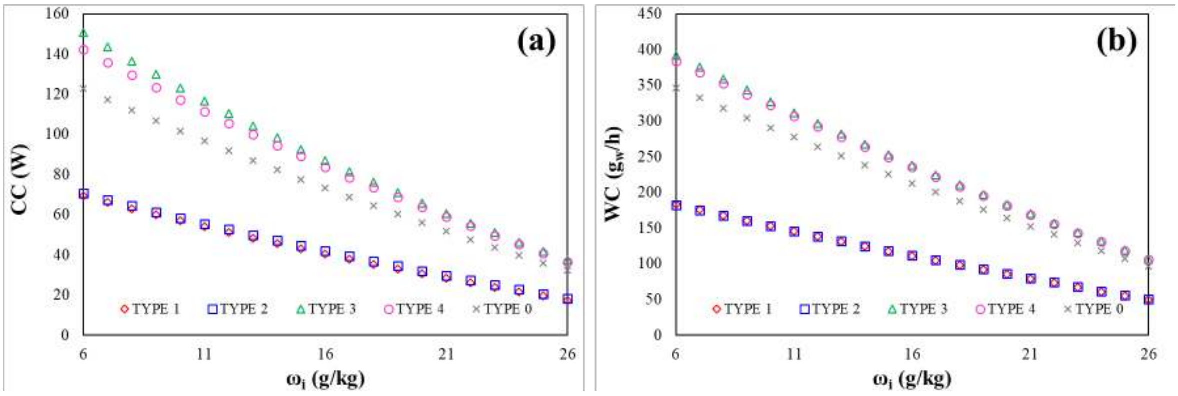

Figure 4.32. Variation of CC (a) and WC (b) with inlet air humidity

To better explain the trends observed in WC_c and COP, Figures 4.32a and 4.32b present the variation of absolute cooling capacity (CC) and absolute water consumption (WC) concerning the inlet air humidity. As expected, both parameters exhibit a pronounced decline as inlet air humidity ratio increases. The reduction in absolute cooling capacity is directly related to the diminishing psychrometric driving force for evaporation; as the incoming air approaches saturation, less cooling can be achieved regardless of the cooler type. This decreasing trend in cooling capacity is mirrored by a corresponding reduction in total water consumption, since the air's ability to absorb additional moisture is limited at higher humidity levels. Notably, the rate of decline in cooling capacity is steeper than that of water consumption, which reinforces the earlier observation that specific water consumption (WC_c) increases despite the reduction in absolute water use. This imbalance, less cooling achieved per unit of evaporated water, underpins the efficiency losses reflected in both WC_c and COP. As seen in Figure 4.32a, multi-layer configurations (Type 3 and Type 4) maintain higher absolute cooling capacities across the humidity range, while Types 1 and 2 continue to demonstrate the lowest absolute water consumption (Figure 4.32b), highlighting its superior water-saving potential.

Summary, rising inlet humidity decreases the thermodynamic cooling potential of the system by reducing the air's capacity for further evaporation. While dew-point effectiveness increases slightly due to higher reference dew-point temperatures, the cooling capacity drops significantly across all configurations. This leads to an increase in specific water consumption and a reduction in COP. Type 2 consistently provides the most balanced performance, with high dew-point effectiveness, low WC_c, and the highest COP. The consistency of performance ranking with that of inlet temperature variation confirms the robustness of the multi-aperture approach under diverse ambient conditions.

4.1.2.3. Effect of inlet air velocity on cooler performance

The process air inlet velocity (u_i) significantly influences the convective heat and mass transfer mechanisms in indirect evaporative cooling systems. In this analysis, the velocity was varied from 1 m/s to 5 m/s, while other parameters were kept constant at their base values (Table 3.2).

The variations of wet-bulb effectiveness (ε_{wb}) and dew-point effectiveness (ε_{dp}) with respect to inlet air velocity are illustrated in Figures 4.33a and 4.33b, respectively. An important observation is that wet-bulb effectiveness values for all cooler configurations, except for Type 0, comfortably exceed 1.0 at lower velocities, particularly below 2 m/s. This result highlights the capability of dew-point indirect evaporative coolers to achieve sub-wet-bulb cooling, an essential performance feature distinguishing them from conventional designs. The primary reason for these elevated wet-bulb effectiveness values at low inlet velocities is the significantly extended residence time of the air within the cooling channels. When the airflow is slow, heat and mass transfer processes have ample time to approach equilibrium, allowing the process air to be cooled not only to its wet-bulb temperature but further toward its dew-point. This phenomenon is especially pronounced in multi-aperture configurations (Type 2 and Type 4), where the distributed air mixing sustains evaporation over a larger portion of the channel.

As inlet air velocity increases, however, both wet-bulb effectiveness and dew-point effectiveness progressively decline. The reduction in residence time reduces the degree to which the air stream can exchange heat and moisture with the wet surfaces, limiting the approach to both wet-bulb and dew-point temperatures. The effect is more severe in Type 1, which relies on a single aperture for air transfer, and in Type 3, where flow disturbances and higher velocities intensify thermal inefficiencies.

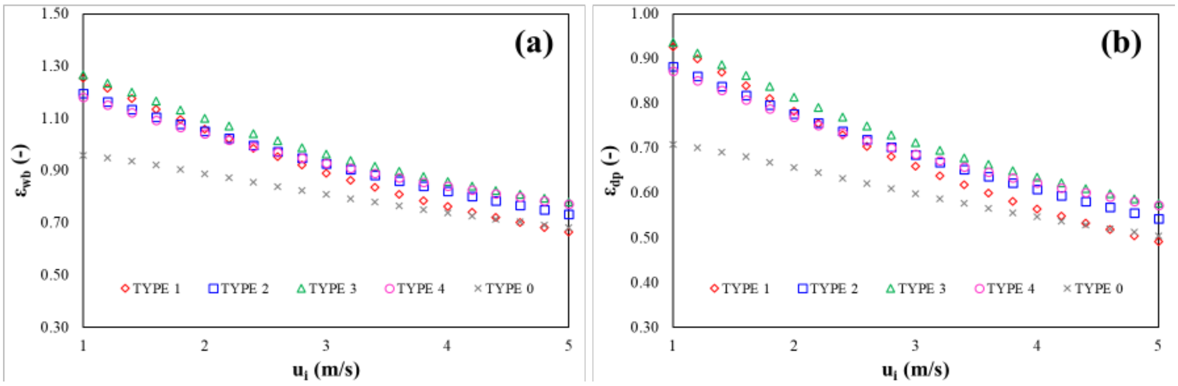

Figure 4.33. Variation of ε_{wb} (a) and ε_{dp} (b) with inlet air velocity

Figure 4.34a illustrates that the cooling capacity per unit area (CC_a) increases steadily with rising inlet air velocity for all configurations. This trend is expected, as higher air velocities bring in more mass flow rates, which directly contributes to greater cooling output. Even if the temperature drop per unit air mass is slightly reduced at high velocities, the increased volume of air compensates for it. Among the configurations, Type 0 consistently shows the highest CC_a values since the entire incoming air stream is used without diversion into a secondary channel.

Figure 4.34b presents the variation of specific water consumption (WC_c) with respect to the inlet velocity. Here, the behavior is less straightforward. In general, WC_c increases with air velocity for all types. This is because faster airflow shortens the residence time in the wet channel, limiting the air's ability to absorb moisture and cooling energy. However, fan power and water evaporation continue to increase, leading to more water being used for each unit of cooling delivered. A noticeable difference occurs above approximately 3.5 m/s, where Type 1 and Type 3, which rely on a single aperture at the end of the channel, show a sharper rise in WC_c. In these designs, evaporative cooling is restricted to the narrow region near the outlet where dry air is injected into the wet channel. As velocity increases, this limited evaporation zone becomes less effective because the air passes through too quickly to fully benefit from the cooling potential. As a result, water is consumed inefficiently, with only modest gains in cooling. In contrast, Type 2 and Type 4, which feature multiple apertures, introduce dry air at several points along the channel. This allows evaporation to take place more evenly and continuously throughout the channel length. Thanks to this design, they maintain lower WC_c values compared to single-aperture alternatives, even at high air velocities.

In summary, while increasing inlet velocity boosts cooling capacity, it also leads to higher water consumption per unit of cooling, especially in single-aperture configurations. Multi-aperture designs offer better water use efficiency under these demanding conditions.

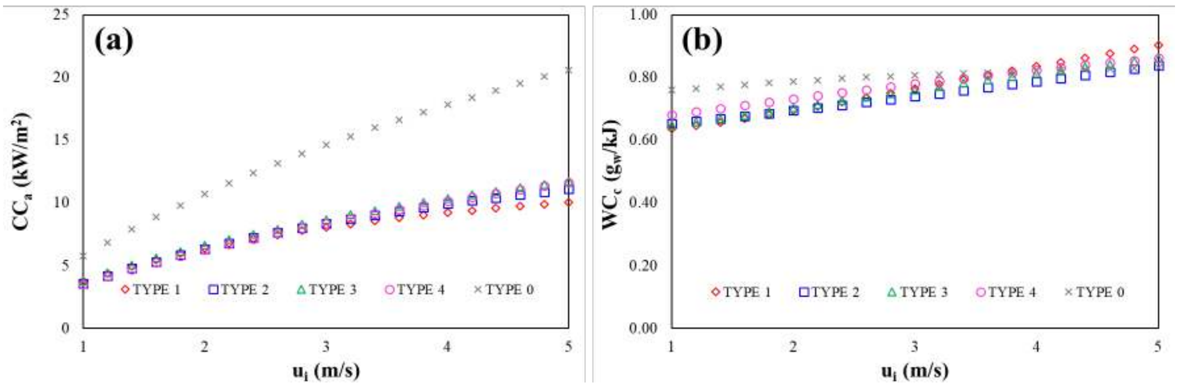

Figure 4.34. Variation of CC_a (a) and WC_c (b) with inlet air velocity

Figure 4.35a illustrates the rapid increase in total fan power consumption (W_f) as inlet air velocity rises from 1 m/s to 5 m/s across all cooler configurations. This outcome is expected due to the cubic relationship between air velocity and pressure loss, as described by the fan power equation (Equation 3.22). The most striking observation is the pronounced separation between the configurations, with Type 3 consuming the highest fan power at every velocity level, followed by Type 4 and Type 0. The elevated W_f values in Type 3 are directly linked to its more complex flow pathways and higher pressure drops across both process and working channels. In contrast, Type 1 and particularly Type 2 demonstrate the lowest fan power demands, reflecting their more streamlined geometries and reduced hydraulic resistance. This highlights a key trade-off: while multi-aperture or auxiliary flow designs enhance cooling performance, they often introduce additional flow obstructions that increase energy consumption on the mechanical side. Turning to Figure 4.35b, COP exhibits a steep decline with increasing velocity for all cooler types, emphasizing the dominant impact of fan power escalation on overall system efficiency. At lower velocities (below 2 m/s), Type 2 and Type 4 maintain the highest COP values, benefiting from both efficient evaporative cooling and moderate fan requirements. However, as velocity increases, the disproportionate rise in fan power outweighs the gains in cooling capacity, leading to convergence of COP values at the lower end of the performance spectrum. Notably, despite its high cooling capacity, Type 0 consistently exhibits lower COP than Type 2 and Type 4 due to inefficient higher relative fan power. Type 3, burdened by both poor hydraulic design and higher energy consumption, delivers the weakest COP across the entire velocity range. These results underscore the critical importance of balancing aerodynamic design with thermodynamic performance to achieve sustainable cooling efficiency, especially under conditions demanding high airflow rates.

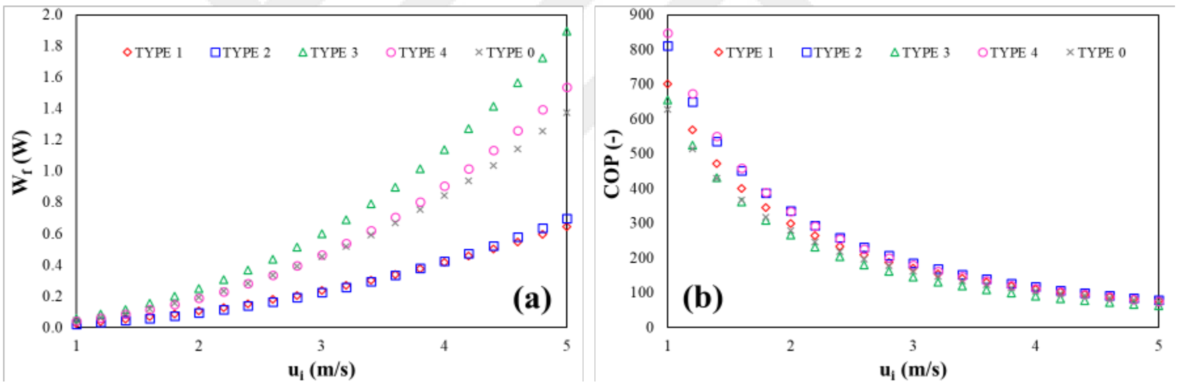

Figure 4.35. Variation of W_f (a) and COP (b) with inlet air velocity

4.1.2.4. Effect of working-to-intake air ratio on cooler performance

The working-to-intake air ratio (β) is a fundamental design and operational parameter that directly governs the internal airflow distribution between the process and working channels in indirect evaporative cooling systems. Unlike other control variables such as inlet temperature, humidity, or velocity, the β ratio uniquely affects both the available cooling mass flow rate and the regenerative evaporation potential, thereby influencing multiple performance indicators simultaneously. To better understand the physical consequences of airflow partitioning, the effect of β on the performance parameters is analyzed. In this study, working-to-intake air ratio varied between 0.2 and 0.8, while other conditions were held constant at base values in Table 3.2.

As shown in Figure 4.36a, the variation of process air temperature reduction (ΔT_p) with respect to the working-to-intake air ratio (β) reveals configuration-dependent trends. While Type 2 demonstrates a clear and steady increase in ΔT_p with rising working-to-intake air ratio, thanks to its distributed multi-aperture structure that enables efficient evaporation across the entire channel, other configurations exhibit more modest behavior. For instance, Type 0, Type 1 and Type 4 show relatively stable ΔT_p values with only limited improvement after $\beta \approx 0.5$, suggesting that increasing the amount of working air beyond a certain point yield diminishing thermal benefits. Interestingly, Type 3 displays a mild decline in ΔT_p at higher working-to-intake air ratios, likely due to complex internal flow interactions and a single point air injection near the process channel end, which limits the effective heat transfer area and shortens residence time under high airflow conditions.

In parallel, the variation of working air humidity change ($\Delta\omega_w$) with working-to-intake air ratio (Figure 4.36b) shows a consistently decreasing trends for all cooler types. This inverse relationship is thermodynamically expected: although increasing working-to-intake air ratio introduces more air into the wet channel, the total evaporation capacity, governed primarily by channel surface area and wall temperature, is relatively fixed. As a result, the moisture gains per unit mass of air decreases, leading to lower $\Delta\omega_w$ values at higher working-to-intake air ratio. This behavior confirms that while more water may evaporate in total, each kilogram of working air absorbs less moisture when the flow rate increases. The effect becomes especially noticeable at $\beta > 0.6$, where $\Delta\omega_w$ values converge across all configurations.

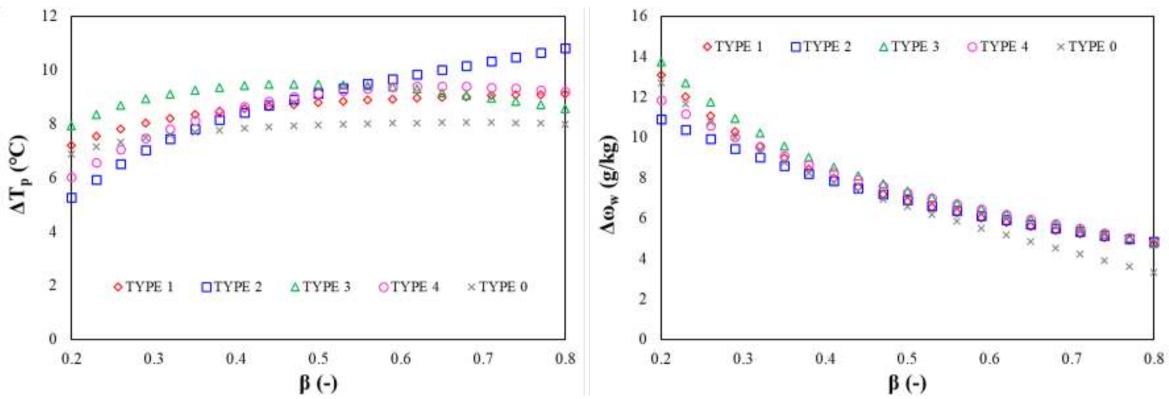

Figure 4.36. Variation of ΔT_p (a) and $\Delta\omega_w$ (b) with working-to-intake air ratio.

To further assess the impact of the working-to-intake air ratio (β) on system performance, two key effectiveness metrics, wet-bulb effectiveness (ε_{wb}) and dew-point effectiveness (ε_{dp}), were evaluated across the full β range for all cooler configurations. These parameters offer deeper insight into how effectively each design leverages the available thermodynamic potential for cooling as internal airflow redistribution varies. As shown in Figure 4.37, both wet-bulb and dew-point effectiveness generally improve as β increases, reflecting enhanced cooling potential as more air is directed into the working channel. This trend is most pronounced in Type 2, where the distributed multi-aperture structure allows for continuous regeneration of evaporation zones, enabling ε_{wb} and ε_{dp} to rise steadily without an apparent saturation point. In contrast, Types 1, 3, and 4 display diminishing returns beyond β values of approximately 0.5, indicating that the cooling benefit of additional working air begins to plateau due to limits in heat and mass transfer capacity. Type 3, with its single aperture design, exhibits the least sensitivity to increasing β, as the regenerative effect is spatially constrained. Notably, Type 2 achieves the highest ε_{wb} and ε_{dp} values across the entire working-to-intake air ratio range, confirming its superior adaptability to airflow redistribution. Type 0 remains largely unaffected, as expected, since no aperture is utilized. These results emphasize that while higher working-to-intake air ratio enhances cooling effectiveness up to a certain point, the geometric design of the cooler fundamentally governs how efficiently this potential is converted into actual performance.

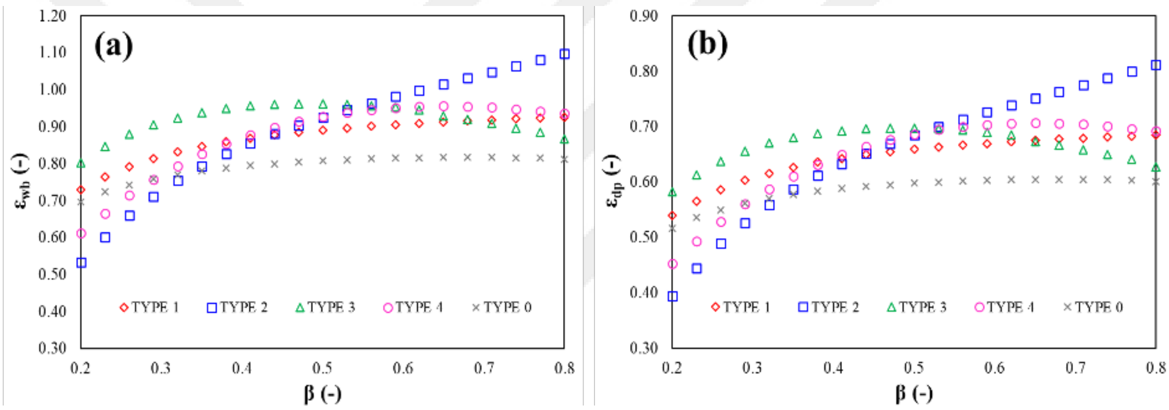

Figure 4.37. Variation of ε_{wb} (a) and ε_{dp} (b) with working-to-intake air ratio

Following the evaluation of cooler effectiveness, the impact of working-to-intake air ratio on cooling capacity is illustrated in Figure 4.38, presented both in absolute terms (Figure 4.38a) and normalized per unit area (Figure 4.38b). For absolute cooling capacity, all configurations initially show an increase in total cooling capacity as working-to-intake air ratio rises. This growth can be attributed to improved evaporative cooling effectiveness due to the higher mass flow rate in the wet channel, which enhances the cooling potential of the system. However, for configurations where the working air is drawn directly from the process stream, such as Types 1 and 2, this increase is short-lived. As more air is redirected, the mass flow rate available in the process channel decreases significantly, leading to a sharp drop in cooling capacity beyond $\beta \approx 0.5$. The regenerative benefit gained by adding more working air is no longer sufficient to compensate for the reduced process-side flow, especially in Type 1, which shows the steepest decline. In contrast, Types 3 and 4, which utilize an independent channel for working air, maintain relatively stable process flow. These configurations continue to benefit from enhanced wet side cooling and achieve a peak cooling capacity at β ≈ 0.6–0.7, before reaching a plateau. Type 0 remains unaffected by working-to-intake air ratio changes, as it lacks a regenerative airflow path and operates on a fixed process stream.

Figure 4.38b provides further insights by normalizing cooling capacity with respect to the unit area (CC_a). Here, Type 0 leads consistently across all working-to-intake air ratio values, primarily because it directs the entire air stream through the process channel without any diversion, maximizing total throughput. However, its advantage in CC_a is somewhat superficial, as it arises from volumetric dominance rather than thermal effectiveness. Types 1 and 2 again demonstrate declining trends at higher β values due to reduced process air mass flow and insufficient regenerative compensation. The drop is particularly sharp beyond β ≈ 0.4. Types 3 and 4, on the other hand, show greater resilience. Their designs allow for independent manipulation of working airflow, enabling them to maintain a better balance between cooling effectiveness and airflow distribution. As a result, their CC_a values remain relatively stable over a broad β range. These trends reinforce the observation that independent air supply architectures (Types 3 and 4) deliver more robust and area-efficient performance under varying operating conditions.

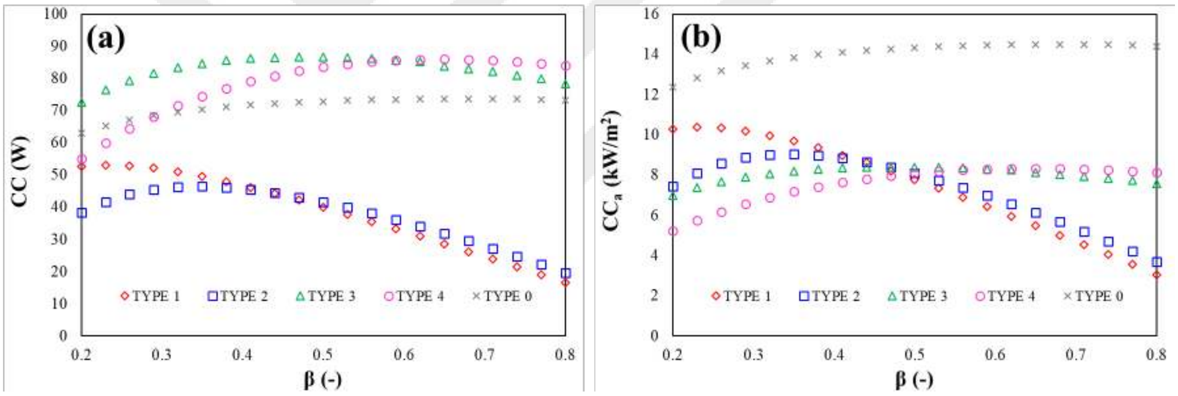

Figure 4.38. Variation of CC (a) and CC_a (b) with working-to-intake air ratio

Figure 4.39 illustrates the influence of the working-to-intake air ratio (β) on absolute water consumption (WC) and specific water consumption per unit cooling capacity (WC_c). As shown in Figure 4.39a, the behavior of water consumption with respect to β is highly configuration dependent. For Types 3, 4, and 0, total water consumption increases markedly with higher β, as expected, since increasing the wet side airflow enhances evaporation rates and overall water usage. In contrast, for Types 1 and 2, both of which extract working air directly from the process channel, water consumption remains nearly constant throughout the working-to-intake air ratio range. This can be attributed to the limited working air flow imposed by the process-side constraints, effectively limiting the wet side air velocity and thus the evaporation rate.

In Figure 4.39b, the trends in WC_c offer further insight into water use efficiency. For all configurations, WC_c remains relatively stable at low working-to-intake air ratio values, reflecting balanced growth in both cooling capacity and water consumption. However, as working-to-intake air ratio increases beyond approximately 0.4, WC_c begins to rise, most notably for Types 3 and 4. This indicates that although more water is being evaporated, the gain in cooling performance diminishes, leading to a less efficient use of water. Once again, Type 2 stands out with the lowest WC_c across the full β range, demonstrating its superior thermohydraulic balance and water conservation capability. These findings highlight that while increasing β can enhance evaporative potential, it must be carefully optimized to avoid excessive water usage that is not matched by proportional gains in thermal performance.

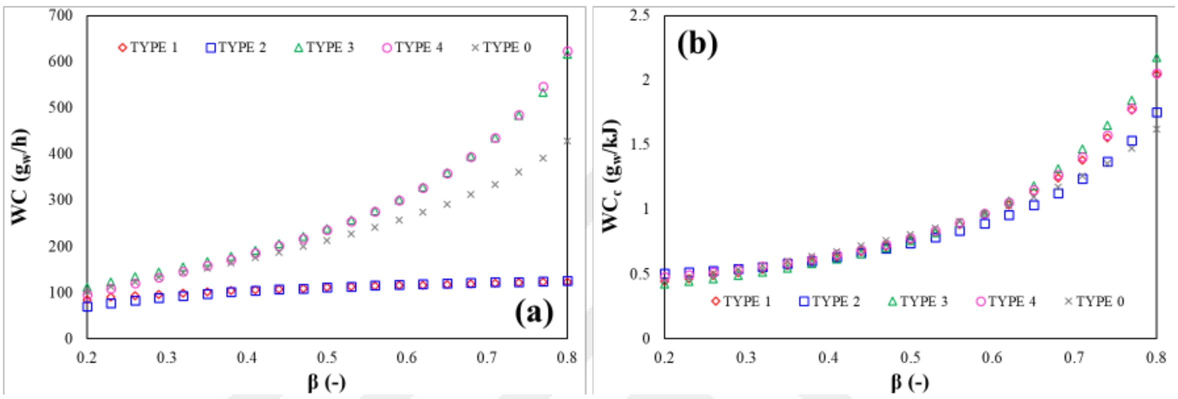

Figure 4.39. Variation of WC (a) and WC_c (b) with working-to-intake air ratio

Figure 4.40 explores the effect of the working-to-intake air ratio (β) on fan power consumption (W_f) and the overall cooling coefficient of performance (COP) of the coolers. As presented in Figure 4.40a, a substantial divergence emerges among the different configurations at higher working-to-intake air ratio values. While fan power remains nearly constant for Types 1 and 2, both of which draw working air directly from the process stream, the required fan power increases dramatically for Types 3, 4, and 0, especially beyond $\beta \approx 0.6$. This is a direct consequence of the elevated air velocity in their independently supplied working channels, which scales with the increasing working air ratio and imposes a significantly higher pressure drop. The most pronounced increase is observed in Type 3, reaching over 10 W at β=0.8, which underscores the energetic penalty of higher airflow rates in this configuration.

As fan power increases, the energy efficiency of the system, quantified by COP, correspondingly declines (Figure 4.40b). While all configurations exhibit a general downward trend in COP with increasing β, the rate and severity of decline vary. Types 3 and 4 show the steepest reductions, due to their sharply rising fan consumption. Type 2, despite its constant W_f, also experiences a drop in COP, although more gradually, as the cooling capacity plateaus or declines beyond its optimal β range. Interestingly, Type 1 maintains a relatively high COP across a wider β interval, owing to its modest fan requirements and reasonably stable performance. Overall, these results emphasize the importance of airflow configuration in maintaining energy efficiency: excessive working airflow may enhance cooling potential but comes at a steep energetic cost that rapidly undermines system-level performance.

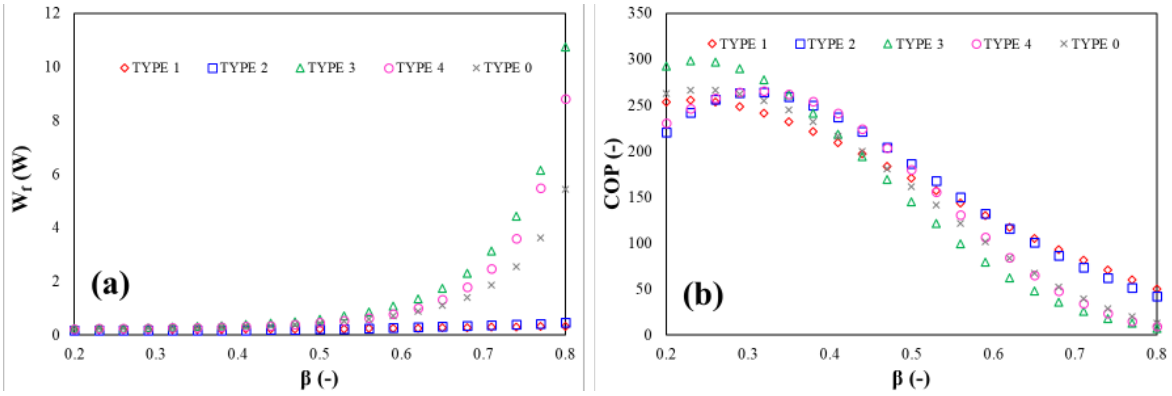

Figure 4.40. Variation of W_f (a) and COP (b) with working-to-intake air ratio

The comprehensive parametric investigation carried out in Phase 1 of this thesis provided a detailed understanding of how key operational variables (inlet air temperature (T_i), inlet air humidity (ω_i), inlet air velocity (u_i) and working-to-intake air ratio (β) influence the thermal, hydraulic and water use performance of various cooler configurations. Among the five evaluated cooler configurations, Type 2 consistently demonstrated superior performance, particularly in terms of effectiveness, COP and specific water consumption under varying conditions. Therefore, Phase 2 of this thesis focuses exclusively on the geometric optimization of Type 2, with the aim of refining its design to achieve even greater performance gains through detailed structural and dimensional adjustments.

4.2. Geometric Optimization of The Multi-Aperture Cooler (Type 2)

The superior performance of the Type 2 configuration, as demonstrated in the comparative evaluation of multiple cooler types, established it as the baseline design for further enhancement through systematic geometric optimization. Although the multi-aperture design inherently improves dew-point cooling by enabling distributed regeneration, the performance of this system is highly dependent on its geometric structure. For this reason, a second phase of this thesis was devoted exclusively to optimizing Type 2. In this phase, four geometric and an operational parameter were systematically varied: aperture number (apN), aperture diameter (apD), channel length (L), channel gap (h) and working-to-intake air ratio (β). These variables influence internal flow behavior, mixing intensity, pressure loss, and the distribution of evaporation, ultimately affecting cooler performance.

The geometric optimization methodology was structured in two main stages. First, to eliminate situations that could violate the fundamental operating principles of indirect evaporative cooling, a logistic regression-based model was developed to detect cases where reverse airflow occurred in the working channel. Any case exhibiting such behavior was considered physically invalid and excluded from further consideration. Second, using only the valid cases, a novel regression model was constructed using the response surface methodology (RSM). This model was structured to predict the cooler's performance based on four key indicators: dew-point effectiveness, cooling capacity, water consumption, and cooling coefficient of performance (COP). The resulting response surfaces served as the foundation for a multi-objective optimization study.

A total of five optimization scenarios were examined, each reflecting a different design priority. These include a baseline and four goal-specific scenarios:

1) Baseline scenario with equal weighting across all performance metrics,
2) Scenario targeting maximum cooling capacity,
3) Scenario targeting minimum outlet air temperature,
4) Scenario targeting minimum water usage,
5) Scenario targeting maximum COP.

The following subsections present the results of this optimization framework in a structured and comparative approach.

4.2.1. Reverse Airflow Check Results

Before proceeding to the optimization stage, it was critical to identify and eliminate any cases that could lead to reverse airflow conditions within the working channel. Such situations are undesirable because they contradict the operating principles of indirect evaporative cooling. To address this, a logistic regression-based model was developed to classify whether a given geometry would result in reverse flow. Two separate models were constructed: a simpler five-variable version offering practical speed and usability, and a more complex, high-accuracy model incorporating second-order and interaction terms. The first model that was designed to be computationally efficient and easy to implement was based on a five-variable linear formulation and used in conjunction with Equation 3.25. The coefficients for this practical model are listed in Table 4.1, and it yielded a classification accuracy of 92.75%. A more comprehensive model incorporating second order and interaction terms was also constructed for enhanced predictive reliability. This complex logistic regression model, defined by Equation 3.26 and detailed in Table 4.2, achieved a significantly higher accuracy of 99.11%. Therefore, in all subsequent stages of the study, particularly during the optimization process, the results of this more robust model were utilized to identify and eliminate configurations exhibiting reverse airflow.

The results of this reverse flow check are illustrated in Figure 4.41, which maps the classification outcomes across the entire geometric design space comprising 4200 unique configurations. Each square in the figure represents a specific case, with blue cells indicating normal airflow (no reverse) and red cells indicating reverse airflow cases. Visual mapping provides a rapid overview of how various parameters influence this critical phenomenon. As seen in the figure, one of the most influential parameters is the number of apertures (apN). Generally, increasing apN increases the likelihood of reverse airflow due to higher flow redistribution and more interaction points between the process and working streams. However, this trend is not absolute; there are configurations with nine apertures that still avoid reverse flow, depending on the combination of other parameters. For instance, larger channel gaps (h) tend to mitigate reverse flow by reducing velocity gradients and pressure imbalances, while increases in aperture diameter (apD), which allow greater mass exchange, generally elevate the risk. Channel length (L) also has a moderate effect. Longer channels offer more room for flow development, which can either suppress or amplify flow separation depending on aperture placement. Finally, the working-to-intake ratio (β) shows a particularly strong influence. At low β values, a smaller fraction of the intake air enters the working channel, leading to concentrated flow through the initial apertures and leaving subsequent ones underutilized. This causes adverse pressure gradients that are conducive to reverse flow. In contrast, higher β values distribute the airflow more evenly and thus significantly reduce the likelihood of reverse motion.

In summary, although reverse flow is more likely under certain geometric and operational combinations, it is not solely affected by any single parameter. The interaction between variables, as captured by the logistic regression model, is key to predicting such behavior. Therefore, only configurations classified as reverse flow-free were retained for the optimization process presented in the next sections.

Table 4.1. Coefficients of the practical logistic model

Estimates	Κ [1]	X_i
c_0	-0.2737764	-
c_1	-1.7185308	apN
c_2	-0.0040667	L
c_3	3.0973801	h
c_4	-23.8309360	apD
c_5	18.1367641	β

Table 4.2. Coefficients of the precise logistic model

Estimates	Κ [1]	X_i
c_0	30.1415376	-
c_1	-11.0589810	apN
c_2	-0.0181291	L
c_3	8.2065705	h
c_4	-184.9044600	apD
c_5	16.8201602	β
c_6	0.9367143	apN*apN
c_7	-0.0046019	apN*L
c_8	0.0000279	L*L
c_9	-0.2573149	apN*h
c_{10}	-0.0075943	L*h
c_{11}	2.0680713	h*h
c_{12}	-11.1408020	apN*apD
c_{13}	-0.0229849	L*apD
c_{14}	-47.7208750	h*apD
c_{15}	571.9883060	apD*apD
c_{16}	-7.9562049	apN*β
c_{17}	-0.0255928	L*β
c_{18}	64.4112159	h*β
c_{19}	-352.1555300	apD*β
c_{20}	70.9576694	β*β

Figure 4.41. Reverse airflow checking results with mapping plot (0: reverse airflow, 1: normal airflow)

4.2.2. Multi-Objective Optimization Results

Following the elimination of configurations exhibiting reverse airflow, a total of 2225 valid CFD simulations were used to construct a predictive model based on Response Surface Methodology (RSM). This model served as the foundation for subsequent multi-objective optimization studies. The regression functions were formulated using response surface methodology and the corresponding coefficients for each performance parameter, namely dew-point effectiveness (ε_{dp}), cooling capacity (CC), water consumption (WC) and cooling coefficient of performance (COP), are presented in Table 4.3. These equations, expressed through Equation 3.26, relate the system's response to the geometric and flow-related inputs: aperture number (apN), aperture diameter (apD), channel length (L), channel gap (h) and working-to-intake air ratio (β). The predictive performance of the regression models was evaluated by comparing the predicted values against the original CFD results, as illustrated in Figure 4.42. The agreement was particularly strong for ε_{dp}, CC and WC, with determination coefficients (R^2) of 0.98, 0.98, and 0.99, respectively. The root mean square error (RMSE) values were also found to be relatively low, with 0.0237 for dew-point effectiveness, 1.5099 W for cooling capacity and 1.548 g/h for water consumption, indicating minimal deviation between the numerical and predicted values. For COP, the regression model yielded an R^2 of 0.94 and an RMSE of 28.483, which, although slightly less precise than the others, still demonstrates sufficient reliability given the compound nature of the COP calculation. Overall, the statistical consistency and low prediction errors confirm that the RSM-based regression models are suitable for guiding optimization efforts and evaluating the performance behavior across a broad parametric space.

Table 4.3. Coefficients of the performance parameters for multi-objective optimization

Estimates	ε_{dp}	**CC (W)**	**WC (g/h)**	**COP**	X_i
c_0	0.6771009	-3.1834120	-6.6619880	-63.5732500	-
c_1	-0.0517970	-3.3286070	-3.2824950	42.3188010	apN
c_2	-0.1093230	-5.7468330	1.2268532	677.4917500	apD
c_3	0.0003046	0.0182409	0.0191895	-0.0247400	L
c_4	-0.1152980	10.0820320	12.4066470	28.4227290	h
c_5	1.0050076	67.0957860	81.4387540	83.0602880	β
c_6	-0.0015530	-0.0709910	-0.0251340	-3.0471080	apN*apN
c_7	-0.0317430	-2.0931620	-3.1530170	60.3435920	apN*apD
c_8	0.1068655	5.9280608	12.9961190	-687.7858000	apD*apD
c_9	-0.0000177	-0.0011080	-0.0012510	-0.0256980	apN*L
c_{10}	-0.0000375	-0.0038670	-0.0041210	-0.1703210	apD*L
c_{11}	-0.0000002	-0.0000101	-0.0000162	0.0000228	L*L
c_{12}	0.0088301	0.4852656	0.4567645	8.0772826	apN*h
c_{13}	0.0101693	0.6643422	-0.7858260	83.5900670	apD*h
c_{14}	0.0000487	0.0054767	0.0085991	0.0064870	L*h
c_{15}	-0.0006690	-1.1727160	-1.6936730	-5.9046040	h*h
c_{16}	0.0863395	5.5872627	4.8961073	-26.0473600	apN*β
c_{17}	0.1539310	11.4146980	-4.3773170	-448.7014000	apD*β
c_{18}	0.0003247	-0.0086530	-0.0016390	0.0970736	L*β
c_{19}	-0.1079290	-6.8321180	17.7535860	-60.4041000	h*β
c_{20}	-0.7175590	-97.6565400	-113.1956000	-143.8851000	β*β

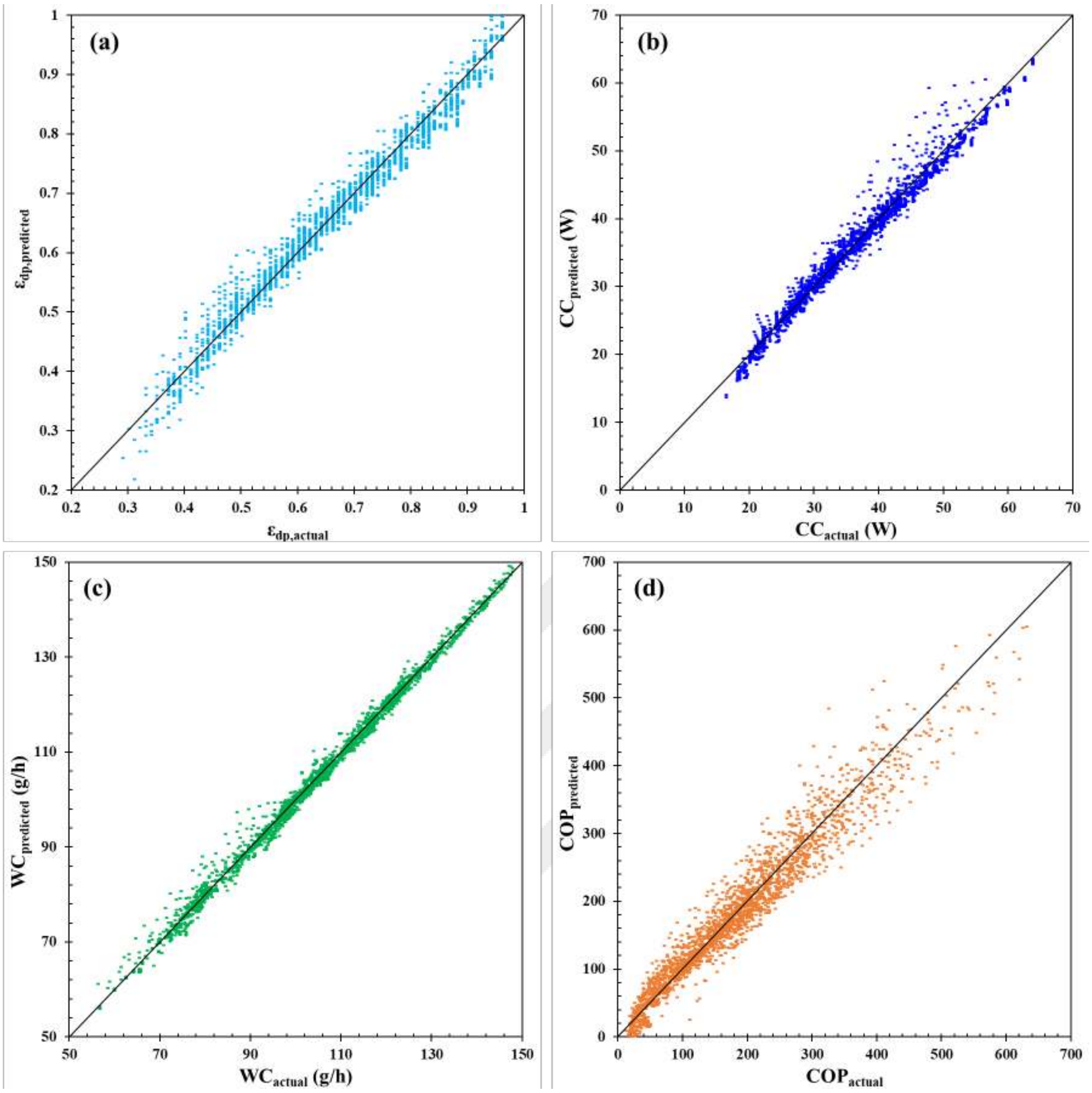

Figure 4.42. Comparison of the numerical results with the predicted data from regression model for dew-point effectiveness (a), cooling capacity (b), water consumption (c) and COP (d)

The geometric multi-objective optimization of the cooler was conducted across five different scenarios, each designed for a specific objective: equal weighting of all parameters (*Scenario 0),* minimization of outlet air temperature (*Scenario 1*), maximization of cooling capacity (*Scenario 2*), minimization of water consumption (*Scenario 3*), and maximization of COP (*Scenario 4*). Some of the boxes in the figures created for the respective scenarios contain multiple curves that also represent the confidence intervals of the regression models.

4.2.2.1. Scenario 0; all parameters weighted equally

In this scenario, all four performance parameters were assigned equal weights during the multi-objective optimization process. The results are presented in Figure 4.43, where the individual effect of each design variable on the objective functions and overall desirability is shown. The initial optimization procedure suggested that the optimal aperture number (apN) would be 3.31. Since this parameter must take integer values, it was rounded to 3, and the optimization was repeated accordingly. This adjustment produced a new optimum set of values while preserving model consistency. The aperture diameter (apD) was identified as 0.5 mm, the maximum allowed value, although its influence on most of the objective functions remained limited, as indicated by the relatively flat response surfaces across all plots. With respect to the channel length (L), the optimization yielded a near-optimal value of 1329 mm, where a slight increase in performance was observed before a plateau. The channel gap (h) was determined to be approximately 4.28 mm, which offered a suitable balance between pressure drop and evaporative cooling potential. Among the decision variables, the working-to-intake air ratio (β) exhibited the most noticeable trade-off effect. While higher β values typically enhance dew-point effectiveness, they also significantly increase water consumption, thereby reducing overall desirability. The optimization found β=0.23 to be the best compromise, offering modest evaporative performance with relatively low water consumption and manageable fan energy demand.

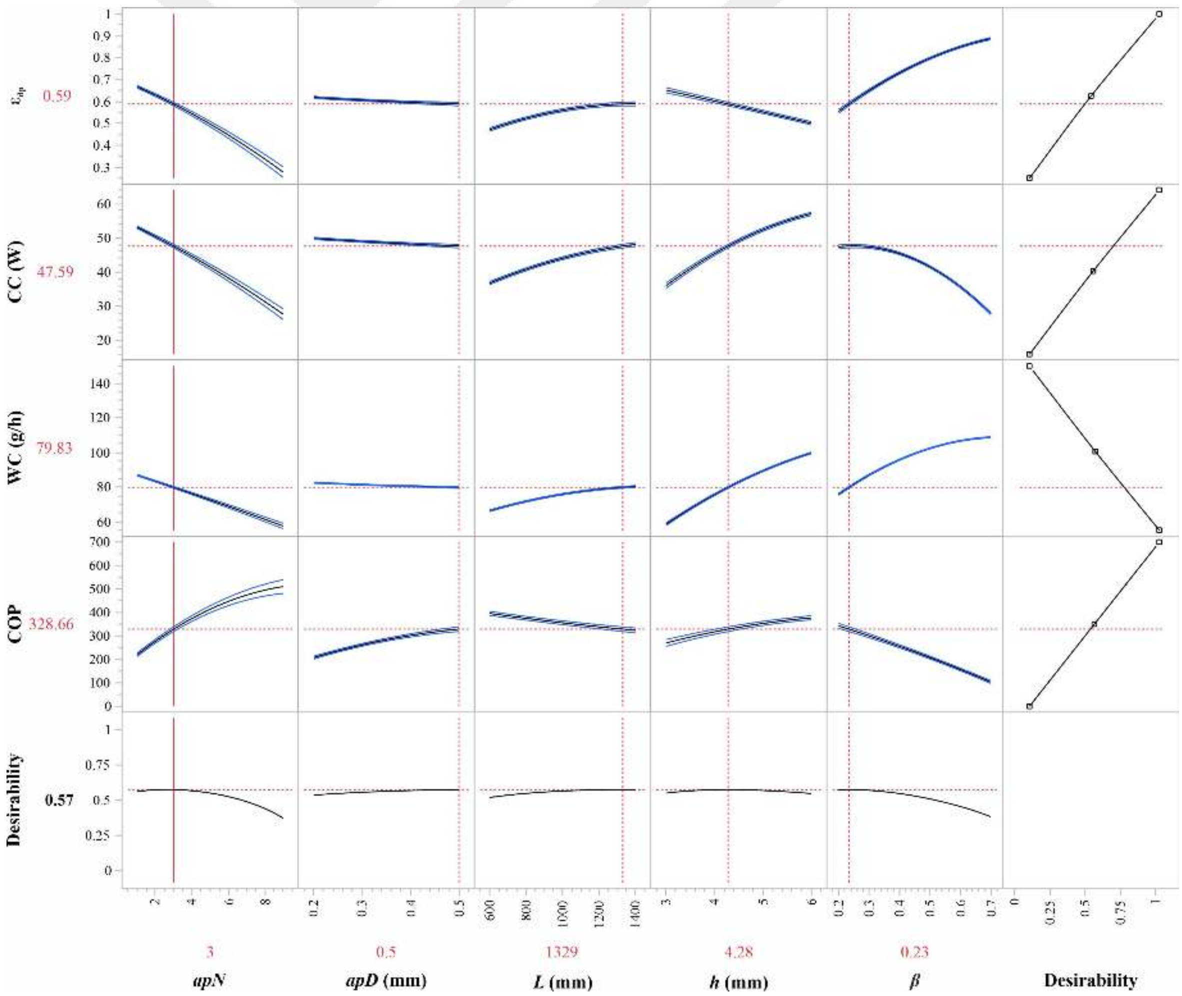

Figure 4.43. Multi-objective optimization using desirability function for *Scenario 0*

This configuration produced a maximum desirability score of 0.57, indicating a balanced yet sub-optimal outcome when all objectives are treated equally. The trade-offs inherent in this scenario suggest that weighting specific objectives more heavily, such as minimizing water use or maximizing COP, could yield configurations with more targeted benefits.

4.2.2.2. Scenario 1; minimum process air outlet temperature

This scenario aimed to achieve the lowest possible process air outlet temperature by prioritizing dew-point effectiveness (ε_{dp}) over other performance parameters. The optimization results are presented in Figure 4.44, where the influence of each design variable on ε_{dp} and overall system desirability is shown. To maximize dew-point effectiveness, the number of apertures (apN) was initially calculated as 1.36. Since this parameter must be an integer, it was rounded to 1, which corresponds to a configuration similar to the conventional single-aperture dew-point cooler. The inverse relationship between ε_{dp} and apN is clearly visible in the figure, affirming that a lower number of apertures is preferable when minimizing outlet temperature is the main objective. The aperture diameter (apD) was found to be 0.41 mm, consistent with its limited influence on system performance. This parameter remained secondary compared to other more impactful geometric variables.

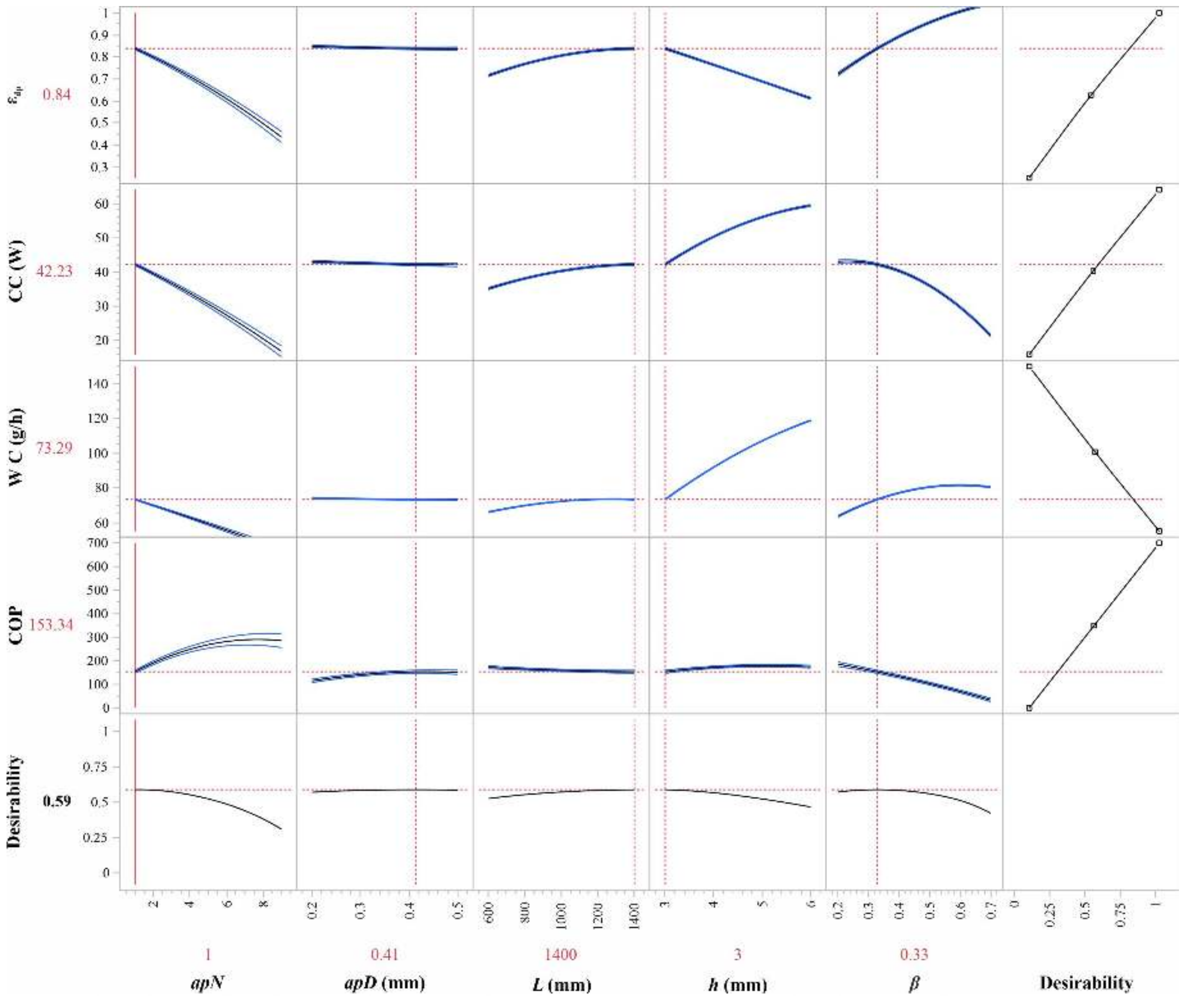

Figure 4.44. Multi-objective optimization using desirability function for *Scenario 1*

Two variables that had a strong influence in this scenario were the channel length (L) and channel gap (h). A longer channel enhances heat exchange due to extended surface contact and residence time, leading to greater cooling. Accordingly, the optimal channel length was found to be 1400 mm, the upper bound of the design range. On the other hand, minimizing the channel gap reduces the diffusion path for thermal energy and increases convective transfer. Hence, h=3 mm emerged as the most favorable gap for this cooling-focused scenario. The optimal working-to-intake air ratio (β) was calculated as 0.33, a moderate value that balances evaporative effectiveness with airflow distribution. Under this configuration, the model achieved a maximum desirability of 0.59, slightly higher than *Scenario 0*, emphasizing the advantage of objective-focused optimization when targeting extreme thermal performance.

4.2.2.3. Scenario 2; maximum cooling capacity

The optimization results for *Scenario 2*, in which cooling capacity (CC) was given the highest priority, are presented in Figure 4.45. The goal was to maximize the amount of thermal energy removed from the process air stream. The aperture number (apN) was initially calculated as 2.76, and subsequently rounded to 3 for practical implementation. This value strikes a balance between enhancing the evaporative potential through air mixing and maintaining a sufficient process flow rate to sustain heat transfer. Once again, the aperture diameter (apD) was found to be 0.5 mm, consistent with previous findings where this parameter showed limited sensitivity across different objectives.

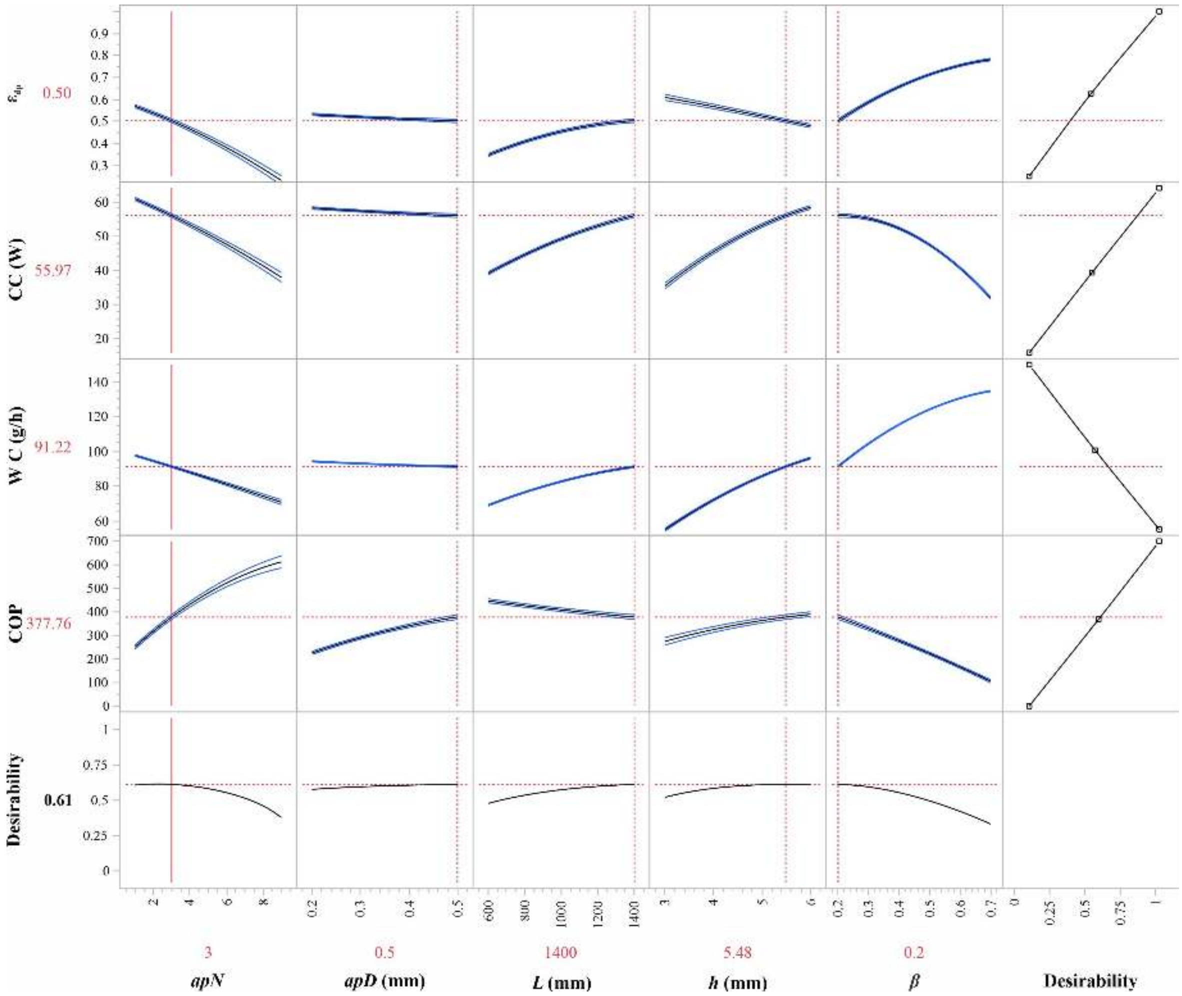

Figure 4.45. Multi-objective optimization using desirability function for *Scenario 2*

A key factor in boosting cooling capacity is the channel gap (h), which significantly influences the volumetric airflow. In this scenario, the channel gap reached its highest optimal value of 5.48 mm among all examined cases. A larger gap allows greater airflow through the process channel, which under constant inlet velocity translates to an increased mass flow rate and thus higher cooling capacity. On the other hand, the working-to-intake air ratio (β) showed an inverse relationship with cooling capacity. Since a higher β means more air is diverted into the working channel, it reduces the flow through the process channel, the very component that determines CC. Therefore, the lowest β value of 0.2 yielded the best results in terms of cooling performance. The channel length again optimized to its upper bound of 1400 mm, this configuration achieved a maximum desirability of 0.61. This confirms that cooling capacity optimization benefits from extended residence time, wide flow channels and minimal diversion of air to the wet side.

4.2.2.4. Scenario 3; minimum water consumption

The optimization outcomes for *Scenario 3*, in which water consumption (WC) is treated as the most critical performance indicator, are presented in Figure 4.46. In this case, all geometric parameters were adjusted to minimize the volume of water evaporated during the cooling process, addressing use cases where water availability is limited or conservation is a priority. The aperture number (apN) was initially calculated as 2.82 and rounded to 3. The aperture diameter (apD) reached its optimal point at 0.5 mm, which was a recurring result across earlier scenarios, and once again confirmed its relatively minor influence on the overall water-use behavior of the system.

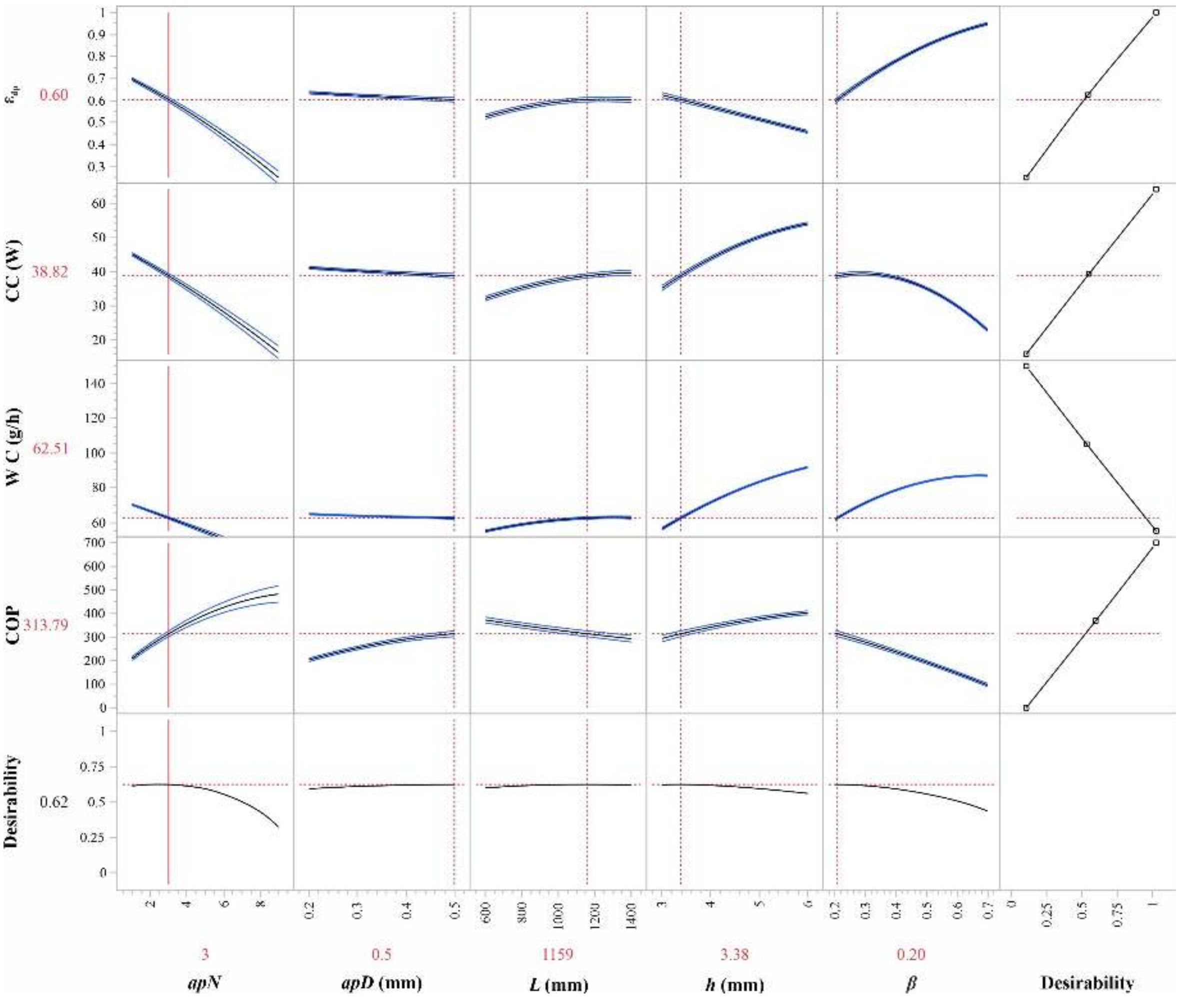

Figure 4.46. Multi-objective optimization using desirability function for *Scenario 3*

Among the key drivers of water consumption is the length of the channel (L). As expected, shorter channels provide less surface area and reduced residence time for evaporation to occur, thus limiting total water usage. In this scenario, the optimized channel length was 1159 mm, which is the shortest value among all scenarios, indicating its effectiveness in reducing water losses. The channel gap (h) was also a decisive factor. While wider gaps tend to increase airflow and thereby water loss, narrower channels facilitate rapid air saturation, shortening the evaporation window. The optimal gap value here was found to be 3.38 mm, a moderately low value that balances saturation efficiency with hydraulic constraints. Finally, the working-to-intake air ratio (β) was minimized at 0.20, again consistent with the aim of reducing the volume of air directed toward the wet channel, hence decreasing the amount of water that can evaporate. This configuration resulted in a maximum desirability score of 0.62, indicating an efficient water-saving design without excessively compromising thermal or energy performance.

4.2.2.5. Scenario 4; maximum COP

One of the most critical indicators for evaluating the performance of an evaporative cooling system is the cooling coefficient of performance (COP), as it reflects the balance between energy input and cooling output. Figure 4.47 presents the optimization results for Scenario 4, in which COP was selected as the primary objective to be maximized. According to the COP definition (Equation 3.21), this parameter is driven by two key elements: cooling capacity (CC) and total fanning power.

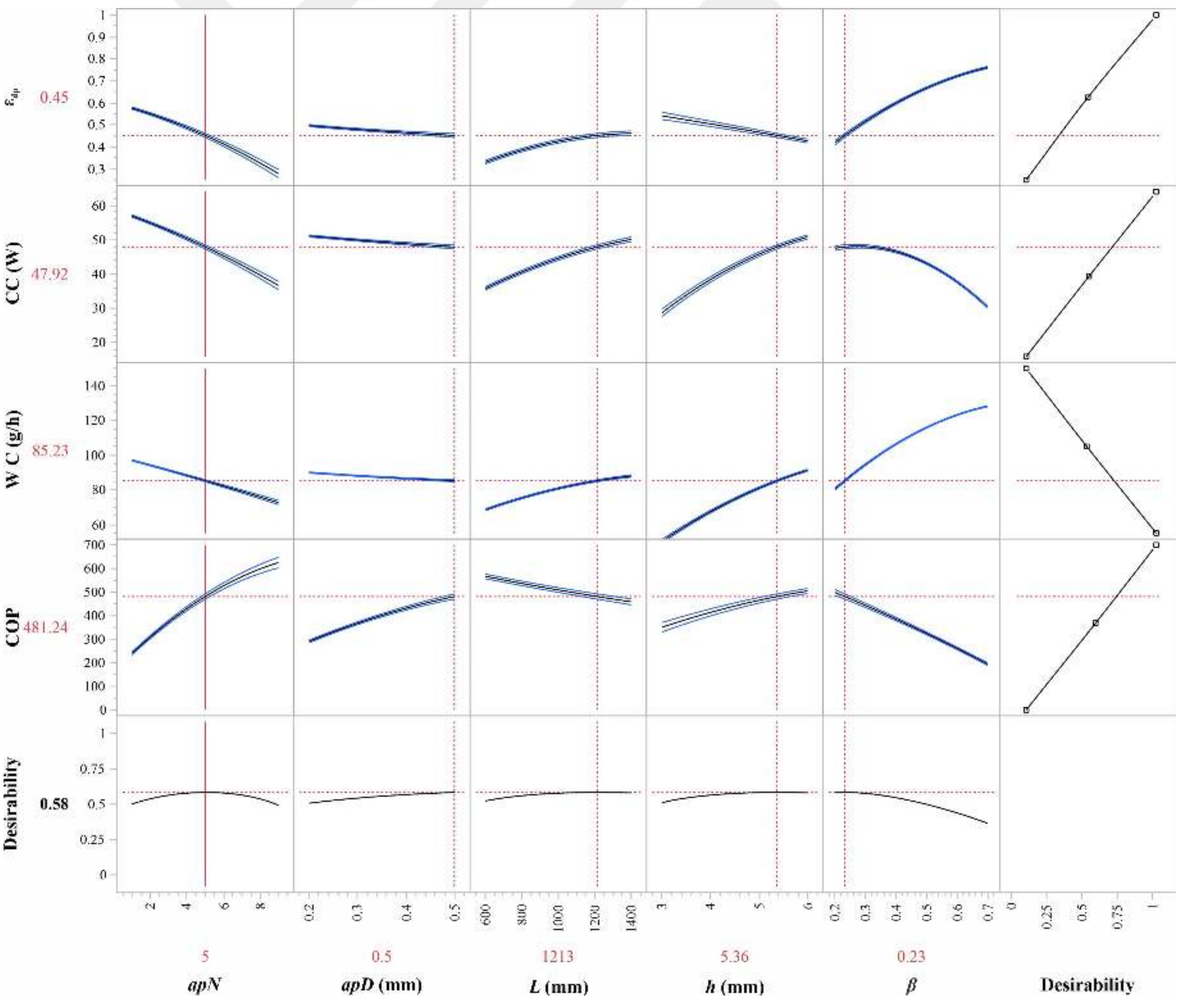

Figure 4.47. Multi-objective optimization using desirability function for *Scenario 4*

Among all the optimization scenarios, *Scenario 4* resulted in the highest aperture number, calculated as 5.16 and then rounded to 5 for model consistency. While a higher aperture number generally decreases cooling capacity, due to air being diverted to the working side, it simultaneously leads to a significant reduction in pressure drop and pumping energy, which strongly benefits the COP. The aperture diameter was again found to be 0.5 mm, consistent with its role in maximizing flow and minimizing resistance across *Scenarios 0, 2* and *3*. The channel length (L) affects both cooling performance and hydraulic resistance. Although longer channels improve cooling by enhancing heat exchange, they also increase pressure losses. In this scenario, the optimization struck a balance at a channel length of 1213 mm, ensuring sufficient heat transfer while limiting hydraulic penalties. The channel gap (h) proved to be a critical design parameter. A wider gap reduces pressure loss and increases airflow volume, both of which contribute to an improved COP. In this case, the optimal gap was found to be 5.36 mm, one of the highest values observed across all scenarios. As for the working-to-intake air ratio (β), the optimizer selected a value of 0.23. While increasing β can raise fan power consumption on the working side, it concurrently reduces demand on the process side. Since the total pressure drop is a combined outcome of both air streams, this trade-off maintains a relatively constant total energy input. However, as increasing β reduces the amount of air available on the process side, cooling capacity drops, negatively impacting the numerator of the COP expression. Thus, the optimal value achieved reflects a balanced trade-off.

This scenario produced a maximum desirability score of 0.58, indicating a high-performing configuration in terms of energy efficiency, particularly valuable for low-energy or off-grid cooling applications.

4.2.2.6. Evaluating all optimization scenarios

The geometric optimization results for the multi-perforated indirect evaporative cooler, considering all five scenarios, are collectively illustrated in Figure 4.48. Each scenario targeted a different performance metric, yet a number of common trends and critical distinctions emerged.

Among the most striking consistencies, the aperture diameter (apD) of 0.5 mm was found to be optimal in four out of five scenarios (*Scenarios 0, 2, 3* and *4*). This suggests that maximizing the aperture cross-section generally supports improved performance, particularly for configurations where cooling capacity or COP is emphasized. However, since both aperture number and diameter directly affect the risk of reverse airflow, these features must be cross-verified with the logistic regression-based flow direction model described in the related section before implementation. In terms of aperture number (apN), value 3 emerged as optimal in *Scenarios 0, 2* and *3*, where either balanced performance or cooling performance and water conservation were prioritized. In contrast, Scenario 1 favored the lowest aperture number (apN=1) to reduce internal mixing, aiding in achieving the lowest outlet temperature, while Scenario 4, which focused on COP, preferred the highest aperture number (apN=5) due to its influence on reducing pressure losses and pumping energy.

All scenarios favored channel lengths exceeding 1000 mm, with 1400 mm being optimal for *Scenarios 1* and *2*. This reflects the importance of extended heat and mass transfer surfaces when minimizing outlet temperature or maximizing cooling output. Shorter channels, such as the 1159 mm seen in *Scenario 3*, help reduce water consumption by limiting residence time in the wet channel. The channel gap (h) emerged as the most variable parameter across all scenarios. Smaller gaps (3.00-3.38 mm) were optimal for scenarios targeting outlet temperature minimization and water conservation (*Scenarios 1* and *3*), where closer spacing enhances evaporative transfer efficiency and saturation. On the other hand, larger gaps (5.36-5.48 mm) were preferred in *Scenarios 2* and *4*, aiming to maximize airflow rate and reduce hydraulic resistance, critical for improving cooling capacity and COP.

Lastly, with regard to the working-to-intake air ratio (β), lower values generally led to better performance. All five scenarios, including the balanced *Scenario 0*, identified optimal β values ranging from 0.20 to 0.33, indicating that supplying only a fraction of the intake air to the wet side suffices for effective cooling while keeping water consumption and pressure losses manageable.

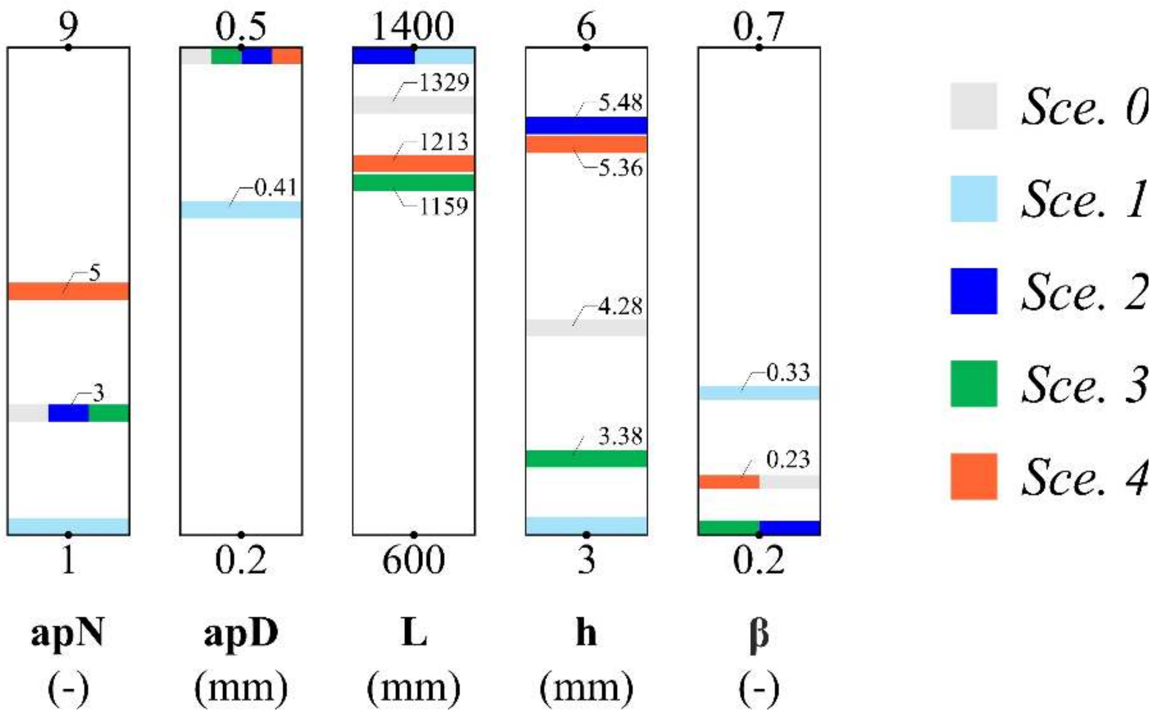

Figure 4.48. Optimum geometric features of multi-perforated indirect evaporative cooler

As illustrated in the last figure, the design parameters of the dew-point indirect evaporative cooler vary considerably depending on which performance metric is prioritized during optimization. Each scenario presents a unique combination of geometric and operational inputs, such as aperture number, channel dimensions and working-to-intake air ratio, highlighting that a universally optimal design is unrealistic. Instead, the cooler must specialize in project requirements, emphasizing the necessity of a scenario-based, performance-driven design approach rather than a one size that fits all solutions. To support this special design philosophy and minimize the computational load of traditional CFD-based performance evaluations, the final phase of this thesis focuses on predictive modeling using multiple linear regression and machine learning techniques. These models aim to provide a fast and easily usable alternative to CFD, enabling engineers to estimate cooler performance under diverse input conditions without the need for time-consuming simulations. By achieving this, the study bridges the gap between design flexibility and computational efficiency.

4.3. Performance Modeling of Type 2 Cooler

In the final phase of this thesis, the focus shifts toward developing predictive models for estimating the performance of the Type 2 dew-point indirect evaporative cooler. While computational fluid dynamics (CFD) has proven effective for in-depth simulation and performance analysis, it is computationally intensive and impractical for iterative tasks such as real-time control, optimization, or integration into building simulation tools.

To overcome this limitation, a total of 20,480 CFD simulations, generated during the modeling phase, were used to train and test alternative predictive modeling approaches. After filtering out reverse flow conditions, a refined dataset of 17,525 valid simulation results formed the basis for modeling. The goal was to build fast, lightweight and accurate models that could replicate CFD-level predictions with significantly lower computational cost. Two main modeling strategies were employed: Multiple Linear Regression (MLR) and Machine Learning (ML). All models were trained using the same set of input parameters, including process air inlet temperature ($T_{p,i}$), humidity ($\omega_{p,i}$) and velocity ($v_{p,i}$), aperture number (apN), channel length (L), channel gap (h), and working-to-intake air ratio (β). Each approach was used to predict five outputs of interest: dew-point effectiveness (ε_{dp}), cooling capacity (CC), water consumption (WC) and cooling coefficient of performance (COP). Additionally, the process air outlet temperature ($T_{p,o}$), which was added as a practical metric for end-users, was predicted via all models.

4.3.1. Multiple Linear Regression (MLR) Models

As a first step toward modeling of the Type 2 cooler, multiple linear regression (MLR) models were developed to establish a mathematical relationship between system inputs and performance outputs. MLR models are widely favored for their simplicity, interpretability and ease of implementation, making them ideal candidates for preliminary modeling and fast estimations.

Seven different regression structures were considered in this part of the study, ranging from simple first-degree polynomials to more complex third-degree models including cross-terms. Additionally, a response surface model (RSM) was included as a compact and user-friendly formulation suitable for practical applications. Each model was trained using the same input dataset including $T_{p,i}$, $\omega_{p,i}$, $v_{p,i}$, apN, L, h and β derived from CFD simulations, with five target outputs: ε_{dp}, CC, WC, COP and $T_{p,o}$. The aim was to evaluate how accurately these models could reproduce the CFD results with minimal computational load.

Table 4.4. Statistical performances of MLR models

			R^2					RMSE				
Code	**Structure**	**No. of coef.**	ε_{dp}	$T_{p,o}$	**CC**	**WC**	**COP**	ε_{dp} (-)	$T_{p,o}$ (°C)	**CC (W)**	**WC (g/h)**	**COP (-)**
MLR-1	1st degree	7	0.9215	0.8865	0.8769	0.8885	0.6413	0.0496	1.5926	8.8580	20.6297	202.3703
MLR-2	1st degree Cross	28	0.9666	0.9816	0.9776	0.9913	0.8442	0.0324	0.6421	3.7841	5.7794	133.4348
MLR-3	2nd degree	14	0.9349	0.8916	0.8851	0.8925	0.7043	0.0451	1.5570	8.5600	20.2651	183.7754
MLR-4	2nd degree Cross	77	0.9906	0.9915	0.9923	0.9957	0.9431	0.0172	0.4358	2.2156	4.0456	80.7424
MLR-5	3rd degree	21	0.9351	0.8916	0.8852	0.8925	0.7118	0.0451	1.5567	8.5545	20.2620	181.4589
MLR-6	3rd degree Cross	126	0.9913	0.9918	0.9927	0.9958	0.9556	0.0165	0.4298	2.1654	4.0108	71.4340
MLR-7	Response Surface	35	0.9833	0.9877	0.9893	0.9943	0.9101	0.0228	0.5249	2.6164	4.6817	101.3797

Table 4.4 presents a comparative evaluation of the seven MLR models developed to predict the performance of the Type 2 cooler. The models differ in terms of polynomial degree, presence of interaction (cross) terms and overall complexity, as indicated by the number of regression coefficients. Among all models, MLR-6, the third-degree model with cross-terms, demonstrated the best overall performance. It achieved the highest R^2 values across all five output parameters, especially for COP (R^2 = 0.9556), CC (R^2 = 0.9927) and WC (R^2 = 0.9958), indicating excellent agreement with CFD results. Furthermore, it yielded the lowest RMSE values, confirming its superior predictive capability. However, this model also has the highest number of coefficients (126), which may limit its practicality in certain applications due to increased complexity and a higher risk of overfitting.

The second-best performance was observed with MLR-4, the second-degree model with cross-terms, which showed a strong balance between accuracy and complexity. With 77 coefficients, it closely followed MLR-6 in terms of both R^2 and RMSE metrics, making it a more computationally efficient alternative but its applicability is still weak and impractical. In contrast, simpler models like MLR-1 (first-degree) and MLR-3 (second-degree), while easier to implement, yielded noticeably lower predictive accuracy, especially for COP and WC.

Interestingly, among the seven regression models developed, MLR-7, the response surface model, has emerged as a particularly noteworthy candidate. While not reaching the absolute top R^2 and RMSE values observed in the most complex third-degree cross-term model (MLR-6), MLR-7 still demonstrated exceptional predictive accuracy across all performance indicators, with R^2 values consistently above 0.98 and RMSE values well within acceptable bounds. Most notably, it achieved this performance with only 35 coefficients, a fraction of the complexity seen in MLR-6 (126 coefficients). This balance between accuracy and simplicity positions MLR-7 as the most practically applicable model in the MLR category. Unlike deeper polynomial models, which may be prone to overfitting or challenging to implement in real-world applications, MLR-7 offers a computationally lightweight structure that can be easily incorporated into analytical tools or embedded design workflows without the need for specialized software. For these reasons, the remainder of the MLR results section will focus solely on the performance of MLR-7, treating it as the main regression model of this study. A complete list of the 35 regression coefficients of MLR-7 is provided in Table 4.5, enabling direct reproduction and deployment of the model across a wide range of psychrometric and geometric conditions. The other MLR models' coefficients are presented in Appendix A.

Figure 4.49a presents a scatter plot comparing the predicted and actual values of the dew-point effectiveness using the MLR-7 model. The results demonstrate a strong agreement between the model predictions and CFD simulations, with the majority of the data points clustered tightly around the reference line. Most predictions fall within the ±5% deviation band and only a small fraction exceed the ±10% limits. This indicates a high level of accuracy and stability across the full range of effectiveness values. The model performs especially well in the mid-to-high dew-point effectiveness range, maintaining reliable predictions even in scenarios where the cooling performance is high.

Figure 4.49b illustrates the distribution of relative errors for the same predictions. The error histogram shows that the highest concentration of predictions lies within the range of −1% to +1% relative error, which accounts for 25.52% of all test data. This is followed by the intervals of +1% to +3% (23.32%) and -3% to -1% (18.93%), respectively. Collectively, almost 68% of the total predictions fall within ±3% error, which reflects the model's strong ability to generalize and minimize deviations. Additionally, the absence of extreme outliers further supports the robustness and consistency of the MLR-7 model when predicting dew-point effectiveness.

Table 4.5. Coefficients of MLR-7 model

		ε_{dp}	$T_{p,o}$	CC	WC	COP
c_0	-	-0.2069480	7.4170531	-33.108490	196.817740	-160.97850
c_1	apN	-0.1240480	1.8837271	-6.2494100	-4.1982510	-33.747770
c_2	L	0.0000996	0.0012495	-0.0210220	-0.0338860	-0.4867460
c_3	h	0.0210397	-1.5091010	7.2206187	-17.859290	275.42910
c_4	β	2.2093190	-26.877860	220.395040	-19.708080	477.616230
c_5	$u_{p,i}$	-0.0085190	-1.0660190	1.8722318	-47.4465300	-409.958900
c_6	$\omega_{p,i}$	0.0356487	1.2305854	-1.1409430	3.4881349	-67.3371600
c_7	$T_{p,i}$	0.0119779	0.3137453	-0.8898350	-9.6799110	57.1648240
c_8	apN*apN	0.0002222	-0.0068300	0.0040347	-0.0773750	10.2410290
c_9	apN*L	-0.0000175	0.0002827	-0.0012380	-0.0012250	-0.0155360
c_{10}	L*L	-0.0000001	0.0000019	-0.0000068	-0.0000110	0.0000512
c_{11}	apN*h	0.0116958	-0.1892190	0.6063442	0.5824165	2.1759698
c_{12}	L*h	0.0000396	-0.0006100	0.0045208	0.0066168	0.0088136
c_{13}	h*h	-0.0046480	0.0679868	-1.1906760	-1.5968530	-12.394390
c_{14}	apN*β	0.1088177	-1.7265630	7.5332870	7.2142969	4.3203453
c_{15}	L*β	0.0002213	-0.0038090	-0.0033090	0.0009555	0.4625017
c_{16}	h*β	-0.1258520	2.1161384	-9.5349980	14.0945800	-232.96350
c_{17}	β*β	-1.0389770	15.8861030	-112.48350	-122.17630	-363.19290
c_{18}	apN*$u_{p,i}$	0.0074435	-0.1199600	0.1761767	-0.0820010	-17.7173500
c_{19}	L*$u_{p,i}$	0.0000347	-0.0005340	0.0062103	0.0088284	0.0947120
c_{20}	h*$u_{p,i}$	-0.0224300	0.3534484	-0.1985030	3.6207776	-36.464960
c_{21}	β*$u_{p,i}$	-0.0980800	1.6969640	-15.2242500	27.6930330	388.2666500
c_{22}	$u_{p,i}$*$u_{p,i}$	0.0062775	-0.1089340	-1.4157380	-1.8037360	84.1635830
c_{23}	apN*$\omega_{p,i}$	0.0002026	-0.0159000	0.0587629	0.1067245	-2.0984400
c_{24}	L*$\omega_{p,i}$	0.0000008	0.0002447	-0.0008940	-0.0010350	0.0070869
c_{25}	h*$\omega_{p,i}$	-0.0003830	-0.0984020	-0.1882860	-0.8498470	-2.0506700
c_{26}	β*$\omega_{p,i}$	-0.0085200	0.9147477	1.7261314	-5.4040820	38.0650940
c_{27}	$u_{p,i}$*$\omega_{p,i}$	-0.0004960	-0.0970000	-0.6902840	-1.8863660	11.6375740
c_{28}	$\omega_{p,i}$*$\omega_{p,i}$	-0.0005890	-0.0105560	0.0267863	0.0424128	0.1948290
c_{29}	apN*$T_{p,i}$	0.0000444	0.0079722	-0.0252700	-0.0709170	2.4134421
c_{30}	L*$T_{p,i}$	0.0000001	-0.0001880	0.0008224	0.0011241	-0.0087600
c_{31}	h*$T_{p,i}$	-0.0000926	0.0773206	0.2516192	1.0091817	2.6595831
c_{32}	β*$T_{p,i}$	-0.0082000	-0.4205860	-3.3614980	3.3956104	-52.5551800
c_{33}	$u_{p,i}$*$T_{p,i}$	0.0000026	0.0762642	0.7844679	2.2163121	-12.0107300
c_{34}	$\omega_{p,i}$*$T_{p,i}$	-0.0001110	-0.0054310	0.0231297	0.0630066	0.1738066
c_{35}	$T_{p,i}$*$T_{p,i}$	-0.0000530	-0.0025570	0.0114064	0.0367586	0.0689900

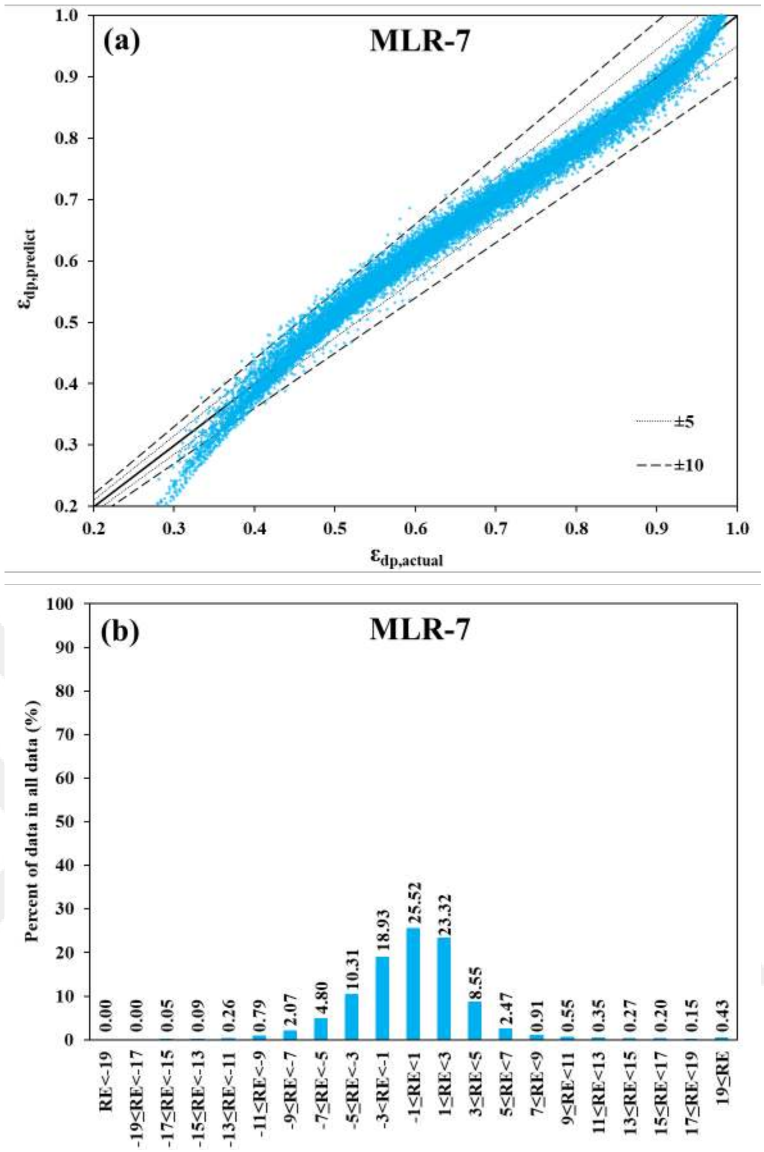

Figure 4.49. Comparison of predicted data from MLR-7 model with actual data (a) and error histogram (b) for dew-point effectiveness

Figure 4.50a illustrates the correlation between the predicted and actual cooling capacity (CC) values using the MLR-7 model. A strong alignment with the reference line is observed across the entire data range, indicating that the model maintains consistent performance, almost all cooling outputs. However, compared to dew-point effectiveness, the data points show slightly more dispersion, particularly at lower CC values. While most predictions remain within the ±10% deviation bands, a portion of the predictions slightly exceed this limit, especially at the upper end of the output spectrum. Nevertheless, the general trend suggests that MLR-7 effectively captures the overall pattern and scale of the cooling capacity behavior, affirming its utility for practical prediction tasks.

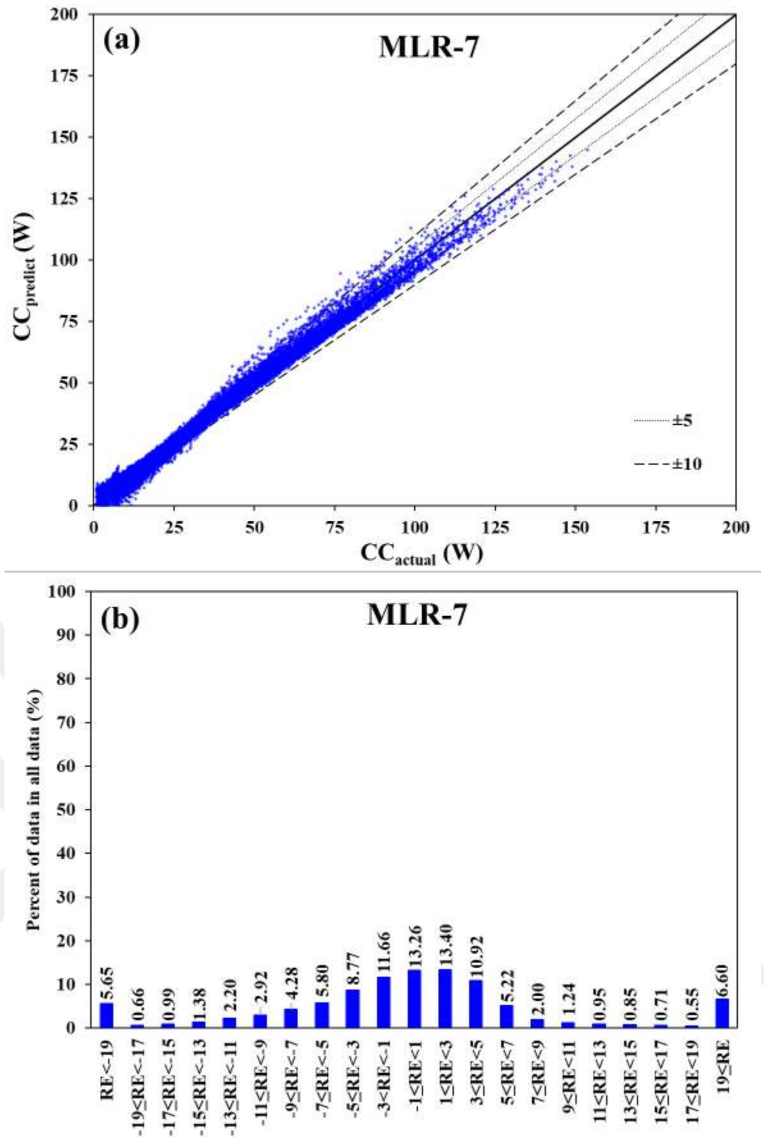

Figure 4.50. Comparison of predicted data from MLR-7 model with actual data (a) and error histogram (b) for cooling capacity

In Figure 4.50b, the relative error distribution for the cooling capacity predictions is presented. The histogram shows a more dispersed error profile than the previous output yet remains within acceptable boundaries for engineering applications. Many predictions fall in the −3% to +3% range, with notable concentrations in the −3% to −1% (11.66%), −1% to +1% (13.26%) and +1% to +3% (13.40%) intervals. As can be seen, more than 37% of the total estimate data falls within the ±3% relative error band. Some data appear in extreme ranges (RE > +19% or RE < −19%), but their occurrence remains minimal. Overall, the MLR-7 model delivers reasonably accurate CC predictions with a slight increase in relative errors, yet it remains a valid and efficient alternative to computationally intensive simulations.

As shown in Figure 4.51a, the MLR-7 model demonstrates excellent agreement between predicted and actual values of water consumption (WC). The data points exhibit a tight linear distribution centered around the reference line, with the vast majority lying within the ±10% error bands and a substantial proportion even within the ±5% range. This indicates that the model is highly effective at capturing the functional relationship between input parameters and WC and remains reliable across the entire output range. Some deviations become more visible at lower consumption, due to the very low consumption level. Regardless, the predictive performance remains robust and acceptable for engineering applications.

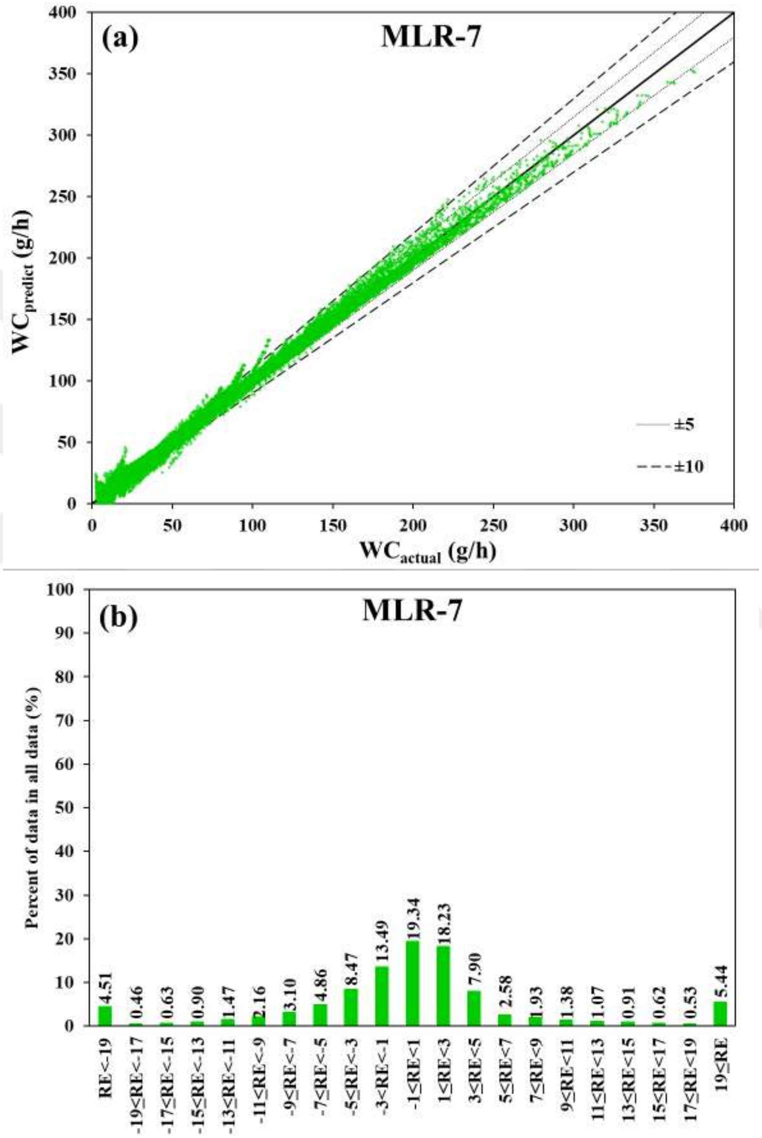

Figure 4.51. Comparison of predicted data from MLR-7 model with actual data (a) and error histogram (b) for water consumption

Figure 4.51b presents the distribution of relative errors in water consumption predictions. The histogram confirms the high accuracy of the MLR-7 model, with 19.34% of data points falling within the tight error band of −1% ≤ RE < +1%, and an additional 18.23% within +1% ≤ RE < +3%. Together, nearly 51% of the predictions fall within ±3% relative error, demonstrating exceptional precision. Furthermore, more than 67% of the data fall within ±5% relative error, showing a relatively symmetric distribution around zero error. Although small percentages of predictions exist in higher error bins (RE > 19%), their contribution is minor and does not significantly impact overall model validity. In conclusion, the MLR-7 model performs impressively in predicting water consumption, affirming its utility as a lightweight, easy-to-implement alternative to computational fluid dynamics simulations.

The evaluation of the MLR-7 model for predicting the cooling coefficient of performance (COP) reveals some notable limitations compared to its performance on other outputs. As seen in Figure 4.52a, although the model captures the overall trend of COP values, the data points are significantly more scattered, especially in regions corresponding to low and high COP values. The deviation from the ±5% and ±10% error bands is visibly larger, suggesting a reduced predictive capability of the linear model in complex, nonlinear regions of the dataset. This is further substantiated by the relative error distribution in Figure 4.52b, where a considerable portion of the predictions fall into extreme error bins. Specifically, 25.24% of the data points exhibit relative errors below −19%, while 33.53% exceed +19%, indicating that over half of the dataset suffers from substantial inaccuracies in COP prediction.

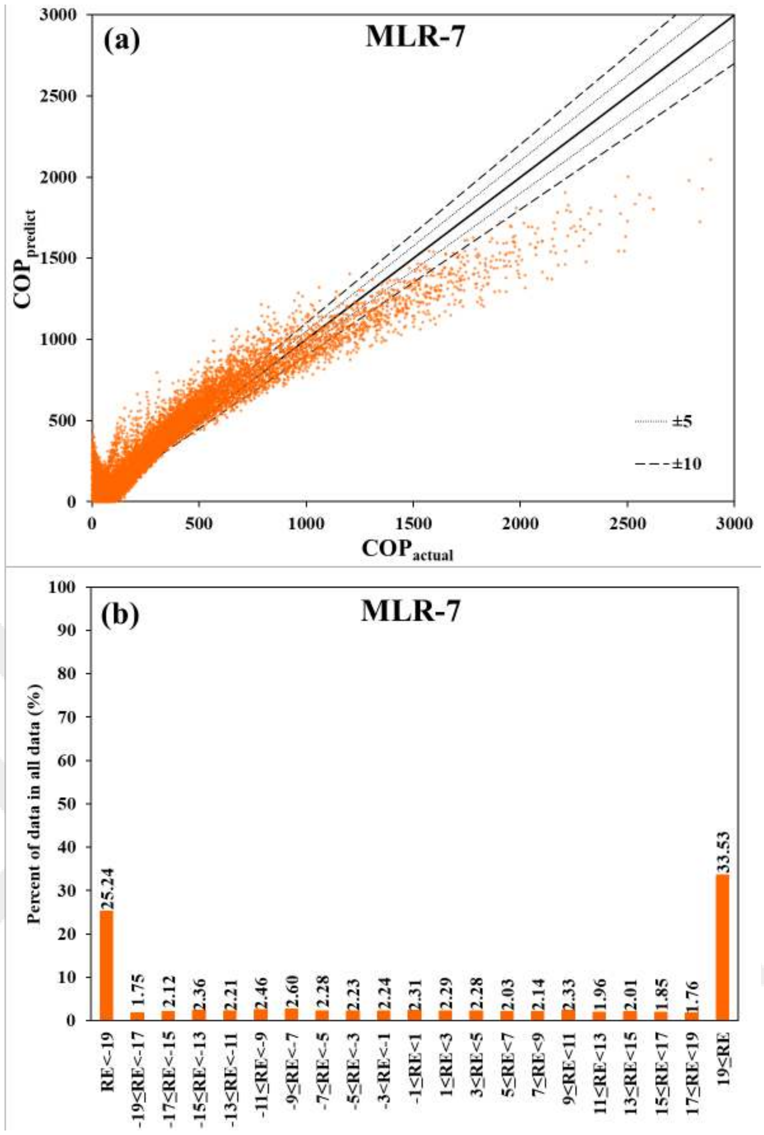

Figure 4.52. Comparison of predicted data from MLR-7 model with actual data (a) and error histogram (b) for COP

These results suggest that MLR-7 may not be an adequate modeling tool for COP estimation, particularly when high fidelity is required. The complex relationship between cooling capacity and fan consumption in the COP calculation exceeds the representation capacity of polynomial regression, even with cross-terms. Therefore, while MLR-7 remains a strong candidate for rapid estimation of most performance indicators, it falls short for COP. This observation highlights the need for more advanced modeling techniques. As will be demonstrated in subsequent sections of this thesis, machine learning approaches offer a promising alternative with the potential to capture these nonlinearities more accurately.

In addition to the four key performance metrics, the outlet temperature of the product air stream $T_{p,o}$ was also examined, as it holds practical importance for end users. As shown in Figure 4.53a, the MLR-7 model demonstrates a highly consistent and accurate prediction performance for

$T_{p,o}$, with the majority of data points aligning closely along the reference line. The prediction errors largely fell within the ±5% bounds, confirming the model’s robustness in estimating this temperature-related output. The histogram in Figure 4.53b further supports this observation. A substantial portion of the data (38.34%) lies within the ±1% relative error range, with more important 80.29% falling in the ±3% band. Only a negligible fraction of the predictions exceeds the ±5% threshold and virtually none surpass ±10%. This tight distribution of errors implies that the MLR-7 model is well-suited for practical applications where reliable estimation of outlet temperature is essential, such as HVAC design, system control, or climate-specific system adaptation.

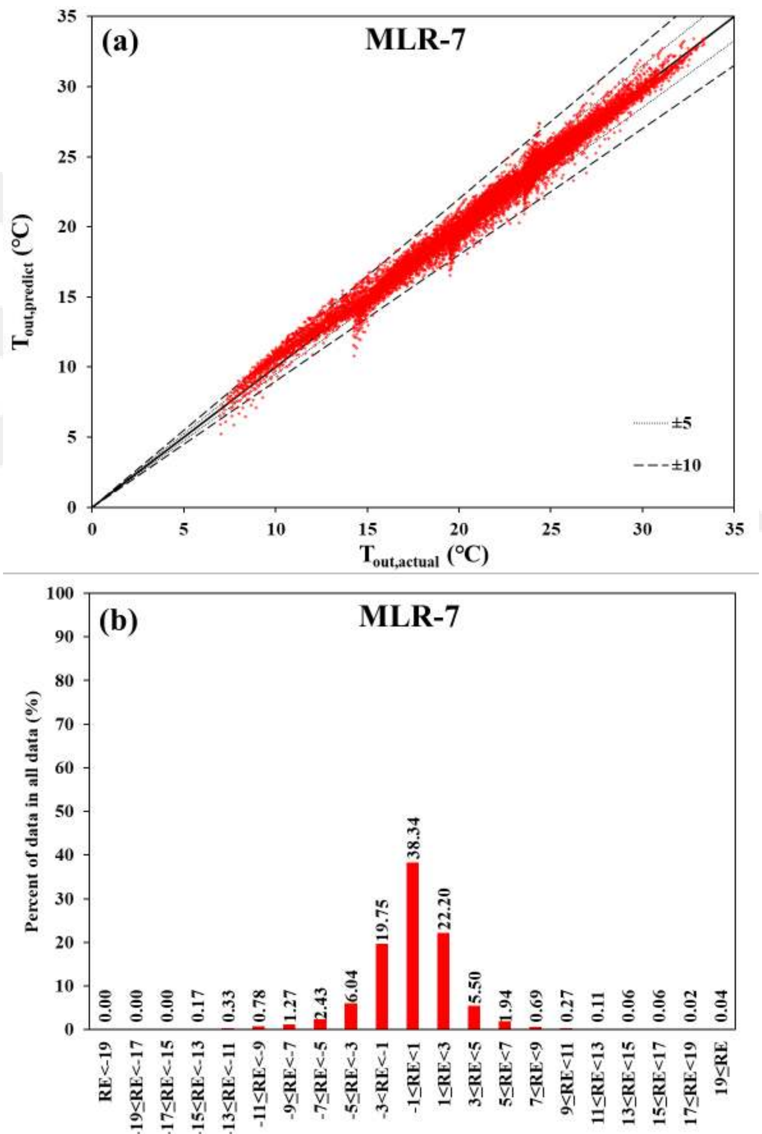

Figure 4.53. Comparison of predicted data from MLR-7 model with actual data (a) and error histogram (b) for process air outlet temperature

4.3.2. Machine Learning Models

Following the development and evaluation of MLR-based models, more advanced predictive approaches were explored using machine learning (ML) algorithms. A total of 32 ML models were developed in three algorithm categories, including 10 decision tree (DT) models, 6 support vector machine (SVM) models and 16 multilayer perceptron (MLP) neural network models. These models were constructed to investigate the predictive capability of different learning patterns and network configurations. All ML models were trained using 17,525 valid data samples, which were extracted from a total of 20,480 CFD simulations after eliminating the cases involving reverse flow or invalid outputs. The input dataset included process air inlet temperature, humidity and velocity, aperture number, channel length, channel gap and working-to-intake air ratio, ensuring that the models captured both geometric and psychrometric influences on performance. The objective of these ML models was to predict four key performance parameters of the Type 2 dew-point indirect evaporative cooler; namely, dew-point effectiveness (ε_{dp}), cooling capacity (CC), water consumption (WC) and cooling coefficient of performance (COP). Additionally, the outlet temperature of process air ($T_{p,o}$) was evaluated as a supplementary parameter due to its practical relevance for end-user applications.

To ensure a comprehensive evaluation, the performance of all models was assessed using statistical indicators such as the coefficient of determination (R^2), root mean square error (RMSE) and relative error metrics, consistent with the MLR section. The complete performance metrics for all models are presented in Table 4.6, allowing for cross-comparison among algorithm types. The comprehensive performance table reveals valuable insights into how structural configurations (especially training functions and activation functions) affect the prediction accuracy of the machine learning models developed in this study.

Among decision tree models, the DT-7 model, which uses “LSBoosting” and “allsplits” predictor selection method with a large number of learners (1000 trees), demonstrates superior performance. It outperforms Random Forest variants (DT-1 to DT-4) and simpler Random Tree models (DT-9 and DT-10) in almost all performance indicators. The sequential learning structure of LSBoosting, which continuously improves the errors of weak learners, appears to increase robustness and accuracy. Notably, models with “interaction-curvature” predictor selection slightly underperform compared to “allsplits”, suggesting that exhaustive splitting enhances prediction fidelity for this dataset.

Support Vector Machine performance is primarily affected by the choice of kernel function. Here, SVM-6, which uses a 4^{th} order polynomial kernel, provides the best balance between complexity and computational time across all performance metrics. In contrast, SVM models with Gaussian and RBF kernels (SVM-1 and SVM-2) perform relatively poorly, especially when predicting more complex outputs such as COP. This highlights the importance of choosing an appropriate kernel function to capture nonlinearities in the data. The Incremental Sequential Minimal

Optimization (ISDA) solver was kept constant for all models, suggesting that kernel complexity plays a more critical role than the solver type in this context.

MLP models exhibit the most diverse configurations, allowing for a more in-depth analysis of how structural changes affect performance. The best-performing model (MLP-4) uses the Levenberg-Marquardt (trainlm) algorithm with two hidden layers (20 neurons each) and a tansig activation configuration. This combination appears to provide both high flexibility and stable convergence. Interestingly, models using trainlm generally outperform those using trainbfg or trainscg, especially in multi-output regression problems. Trainoss based models (MLP-13 to MLP-16), while effective in some cases, exhibit relatively larger prediction errors and lower R^2 values in complex scenarios, likely due to slower or unstable convergence. Increasing the number of neurons and using multiple hidden layers (especially 2x20) consistently improves performance. However, this comes at the expense of increased computational load and potential overfitting in less optimized structures. In terms of the activation function, the universal use of tansig across all MLP configurations ensures consistent nonlinearity across layers.

Table 4.6. Complete performance metrics for all machine learning models

Model	Training Function	Max Tree	Max Split	Activation Function	R^2 ε_{dp}	R^2 $T_{p,o}$	R^2 CC	R^2 WC	R^2 COP	RMSE ε_{dp} (-)	RMSE $T_{p,o}$ (°C)	RMSE CC (W)	RMSE WC (g/h)	RMSE COP (-)
DT-1	Random Forest	500	500	allsplits	0.9784	0.9782	0.9834	0.9875	0.9793	0.0260	0.6985	3.2519	6.9165	48.6090
DT-2	Random Forest	500	500	interaction-curvature	0.9387	0.9404	0.9403	0.9514	0.9545	0.0438	1.1536	6.1676	13.6207	72.0534
DT-3	Random Forest	1000	500	allsplits	0.9791	0.9782	0.9833	0.9874	0.9796	0.0256	0.6985	3.2618	6.9400	48.2928
DT-4	Random Forest	1000	500	interaction-curvature	0.9384	0.9446	0.9458	0.9441	0.9517	0.0439	1.1123	5.8777	14.6026	74.2170
DT-5	AdaBoosting	500	500	allsplits	0.9984	0.9984	0.9993	0.9997	0.9973	0.0070	0.1872	1.2334	0.9963	17.4236
DT-6	AdaBoosting	500	500	interaction-curvature	0.9877	0.9907	0.9925	0.9938	0.9879	0.0196	0.4563	2.1851	4.8621	37.2008
DT-7	**AdaBoosting**	**1000**	**500**	**allsplits**	**0.9984**	**0.9984**	**0.9993**	**0.9997**	**0.9973**	**0.0070**	**0.1870**	**0.6748**	**0.9955**	**17.4050**
DT-8	AdaBoosting	1000	500	interaction-curvature	0.9877	0.9907	0.9925	0.9938	0.9879	0.0196	0.4563	2.1851	4.8621	37.2008
DT-9	Random Treee	-	500	allsplits	0.9633	0.9636	0.9744	0.9858	0.9672	0.0339	0.9015	4.0411	7.3653	61.2107
DT-10	Random Treee	-	500	interaction-curvature	0.9195	0.9309	0.9276	0.9380	0.9359	0.0502	1.2422	6.7909	15.3850	85.5001

Model	Training Function	Degree	Solver	ε_{dp}	$T_{p,o}$	CC	WC	COP	ε_{dp} (-)	$T_{p,o}$ (°C)	CC (W)	WC (g/h)	COP (-)
SVM-1	Gaussian	-	ISDA	0.9992	0.9997	0.9990	0.9979	0.7579	0.0051	0.0809	0.7929	2.8576	166.2167
SVM-2	RBF	-	ISDA	0.9992	0.9997	0.9989	0.9979	0.7593	0.0050	0.0805	0.8261	2.8108	165.7271
SVM-3	Polynomial	1	ISDA	0.9154	0.8854	0.8752	0.8871	0.5138	0.0514	1.6001	8.9145	20.7575	235.5618
SVM-4	Polynomial	2	ISDA	0.9816	0.9870	0.9889	0.9940	0.5138	0.0240	0.5393	2.6598	4.7807	148.9950
SVM-5	Polynomial	3	ISDA	0.9977	0.9982	0.9986	0.9995	0.9017	0.0085	0.2029	0.9314	1.3404	105.9033
SVM-6	**Polynomial**	**4**	**ISDA**	**0.9989**	**0.9997**	**0.9998**	**0.9999**	**0.9532**	**0.0058**	**0.0807**	**0.3594**	**0.4548**	**73.0778**

Model	Training Function	Layer Number	Neuron Numbers	Activation Function	ε_{dp}	$T_{p,o}$	CC	WC	COP	ε_{dp} (-)	$T_{p,o}$ (°C)	CC (W)	WC (g/h)	COP (-)
MLP-1	trainlm	1	10	tansig	0.9974	0.9954	0.9970	0.9969	0.9929	0.0091	0.3208	1.3826	3.4478	28.4366
MLP-2	trainlm	1	20	tansig	0.9993	0.9987	0.9995	0.9997	0.9963	0.0046	0.1687	0.5797	1.0976	20.6534
MLP-3	trainlm	2	10/10	tansig/tansig	0.9993	0.9967	0.9995	0.9990	0.9981	0.0047	0.2726	0.5572	1.9333	14.7184
MLP-4	**trainlm**	**2**	**20/20**	**tansig/tansig**	**0.9999**	**0.9998**	**0.9999**	**0.9996**	**0.9999**	**0.0009**	**0.0703**	**0.2648**	**1.2118**	**3.8063**
MLP-5	trainbfg	1	10	tansig	0.9221	0.9893	0.7754	0.8802	0.4248	0.0494	0.4888	11.9604	21.3792	256.2184
MLP-6	trainbfg	1	20	tansig	0.9709	0.9940	0.8231	0.8131	0.4201	0.0301	0.3673	10.6149	26.7027	257.2583
MLP-7	trainbfg	2	10/10	tansig/tansig	0.9328	0.9824	0.7004	0.6035	0.6994	0.0458	0.6269	13.8148	38.8961	185.2321
MLP-8	trainbfg	2	20/20	tansig/tansig	0.9487	0.9956	0.2935	0.7984	0.0573	0.0401	0.3143	21.2128	27.7323	328.0066
MLP-9	trainscg	1	10	tansig	0.9668	0.9477	0.9471	0.9571	0.8427	0.0322	1.0805	5.8018	12.7915	133.9908
MLP-10	trainscg	1	20	tansig	0.9742	0.9335	0.9484	0.9479	0.8986	0.0284	1.2186	5.7346	14.1010	107.5833
MLP-11	trainscg	2	10/10	tansig/tansig	0.9343	0.9177	0.9207	0.9503	0.8808	0.0453	1.3559	7.1076	13.7633	116.6225
MLP-12	trainscg	2	20/20	tansig/tansig	0.9529	0.9278	0.9144	0.9585	0.7935	0.0384	1.2698	7.3823	12.5856	153.5190
MLP-13	trainoss	1	10	tansig	0.9043	0.8825	0.9307	0.9298	0.9081	0.0547	1.6200	6.6418	16.3627	102.4193
MLP-14	trainoss	1	20	tansig	0.9627	0.9039	0.9211	0.9449	0.8639	0.0342	1.4652	7.0910	14.5045	124.6442
MLP-15	trainoss	2	10/10	tansig/tansig	0.9165	0.8885	0.9119	0.9251	0.8604	0.0511	1.5779	7.3140	16.9082	126.2148
MLP-16	trainoss	2	20/20	tansig/tansig	0.9236	0.9110	0.9261	0.9498	0.8632	0.0489	1.4101	6.8598	13.8412	124.9539

The performance table emphasizes that the selection of training algorithm, kernel or tree configuration, and network architecture critically affects the predictive success of machine learning models. Among the explored options, LSBoosting for DT, high-degree polynomial kernels for SVM, and deep MLPs trained with trainlm show the most promise. These findings guide the selection of optimal models for deeper analysis, where DT-7, SVM-6, and MLP-4 will be examined further in the following sections.

4.3.2.1. Decision Tree

Among the ten DT models developed in this study, DT-7 emerged as the most successful configuration in predicting the cooler's performance outputs. This model was built using LSBoosting training function, with a maximum of 1000 trees and 500 splits. Additionally, the allsplits was chosen for the activation function during the structuring of DT-7. Figure 4.54a clearly shows that the DT-7 model, a variant of a decision tree developed using LSBoosting with 1000 trees, exhibits strong agreement between the predicted and actual dew-point effectiveness values. The vast majority of the data points fall within the ±5% deviation band, indicating excellent prediction accuracy. This observation is also supported by the relative error (RE) distribution in Figure 4.54b. This distribution shows that 84.33% of the predictions fall within the narrow band of $-1\% < RE < 1\%$, and more than 96% fall within the ±3% error range. Such a compact error distribution demonstrates that the model is not only accurate but also robust across the entire operating range. The almost complete absence of outliers beyond ±5% confirms the model's high predictive ability. In conclusion, the DT-7 model stands out as a highly reliable machine learning tool for predicting dew-point effectiveness in multi-aperture dew-point indirect evaporative coolers.

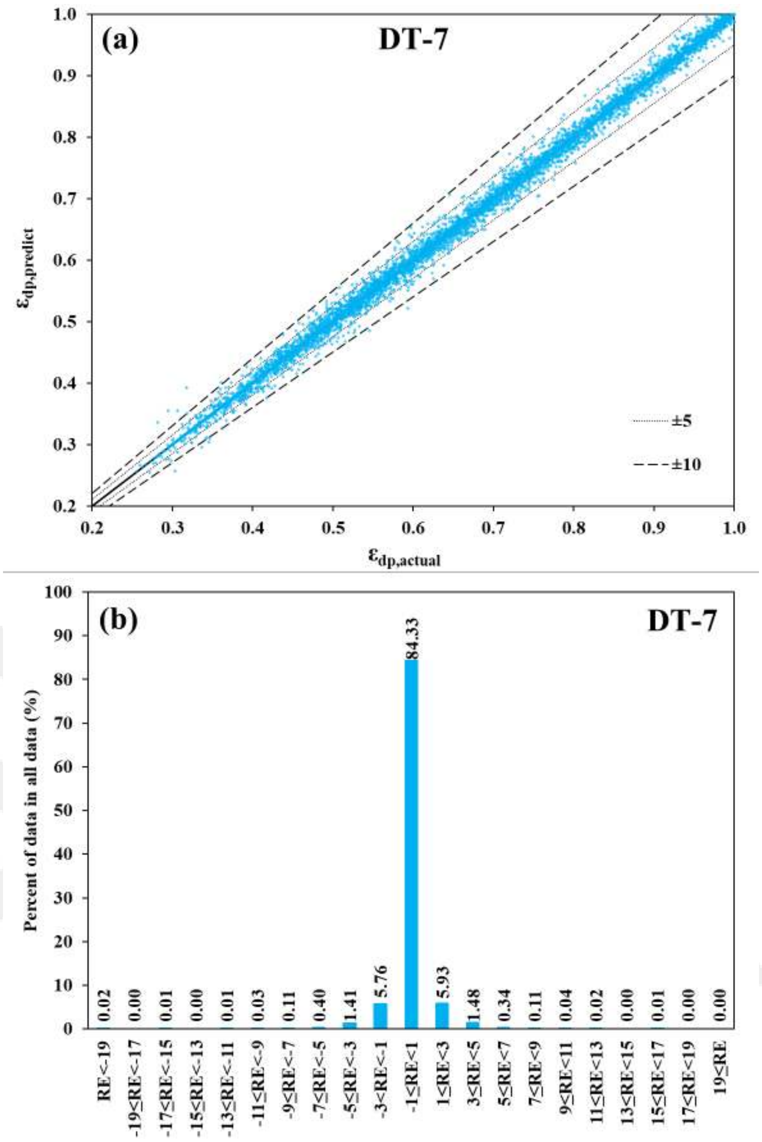

Figure 4.54. Comparison of predicted data from DT-7 model with actual data (a) and error histogram (b) for dew-point effectiveness

Figure 4.55a demonstrates the regression fit between the predicted and actual cooling capacity (CC) values for the DT-7 model. The data points are tightly clustered along the reference line, and most data fall within the ±5% deviation band, indicating strong predictive performance. The goodness of fit suggests that the DT-7 model captures the nonlinearities in the CC behavior with high accuracy. Supporting this, the histogram in Figure 4.55b shows that 78.66% of the predictions lie within the ±1% relative error range. Additionally, over 90% of the data fall within ±3%, while higher error values beyond ±7% are almost negligible. This high concentration of accurate predictions confirms that DT-7 is highly effective at modeling cooling capacity, demonstrating both precision and robustness. The results indicate that this model can be confidently used for estimating cooling capacity in practical applications of the cooler system.

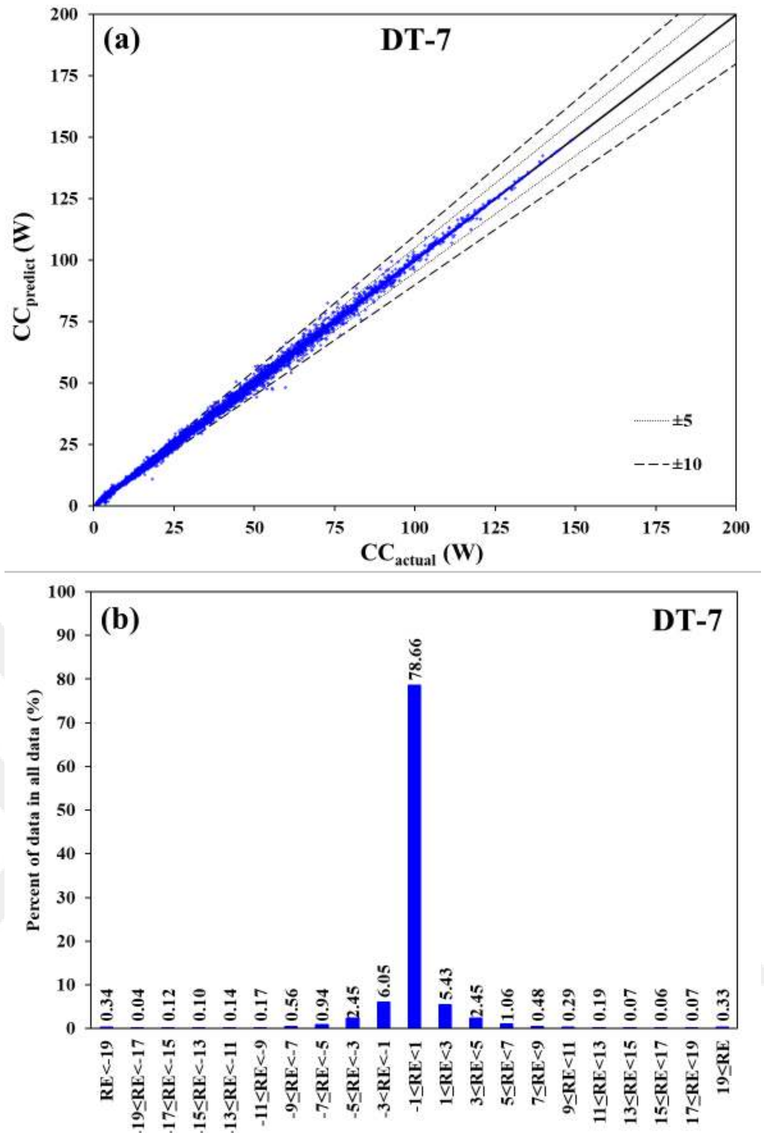

Figure 4.55. Comparison of predicted data from DT-7 model with actual data (a) and error histogram (b) for cooling capacity

The performance of the DT-7 model in predicting water consumption (WC) is depicted in Figure 4.56a, where the predicted values closely align with the actual data along the reference line. A significant portion of the predictions lies well within the ±5% deviation band, highlighting the model's excellent regression accuracy for this parameter. The associated histogram in Figure 4.56b further confirms this performance; 85.01% of the predicted data falls within the ±1% relative error range. When including the ±3% margin, over 95% of all predictions are captured, indicating strong precision and consistency. The presence of outliers is negligible, as the proportion of predictions with errors greater than ±9% is virtually zero. These results demonstrate the DT-7 model's capability to predict water consumption of multi-aperture dew-point evaporative cooler with high reliability. This strong prediction capability makes it particularly suitable for use in both real-time applications and engineering design frameworks where water efficiency is critical.

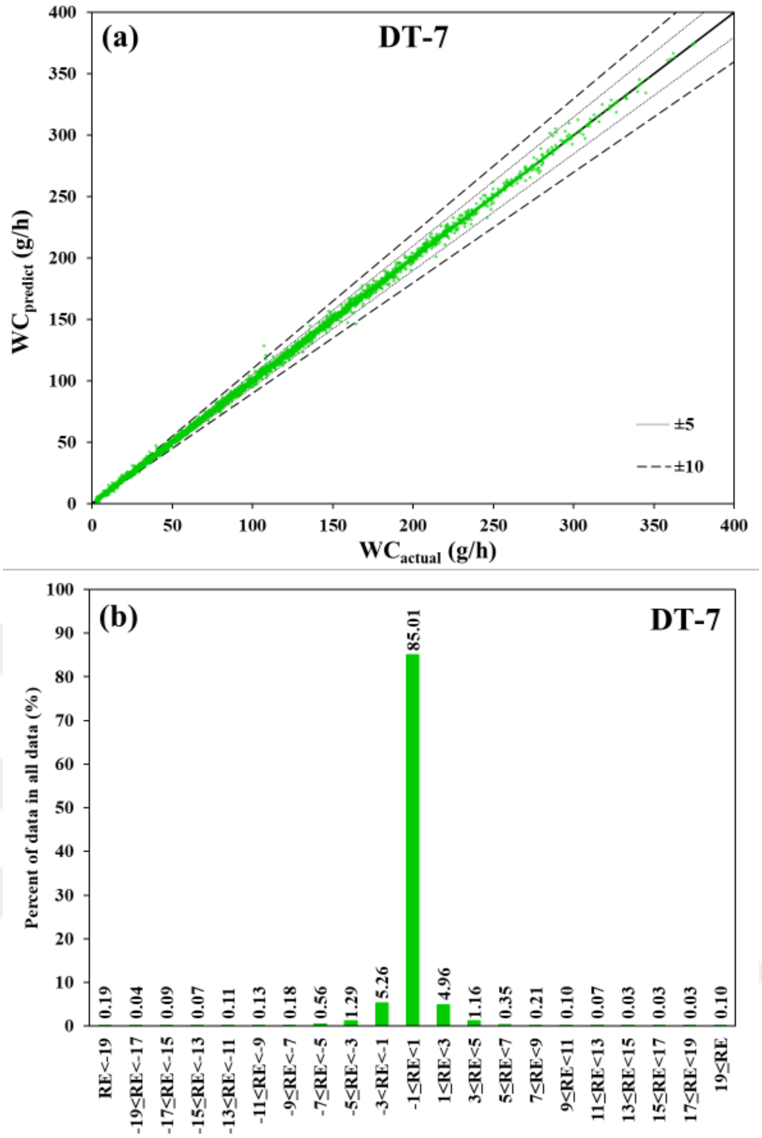

Figure 4.56. Comparison of predicted data from DT-7 model with actual data (a) and error histogram (b) for water consumption

Although a quick glance at the regression plot in Figure 4.57a may suggest that DT-7 yields slightly scattered predictions for the COP, a deeper analysis based on the histogram in Figure 4.57b reveals the true performance of the model. While some points appear dispersed in the high-value region of the plot, most of the predictions cluster tightly around the reference line, especially within the ±5% and ±10% deviation bands. The histogram figure substantiates this with compelling evidence; 73.10% of the predictions fall within the ±1% relative error (RE) range, and almost 85% are within ±5%. These results demonstrate that the DT-7 model exhibits strong overall accuracy in predicting COP. Despite estimating a performance parameter such as COP that is influenced by multiple inputs, extreme errors are limited and the model remains reliable for practical use.

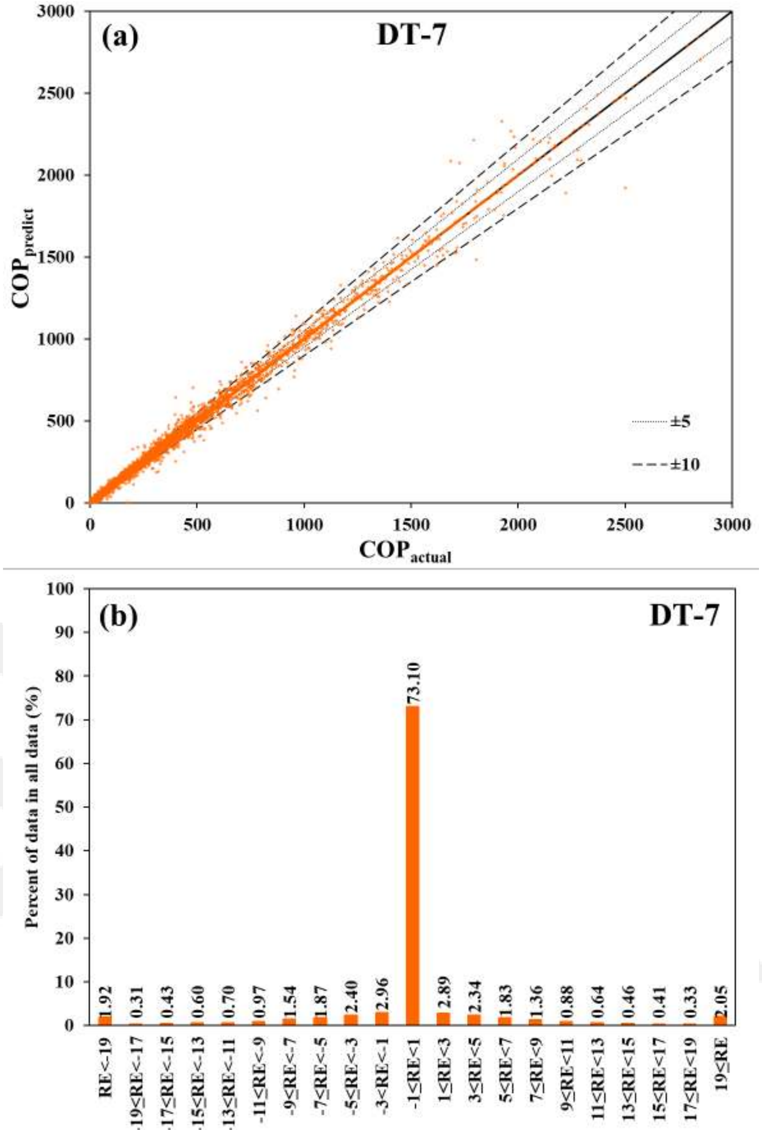

Figure 4.57. Comparison of predicted data from DT-7 model with actual data (a) and error histogram (b) for COP

When evaluating the fifth output parameter, process air outlet temperature, which was included to support fast and practical decision-making by end-users, DT-7 exhibited its strongest prediction performance. As shown in the regression plot in Figure 4.58a, the predicted outlet temperatures align almost perfectly with the actual values, tightly clustering around the reference line. This visual impression is further validated by the histogram in Figure 4.58b, where an outstanding 87.82% of the predictions fall within the ±1% relative error (RE) range, and more than 97% are within ±3%. Such a high level of accuracy indicates that DT-7 can reliably estimate the process air outlet temperature of the multi-aperture Type 2 cooler without the need for any CFD setup, making it highly suitable for real-time applications or rapid prototyping processes.

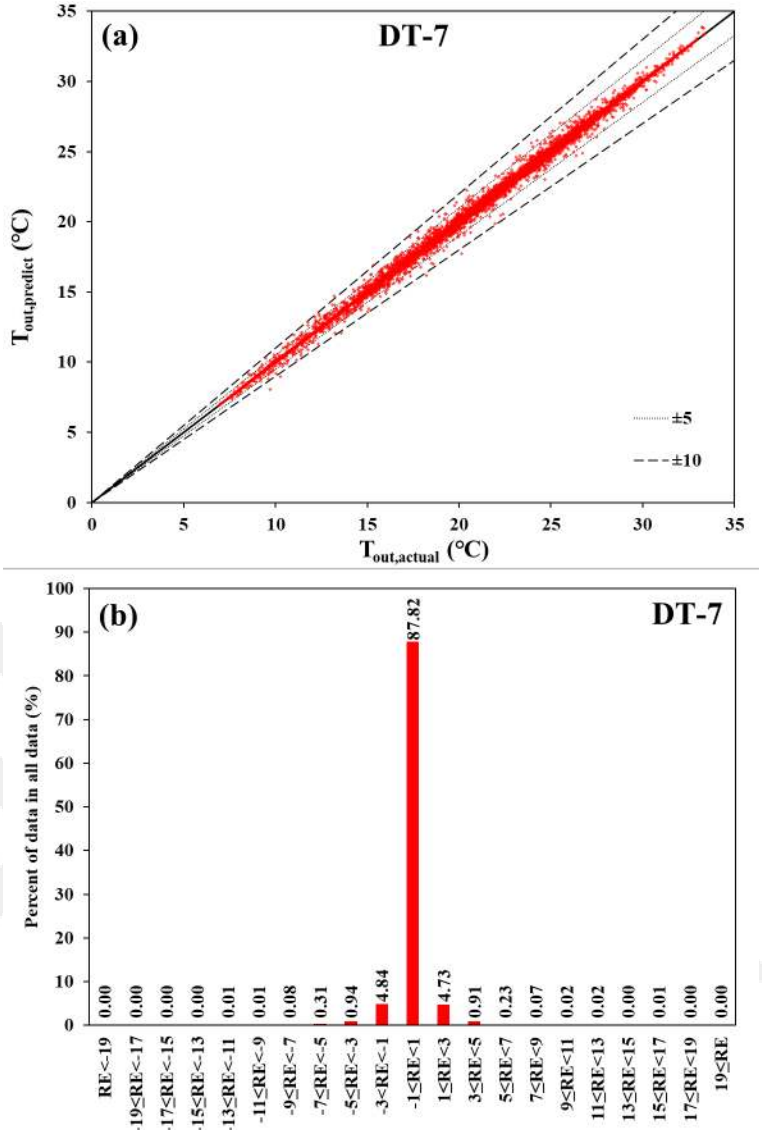

Figure 4.58. Comparison of predicted data from DT-7 model with actual data (a) and error histogram (b) for process air outlet temperature

4.3.2.2. Support Vector Machine

Following the evaluation of decision tree-based models, the focus was shifted to Support Vector Machine (SVM) algorithms to investigate their ability to predict the cooler's performance. A total of six SVM models were constructed using various kernel functions and hyperparameter combinations. The SVM models were particularly explored due to their robustness in handling high-dimensional data and their proven success in regression tasks with limited scatter. Each model was trained using the validated dataset of 17,525 CFD cases, and their performance was assessed across five performance parameters: dew-point effectiveness, cooling capacity, water consumption, COP and, along with the practically valuable output, process air outlet temperature. Among all the tested support vector machine models, SVM-6 proved to be the most accurate.

The performance of the SVM-6 model in estimating the effectiveness (ε_{dp}) of the Type 2 cooler is presented in Figure 4.59. As shown in the scatter plot (Figure 4.59a), the predicted values align closely with the actual data across the entire effectiveness range, with most of points distributed tightly around the reference line. While there is minor dispersion observed at the lower end of the prediction spectrum, the overall clustering within the ±5% and ±10% error bands demonstrate a high level of accuracy.

The reliability of these predictions is further validated by the histogram of relative errors (Figure 4.59b). A dominant portion of the data, 71.12%, falls within the narrow ±1% error range and a total 99.48% lies within the ±3% interval, the model showcases its strong regression capability. These results indicate that SVM-6 can offer a strong alternative to decision tree-based models like DT-7 for predicting the effectiveness of the cooler.

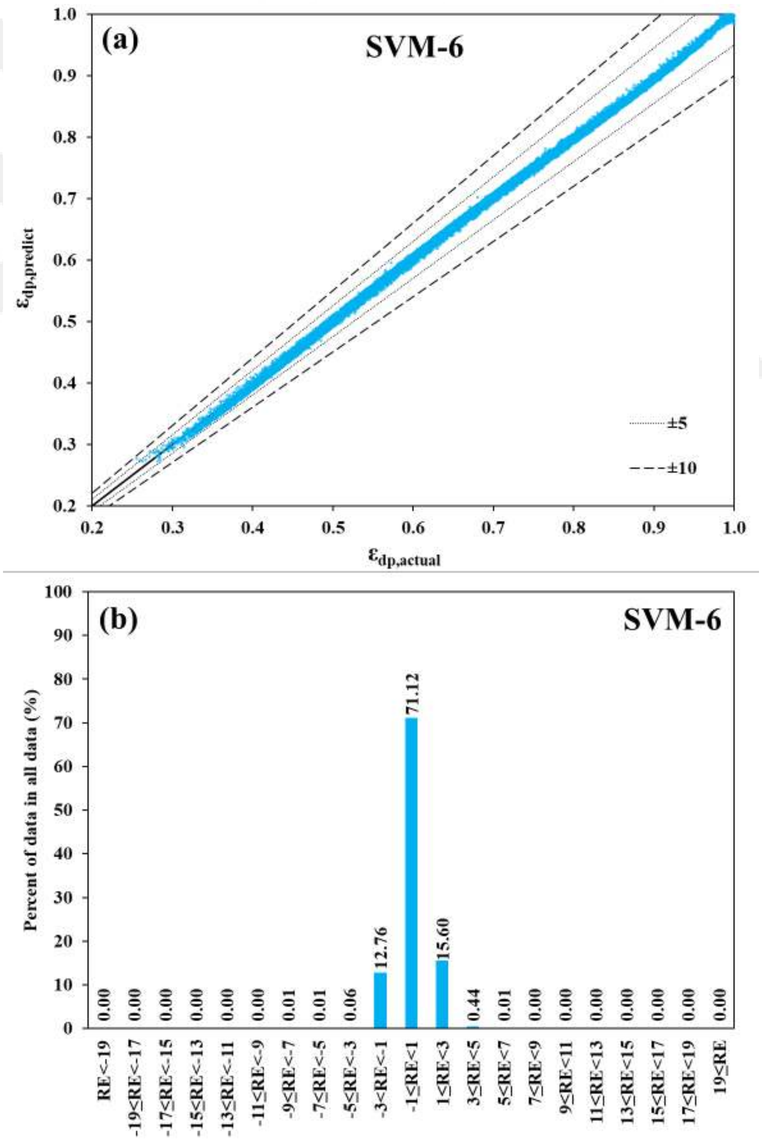

Figure 4.59. Comparison of predicted data from SVM-6 model with actual data (a) and error histogram (b) for dew-point effectiveness

The prediction performance of SVM-6 for cooling capacity (CC) is illustrated in Figure 4.60. The scatter plot (Figure 4.60a) shows that the model provides a highly linear and consistent prediction across the full range of cooling capacities, with most data points densely clustered around the reference line. This dense alignment within the ±5% and ±10% tolerance bands demonstrate the model's strong fitting capability, even for a wide spectrum of values from very low to high-capacity regions.

The histogram of relative errors (Figure 4.60b) further reinforces the accuracy of the model. Approximately 79% of the predictions fall within the ±1% error range, while 7.98% are between -3% and -1%, and 6.18% are between the 1% and 3% interval. These metrics indicate that more than 92% of the data is predicted with less than ±3% error, reflecting the model’s ability to predict well and maintain stability even with complex nonlinear behavior in CC output. SVM-6, therefore, proves to be a reliable alternative for estimating the cooling load performance of the cooler without the computational burden of CFD simulations.

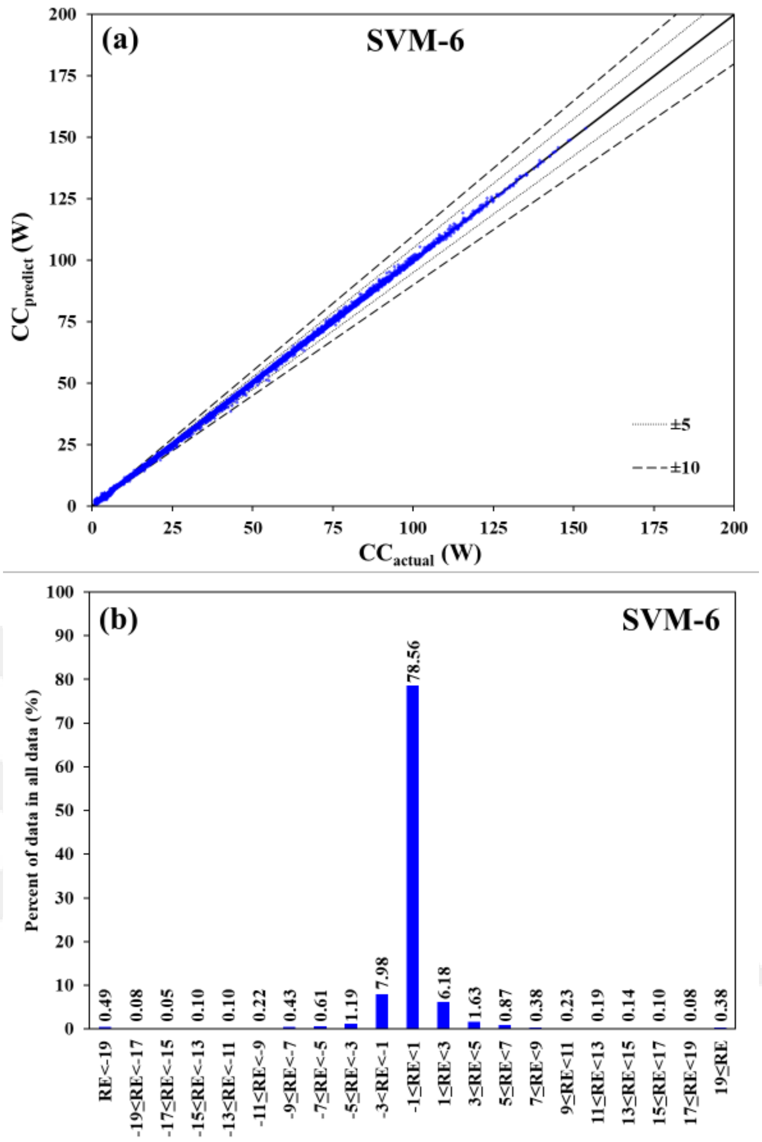

Figure 4.60. Comparison of predicted data from SVM-6 model with actual data (a) and error histogram (b) for cooling capacity

The predictive capability of SVM-6 for the water consumption output is shown in Figure 4.61. The scatter plot, Figure 4.61a, indicates an impressively linear relationship between the predicted and actual WC values, with almost all data points lying close to the ideal reference line. The model's predictions fall comfortably within the ±5% error bound, illustrating a strong fitting accuracy even across a broad range of values.

The histogram (Figure 4.61b) further confirms this performance quantitatively. A significant 88.62% of the predicted WC values fall within the ±1% relative error range, while another 7.75% lie between ±1% and ±3%. This highlights the robustness and high reliability of the model in predicting water use, as only 1.77% of the dataset falls outside the 5% error band. Overall, the SVM-6 model demonstrates a consistent and accurate prediction profile for the WC parameter, making it a solid alternative for practical applications in cooler performance evaluation.

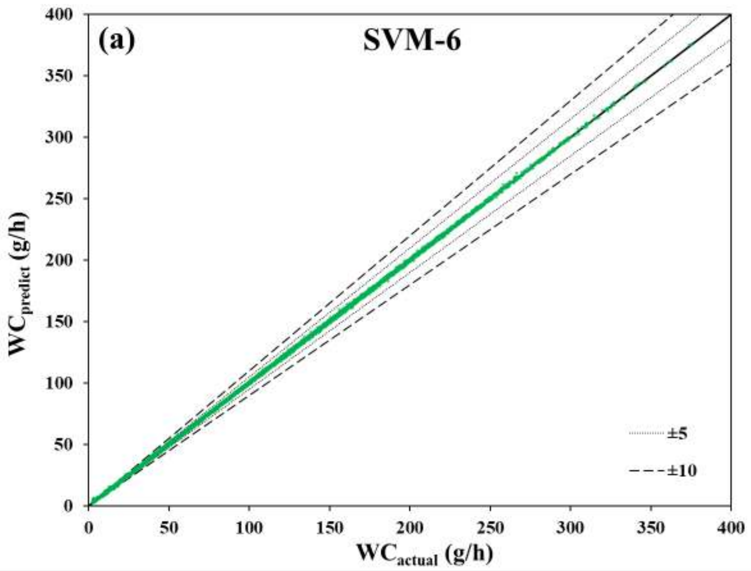

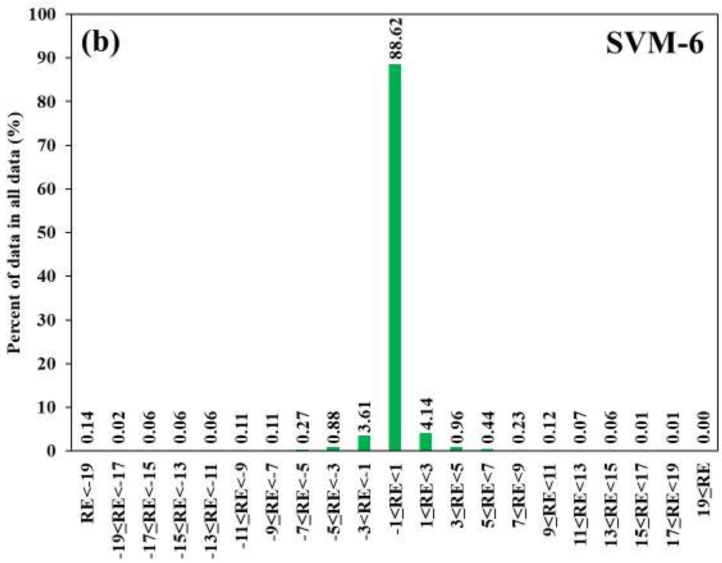

Figure 4.61. Comparison of predicted data from SVM-6 model with actual data (a) and error histogram (b) for water consumption

In terms of COP prediction, SVM-6 showed a poor level of accuracy compared to its performance in other output parameters. As seen in Figure 4.62a, although a dense cluster of points adheres to the ideal reference line, there is a noticeable dispersion, particularly at higher COP values. This scattering beyond the ±10% boundaries indicate increasing difficulty of the model to maintain accuracy as the target values rise, a common challenge in regression problems with skewed or high-magnitude outputs.

This performance drop is further confirmed by the histogram in Figure 4.62b, where only 9.22% of the predicted values fall within the ±1% relative error range, a significantly lower rate compared to the other parameters. Furthermore, the error distribution is widely spread, with substantial portions of the data exceeding ±10% error, and 20.30% even going beyond ±19% relative error. This indicates that SVM-6, although generally less effective, struggles with the dynamic range and nonlinearity of COP, and may require more special kernel functions or hyperparameter tuning to enhance reliability for this specific output. However, caution should still be exercised when using this model to estimate the COP of a multi-perforated cooler, especially at very high and very low COP values.

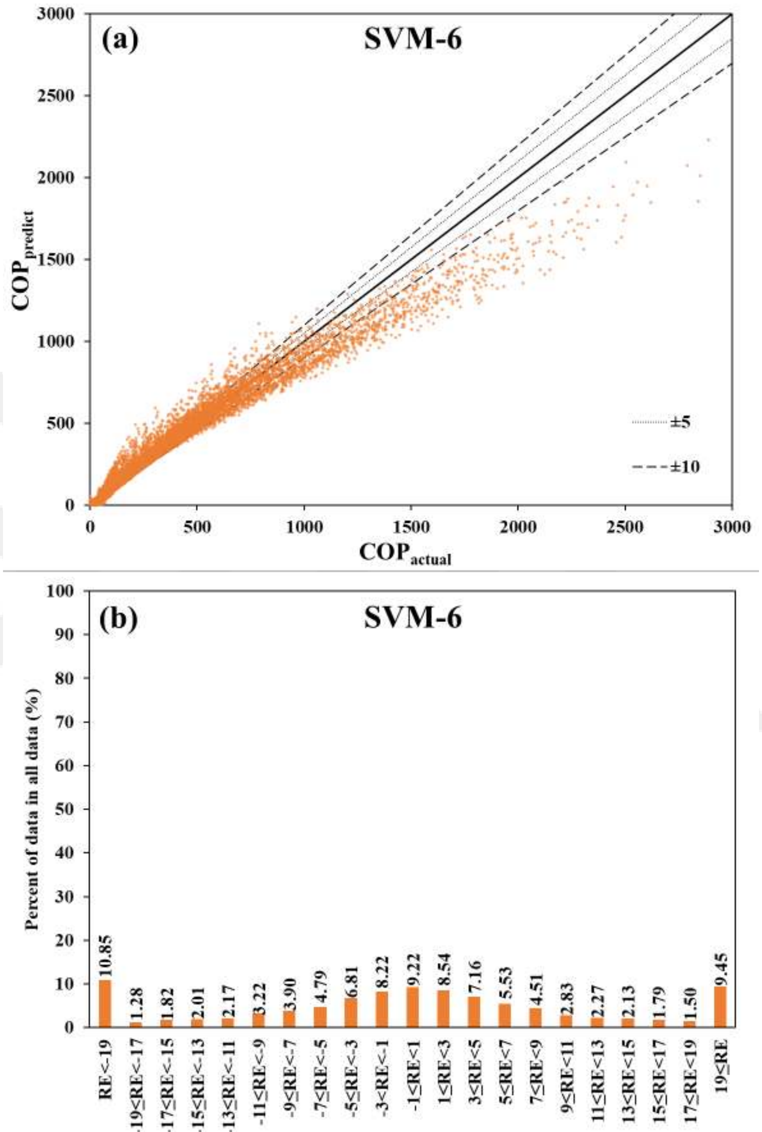

Figure 4.62. Comparison of predicted data from SVM-6 model with actual data (a) and error histogram (b) for COP

When assessing the SVM-6 model's prediction performance for the process air outlet temperature ($T_{p,o}$), results demonstrate exceptional accuracy. As depicted in Figure 4.63a, the predicted values are tightly aligned with the actual values along the ideal reference line, and all the data points fall well within the ±5% bounds, indicating a very consistent and low-error estimation behavior. This high prediction quality is even more clearly affirmed in Figure 4.63b, where 95.90% of all data points fall within the ±1% relative error range, the best performance achieved by SVM-6 across all performance parameters. The almost negligible presence of data outside the ±3% relative error range confirms that the model is highly reliable for estimating $T_{p,o}$, making it particularly suitable for practical, real-time implementations where temperature monitoring is critical but running a full CFD simulation is not feasible.

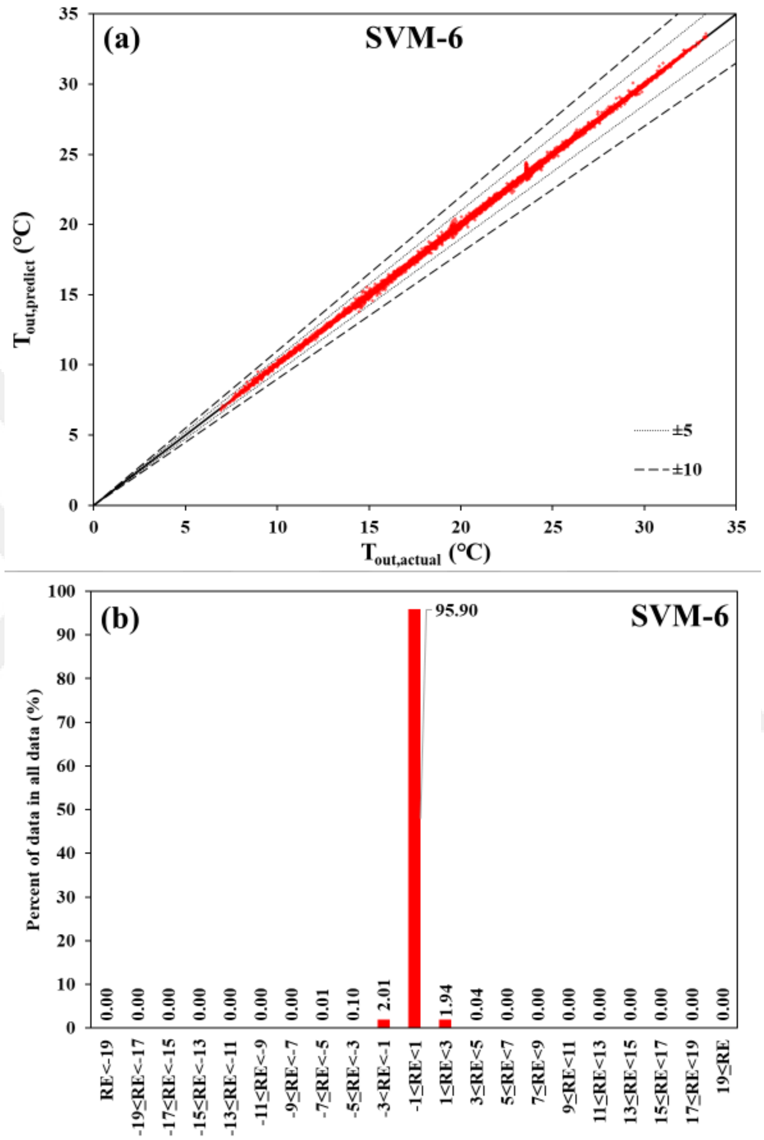

Figure 4.63. Comparison of predicted data from SVM-6 model with actual data (a) and error histogram (b) for process air outlet temperature

4.3.2.3. Multilayer Perceptron

Following the evaluation of decision tree and support vector machine models, the final stage of machine learning-based prediction in this study involved the application of multilayer perceptron (MLP) neural networks. MLP is a class of feedforward artificial neural networks that consists of at least one hidden layer and is capable of modeling complex, nonlinear relationships between input and output variables. Given its adaptability and strong approximation capabilities, MLP was considered a promising candidate for capturing the intricate thermofluidic behaviors of the multi-aperture cooler under a wide range of operating conditions. A total of 16 MLP models were constructed by systematically varying the training algorithms, activation functions, and network architectures, including the number of hidden layers and the number of neurons per layer. These models were trained using the previously prepared dataset of 17,525 valid CFD cases to predict the four key performance parameters along with the outlet temperature ($T_{p,o}$). The evaluation focuses on identifying the most efficient network configuration in terms of accuracy and computational efficiency.

The first performance output of the MLP-4 model, the dew-point effectiveness estimation, demonstrates exceptionally high accuracy. As seen in Figure 4.64a, the model output is almost perfectly clustered on the reference line. The ±5% deviation limits were never exceeded, demonstrating systematic and low-variance learning. Supporting this assessment, the histogram plot (Figure 4.64b) reveals that 99.99% of the results fall within the absolute error range of -1%<RE<1%. This demonstrates the MLP-4 model's exceptional performance not only in terms of regression accuracy but also in terms of statistical consistency. Therefore, the MLP-4 model stands out as one of the most successful models tested to date in estimating a sensitive parameter such as dew-point effectiveness (ε_{dp}), in terms of both distribution and error analysis. This success demonstrates that the MLP-4 model would be highly suitable as a preliminary design tool during the design phase of a multi-aperture cooler, immediately preceding the labor-intensive CFD solutions.

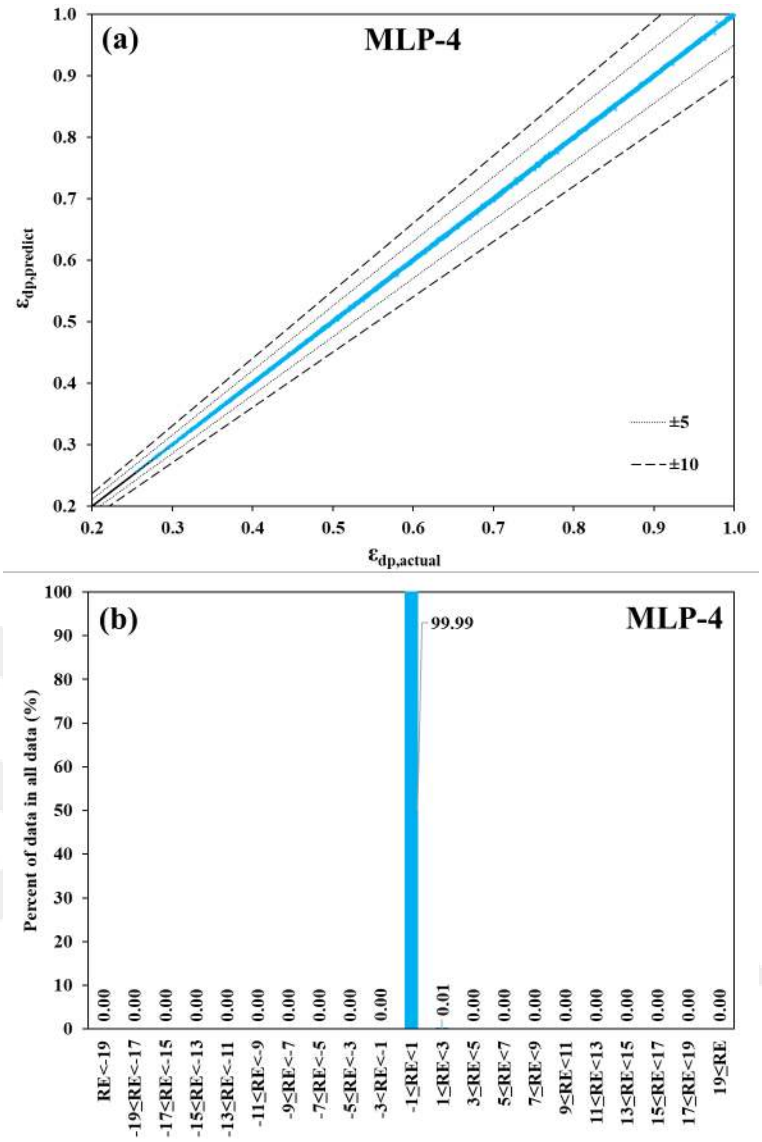

Figure 4.64. Comparison of predicted data from MLP-4 model with actual data (a) and error histogram (b) for dew-point effectiveness

As illustrated in Figure 4.65a, the MLP-4 model performs well in predicting cooling capacity, though its performance is slightly behind that observed for dew-point effectiveness. It can be seen that a very small portion of the data (approximately 1%) scatters outside the 10% dashed line. A clear correlation is exhibited, with 76.59% of the data falling within the ±1% relative error (RE) range (Figure 4.65b). While this rate may be considered moderate, extending the tolerance to ±3% captures nearly 95% of all predictions. This indicates that, despite some deviations, the model maintains overall consistency. Notably, around 5% of the samples lie outside the ±3% RE band, suggesting the need for additional careful examination, especially under extreme operating conditions such as extreme cooler designs. Nevertheless, the MLP-4 model proves sufficiently accurate for early-stage engineering analyses and preliminary design studies.

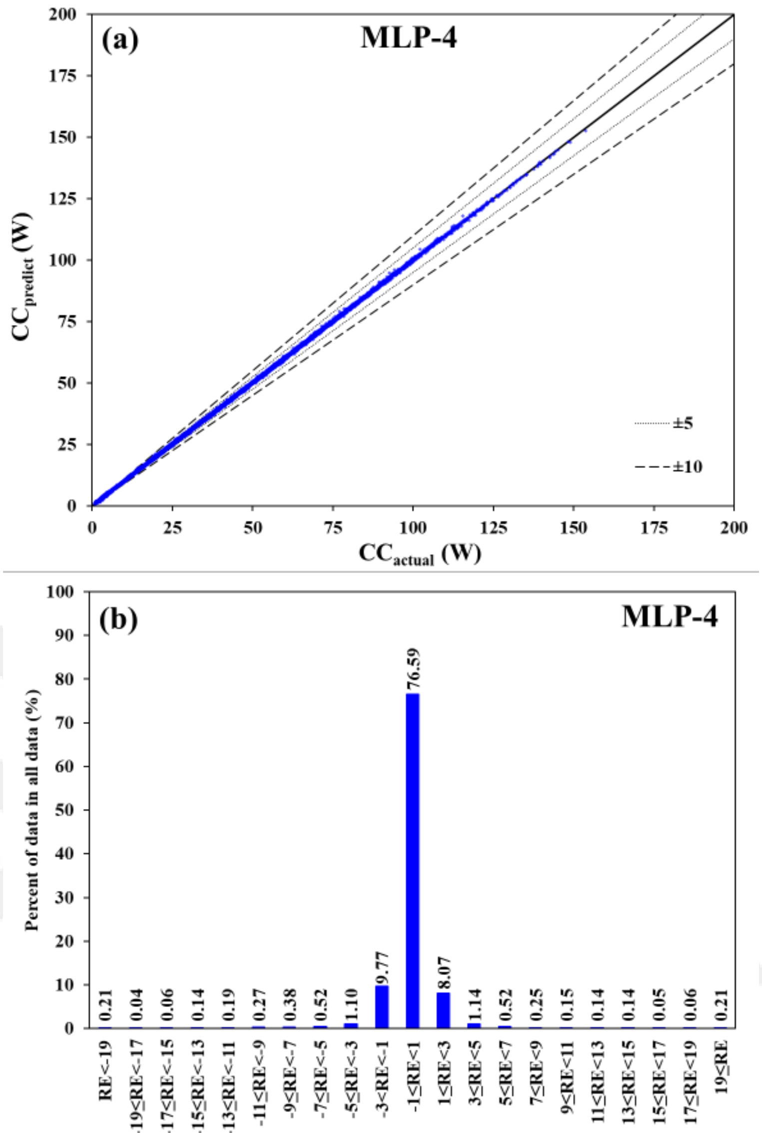

Figure 4.65. Comparison of predicted data from MLP-4 model with actual data (a) and error histogram (b) for cooling capacity

The prediction performance of the MLP-4 model in estimating water consumption (WC) reveals a diverse distribution in terms of accuracy (Figure 4.66). While approximately 51.5% of the predictions fall within the narrow ±1% relative error (RE) range, this performance is relatively modest when compared to alternative models such as DT-7 and SVM-6, which achieved 85% and 89% accuracy within the same error band, respectively. This suggests that, in terms of highly precise estimation, MLP-4 may not match the top-performing models. However, it is important to note that the proportion of data within the broader ±3% RE interval increases significantly, encompassing more than 86% of the total dataset. This expansion indicates that although ultra-precise predictions are less frequent, the model still maintains a high degree of reliability for general applications. Furthermore, only a very limited portion of the predictions (less than 7%) exceed the ±5% RE threshold, and the share of data points with errors greater than ±10% remains below 2%, which underscores the robustness of the model even under more extreme conditions. Taken together, these findings suggest that the MLP-4 model possesses a solid estimation capability for water consumption.

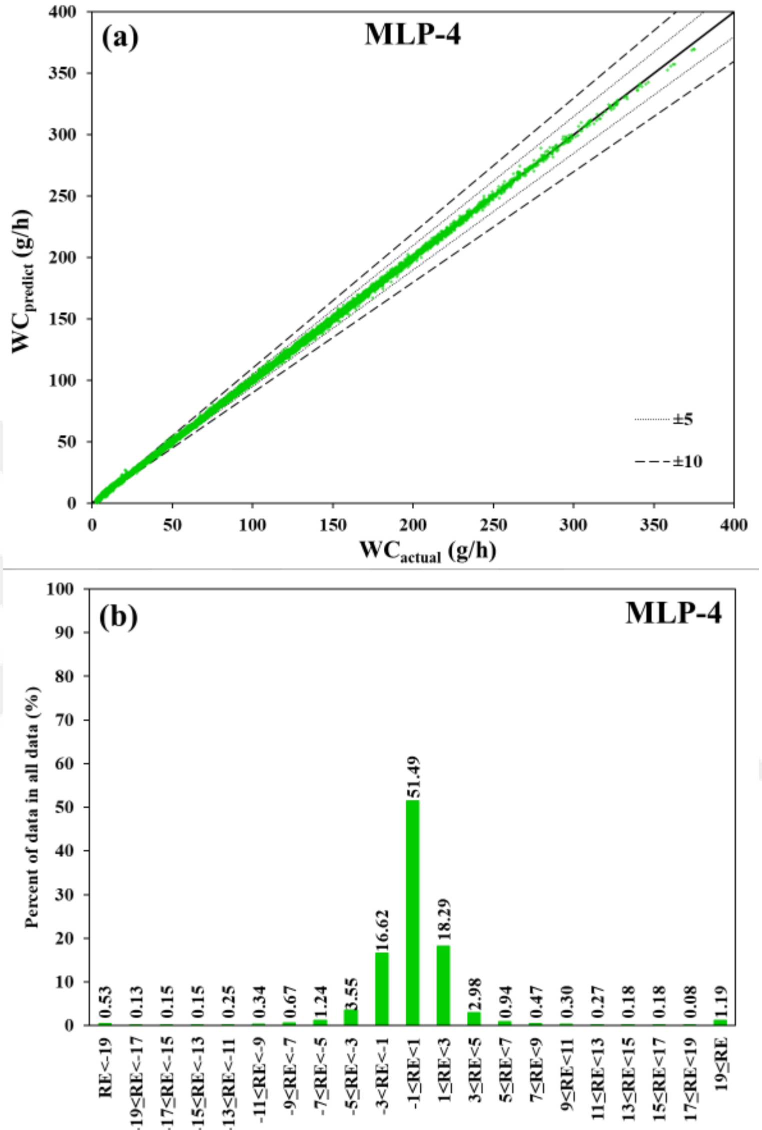

Figure 4.66. Comparison of predicted data from MLP-4 model with actual data (a) and error histogram (b) for water consumption

As observed in the previous models, the cooling coefficient of performance (COP) consistently emerges as the most challenging parameter to predict accurately, and the MLP-4 model is no exception to this trend. Each predictor model examined in this study demonstrates its weakest predictive accuracy when estimating COP values. In this context, the performance of MLP-4 falls between that of the other two machine learning models: it outperforms SVM-6, which could only predict 9.22% of the predicted data within the narrow ±1% relative error range, but remains considerably behind DT-7, which achieved a remarkable 73.1% within the same error margin. As illustrated in Figure 4.67a, the regression fit plot confirms a generally strong correlation between predicted and actual COP values. This observation is supported by Figure 4.67b, where only 45.1% of the data lies within the ±1% RE band. Nevertheless, when the acceptable error range is expanded to ±3%, the coverage improves substantially, reaching approximately 78%. Despite this moderate performance, the model maintains robustness, with only around 12% of the data exceeding the ±5% RE threshold. Importantly, the proportion of inaccurate predictions, defined as errors greater than ±10%, remains minimal. Thus, the model can be considered reliable and valid for use in preliminary design and performance estimation tasks, especially when small trade-offs in predictive precision are acceptable in exchange for modeling efficiency.

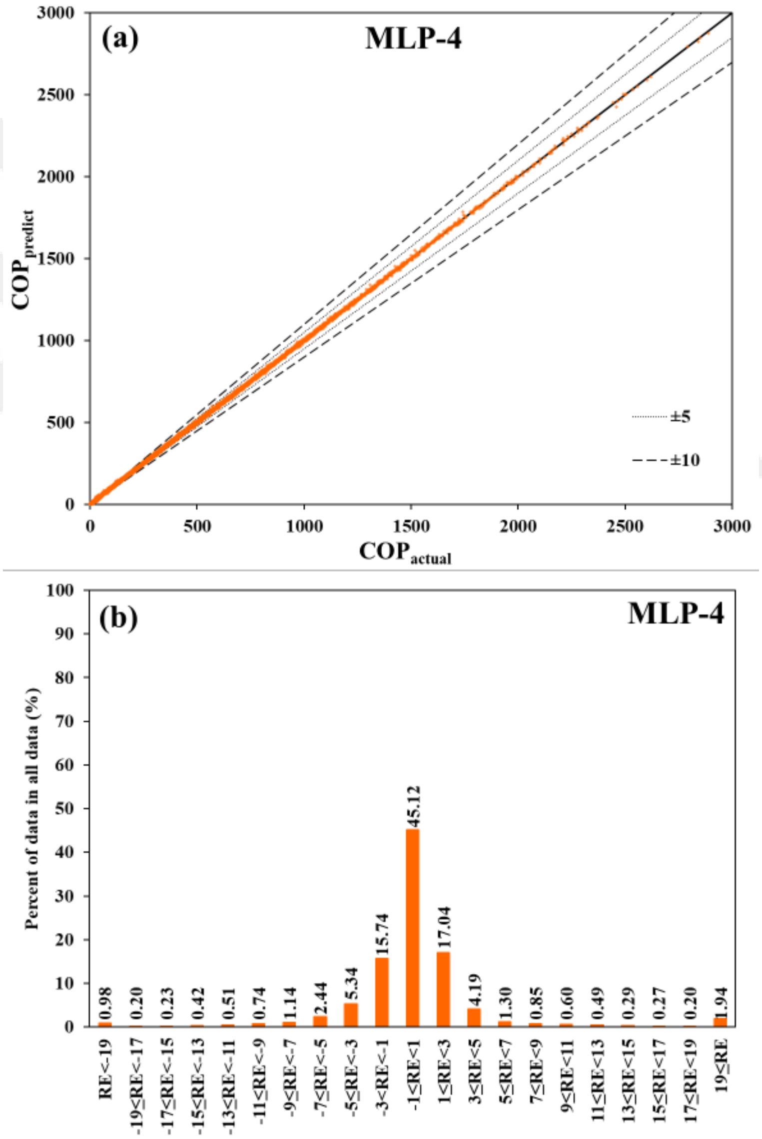

Figure 4.67. Comparison of predicted data from MLP-4 model with actual data (a) and error histogram (b) for COP

The MLP-4 model demonstrates exceptional performance in predicting the outlet air temperature ($T_{p,o}$), a parameter of substantial practical relevance in HVAC and thermal system design. As illustrated in Figure 4.68a, the predicted values exhibit an almost perfect alignment with the actual values. Furthermore, Figure 4.68b reveals that 97.4% of the data falls within the narrow ±1% relative error margin, and more than 99.9% is confined within the ±3% band. Notably, there are virtually no data points exceeding the ±3% relative error threshold and no evidence of extreme prediction errors, further supporting the model's robustness. The absence of significant outliers implies that the model maintains its predictive quality even under less typical operating conditions. While the MLP-4 model demonstrates acceptable performance in predicting cooling capacity (CC), water consumption (WC) and cooling coefficient of performance (COP), it excels in predicting dew-point effectiveness, and this level of precision is mirrored in its $T_{p,o}$ predictions. Given these results, MLP-4 stands out as the most reliable model among those examined in this study for estimating outlet air temperature and is therefore strongly recommended for use in preliminary system design and performance assessment tasks where temperature estimation is a critical factor.

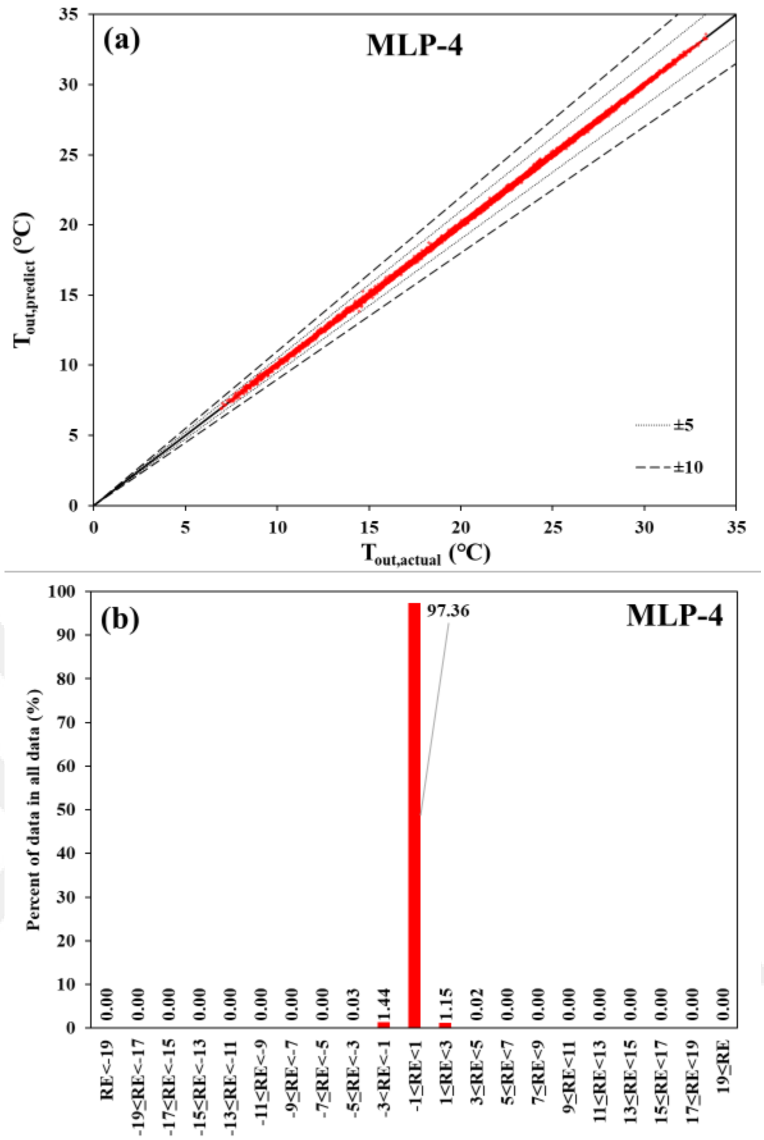

Figure 4.68. Comparison of predicted data from MLP-4 model with actual data (a) and error histogram (b) for process air outlet temperature

4.3.3. Evaluation of All Predictor Models

In this thesis, a comprehensive modeling framework was developed to predict key performance parameters of the investigated system, namely dew-point effectiveness (ε_{dp}), cooling capacity (CC), water consumption (WC), cooling coefficient of performance (COP) and process air outlet temperature ($T_{p,o}$). Both multiple linear regression (MLR) and machine learning (ML) approaches were employed. The models were trained and tested using a dataset generated from CFD simulations, with input variables including process air inlet temperature, humidity and velocity, aperture number, channel length, channel gap and working-to-intake air ratio. These inputs were chosen to represent the full range of geometric and psychrometric factors influencing cooler performance, ensuring that the predictive framework remained robust and applicable under diverse operating conditions. Within the MLR category, 7 models with varying degrees of equations were constructed, while in the ML category, decision tree (DT), support vector machine (SVM), and multi-layer perceptron (MLP) models were developed. For each ML algorithm, several variants were generated by tuning hyperparameters, resulting in a total of 32 models. The performance of each model was assessed using statistical indicators. In addition, the proportion of predictions falling within relative error (RE) thresholds was determined (±1%, ±3%, ±5%, ±10%, and ±20%). Table 4.7 summarizes these results, providing a direct side-by-side comparison of all models across all parameters. This unified evaluation enables a clear identification of the strengths and limitations of each modeling approach.

Table 4.7. The proportion of predictions falling within relative error (RE) thresholds

Parameter	Code	Percentage of data in related relative error range				
		±1% RE	±3% RE	±5% RE	±10% RE	±20% RE
ε_{dp}	MLR-7	25.52	67.77	86.62	97.66	99.63
	DT-7	84.33	96.03	98.92	99.94	99.99
	SVM-6	71.12	99.48	99.98	100.00	100.00
	MLP-4	99.99	100.00	100.00	100.00	100.00
CC	MLR-7	13.26	38.32	58.01	77.46	88.25
	DT-7	78.66	90.14	95.04	98.35	99.37
	SVM-6	78.56	92.72	95.54	98.11	99.20
	MLP-4	76.59	94.44	96.68	98.58	99.63
WC	MLR-7	19.34	51.06	67.43	81.79	90.36
	DT-7	85.01	95.23	97.68	99.12	99.77
	SVM-6	88.62	96.38	98.22	99.42	99.87
	MLP-4	51.49	86.41	92.94	96.62	98.41
COP	MLR-7	2.31	6.84	11.36	22.92	42.78
	DT-7	73.10	78.95	83.69	91.30	96.32
	SVM-6	9.22	25.98	39.95	61.91	80.81
	MLP-4	45.12	77.90	87.44	93.95	97.31
$T_{p,o}$	MLR-7	38.34	80.30	91.83	98.78	99.97
	DT-7	87.82	97.39	99.24	99.95	100.00
	SVM-6	95.90	99.85	99.99	100.00	100.00
	MLP-4	97.36	99.95	100.00	100.00	100.00

The comparative analysis in Table 4.7 highlights several key trends across the evaluated models:

I. Dew-point effectiveness (ε_{dp})

- All ML models demonstrate very high accuracy, with MLP-4 achieving a perfect score (100%) across all error bands, and DT-7 and SVM-6 surpassing 98% within the ±5% range.
- MLR-7 performs significantly worse (25.5% within ±1%), indicating that linear methods are inadequate for capturing the non-linear patterns in dew-point effectiveness prediction.

Recommendation: For ε_{dp} prediction, MLP-4 is the best choice, followed closely by SVM-6 and DT-7.

II. Cooling capacity (CC)

- DT-7 and SVM-6 offer the highest proportion of accurate predictions, both exceeding 78%, within 1% RE.
- MLP-4 is close behind, with a notable 76.6% within the ±1% range, though its ±3% accuracy (94.4%) is slightly higher than SVM-6's (92.7%).

Recommendation: For CC prediction, SVM-6 is preferred for maximum accuracy, but MLP-4 provides comparable reliability.

III. Water consumption (WC)

- SVM-6 again leads with 88.6% within ±1% and 98.2% within ±5%, with DT-7 performing nearly as well.
- MLP-4 shows considerably lower ±1% accuracy (51.5%), although 92.9% of predictions fall within ±5%.

Recommendation: SVM-6 and DT-7 are the best options for WC estimation; MLP-4 should be used cautiously, especially in extreme operational conditions.

IV. Cooling coefficient of performance (COP)

- This parameter is the most difficult to predict across all models. DT-7 leads with 73.1% in ±1%, while SVM-6 struggles (only 9.2% in ±1%).
- MLP-4 provides a balanced middle ground (45.1% in ±1% and 87.4% in ±5%), making it more dependable than SVM-6 but less precise than DT-7 in ±1% and ±3%.

Recommendation: DT-7 is the primary choice for COP, with MLP-4 as a secondary option where a trade-off between complexity and accuracy is acceptable.

V. Process air outlet temperature ($T_{p,o}$)

- All ML models perform excellently, with MLP-4 and DT-7 exceeding 97% in ±1% and achieving near-perfect scores at higher bands.
- MLR-7 again performs significantly worse (38.3% in ±1%).

Recommendation: MLP-4 is the top recommendation for $T_{p,o}$, with DT-7 as a strong alternative.

Overall:

- ✓ MLP-4 is the most versatile model, offering top-tier accuracy in ε_{dp} and $T_{p,o}$ predictions while also performing well in CC and COP.
- ✓ SVM-6 is ideal for WC and CC estimations, whereas DT-7 is best suited for COP.
- ✓ MLR-based models generally perform poorly and are not recommended as the primary choice for nonlinear parameter estimation. However, they may be considered when machine learning models are unavailable, given their practicality and ease of use. While their performance in estimating cooling capacity and water consumption is moderate, their accuracy in dew-point effectiveness and process outlet air temperature predictions is quite high.

5. CONCLUSION

This thesis presented a comprehensive, multi-phase investigation into the performance, optimization and predictive modeling of dew-point indirect evaporative coolers. By integrating CFD analysis, geometric optimization and machine learning, the study established a unified framework that improves the understanding of heat and mass transfer processes. This framework also enables fast and reliable prediction of cooler performance under different climatic and operational conditions.

5.1. General Summary and Key Findings

The research was conducted in three distinct yet interconnected phases, each building upon the results gained from the previous one.

❖ *Phase 1: CFD-Based Comparative Performance Analysis*

The first phase focused on a comprehensive CFD-based evaluation of five distinct cooler configurations (Type 0 to Type 4), representing different structural complexities and airflow arrangements. Each configuration was modeled and analyzed under systematically varied psychrometric and operational conditions. The independent input parameters included process air inlet temperature ($T_{p,i}$), humidity ratio ($\omega_{p,i}$), velocity ($v_{p,i}$), and working-to-intake air ratio (β).

The corresponding performance metrics evaluated were dew-point effectiveness (ε_{dp}), cooling capacity per unit area (CC_a), water consumption per cooling capacity (WC_c) and cooling coefficient of performance (COP), along with process outlet temperature ($T_{p,o}$) as an additional practical measure. The findings revealed that airflow structure and aperture configuration play dominant roles in determining overall system performance. While single-aperture designs such as Type 1 and Type 3 demonstrated stable but limited cooling due to localized evaporation zones, the multi-aperture Type 2 configuration achieved a more uniform distribution of the evaporative surface, leading to higher dew-point effectiveness and energy efficiency. Type 2 also maintained moderate water consumption despite enhanced cooling, establishing it as the most balanced design among all configurations.

Psychrometric analyses provided novel insight by visualizing actual CFD data on psychrometric charts, a methodology rarely found in existing literature. These analyses confirmed that, in Type 2, the process air outlet approached the dew-point temperature more closely than in conventional IECs, demonstrating the potential for achieving sub-wet-bulb cooling. Furthermore, pressure and flow field analyses revealed how multi-aperture channels distribute mass and momentum, minimizing stagnant zones and promoting continuous evaporation.

❖ *Phase 2: Geometric Optimization of the Type 2 Cooler*

Building upon the superior performance of the Type 2 configuration, the second phase was dedicated to its systematic geometric optimization. Five parameters were selected for variation: channel length (L), channel gap (h), aperture number (apN), aperture diameter (apD) and working-to-intake air ratio (β). These parameters were chosen based on their direct influence on heat transfer surface area, air velocity distribution and evaporation dynamics.

A total of 4,200 CFD simulations were performed, and after filtering out physically invalid reverse flow conditions, 2,225 valid datasets were analyzed. Using the desirability function method, a multi-objective optimization framework was established to balance competing performance indicators. Five optimization scenarios were defined to reflect different design priorities:

I. Equal weighting of all performance metrics (Scenario 0)
II. Minimization of outlet air temperature (Scenario 1)
III. Maximization of cooling capacity (Scenario 2)
IV. Minimization of water consumption (Scenario 3)
V. Maximization of cooling coefficient of performance (Scenario 4)

The optimization results revealed that no single geometry can satisfy all objectives simultaneously, emphasizing nature trade-offs in evaporative cooler design. For example, increasing the channel length or reducing the gap improved cooling effectiveness but at the cost of higher pressure drop and lower COP. Similarly, increasing the aperture diameter enhanced air mixing but raised water consumption. This phase concluded that the optimal geometry must be selected according to the intended application, whether the priority is maximizing thermal performance, minimizing resource use or achieving the best energy efficiency balance.

❖ *Phase 3: Predictive Modeling Using MLR and Machine Learning*

In the final phase, the study transitioned from CFD-based simulation to data-driven predictive modeling, aiming to strongly reduce computational cost while maintaining CFD-level accuracy. A total of 20,480 CFD simulations were performed, from which 17,525 valid cases were extracted after eliminating reverse flow conditions. Two main modeling approaches were explored: Multiple Linear Regression (MLR) and Machine Learning (ML).

Seven MLR models were developed using polynomial and cross-term regression structures, including a compact response surface model for practical use. Thirty-two ML models were created using three algorithm families: Decision Tree (DT), Support Vector Machine (SVM) and Multilayer Perceptron (MLP), each with multiple hyperparameter configurations. All models were trained to predict five key outputs: dew-point effectiveness, cooling capacity, water consumption, cooling coefficient of performance and process outlet temperature. Model accuracy was quantified using coefficient of determination (R^2), root mean squared error (RMSE) and relative error (RE) distributions. Results showed that while MLR models provided transparent and easily interpretable equations, the ML-based models achieved significantly higher predictive accuracy.

The DT-7 model (based on LSBoosting with 1,000 trees) and the MLP-4 model (a two-layer neural network trained with the Levenberg–Marquardt algorithm) outperformed all others. Both models yielded R^2 values above 0.99 for dew-point effectiveness and outlet temperature and maintained RE within ±3% for over 95% of all test samples. The predictive framework demonstrated that machine learning can effectively replace CFD for fast and accurate performance estimation, making it possible to integrate these models into design tools, building simulations, or real-time control systems without sacrificing precision.

5.2. Contributions of Thesis

This thesis makes several significant contributions to the fields of thermal system design, sustainable cooling, and computational modeling:

- ✓ Novel CFD-based comparative framework: A complete CFD analysis methodology was established for multiple cooler geometries, including multi-aperture CFD solutions, a first in open literature for dew-point evaporative coolers.
- ✓ Introduction and modeling of a new cooler geometry (Type 4): For the first time, this thesis introduces and numerically investigates the Type 4 configuration, a hybrid geometry combining auxiliary-channel routing with multi-apertures. This configuration has not appeared previously in academic literature, and its inclusion enables a broader comparison of structural design strategies in dew-point evaporative cooling.
- ✓ First identification and detection of reverse-flow: This thesis is the first to demonstrate that multi-aperture dew-point coolers may exhibit reverse flow under certain geometric and operating conditions, that a phenomenon that violates the fundamental cooling mechanism and has not been previously reported. Beyond identifying the problem, the thesis develops a logistic-regression-based detection model capable of predicting whether a given parameter set will lead to reverse flow, providing an essential diagnostic tool for future design studies.
- ✓ Comprehensive geometric optimization: The systematic application of the desirability function method to multi-aperture dew-point coolers provided detailed insight into how structural parameters influence energy efficiency and resource consumption.
- ✓ Creation of an extensive CFD dataset: Over 20,000 high accuracy CFD simulations were conducted, forming one of the largest datasets available for DPIEC systems and enabling future data-driven research.
- ✓ Development of predictive models: The study produced and validated 39 predictive models, combining MLR and ML approaches, which replicate CFD results with high precision and minimal computational load.

- ✓ Practical usability: Simplified regression-based models were formulated to allow designers to estimate cooler performance without the need for CFD or complex software. These equations can be directly embedded into building energy modeling platforms or system control algorithms.
- ✓ Bridging CFD and AI: By integrating physical modeling and data-driven prediction, this work provides a hybrid framework that links detailed thermodynamic simulation with artificial intelligence, setting a precedent for future HVAC design studies.
- ✓ Together, these contributions demonstrate that data-driven methodologies can complement and extend CFD analysis, enabling faster, more adaptive, and more sustainable cooling system design.

5.3. Recommendations and Future Perspectives

Although this study establishes a robust foundation for DPIEC performance modeling, several avenues remain for future exploration:

- o Experimental validation: The optimized geometries and predictive models can be tested under controlled laboratory and real-world conditions to verify model accuracy and account for manufacturing tolerances or water distribution effects.
- o Transient simulations: Future studies can incorporate time-dependent effects, such as fluctuating ambient humidity and temperature, to evaluate system response under realistic dynamic conditions.
- o Hybrid system integration: The predictive framework can be expanded to include hybrid cooling systems, combining evaporative cooling with mechanical or desiccant-based processes for broader climate adaptability.
- o Material and surface research: Investigating advanced materials (e.g., hydrophilic coatings, polymer composites, porous surfaces) could improve water distribution, enhance evaporation uniformity, and extend operational durability.
- o Exploration of alternative geometries: Beyond the optimized multi-aperture configuration, future studies can explore novel channel geometries, such as triangular, circular or finned passages, to enhance internal flow mixing and heat transfer rates. Incorporating roughened or fin-embedded surfaces may further increase the effective surface area and evaporation, potentially improving the already superior performance of the Type 2 design. Comparative evaluations among such modified geometries could reveal additional pathways to optimize performance without significantly increasing complexity or pressure loss.
- o AI-driven control and optimization: Incorporating ML models into real-time control strategies can allow immediate optimization of airflow, water flow and energy use, improving system intelligence and adaptability.

- Lifecycle and environmental analysis: Coupling performance prediction with environmental metrics such as water footprint, embodied energy and carbon savings could strengthen the case for adopting dew-point evaporative coolers in sustainable building design.

5.4. Closing Remarks

In conclusion, this thesis demonstrates that the integration of CFD analysis, optimization and machine learning provides a powerful, multi-dimensional approach to designing next generation dew-point indirect evaporative coolers. By bridging the gap between high-fidelity physical modeling and rapid predictive tools, the developed framework not only deepens the understanding of fundamental mechanisms but also enables practical, energy-efficient and scalable applications for sustainable cooling technologies.

The methodologies and findings presented in this thesis have the potential to serve as a reference framework for future research in evaporative cooling, hybrid HVAC systems and data-driven thermal modeling, ultimately contributing to a more sustainable and energy-efficient future.

REFERENCES

Agresti, A., Kateri, M., 2011. Categorical data analysis, International encyclopedia of statistical science. Springer, pp. 206-208.

Akhlaghi, Y.G., Aslansefat, K., Zhao, X., Sadati, S., Badiei, A., Xiao, X., Shittu, S., Fan, Y., Ma, X., 2021. Hourly performance forecast of a dew point cooler using explainable Artificial Intelligence and evolutionary optimisations by 2050. Applied Energy, 281: 116062.

Akhlaghi, Y.G., Badiei, A., Zhao, X., Aslansefat, K., Xiao, X., Shittu, S., Ma, X., 2020. A constraint multi-objective evolutionary optimization of a state-of-the-art dew point cooler using digital twins. Energy Conversion and Management, 211: 112772.

Akhlaghi, Y.G., Ma, X., Zhao, X., Shittu, S., Li, J., 2019. A statistical model for dew point air cooler based on the multiple polynomial regression approach. Energy, 181: 868-881.

Alam, M.S., Zubir, M.N.B.M., Muhamad, M.R.B., Md, S.N.K., Öztop, H.F., Abdullah, S., Shaikh, K., 2024. A technological review of dew point evaporative cooling: experimental, analytical, numerical and optimization perspectives. Journal of Building Engineering: 109544.

Ali, M., Ahmad, W., Sheikh, N.A., Ali, H., Kousar, R., Rashid, T.u., 2021. Performance enhancement of a cross flow dew point indirect evaporative cooler with circular finned channel geometry. Journal of Building Engineering, 35: 101980.

Anisimov, S., Pandelidis, D., 2014. Numerical study of the Maisotsenko cycle heat and mass exchanger. International Journal of Heat and Mass Transfer, 75: 75-96.

Anisimov, S., Pandelidis, D., Danielewicz, J., 2014. Numerical analysis of selected evaporative exchangers with the Maisotsenko cycle. Energy Conversion and Management, 88: 426-441.

Asfahan, H.M., Sajjad, U., Sultan, M., Hussain, I., Hamid, K., Ali, M., Wang, C.-C., Shamshiri, R.R., Khan, M.U., 2021. Artificial Intelligence for the Prediction of the Thermal Performance of Evaporative Cooling Systems. Energies, 14(13): 3946.

Baakeem, S.S., Orfi, J., Mohamad, A.A., 2021. Investigations of geometrical and operational aspects of a dew-point air-cooling system (M-cycle). Journal of Building Engineering, 36: 102117.

Badiei, A., Akhlaghi, Y.G., Zhao, X., Li, J., Yi, F., Wang, Z., 2020. Can whole building energy models outperform numerical models, when forecasting performance of indirect evaporative cooling systems? Energy Conversion and Management, 213: 112886.

Bom, G.J., 1999. Evaporative air-conditioning: applications for environmentally friendly cooling. World Bank Publications.

Boudjabi, A.F., Maalouf, C., Moussa, T., Abada, D., Rouag, D., Lachi, M., Polidori, G., 2021. Analysis and multi-response optimization of two dew point cooler configurations using the desirability function approach. Energy Reports, 7: 5289-5304.

Bruno, F., 2011. On-site experimental testing of a novel dew point evaporative cooler. Energy and Buildings, 43(12): 3475-3483.

Büyükalaca, O., Kılıç, H.M., Olmuş, U., Güzelel, Y.E., Çerçi, K.N., 2023. Numerical investigation and ANN modeling of performance for hexagonal boron Nitride-water nanofluid PVT collectors. Thermal Science and Engineering Progress, 43.

Caliskan, H., Hepbasli, A., Dincer, I., Maisotsenko, V., 2011. Thermodynamic performance assessment of a novel air cooling cycle: Maisotsenko cycle. International Journal of Refrigeration, 34(4): 980-990.

Caruana, R., De Antonellis, S., Marocco, L., Guilizzoni, M., 2023. Modeling of Indirect Evaporative Cooling Systems: A Review. Fluids, 8(11): 303.

Castillo-González, J., Comino, F., Navas-Martos, F.J., Ruiz de Adana, M., 2023. Manufacturing and experimental analysis of a dew-point indirect evaporative cooler using fused deposition modelling 3D printing and polymeric materials. Applied Thermal Engineering, 230: 120683.

Chen, Z., Zhao, W.J., Wang, B.C., Huang, L.F., Ding, J.N., Cheng, G.G., Bui, D.T., 2025. A first-of-its-kind two-stage dew-point evaporative cooler with high energy efficiency and compact design. Energy Conversion and Management, 341.

Chu, J., Xu, W., Fu, Y., Huo, H., 2021. Experimental research on the cooling performance of a new regenerative dew point indirect evaporative cooler. Journal of Building Engineering, 43.

Chua, K.J., Chou, S.K., Yang, W., Yan, J., 2013. Achieving better energy-efficient air conditioning–a review of technologies and strategies. Applied energy, 104: 87-104.

Comino, F., Romero-Lara, M.J., Ruiz de Adana, M., 2022. Experimental and numerical study of dew-point indirect evaporative coolers to optimize performance and design. International Journal of Refrigeration, 142: 92-102.

Coolerado, 2025. Coolerado Corporation. http://www.coolerado.com. [Accessed 16.10.2025 2025].

Cuce, P.M., Riffat, S., 2016. A state of the art review of evaporative cooling systems for building applications. Renewable and Sustainable Energy Reviews, 54: 1240-1249.

Cui, X., Chua, K.J., Islam, M.R., Ng, K.C., 2015. Performance evaluation of an indirect pre-cooling evaporative heat exchanger operating in hot and humid climate. Energy Conversion and Management, 102: 140-150.

Cui, X., Islam, M.R., Mohan, B., Chua, K.J., 2016. Developing a performance correlation for counter-flow regenerative indirect evaporative heat exchangers with experimental validation. Applied Thermal Engineering, 108: 774-784.

Cui, Y., Zhu, J., Zoras, S., Liu, L., 2021. Review of the recent advances in dew point evaporative cooling technology: 3E (energy, economic and environmental) assessments. Renewable and Sustainable Energy Reviews, 148: 111345.

Çerçi, K.N., Hürdoğan, E., 2020. Comparative study of multiple linear regression (MLR) and artificial neural network (ANN) techniques to model a solid desiccant wheel. International Communications in Heat and Mass Transfer, 116: 104713.

De Antonellis, S., Joppolo, C.M., Liberati, P., Milani, S., Romano, F., 2017. Modeling and experimental study of an indirect evaporative cooler. Energy and Buildings, 142: 147-157.

Dhamneya, A.K., Rajput, S.P.S., Singh, A., 2018. Thermodynamic performance analysis of direct evaporative cooling system for increased heat and mass transfer area. Ain Shams Engineering Journal, 9(4): 2951-2960.

Dizaji, H.S., Hu, E.J., Chen, L., Pourhedayat, S., 2018. Development and validation of an analytical model for perforated (multi-stage) regenerative M-cycle air cooler. Applied Energy, 228: 2176-2194.

Dizaji, H.S., Hu, E.J., Chen, L., Pourhedayat, S., 2020. Analytical/experimental sensitivity study of key design and operational parameters of perforated Maisotsenko cooler based on novel wet-surface theory. Applied Energy, 262: 114557.

Dizaji, H.S., Pourhedayat, S., Moria, H., Aldawi, F., Anqi, A.E., Alsenani, T.R., 2025. Full optimal geometric exploration of M-cycle indirect evaporative dewpoint cooler using a substantial experiment-oriented AI algorithm. Applied Thermal Engineering, 261.

Duan, Z., Zhan, C., Zhang, X., Mustafa, M., Zhao, X., Alimohammadisagvand, B., Hasan, A., 2012. Indirect evaporative cooling: Past, present and future potentials. Renewable and Sustainable Energy Reviews, 16(9): 6823-6850.

Duan, Z., Zhan, C., Zhao, X., Dong, X., 2016. Experimental study of a counter-flow regenerative evaporative cooler. Building and Environment, 104: 47-58.

Duan, Z., Zhao, X., Li, J., 2017. Design, fabrication and performance evaluation of a compact regenerative evaporative cooler: Towards low energy cooling for buildings. Energy, 140: 506-519.

Duan, Z., Zhao, X., Liu, J., Zhang, Q., 2019. Dynamic simulation of a hybrid dew point evaporative cooler and vapour compression refrigerated system for a building using EnergyPlus. Journal of Building Engineering, 21: 287-301.

Ergun, B., Kavzoglu, T., Colkesen, I., Sahin, C., 2010. Data filtering with support vector machines in geometric camera calibration. Optics Express, 18(3): 1927.

Gao, F., Thu, K., Wang, S., Zhao, F., Lin, J., Wu, K., 2023. Numerical investigation of a novel tubular dew-point evaporative cooler. Applied Thermal Engineering, 223: 120064.

Gupta, A.K., Kashyap, S., Sarkar, J., 2022. Machine learning model of regenerative evaporative cooler for performance prediction based on experimental investigation. International Journal of Refrigeration, 137: 178-187.

Gürük, A.B., Güzelel, Y.E., Olmuş, U., Çerçi, K.N., Büyükalaca, O., 2025. Predicting process and regeneration air conditions in LT3 molecular sieve desiccant wheels using machine learning and regression methods. International Communications in Heat and Mass Transfer, 164: 108811.

Güzelel, Y.E., Olmuş, U., Büyükalaca, O., 2022a. Simulation of a desiccant air-conditioning system integrated with dew-point indirect evaporative cooler for a school building. Applied Thermal Engineering, 217: 119233.

Güzelel, Y.E., Olmuş, U., Büyükalaca, O., 2024. Performance evaluation of different types of indirect evaporative coolers: a CFD-based comparative study. Journal of Building Engineering: 110399.

Güzelel, Y.E., Olmuş, U., Çerçi, K.N., Büyükalaca, O., 2021. Comprehensive modelling of rotary desiccant wheel with different multiple regression and machine learning methods for balanced flow. Applied Thermal Engineering, 199: 117544.

Güzelel, Y.E., Olmuş, U., Çerçi, K.N., Büyükalaca, O., 2022b. New multiple regression and machine learning models of rotary desiccant wheel for unbalanced flow conditions. International Communications in Heat and Mass Transfer, 134: 106006.

Güzelel, Y.E., Olmuş, U., Gürük, A.B., Büyükalaca, O., 2025. Geometric optimization of multi-perforated dew-point indirect evaporative coolers: A multi-objective approach. Energy, 320.

Halasz, B., 1998. A general mathematical model of evaporative cooling devices. Revue générale de thermique, 37(4): 245-255.

Hasan, A., 2010. Indirect evaporative cooling of air to a sub-wet bulb temperature. Applied Thermal Engineering, 30(16): 2460-2468.

Hasan, A., 2012. Going below the wet-bulb temperature by indirect evaporative cooling: Analysis using a modified ε-NTU method. Applied Energy, 89(1): 237-245.

Heidarinejad, G., Bozorgmehr, M., Delfani, S., Esmaeelian, J., 2009. Experimental investigation of two-stage indirect/direct evaporative cooling system in various climatic conditions. Building and Environment, 44(10): 2073-2079.

Hua, B., Sadighi Dizaji, H., Aldawi, F., Loukil, H., Mouldi, A., Damian, M.A.E., 2024. Developing an experiment-based strong machine learning model for performance prediction and full analysis of Maisotsenko dewpoint evaporative air cooler. Energy, 310.

IEA, 2025. World Energy Outlook 2025. Internal Energy Agency.

Jafarian, H., Sayyaadi, H., Torabi, F., 2017a. Modeling and optimization of dew-point evaporative coolers based on a developed GMDH-type neural network. Energy Conversion and Management, 143: 49-65.

Jafarian, H., Sayyaadi, H., Torabi, F., 2017b. A numerical model for a dew-point counter-flow indirect evaporative cooler using a modified boundary condition and considering effects of entrance regions. International Journal of Refrigeration, 84: 36-51.

Jia, L., Liu, J., Wang, C., Cao, X., Zhang, Z., 2019. Study of the thermal performance of a novel dew point evaporative cooler. Applied Thermal Engineering, 160: 114069.

Jradi, M., Riffat, S., 2014. Experimental and numerical investigation of a dew-point cooling system for thermal comfort in buildings. Applied Energy, 132: 524-535.

Kabeel, A.E., Abdelgaied, M., 2016. Numerical and experimental investigation of a novel configuration of indirect evaporative cooler with internal baffles. Energy Conversion and Management, 126: 526-536.

Kashyap, S., Sarkar, J., Kumar, A., 2021. Effect of surface modifications and using hybrid nanofluids on energy-exergy performance of regenerative evaporative cooler. Building and Environment, 189: 107507.

Kassie, T.D., Bizuneh, Y.E., Amsal, A.M., 2025. Experimental investigation of air velocity, water flow rate, and staging of cooling pad on the performance of direct evaporative coolers. International Journal of Air-Conditioning and Refrigeration, 33(1).

Kowalek, P., Loch-Olszewska, H., Szwabiński, J., 2019. Classification of diffusion modes in single-particle tracking data: Feature-based versus deep-learning approach. Physical Review E, 100(3).

Lee, J., Lee, D.-Y., 2013. Experimental study of a counter flow regenerative evaporative cooler with finned channels. International Journal of Heat and Mass Transfer, 65: 173-179.

Li, W.-Y., Li, Y.-C., Zeng, L.-y., Lu, J., 2018. Comparative study of vertical and horizontal indirect evaporative cooling heat recovery exchangers. International Journal of Heat and Mass Transfer, 124: 1245-1261.

Lin, J., Bui, D.T., Wang, R., Chua, K.J., 2018. The counter-flow dew point evaporative cooler: Analyzing its transient and steady-state behavior. Applied Thermal Engineering, 143: 34-47.

Lin, J., Shahzad, M.W., Li, J., Long, J., Li, C., Chua, K.J., 2021a. A robust physics-based model framework of the dew point evaporative cooler: From fundamentals to applications. Energy Conversion and Management, 233: 113925.

Lin, J., Thu, K., Bui, T.D., Wang, R.Z., Ng, K.C., Chua, K.J., 2016. Study on dew point evaporative cooling system with counter-flow configuration. Energy Conversion and Management, 109: 153-165.

Lin, J., Thu, K., Karthik, S., Shahzad, M.W., Wang, R., Chua, K.J., 2021b. Understanding the transient behavior of the dew point evaporative cooler from the first and second law of thermodynamics. Energy Conversion and Management, 244: 114471.

Lin, J., Wang, R., Li, C., Wang, S., Long, J., Chua, K.J., 2020. Towards a thermodynamically favorable dew point evaporative cooler via optimization. Energy Conversion and Management, 203: 112224.

Lin, J., Wang, R.Z., Kumja, M., Bui, T.D., Chua, K.J., 2017. Modelling and experimental investigation of the cross-flow dew point evaporative cooler with and without dehumidification. Applied Thermal Engineering, 121: 1-13.

Liu, X., Jing, C., Li, Y., Lu, S., 2025. Study on performance of perforated dew point indirect : Evaporative coolers. Scientific Reports, 15(1): 939.

Liu, Y., Li, J.M., Yang, X., Zhao, X., 2019. Two-dimensional numerical study of a heat and mass exchanger for a dew-point evaporative cooler. Energy, 168: 975-988.

Loh, W.Y., 2011. Classification and regression trees. WIREs Data Mining and Knowledge Discovery, 1(1): 14-23.

Lv, J., Yi, J., Fu, Y., Liu, H., 2020. Experimental and numerical study of a multi-unit evaporative cooling device in series. Case Studies in Thermal Engineering, 21: 100727.

Mahmood, M.H., Sultan, M., Miyazaki, T., Koyama, S., Maisotsenko, V.S., 2016. Overview of the Maisotsenko cycle – A way towards dew point evaporative cooling. Renewable and Sustainable Energy Reviews, 66: 537-555.

Maisotsenko, V., Gillian, L.E., Heaton, T.L., Gillan, A.D., 2003. Method and plate apparatus for dew point evaporative cooler. Google Patents.

Moore, D.S., McCabe, G.P., Craig, B.A., 2009. Introduction to the Practice of Statistics. WH Freeman New York.

Ndukwu, M.C., Ibeh, M.I., Ugwu, E.C., Igbojionu, D.O., Ahiakwo, A.A., Wu, H., 2022. Evaluating coefficient of performance and rate of moisture loss of some biomass humidifiers materials with a developed simple direct stand-alone evaporative cooling system for farmers. Energy Nexus, 8.

Oh, S.J., Shahzad, M.W., Burhan, M., Chun, W., Kian Jon, C., KumJa, M., Ng, K.C., 2019. Approaches to energy efficiency in air conditioning: A comparative study on purge configurations for indirect evaporative cooling. Energy, 168: 505-515.

Olmuş, U., Güzelel, Y.E., Büyükalaca, O., 2023. Seasonal analysis of a desiccant air-conditioning system supported by water-cooled PV/T units. Energy and Buildings, 291: 113101.

Pacak, A., Worek, W., 2021. Review of Dew Point Evaporative Cooling Technology for Air Conditioning Applications. Applied Sciences, 11(3): 934.

Pakari, A., Ghani, S., 2019a. Comparison of 1D and 3D heat and mass transfer models of a counter flow dew point evaporative cooling system: Numerical and experimental study. International Journal of Refrigeration, 99: 114-125.

Pakari, A., Ghani, S., 2019b. Regression models for performance prediction of counter flow dew point evaporative cooling systems. Energy Conversion and Management, 185: 562-573.

Pandelidis, D., Anisimov, S., 2016. Numerical study and optimization of the cross-flow Maisotsenko cycle indirect evaporative air cooler. International Journal of Heat and Mass Transfer, 103: 1029-1041.

Pandelidis, D., Anisimov, S., Worek, W.M., 2015a. Comparison study of the counter-flow regenerative evaporative heat exchangers with numerical methods. Applied Thermal Engineering, 84: 211-224.

Pandelidis, D., Anisimov, S., Worek, W.M., 2015b. Performance study of counter-flow indirect evaporative air coolers. Energy and Buildings, 109: 53-64.

Pandelidis, D., Cichoń, A., Pacak, A., Anisimov, S., Drąg, P., 2018. Counter-flow indirect evaporative cooler for heat recovery in the temperate climate. Energy, 165: 877-894.

Porumb, B., Ungureşan, P., Tutunaru, L.F., Şerban, A., Bălan, M., 2016. A Review of Indirect Evaporative Cooling Technology. Energy Procedia, 85: 461-471.

Rey Martínez, F.J., Velasco Gómez, E., Herrero Martín, R., Martínez Gutiérrez, J., Varela Diez, F., 2004. Comparative study of two different evaporative systems: an indirect evaporative cooler and a semi-indirect ceramic evaporative cooler. Energy and Buildings, 36(7): 696-708.

Riangvilaikul, B., Kumar, S., 2010a. An experimental study of a novel dew point evaporative cooling system. Energy and Buildings, 42(5): 637-644.

Riangvilaikul, B., Kumar, S., 2010b. Numerical study of a novel dew point evaporative cooling system. Energy and Buildings, 42(11): 2241-2250.

Saman, W.Y., Alizadeh, S., 2001. Modelling and performance analysis of a cross-flow type plate heat exchanger for dehumidification/cooling. Solar Energy, 70(4): 361-372.

Scofield, C., DesChamps, N., 1984. Indirect evaporative cooling using plate type heat exchangers. ASHRAE transactions, 90(1B): 148-153.

Sulaiman, M.A., Saber, H.A., Hasan, H.F., Benim, A.C., 2025. Experimental and numerical investigation of novel dew-point evaporative cooler with shell and tube design. Energy, 317.

Tariq, R., Zhan, C., Zhao, X., Sheikh, N.A., 2018. Numerical study of a regenerative counter flow evaporative cooler using alumina nanoparticles in wet channel. Energy and Buildings, 169: 430-443.

Tulsidasani, T., Sawhney, R., Singh, S., Sodha, M., 1997. Recent research on an indirect evaporative cooler (IEC) part 1: optimization of the COP. International journal of energy research, 21(12): 1099-1108.

Urso, A., Velasco-Gómez, E., Tejero-González, A., Andrés-Chicote, M., Nocera, F., 2024. Experimental study of the optimal design and performance of a mixed-flow dew-point indirect evaporative cooler. Applied Thermal Engineering: 124294.

Velasco Gómez, E., Rey Martínez, F.J., Varela Diez, F., Molina Leyva, M.J., Herrero Martín, R., 2005. Description and experimental results of a semi-indirect ceramic evaporative cooler. International Journal of Refrigeration, 28(5): 654-662.

Wan, Y., Lin, J., Chua, K.J., Ren, C., 2018. A new method for prediction and analysis of heat and mass transfer in the counter-flow dew point evaporative cooler under diverse climatic, operating and geometric conditions. International Journal of Heat and Mass Transfer, 127: 1147-1160.

Wan, Y., Ren, C., Xing, L., 2017. An approach to the analysis of heat and mass transfer characteristics in indirect evaporative cooling with counter flow configurations. International Journal of Heat and Mass Transfer, 108: 1750-1763.

Wan, Y., Xue, T., Huang, Z., Soh, A., Liu, H., Chua, K.J., 2024. Comparative study on performance of counter-flow dew-point indirect evaporative cooling systems via a more realistic and experimentally validated three-dimensional model. Journal of Building Engineering, 82: 108408.

Wang, B.C., Chen, Z., You, G.L., Ding, J.N., Cheng, G.G., Bui, T.D., 2024. Performance assessment of a high-efficiency indirect dew-point evaporative cooler through three-dimensional modeling. Energy, 312.

Watt, J.R., 1963. Evaporative air conditioning. The Industrial Press.

White, F.M., 2011. Fluid Mechanics, 7th ed. McGraw-Hill, NY.

Wu, K., Wang, S., Lin, J., Shao, Y., Gao, F., Chua, K.J., 2024. The enhanced dew-point evaporative cooling with a macro-roughened structure. International Journal of Heat and Mass Transfer, 219: 124898.

Xiao, X., Liu, J., 2024. A state-of-art review of dew point evaporative cooling technology and integrated applications. Renewable and Sustainable Energy Reviews, 191.

Xu, P., Ma, X., Zhao, X., Fancey, K., 2017. Experimental investigation of a super performance dew point air cooler. Applied Energy, 203: 761-777.

Xu, P., Mu, X., Chen, H., Ma, X., Zhao, X., 2024. Experimental and numerical investigation of the temperature and humidity distribution inside the channels for a regenerative indirect evaporative cooler. Applied Thermal Engineering, 236: 121586.

Xuan, Y.M., Xiao, F., Niu, X.F., Huang, X., Wang, S.W., 2012. Research and application of evaporative cooling in China: A review (I) – Research. Renewable and Sustainable Energy Reviews, 16(5): 3535-3546.

Yan, W., Cui, X., Zhao, M., Meng, X., Yang, C., Zhang, Y., Liu, Y., Jin, L., 2024. Multi-objective optimization of dew point indirect evaporative coolers for data centers. Applied Thermal Engineering, 241: 122425.

Yang, H., Ren, C., Cui, P., 2011. Study on Performance Correlations of an Indirect Evaporative Cooler with Condensation from Primary Airflow. HVAC&R Research, 12(3): 519-532.

Zhan, C., Zhao, X., Smith, S., Riffat, S.B., 2011. Numerical study of a M-cycle cross-flow heat exchanger for indirect evaporative cooling. Building and Environment, 46(3): 657-668.

Zhao, X., 2010. Porous materials for direct and indirect evaporative cooling in buildings, Materials for Energy Efficiency and Thermal Comfort in Buildings. pp. 399-426.

Zhao, X., Li, J.M., Riffat, S.B., 2008. Numerical study of a novel counter-flow heat and mass exchanger for dew point evaporative cooling. Applied Thermal Engineering, 28(14): 1942-1951.

Zhao, X., Yang, S., Duan, Z., Riffat, S.B., 2009. Feasibility study of a novel dew point air conditioning system for China building application. Building and Environment, 44(9): 1990-1999.

Zhou, B., Lv, J., Zhu, M., Wang, L., Li, S., Hu, E., 2024. Experiment for the performance of a thin membrane inclined automatic wicking dew-point evaporative cooling device based on simulation results. Energy and Buildings, 308: 114021.

Zhou, B., Lv, J., Zhu, M., Wang, L., Liang, L., Chen, Q., 2023. Simulation study of a thin membrane inclined automatic wicking dew-point evaporative cooling device. Journal of Building Engineering, 72: 106601.

Zhu, G., Chen, W., Zhang, D., Wen, T., 2023. Performance evaluation of counter flow dew-point evaporative cooler with a three-dimensional numerical model. Applied Thermal Engineering, 219: 119483.

Zhu, G., Chow, T.-T., Lee, C.K., 2017. Performance analysis of counter-flow regenerative heat and mass exchanger for indirect evaporative cooling based on data-driven model. Energy and Buildings, 155: 503-512.

CURRICULUM VITAE

Yunus Emre GÜZELEL graduated from Adana Anatolian High School in 2009 and in the same year enrolled in the Department of Mechanical Engineering at Çukurova University. He received his Bachelor of Science degree in Mechanical Engineering from Çukurova University in 2015 and started his Master of Science studies in the same department in 2016. He completed his M.Sc. degree in 2019 and then began his Ph.D. studies in Mechanical Engineering in the same year. Since 2018, he has been working as a Research Assistant in the Department of Mechanical Engineering at Çukurova University.

APPENDIX

APPENDIX A

Equations for dew-point effectiveness (ε_{dp}), process air outlet temperature ($T_{p,o}$), cooling capacity (CC), water consumption (WC) and cooling coefficient of performance (COP) are listed below.

MLR-1 (1^{st} Degree)

$\boldsymbol{\varepsilon_{dp}}$=0.541957466057431-0.00866980926051418*apN+0.000185761863722572*L+
-0.0757999854489692*h+0.550806888866964*β-0.0754604111796782*$u_{p,i}$
+0.0122618466334794*$\omega_{p,i}$+0.00332292625036841*$T_{p,i}$

$\boldsymbol{T_{p,o}}$=2.23727166228097+0.151065989583371*apN-0.0030440990825597*L
+1.24068623043211*h-9.0583764974945*β+1.23360235249793*$u_{p,i}$
+0.735436684575778*$\omega_{p,i}$+0.262548820126979*$T_{p,i}$

CC=-56.0159696292301-0.488560237621557*apN+0.0126449182182675*L
+3.45062511296232*h-40.7966549842371*β+11.2373605467377*$u_{p,i}$+
-2.41039381758816*$\omega_{p,i}$+2.59570399567481*$T_{p,i}$

WC=-243.866088138057-1.18175371628954*apN+0.0162266837167073*L
+14.4396935995368*h+67.9205878231486*β+31.7807757717804*$u_{p,i}$+
-5.50827193151818*$\omega_{p,i}$+6.3976546000768*$T_{p,i}$

COP=516.325855693837+34.4249261072431*apN-0.12304326047122*L
+37.3237023610289*h-710.211028211284*β-177.803362888682*$u_{p,i}$+
-17.8031682952083*$\omega_{p,i}$+18.898999762055*$T_{p,i}$

MLR-2 (1st Degree Cross)

$\boldsymbol{\varepsilon_{dp}}$$=0.321516739489067-0.107500927589308*apN-0.000149407438743607*L+$
$-0.0274309957473854*h+1.17936985849879*\beta+0.0205406075233706*u_{p,i}$
$+0.021346615294557*\omega_{p,i}+0.00859355594731072*T_{p,i}+apN*L*$
$-0.0000163016934259664+apN*h*0.00997756136072867+apN*\beta*$
$0.0941527144058727+apN*u_{p,i}*0.00719078905213178+apN*\omega_{p,i}*$
$0.000197891500005206+apN*T_{p,i}*0.0000494525469927066+L*h*$
$0.0000381244667091859+L*\beta*0.00020566476971971+L*u_{p,i}*$
$0.0000343159588573631+L*\omega_{p,i}*0.0000007295523661637+L*T_{p,i}*$
$0.0000001501623332268+h*\beta*-0.1032915773439+h*u_{p,i}*$
$-0.02212773878157+h*\omega_{p,i}*-0.000364633046987497+h*T_{p,i}*$
$-0.000102430952934163+\beta*u_{p,i}*-0.0936031195864324+\beta*\omega_{p,i}*$
$-0.00851036572732149+\beta*T_{p,i}*-0.00828760470986067+u_{p,i}*\omega_{p,i}*$
$-0.000481113585890282+u_{p,i}*T_{p,i}*-0.0000046077104699959+\omega_{p,i}*T_{p,i}*$
-0.00010955085643463

$\boldsymbol{T_{p,o}}$$=5.29290284097159+1.62230691567644*apN+0.0052241113485477*L+$
$-0.802095517028435*h-11.1597527359176*\beta-1.58046913713834*u_{p,i}$
$+0.97890222648582*\omega_{p,i}+0.146579996335668*T_{p,i}+apN*L*0.00026176084847293$
$+apN*h*-0.163845227788511+apN*\beta*-1.5094816050822+apN*$
$u_{p,i}*-0.116371531290912+apN*\omega_{p,i}*-0.0160369592671343+apN*T_{p,i}*$
$0.0079426474837202+L*h*-0.000585603186706881+L*\beta*$
$-0.00356803186130675+L*u_{p,i}*-0.000527779533558669+L*\omega_{p,i}*$
$0.00024512333806189+L*T_{p,i}*-0.000188193482497059+h*\beta*$
$1.77927415645791+h*u_{p,i}*0.349455377818147+h*\omega_{p,i}*$
$-0.0985416167304721+h*T_{p,i}*0.0774444814827357+\beta*u_{p,i}*$
$1.63369539518713+\beta*\omega_{p,i}*0.914731133496965+\beta*T_{p,i}*-0.41945679818488$
$+u_{p,i}*\omega_{p,i}*-0.0971654915926134+u_{p,i}*T_{p,i}*0.0763595370091997+\omega_{p,i}*T_{p,i}*$
-0.00544524712816411

CC$=13.7042463623474-3.16110462274479*apN-0.0340590534497126*L+$
$-4.7235806549367*h+102.798395131856*\beta-6.18155039565013*u_{p,i}+$
$-0.515444846622892*\omega_{p,i}-0.135429888508812*T_{p,i}+apN*L*$
$-0.00109583318379086+apN*h*0.248560921011854+apN*\beta*$
$5.27988748054239+apN*u_{p,i}*0.0484980532727518+apN*\omega_{p,i}*$
$0.0580532257613603+apN*T_{p,i}*-0.0239449368097384+L*h*$
$0.0042840989464173 7+L*\beta*-0.0047867220393286+L*u_{p,i}*$
$0.00610568794654455+L*\omega_{p,i}*-0.000896627253236434+L*T_{p,i}*$
$0.000824290827904852+h*\beta*-5.89048112687957+h*u_{p,i}*$
$-0.0114861950287378+h*\omega_{p,i}*-0.186805847391703+h*T_{p,i}*$
$0.249284819135696+\beta*u_{p,i}*-14.0403179579952+\beta*\omega_{p,i}*1.71998109153209$
$+\beta*T_{p,i}*-3.37490136790619+u_{p,i}*\omega_{p,i}*-0.688611777030683+u_{p,i}*T_{p,i}*$
$0.782297946924863+\omega_{p,i}*T_{p,i}*0.0234583150004268$

WC$=233.058952307761-0.764424055046953*apN-0.0557904603398802*L+$
$-33.6544155581106*h-149.304415539819*\beta-57.6899747198318*u_{p,i}$
$+4.48801618233954*\omega_{p,i}-7.27657455093446*T_{p,i}+apN*L*-0.00102185597980984$
$+apN*h*0.114455775395531+apN*\beta*4.45829388675877+apN*u_{p,i}$
$*-0.24503636898858+apN*\omega_{p,i}*0.105700904508175+apN*T_{p,i}*$
$-0.0694392341580661+L*h*0.0062817110212350 7+L*\beta*$
$-0.000774247619672048+L*u_{p,i}*0.00869956453506408+L*\omega_{p,i}*$
$-0.00103719146958171+L*T_{p,i}*0.001126174697069+h*\beta*$
$18.5419104753115+h*u_{p,i}*3.86101994360104+h*\omega_{p,i}*-0.84810331819931$
$+h*T_{p,i}*1.00657862671352+\beta*u_{p,i}*29.117694213223 8+\beta*\omega_{p,i}*$

-5.41356957741033+β*$T_{p,i}$*3.38155048685423+$u_{p,i}$*$\omega_{p,i}$*-1.88451300438351
+$u_{p,i}$*$T_{p,i}$*2.2138817345658+$\omega_{p,i}$*$T_{p,i}$*0.0633715792163696

COP=-510.684358434377+7.44202587211301*apN-0.372002841273764*L
+168.248213509043*h+154.899958675231*β+26.7051149474202*$u_{p,i}$+
-62.7760550401621*$\omega_{p,i}$+61.6653952252806*$T_{p,i}$+apN*L*-0.0163468663087324
+apN*h*3.59899823869602+apN*β*15.5847786651975+apN*$u_{p,i}$
-14.2621938469174+apN$\omega_{p,i}$*-2.06278481459703+apN*$T_{p,i}$*
2.38131939842272+L*h*0.00760731129645569+L*β*
0.458247973138228+L*$u_{p,i}$*0.0977600929926728+L*$\omega_{p,i}$*0.00704328069864543
+L*$T_{p,i}$*-0.00881276235423164+h*β*-230.622232854317+h*
$u_{p,i}$*-40.2362235143763+h*$\omega_{p,i}$*-2.01414815294097+h*$T_{p,i}$*
2.67265269095488+β*$u_{p,i}$*365.660902148654+β*$\omega_{p,i}$*38.2585684209314
+β*$T_{p,i}$*-52.4820843717011+$u_{p,i}$*$\omega_{p,i}$*11.642656174501+$u_{p,i}$*$T_{p,i}$*
-11.9646817185368+$\omega_{p,i}$*$T_{p,i}$*0.167898717694141

MLR-3 (2^{nd} Degree)

$\boldsymbol{\varepsilon_{dp}}$$=0.2654683369304-0.0274704816781694*apN+apN*apN*0.00318590353891853$
$+0.000421153068566029*L+L*L*-0.000001071646622068+$
$-0.101234254358181*h+h*h*0.00279476325872814+1.25346003060205$
$*\beta+\beta*\beta*-0.754671357035394-0.120576308092914*u_{p,i}+u_{p,i}*u_{p,i}*$
$0.00896819388929228+0.0264939565828301*\omega_{p,i}+\omega_{p,i}*\omega_{p,i}*-0.000592658491172645$
$+0.00694329435388891*T_{p,i}+T_{p,i}*T_{p,i}*-0.000557394062668001$

$\mathbf{T_{p,o}}$$=0.511253554264275+0.470496445230303*apN+apN*apN*-0.0541171283834778-$
$0.00681801924650422*L+L*L*0.0000017180658143141+1.67881339147121*h+h*h*-$
$0.0481476901909984-$
$19.6572940045134*\beta+\beta*\beta*11.3858177275345+1.9959301635522*u_{p,i}+u_{p,i}*u_{p,i}*-$
$0.151597254157564+0.986414679818012*\omega_{p,i}+\omega_{p,i}*\omega_{p,i}*-$
$0.0104566130188355+0.421485365762764*T_{p,i}+T_{p,i}*T_{p,i}*-0.00244541755676092$

CC$=-84.8450566829832-1.59378638445039*apN+apN*apN*0.17630202539297$
$+0.0253079175563465*L+L*L*-0.0000057876902299059+10.4789527801861*$
$h+h*h*-0.764629979025259+42.7295528832846*\beta+\beta*\beta$
$*-89.3231731603319+17.5184379157476*u_{p,i}+u_{p,i}*u_{p,i}*-1.24858947155242+$
$-3.0524905856418*\omega_{p,i}+\omega_{p,i}*\omega_{p,i}*0.0267926894086044+1.83932325727952*T_{p,i}+T_{p,i}$
$*T_{p,i}*0.0116404654165219$

WC$=-278.906661485517-1.9514914707585*apN+apN*apN*0.107795892733573$
$+0.0354116616372353*L+L*L*-0.0000087810402041643+31.0323522565466*$
$h+h*h*-1.80762674556514+191.301320234559*\beta+\beta*\beta*$
$-131.705935362539+42.3633311688152*u_{p,i}+u_{p,i}*u_{p,i}*-2.1031844899171+$
$-6.50563036537667*\omega_{p,i}+\omega_{p,i}*\omega_{p,i}*0.0416212180685973+3.80483416513648*T_{p,i}+T_{p,i}$
$*T_{p,i}*0.0398976485603915$
COP$=1038.75969058153-23.3041151358666*apN+apN*apN*9.82060712012326+$
$-0.259308953975289*L+L*L*0.0000626104707178098+70.3586328349598*$
$h+h*h*-3.66764390226714-467.635668843434*\beta+\beta*\beta$
$*-260.692503881989-595.109982423423*u_{p,i}+u_{p,i}*u_{p,i}*82.9988501762217+$
$-22.4216935926519*\omega_{p,i}+\omega_{p,i}*\omega_{p,i}*0.192150965634608+15.1583469171924*T_{p,i}+T_{p,i}$
$*T_{p,i}*0.0573885941283886$

MLR-4 (2nd DegreeCross)

ε_{dp}=0.00646885413832587-0.294912448989354*apN+apN*apN*0.0271244522935527
-0.000648811611424749*L+L*L*0.000000474321921646+
-0.01968163868476*h+h*h*0.00792905055427165+2.80426443724382*
β+β*β*-2.19412410237177+0.174618572137792*$u_{p,i}$+$u_{p,i}$*$u_{p,i}$*
-0.00508875083526547+0.0268029361830258*$\omega_{p,i}$+$\omega_{p,i}$*$\omega_{p,i}$*-0.000981082504059617
+0.0166656493455166*$T_{p,i}$+$T_{p,i}$*$T_{p,i}$*-0.000108997667339504+apN*L*
-0.0000567791623400382+apN*h*0.0387727603155172+apN*β*
0.259862907893585+apN*$u_{p,i}$*0.0229401183123332+apN*$\omega_{p,i}$*
0.000467574784783703+apN*$T_{p,i}$*-0.000277057018376557+apN*apN*L*
0.0000031242239484667+apN*apN*h*-0.0023541472348928+apN*
apN*β*-0.0276612222756002+apN*apN*$u_{p,i}$*-0.0018792238078 3886
+apN*apN*$\omega_{p,i}$*-0.0000583430234737195+apN*apN*$T_{p,i}$*
-0.0000231397477471281+L*h*0.000137878701571284+L*β*
0.00132155890264619+L*$u_{p,i}$*0.000106183778441526+L*$\omega_{p,i}$*
0.0000082842913393009+L*$T_{p,i}$*0.00000258725839 3016+L*L*apN*
0.0000000097275475796+L*L*h*-0.0000000100193608745+L*L*
β*-0.0000002025464429864+L*L*$u_{p,i}$*-0.000000085567786649+L*
L*$\omega_{p,i}$*-0.000000017125388324+L*L*$T_{p,i}$*-3.08433880570292e-10+
h*β*-0.27168809549304+h*$u_{p,i}$*-0.0901044932685639+h*$\omega_{p,i}$
0.000617793322574852+h$T_{p,i}$*-0.000296099114402851+h*h*
apN*-0.00154238785929867+h*h*L*-0.0000082989416816557+h
*h*β*-0.0084360795908 2338+h*h*$u_{p,i}$*0.00405927384188203
+h*h*$\omega_{p,i}$*-0.000293992371896776+h*h*$T_{p,i}$*
-0.0000699884375682303+β*$u_{p,i}$*-0.401103119204961+β*$\omega_{p,i}$*
0.029387374690 6815+β*$T_{p,i}$*-0.026458978081006+β*β*apN*
0.00968930758045662+β*β*L*-0.000699622307650049+β*β
*h*0.237610967274776+β*β*$u_{p,i}$*0.317995139304706+β*
β*$\omega_{p,i}$*-0.0303265676393324+β*β*$T_{p,i}$*0.0106999670489997+$u_{p,i}$
$\omega_{p,i}$-0.000821712901585538+$u_{p,i}$*$T_{p,i}$*0.000246437416433626+$u_{p,i}$*$u_{p,i}$*
apN*-0.000856267826938928+$u_{p,i}$*$u_{p,i}$*L*-0.000010393558560 9961+$u_{p,i}$*
$u_{p,i}$*h*0.00601907199063262+$u_{p,i}$*$u_{p,i}$*β*0.000919024947158482+$u_{p,i}$
$u_{p,i}$ $\omega_{p,i}$*-0.000184371352321806+$u_{p,i}$*$u_{p,i}$*$T_{p,i}$*-0.0000403041866957014
+$\omega_{p,i}$*$T_{p,i}$*-0.000102393082933626+$\omega_{p,i}$*$\omega_{p,i}$*apN*0.0000023338784388526
+$\omega_{p,i}$*$\omega_{p,i}$*L*-0.0000001553874243511+$\omega_{p,i}$*$\omega_{p,i}$*h*0.000070024838197187
+$\omega_{p,i}$*$\omega_{p,i}$*β*-0.000396349185133496+$\omega_{p,i}$*$\omega_{p,i}$*$u_{p,i}$*
0.0000515476245974342+$\omega_{p,i}$*$\omega_{p,i}$*$T_{p,i}$*0.0000086473237790242+$T_{p,i}$*$T_{p,i}$*
apN*0.0000033200660853102+$T_{p,i}$*$T_{p,i}$*L*-0.000000027275565598+$T_{p,i}$*$T_{p,i}$
*h*0.0000129141833018386+$T_{p,i}$*$T_{p,i}$*β*0.00012690877100801+$T_{p,i}$
*$T_{p,i}$*$u_{p,i}$*-0.0000006728473072671+$T_{p,i}$*$T_{p,i}$*$\omega_{p,i}$*-0.0000033469028750558

$T_{p,o}$=-4.35573546406543+4.31841007079953*apN+apN*apN*-0.394346353200706
+0.0153481185064255*L+L*L*-0.0000025227105643483-0.592172676096854
*h+h*h*-0.0819642281557445-19.2870155936921*β+β*
β*19.9691876327509-4.34634593399491*$u_{p,i}$+$u_{p,i}$*$u_{p,i}$*0.240516855668882
+1.35554743692515*$\omega_{p,i}$+$\omega_{p,i}$*$\omega_{p,i}$*-0.0111205833925888+0.738895471332481*$T_{p,i}$
+$T_{p,i}$*$T_{p,i}$*-0.0064077903244 4876+apN*L*0.000960878794767276+apN*
h*-0.637993550009556+apN*β*-3.98852607229567+apN*$u_{p,i}$*
-0.377379466386987+apN*$\omega_{p,i}$*-0.0658603240602799+apN*$T_{p,i}$*
0.0350154445757938+apN*apN*L*-0.0000531444437122706+apN*apN
*h*0.0388750048835705+apN*apN*β*0.4423897892437+apN*
apN*$u_{p,i}$*0.0316017325320225+apN*apN*$\omega_{p,i}$*0.00556757781778226+
apN*apN*$T_{p,i}$*-0.0028457564737 5378+L*h*-0.00214717243773817+
L*β*-0.021049944503 0518+L*$u_{p,i}$*-0.0016634350790 8991+L*$\omega_{p,i}$*

$0.000677354868591111+L*T_{p,i}*-0.00044510426822319+L*L*apN*$
$-0.000001698382528227+L*L*h*0.000001625913647575+L*L*$
$\beta*0.000003376204323126+L*L*u_{p,i}*0.000001381256463843+L*L$
$*\omega_{p,i}*-0.0000001231918270341+L*L*T_{p,i}*0.000001136832876635+h$
$*\beta*4.33777017981321+h*u_{p,i}*1.45270263894033+h*\omega_{p,i}*$
$-0.239534631354554+h*T_{p,i}*0.0911172317628234+h*h*apN*$
$0.0255970229612166+h*h*L*0.000128078220250948+h*h*$
$\beta*0.114452777033678+h*h*u_{p,i}*-0.0658863932613769+h*$
$h*\omega_{p,i}*0.00881937561306161+h*h*T_{p,i}*-0.00151516552692371+$
$\beta*u_{p,i}*6.46627138972183+\beta*\omega_{p,i}*2.29783967987673+\beta*T_{p,i}*$
$-1.46722080686899+\beta*\beta*apN*-0.316045832070773+\beta*\beta*$
$L*0.0104937562836754+\beta*\beta*h*-3.48395366204206+\beta*$
$\beta*u_{p,i}*-4.7557828999256+\beta*\beta*\omega_{p,i}*-0.551183918060167+\beta$
$*\beta*T_{p,i}*0.621198025113998+u_{p,i}*\omega_{p,i}*-0.236166076964464+u_{p,i}*T_{p,i}*$
$0.115687796636445+u_{p,i}*u_{p,i}*apN*0.0138116221034366+u_{p,i}*u_{p,i}*L*$
$0.000162769582930662+u_{p,i}*u_{p,i}*h*-0.0977641816943562+u_{p,i}*u_{p,i}*\beta$
$*-0.0609344104826689+u_{p,i}*u_{p,i}*\omega_{p,i}*0.0156062192318375+u_{p,i}*u_{p,i}*T_{p,i}*$
$-0.0082235561557664+\omega_{p,i}*T_{p,i}*-0.0128726942390458+\omega_{p,i}*\omega_{p,i}*apN*$
$0.000733639897460719+\omega_{p,i}*\omega_{p,i}*L*-0.0000067615250581837+\omega_{p,i}*\omega_{p,i}*$
$h*0.00252587668413246+\omega_{p,i}*\omega_{p,i}*\beta*-0.036357883002125+\omega_{p,i}*\omega_{p,i}*$
$u_{p,i}*0.00253376651977924+\omega_{p,i}*\omega_{p,i}*T_{p,i}*0.000128523584361214+T_{p,i}*T_{p,i}*$
$apN*-0.000159175811521083+T_{p,i}*T_{p,i}*L*0.0000001127386038711+T_{p,i}*T_{p,i}$
$*h*-0.0000006415069819125+T_{p,i}*T_{p,i}*\beta*0.00721987727073609+T_{p,i}$
$*T_{p,i}*u_{p,i}*0.0000305855169842922+T_{p,i}*T_{p,i}*\omega_{p,i}*0.0000670998993452792$

$CC=82.7471556669675-12.1689740778706*apN+apN*apN*0.96010698451848+$
$-0.0802946477700194*L+L*L*0.000158788472570417-12.6995913267439*$
$h+h*h*0.843321601997969+18.5214784749434*\beta+\beta*\beta*$
$57.8453950052108-20.7017683975848*u_{p,i}+u_{p,i}*u_{p,i}*1.50007987884339$
$+2.4952764447328*\omega_{p,i}+\omega_{p,i}*\omega_{p,i}*-0.0087475480287128-3.7688255609027*T_{p,i}+T_{p,i}$
$*T_{p,i}*0.0123213982029095+apN*L*-0.00384107205428949+apN*h*$
$1.09000172974022+apN*\beta*28.4626327547815+apN*u_{p,i}*$
$-0.149366504282246+apN*\omega_{p,i}*0.233602321256499+apN*T_{p,i}*$
$-0.130630411586861+apN*apN*L*0.000208775633217072+apN*apN*$
$h*-0.113754958074734+apN*apN*\beta*-1.34157469664157+apN*$
$apN*u_{p,i}*-0.0184613656661997+apN*apN*\omega_{p,i}*-0.0190593979045151+$
$apN*apN*T_{p,i}*0.00759757208334711+L*h*0.00920329180497555+L$
$*\beta*0.0624843656867813+L*u_{p,i}*0.0119542345553804+L*\omega_{p,i}*$
$-0.00213256571195827+L*T_{p,i}*0.00163421531665771+L*L*apN*$
$0.00000064059600235+L*L*h*-0.000017425340232132+L*L*$
$\beta*-0.000014309277873718+L*L*u_{p,i}*-0.000027007600531237+L*$
$L*\omega_{p,i}*0.0000003833452102836+L*L*T_{p,i}*-0.000004150306610978+$
$h*\beta*-18.4359092079074+h*u_{p,i}*4.56020049003378+h*\omega_{p,i}*$
$-0.591398766350599+h*T_{p,i}*0.641336537092626+h*h*apN*$
$0.0168609215528306+h*h*L*-0.000960670781524676+h*h$
$*\beta*0.213121018917889+h*h*u_{p,i}*-0.321393563122808+h*$
$h*\omega_{p,i}*0.044082530290306+h*h*T_{p,i}*-0.0547993890273602+$
$\beta*u_{p,i}*-3.49860352954128+\beta*\omega_{p,i}*-6.27518165865252+\beta*T_{p,i}*$
$3.61597016991476+\beta*\beta*apN*-13.9196385219834+\beta*\beta*L$
$*-0.0670992590318309+\beta*\beta*h*7.23803460803787+\beta*\beta$
$*u_{p,i}*-15.3368331990026+\beta*\beta*\omega_{p,i}*7.39845488132856+\beta*$
$\beta*T_{p,i}*-4.38820318101454+u_{p,i}*\omega_{p,i}*-1.23832029442416+u_{p,i}*T_{p,i}*$
$0.959053675384849+u_{p,i}*u_{p,i}*apN*0.0806270565835092+u_{p,i}*u_{p,i}*L*$
$0.000355106729816916+u_{p,i}*u_{p,i}*h*-0.360556103550759+u_{p,i}*u_{p,i}*\beta$
$*0.517704217645331+u_{p,i}*u_{p,i}*\omega_{p,i}*0.0825456749612316+u_{p,i}*u_{p,i}*T_{p,i}*$

-0.0838577786508959+$\omega_{p,i}$*$T_{p,i}$*0.0456113559902784+$\omega_{p,i}$*$\omega_{p,i}$*apN*
-0.00246232433885963+$\omega_{p,i}$*$\omega_{p,i}$*L*0.0000166017758785317+$\omega_{p,i}$*$\omega_{p,i}$*h
-0.0000614225491423348+$\omega_{p,i}$ $\omega_{p,i}$*β*0.0453493891672171+$\omega_{p,i}$*$\omega_{p,i}$*
$u_{p,i}$*0.00557967917396944+$\omega_{p,i}$*$\omega_{p,i}$*$T_{p,i}$*-0.000324312518470966+$T_{p,i}$*$T_{p,i}$*
apN*0.000871008947567455+$T_{p,i}$*$T_{p,i}$*L*0.0000014884504579633+$T_{p,i}$*$T_{p,i}$
*h*0.00174248531494714+$T_{p,i}$*$T_{p,i}$*β*-0.0441049813631196+$T_{p,i}$*
$T_{p,i}$*$u_{p,i}$*0.00380171126931204+$T_{p,i}$*$T_{p,i}$*$\omega_{p,i}$*-0.000224434628201612

WC=394.513170787332-10.6014813660706*apN+apN*apN*1.14849505261559+
-0.131023559372341*L+L*L*0.0000341148464994595-67.6506883269373*
h+h*h*3.69392143476624-398.374884265395*β+β*β*
201.427275160639-90.4072808186231*$u_{p,i}$+$u_{p,i}$*$u_{p,i}$*4.25014341761719
+10.4238905224018*$\omega_{p,i}$+$\omega_{p,i}$*$\omega_{p,i}$*-0.0611775226082124-12.3151455057971*$T_{p,i}$
+$T_{p,i}$*$T_{p,i}$*-0.00857005559520397+apN*L*-0.00331159779538392+apN*
h*0.741533263191137+apN*β*27.4854237069098+apN*$u_{p,i}$*
-0.527167045056588+apN*$\omega_{p,i}$*0.265434171502533+apN*$T_{p,i}$*
-0.13416805324597+apN*apN*L*0.000061457221084007 8+apN*apN*
h*-0.101603400777712+apN*apN*β*-1.49625922636165+apN*
apN*$u_{p,i}$*-0.0373368991934794+apN*apN*$\omega_{p,i}$*-0.0161936215249929+
apN*apN*$T_{p,i}$*0.0047020889603189 1+L*h*0.0132563768409193+L
*β*0.0764568130350081+L*$u_{p,i}$*0.0173797180339397+L*$\omega_{p,i}$*
-0.0025534617064077 2+L*$T_{p,i}$*0.0021348379368490 2+L*L*apN*
0.0000008029493546743+L*L*h*-0.0000034889853018559+L*L*
β*-0.0000085550648849647+L*L*$u_{p,i}$*-0.0000048681066093556+L*
L*$\omega_{p,i}$*0.0000005313235513094+L*L*$T_{p,i}$*-0.0000006586770396111+
h*β*26.1923889734578+h*$u_{p,i}$*14.47209708625 1+h*$\omega_{p,i}$*
-1.93874927078473+h*$T_{p,i}$*1.78265653679592+h*h*apN*
0.0415332651784784+h*h*L*0.00010480692802644+h*h*
β*-1.13312926445507+h*h*$u_{p,i}$*-0.805314719333441+h*
h*$\omega_{p,i}$*0.108296415428814+h*h*$T_{p,i}$*-0.130385042064121+β
*$u_{p,i}$*61.2497925043476+β*$\omega_{p,i}$*-17.1682036718384+β*$T_{p,i}$*
13.3635619226492+β*β*apN*-12.3271772563012+β*β*L
*-0.0610187745716611+β*β*h*-1.89804278273255+β*β
$u_{p,i}$-31.4971246310812+β*β*$\omega_{p,i}$*9.2094897250447+β*β
$T_{p,i}$-7.54106576567072+$u_{p,i}$*$\omega_{p,i}$*-2.8595752998607+$u_{p,i}$*$T_{p,i}$*
2.09867927711245+$u_{p,i}$*$u_{p,i}$*apN*0.121718881446269+$u_{p,i}$*$u_{p,i}$*L*
0.000417215427927388+$u_{p,i}$*$u_{p,i}$*h*-0.690059514454554+$u_{p,i}$*$u_{p,i}$*β
*-0.799824987278656+$u_{p,i}$*$u_{p,i}$*$\omega_{p,i}$*0.135303766955693+$u_{p,i}$*$u_{p,i}$*$T_{p,i}$*
-0.150443248439759+$\omega_{p,i}$*$T_{p,i}$*0.115229467349485+$\omega_{p,i}$*$\omega_{p,i}$*apN*
-0.00236189804349593+$\omega_{p,i}$*$\omega_{p,i}$*L*0.0000147801580655432+$\omega_{p,i}$*$\omega_{p,i}$*h
0.00404947394898819+$\omega_{p,i}$ $\omega_{p,i}$*β*0.130878721257098+$\omega_{p,i}$*$\omega_{p,i}$*$u_{p,i}$
0.0122722669627444+$\omega_{p,i}$ $\omega_{p,i}$*$T_{p,i}$*-0.000499867703187223+$T_{p,i}$*$T_{p,i}$*
apN*0.000404407658911732+$T_{p,i}$*$T_{p,i}$*L*0.0000065982787359123+$T_{p,i}$*$T_{p,i}$
*h*0.0065056113029843+$T_{p,i}$*$T_{p,i}$*β*-0.0444456468209684+$T_{p,i}$*
$T_{p,i}$*$u_{p,i}$*0.0134575209182538+$T_{p,i}$*$T_{p,i}$*$\omega_{p,i}$*-0.000616163442552916

COP=-642.468920446208+6.4787073640309*apN+apN*apN*1.18477683885538
-1.28026102864865*L+L*L*0.000278186545620761+554.589151982461*
h+h*h*-21.9658174807091+95.0996432050025*β+β*β*
-1752.44421568634+22.2573281309397*$u_{p,i}$+$u_{p,i}$*$u_{p,i}$*-12.6581910930416+
-99.9000668630406*$\omega_{p,i}$+$\omega_{p,i}$*$\omega_{p,i}$*0.561423253854013+77.4153400623157*$T_{p,i}$+$T_{p,i}$
*$T_{p,i}$*0.28562696009777 1+apN*L*0.0219606079548996+apN*h*
-30.1189721474401+apN*β*380.499639149591+apN*$u_{p,i}$*
-21.5901294695866+apN*$\omega_{p,i}$*1.71256249187183+apN*$T_{p,i}$*-1.95348367532906
+apN*apN*L*-0.0103237430106158+apN*apN*h*

$5.19530659689785+apN*apN*\beta*-1.58040279603204+apN*apN*u_{p,i}$
$*-6.05628363961616+apN*apN*\omega_{p,i}*-0.727696583033267+apN*apN*$
$T_{p,i}*0.631012456893414+L*h*-0.00817289761566648+L*\beta*$
$1.50571532171471+L*u_{p,i}*0.453988413152181+L*\omega_{p,i}*0.0142404497063262$
$+L*T_{p,i}*-0.0169643139797456+L*L*apN*0.000103541101278897+L$
$*L*h*-0.0000227332555546567+L*L*\beta*-0.000293113899583637$
$+L*L*u_{p,i}*-0.0000526610006365101+L*L*\omega_{p,i}*$
$-0.0000031222916052137+L*L*T_{p,i}*0.0000048565507581177+h*\beta$
$*-490.138250568327+h*u_{p,i}*-157.434773079388+h*\omega_{p,i}*$
$-5.35258135932312+h*T_{p,i}*3.66544458138034+h*h*apN*$
$0.314547554597973+h*h*L*0.00736899024653152+h*h*$
$\beta*-6.63419463531474+h*h*u_{p,i}*2.30957522935308+h*h$
$*\omega_{p,i}*0.380252482593503+h*h*T_{p,i}*-0.23311420981569+\beta*u_{p,i}$
$*995.727628171105+\beta*\omega_{p,i}*-4.68641876597299+\beta*T_{p,i}*$
$-33.4312503111656+\beta*\beta*apN*-383.193191359601+\beta*\beta*L$
$*-0.423866983722553+\beta*\beta*h*327.494131620604+\beta*\beta$
$*u_{p,i}*299.315465637231+\beta*\beta*\omega_{p,i}*42.1451688623321+\beta*\beta$
$*T_{p,i}*4.08129328412009+u_{p,i}*\omega_{p,i}*43.0417241433814+u_{p,i}*T_{p,i}*$
$-37.7767516268646+u_{p,i}*u_{p,i}*apN*7.87949516170482+u_{p,i}*u_{p,i}*L*$
$-0.0485539258958165+u_{p,i}*u_{p,i}*h*19.8941469861793+u_{p,i}*u_{p,i}*\beta*$
$-176.649597680016+u_{p,i}*u_{p,i}*\omega_{p,i}*-5.54850974152528+u_{p,i}*u_{p,i}*T_{p,i}*$
$5.59879428106006+\omega_{p,i}*T_{p,i}*0.383566205767634+\omega_{p,i}*\omega_{p,i}*apN*$
$0.0214747041050514+\omega_{p,i}*\omega_{p,i}*L*-0.000162412328242106+\omega_{p,i}*\omega_{p,i}*h$
$*-0.00627535764058463+\omega_{p,i}*\omega_{p,i}*\beta*0.147872879636506+\omega_{p,i}*\omega_{p,i}*u_{p,i}$
$*-0.145987268240752+\omega_{p,i}*\omega_{p,i}*T_{p,i}*-0.0022322246551391 8+T_{p,i}*T_{p,i}*apN$
$*0.0101012092144959+T_{p,i}*T_{p,i}*L*-0.000367572081031913+T_{p,i}*T_{p,i}*$
$h*0.016866017537029+T_{p,i}*T_{p,i}*\beta*-0.354167230454968+T_{p,i}*T_{p,i}*$
$u_{p,i}*-0.036600856983614+T_{p,i}*T_{p,i}*\omega_{p,i}*-0.0024376898212795 6$

MLR-5 (3rd Degree)

$\boldsymbol{\varepsilon_{dp}}$=$-0.117451871444853-0.0509197021031*apN+apN*apN*$
$0.0122464644508581+apN*apN*apN*-0.00101846015934663$
$+0.000760352466635007*L+L*L*-0.000004228941129+L*L*L*$
$9.5747662718184e-11-0.04030741883167*h+h*h*$
$-0.0112026809732221+h*h*h*0.00103580475197427$
$+1.8517692420357*\beta+\beta*\beta*-2.12612789237893+\beta*\beta*\beta$
$*0.984126256080811-0.119789380203247*u_{p,i}+u_{p,i}*u_{p,i}*0.00862698038129009$
$+u_{p,i}*u_{p,i}*u_{p,i}*0.000044317898771809 5+0.0359506271090922*\omega_{p,i}+\omega_{p,i}*\omega_{p,i}*$
$-0.00144539281808116+\omega_{p,i}*\omega_{p,i}*\omega_{p,i}*0.0000236862149116215$
$+0.0148549226064082*T_{p,i}+T_{p,i}*T_{p,i}*-0.000303251854463037+T_{p,i}*T_{p,i}*T_{p,i}*$
0.0000025393306072982

$\mathbf{T_{p,o}}$=$3.11389822747582+0.912007187632374*apN+apN*apN*-0.22475048198384+$
$apN*apN*apN*0.0191808761906592-0.0113918512217488*L+L*L*$
$0.0000059746048873914+L*L*L*-0.0000000012906167784$
$+0.689038027678289*h+h*h*0.179321753349294+h*h*h$
$*-0.0168357506999543-28.1050119649993*\beta+\beta*\beta*$
$30.7586724434585+\beta*\beta*\beta*-13.9055248014923+2.02537347265789*$
$u_{p,i}+u_{p,i}*u_{p,i}*-0.164912262534489+u_{p,i}*u_{p,i}*u_{p,i}*0.00178583827228205$
$+1.05610262533252*\omega_{p,i}+\omega_{p,i}*\omega_{p,i}*-0.0167386571968019+\omega_{p,i}*\omega_{p,i}*\omega_{p,i}*$
$0.000174425910602046+0.512690600692172*T_{p,i}+T_{p,i}*T_{p,i}*-0.00529727109493535$
$+T_{p,i}*T_{p,i}*T_{p,i}*0.0000292428802511842$

CC=$-107.86604790914-2.93981932641179*apN+apN*apN*0.695490052754982$
$+apN*apN*apN*-0.0583586585672404+0.0420748518212306*L+L*L$
$*-0.0000214249370792051+L*L*L*0.0000000047504187901$
$+16.0043650808365*h+h*h*-2.03465440109412+h*h*h$
$*0.0940697245753962+145.858642593788*\beta+\beta*\beta*-325.506918519516$
$+\beta*\beta*\beta*169.395905990202+21.5433049806573*u_{p,i}+u_{p,i}*u_{p,i}*$
$-3.04798615375711+u_{p,i}*u_{p,i}*u_{p,i}*0.239184609708519-3.15653538673656*\omega_{p,i}$
$+\omega_{p,i}*\omega_{p,i}*0.0361675979804785+\omega_{p,i}*\omega_{p,i}*\omega_{p,i}*-0.000260303765474377$
$+1.29178429852238*T_{p,i}+T_{p,i}*T_{p,i}*0.0287575083501376+T_{p,i}*T_{p,i}*T_{p,i}*$
-0.000175484306316572

WC=$-300.015214606954+1.50137851827913*apN+apN*apN*-1.23002437763025$
$+apN*apN*apN*0.150445776390857+0.0446446972434206*L+L*L*$
$-0.000017437084806351 5+L*L*L*0.0000000026413247995$
$+37.7540701445302*h+h*h*-3.34317551463999+h*h*h$
$*0.113251226466616+345.262670243315*\beta+\beta*\beta*-484.013649201037$
$+\beta*\beta*\beta*252.578735213107+46.6524859189407*u_{p,i}+u_{p,i}*u_{p,i}*$
$-4.01871434893915+u_{p,i}*u_{p,i}*u_{p,i}*0.254536641567706-6.62037519973822*\omega_{p,i}$
$+\omega_{p,i}*\omega_{p,i}*0.0519740443501368+\omega_{p,i}*\omega_{p,i}*\omega_{p,i}*-0.000288050470366748$
$+2.166960638619*T_{p,i}+T_{p,i}*T_{p,i}*0.091107962557621+T_{p,i}*T_{p,i}*T_{p,i}*$
-0.000525092427396069

COP=$1435.84679084432-247.133070372512*apN+apN*apN*96.4524810048708+$
$apN*apN*apN*-9.74536761273278-0.201247577547537*L+L*L*$
$0.000117381636001398+L*L*L*0.000000145343614664+$
$-43.9206977728236*h+h*h*22.024062060605+h*h*h*$
$-1.87004401313706+1577.80174297002*\beta+\beta*\beta*-4954.05839440528$
$+\beta*\beta*\beta*3368.00694460939-1178.97659246627*u_{p,i}+u_{p,i}*u_{p,i}*$
$344.376501835884+u_{p,i}*u_{p,i}*u_{p,i}*-34.7735426637062-23.6934965576469*\omega_{p,i}$
$+\omega_{p,i}*\omega_{p,i}*0.306904717092939+\omega_{p,i}*\omega_{p,i}*\omega_{p,i}*-0.00316677863748145$

$+15.1472601104809*T_{p,i}+T_{p,i}*T_{p,i}*0.057434478643614+T_{p,i}*T_{p,i}*T_{p,i}*$
0.0000032457125394472

MLR-6 (3rd DegreeCross)

$\boldsymbol{\varepsilon_{dp}}$=0.119063565762979-0.400088029001276*apN+apN*apN*0.086803859297794
+apN*apN*apN*-0.00682013918270792-0.00082042914809932 3*L+L*
L*-0.000000642967661752+L*L*L*3.40645420002631e-11+
-0.164678263417144*h+h*h*0.0570826542142317+h*h*
h*-0.00360876329886185+3.98055796561741*β+β*β*
-7.01421949130573+β*β*β*3.44036520974386+0.233404081728885
*$u_{p,i}$+$u_{p,i}$*$u_{p,i}$*-0.0239159217066157+$u_{p,i}$*$u_{p,i}$*$u_{p,i}$*0.00244329038066338
+0.000883185588423104*$\omega_{p,i}$+$\omega_{p,i}$*$\omega_{p,i}$*-0.00145880508597654+$\omega_{p,i}$*$\omega_{p,i}$*$\omega_{p,i}$*
0.0000131618223055476+0.00861589525252779*$T_{p,i}$+$T_{p,i}$*$T_{p,i}$*0.00011934335611681
+$T_{p,i}$*$T_{p,i}$*$T_{p,i}$*-0.000002327542196202+apN*L*-0.0000574724604209108
+apN*h*0.0378834659375338+apN*β*0.250907242455615+apN*
$u_{p,i}$*0.0301503152137009+apN*$\omega_{p,i}$*0.00117978661938584+apN*$T_{p,i}$*
-0.000501196125081716+apN*apN*L*0.0000056829779585355+apN*apN
h-0.0065007743947678 3+apN*apN*β*-0.0927282458136419+
apN*apN*$u_{p,i}$*-0.00472765076620069+apN*apN*$\omega_{p,i}$*
-0.000397627920761731+apN*apN*$T_{p,i}$*-0.000172157975673543+apN*
apN*apN*L*-0.000000299685352636 8+apN*apN*apN*h*
0.000482299070286142+apN*apN*apN*β*0.00735316026031 33+
apN*apN*apN*$u_{p,i}$*0.000322907850565075+apN*apN*apN*$\omega_{p,i}$*
0.0000381491013334126+apN*apN*apN*$T_{p,i}$*0.0000167496330165827+
L*h*0.000167718670111907+L*β*0.00263657669741402+L*$u_{p,i}$*
0.000167029367220607+L*$\omega_{p,i}$*0.0000109415941711753+L*$T_{p,i}$*
0.0000082505566101341+L*L*apN*0.0000000045583889+L*L*h
*0.000000008589147623 7+L*L*β*-0.00000063175017446+L*L*
$u_{p,i}$*-0.000000045452142350 7+L*L*$\omega_{p,i}$*-0.000000001629909071 7+L*
L*$T_{p,i}$*0.000000001954193020 6+L*L*L*apN*1.54660086968633e-12
+L*L*L*h*-5.66341569215077e-12+L*L*L*β*
1.30132115955406e-10+L*L*L*$u_{p,i}$*1.12624454592128e-11+L*L
L$\omega_{p,i}$*-1.38214014905586e-14+L*L*L*$T_{p,i}$*
-6.95843424659547e-13+h*β*0.0437951397894689+h*$u_{p,i}$*
-0.112157940104047+h*$\omega_{p,i}$*0.0046666085161864+h*$T_{p,i}$*
-0.00242887193944648+h*h*apN*0.000987196951061016+h*h
L-0.0000195489533539937+h*h*β*-0.118768300500586+
h*h*$u_{p,i}$*0.00429784925770868+h*h*$\omega_{p,i}$*
-0.00150510381350898+h*h*$T_{p,i}$*-0.000237491159241664+h*h
*h*apN*-0.000184535908353823+h*h*h*L*
0.0000008234614657845+h*h*h*β*0.0081302747122938+
h*h*h*$u_{p,i}$*-0.0000153008324338755+h*h*h*$\omega_{p,i}$
*0.0000892198450020416+h*h*h*$T_{p,i}$*0.0000122375991853293
+β*$u_{p,i}$*-0.68599101027689+β*$\omega_{p,i}$*0.0750406920100178+β*$T_{p,i}$
*-0.0386041989788254+β*β*apN*0.430841834285983+β*β
L-0.0026414085108348+β*β*h*0.604345076779907+β
β$u_{p,i}$*1.06608900225405+β*β*$\omega_{p,i}$*-0.096468611133929+
β*β*$T_{p,i}$*0.0166612134833993+β*β*β*apN*
-0.312397705803886+β*β*β*L*0.0013854079154105+β*
β*β*h*-0.253269146450751+β*β*β*$u_{p,i}$*
-0.532798888994516+β*β*β*$\omega_{p,i}$*0.0475557359851919+β*
β*β*$T_{p,i}$*-0.00436572945087717+$u_{p,i}$*$\omega_{p,i}$*-0.0016756859603533+$u_{p,i}$
*$T_{p,i}$*0.0021015776966571 2+$u_{p,i}$*$u_{p,i}$*apN*-0.000797823248702498+$u_{p,i}$*
$u_{p,i}$*L*-0.0000198847793097068+$u_{p,i}$*$u_{p,i}$*h*0.0152581919627051+$u_{p,i}$
*$u_{p,i}$*β*-0.0195396050657994+$u_{p,i}$*$u_{p,i}$*$\omega_{p,i}$*-0.000695526332390522
+$u_{p,i}$*$u_{p,i}$*$T_{p,i}$*-0.0000514381096823234+$u_{p,i}$*$u_{p,i}$*$u_{p,i}$*apN*
-0.0000096189743143681+$u_{p,i}$*$u_{p,i}$*$u_{p,i}$*L*0.0000012597998825328+$u_{p,i}$*

$u_{p,i}*u_{p,i}*h*-0.00121936405307317+u_{p,i}*u_{p,i}*u_{p,i}*\beta*$
$0.00277870307648412+u_{p,i}*u_{p,i}*u_{p,i}*\omega_{p,i}*0.0000679856056023103+u_{p,i}*u_{p,i}$
$*u_{p,i}*T_{p,i}*0.0000012167618635964+\omega_{p,i}*T_{p,i}*0.00183703068210323+\omega_{p,i}*\omega_{p,i}$
$*apN*0.0000171411126968978+\omega_{p,i}*\omega_{p,i}*L*-0.000000406960075988+\omega_{p,i}$
$*\omega_{p,i}*h*0.000182864538831502+\omega_{p,i}*\omega_{p,i}*\beta*-0.00191540433793057$
$+\omega_{p,i}*\omega_{p,i}*u_{p,i}*0.000231465460858964+\omega_{p,i}*\omega_{p,i}*T_{p,i}*-0.0000057890007340628$
$+\omega_{p,i}*\omega_{p,i}*\omega_{p,i}*apN*-0.0000004109059692556+\omega_{p,i}*\omega_{p,i}*\omega_{p,i}*L*$
$0.0000000069988161667+\omega_{p,i}*\omega_{p,i}*\omega_{p,i}*h*-0.0000031258895776294+\omega_{p,i}$
$*\omega_{p,i}*\omega_{p,i}*\beta*0.0000421927026985224+\omega_{p,i}*\omega_{p,i}*\omega_{p,i}*u_{p,i}*$
$-0.0000049909847373279+\omega_{p,i}*\omega_{p,i}*\omega_{p,i}*T_{p,i}*0.0000004020858089676+T_{p,i}*$
$T_{p,i}*apN*0.0000300403443394312+T_{p,i}*T_{p,i}*L*-0.0000002791228261358+$
$T_{p,i}*T_{p,i}*h*0.000102899162228948+T_{p,i}*T_{p,i}*\beta*0.000428458165006744$
$+T_{p,i}*T_{p,i}*u_{p,i}*-0.0000575549020723363+T_{p,i}*T_{p,i}*\omega_{p,i}*$
$-0.0000590642842273466+T_{p,i}*T_{p,i}*T_{p,i}*apN*-0.0000002724939477039+T_{p,i}$
$*T_{p,i}*T_{p,i}*L*0.0000000025795255823+T_{p,i}*T_{p,i}*T_{p,i}*h*$
$-0.0000009246740011357+T_{p,i}*T_{p,i}*T_{p,i}*\beta*-0.0000031053008104506+T_{p,i}$
$*T_{p,i}*T_{p,i}*u_{p,i}*0.0000005815995342522+T_{p,i}*T_{p,i}*T_{p,i}*\omega_{p,i}*$
0.0000005718892271221

$\mathbf{T_{p,o}}=-13.3160043810658+5.73169649579528*apN+apN*apN*-1.20493753971568$
$+apN*apN*apN*0.0928653225225868+0.0165288790254946*L+L*L*$
$-0.0000012026843534147+L*L*L*-0.000000004024145391$
$+3.14289624107472*h+h*h*-1.0578276114024+h*h*h$
$*0.0717773456866699-19.1732154334051*\beta+\beta*\beta*62.1322389548845$
$+\beta*\beta*\beta*-29.9784966888209-5.40362851473625*u_{p,i}+u_{p,i}*u_{p,i}$
$*0.674116721254007+u_{p,i}*u_{p,i}*u_{p,i}*-0.0566781874029112+1.15139402938153*$
$\omega_{p,i}+\omega_{p,i}*\omega_{p,i}*-0.00542753735603771+\omega_{p,i}*\omega_{p,i}*\omega_{p,i}*-0.000156500421612937$
$+1.5334757103375*T_{p,i}+T_{p,i}*T_{p,i}*-0.0224723630938046+T_{p,i}*T_{p,i}*T_{p,i}*$
$0.000164640906171339+apN*L*0.000991404015501048+apN*h*$
$-0.582936623377669+apN*\beta*-4.30981802049848+apN*u_{p,i}*$
$-0.483553476944564+apN*\omega_{p,i}*-0.135412675650328+apN*T_{p,i}*$
$0.0636803607303837+apN*apN*L*-0.0000711695606455759+apN*apN$
$*h*0.0971476199470001+apN*apN*\beta*1.50079135965623+apN$
$*apN*u_{p,i}*0.0729929987507218+apN*apN*\omega_{p,i}*0.0249818173770416$
$+apN*apN*T_{p,i}*-0.00964474997719847+apN*apN*apN*L*$
$0.0000022200765619817+apN*apN*apN*h*-0.00680387422997779$
$+apN*apN*apN*\beta*-0.119578793190627+apN*apN*apN*u_{p,i}$
$*-0.0046951668629367+apN*apN*apN*\omega_{p,i}*-0.00218221003443299+$
$apN*apN*apN*T_{p,i}*0.000763863857967609+L*h*$
$-0.0016399968623746+L*\beta*-0.0408809373673352+L*u_{p,i}*$
$-0.00260291171072274+L*\omega_{p,i}*0.00119935899640296+L*T_{p,i}*$
$-0.000730881215481653+L*L*apN*-0.000001597603093278+L*L*$
$h*-0.0000007993458764693+L*L*\beta*0.0000113489372086046+L*$
$L*u_{p,i}*0.0000007031770697906+L*L*\omega_{p,i}*-0.0000005526561474678+L$
$*L*T_{p,i}*0.0000003522093417903+L*L*L*apN*$
$-2.96759795852477e-12+L*L*L*h*2.92312933685895e-10+L*$
$L*L*\beta*-0.0000000024174454927+L*L*L*u_{p,i}*$
$-1.72539226548692e-10+L*L*L*\omega_{p,i}*1.30085246726043e-10+L*L$
$*L*T_{p,i}*-7.22234077495556e-11+h*\beta*-0.919791575983278+h$
$*u_{p,i}*1.84797020072993+h*\omega_{p,i}*-0.251827175280886+h*T_{p,i}*$
$-0.0124943613040565+h*h*apN*-0.0193918709697048+h*h$
$*L*0.000245744996286027+h*h*\beta*1.84330867392728+h$
$*h*u_{p,i}*-0.0694864767834863+h*h*\omega_{p,i}*0.00863807767830692$
$+h*h*T_{p,i}*0.0169386439896057+h*h*h*apN*$
$0.0032801901722432 1+h*h*h*L*-0.0000085694576464696+$

$h*h*h*\beta*-0.127381160254536+h*h*h*u_{p,i}*$
$0.000229668993104012+h*h*h*\omega_{p,i}*0.000020532765846761+$
$h*h*h*T_{p,i}*-0.00136344254797l+\beta*u_{p,i}*10.6937463544514$
$+\beta*\omega_{p,i}*3.19039726178302+\beta*T_{p,i}*-2.56198124648129+\beta*\beta$
$*apN*-6.08260601853638+\beta*\beta*L*0.0360987415303288+\beta*$
$\beta*h*-8.52364392732152+\beta*\beta*u_{p,i}*-15.261638213504+\beta$
$*\beta*\omega_{p,i}*-1.57832508633754+\beta*\beta*T_{p,i}*2.16187773419304+$
$\beta*\beta*\beta*apN*4.29456206732036+\beta*\beta*\beta*L*$
$-0.0182641821762816+\beta*\beta*\beta*h*3.46779276890705+\beta$
$*\beta*\beta*u_{p,i}*7.4802858738819+\beta*\beta*\beta*\omega_{p,i}*$
$0.735320721433247+\beta*\beta*\beta*T_{p,i}*-1.10423304807875+u_{p,i}*\omega_{p,i}$
$*-0.271151921764174+u_{p,i}*T_{p,i}*0.0901110324768644+u_{p,i}*u_{p,i}*apN*$
$0.0134654848409184+u_{p,i}*u_{p,i}*L*0.000312000972616353+u_{p,i}*u_{p,i}*h*$
$-0.265010682170012+u_{p,i}*u_{p,i}*\beta*0.126743295126664+u_{p,i}*u_{p,i}*\omega_{p,i}*$
$0.0238556648893838+u_{p,i}*u_{p,i}*T_{p,i}*-0.00759493933462802+u_{p,i}*u_{p,i}*u_{p,i}*$
$apN*0.0000887711837174136+u_{p,i}*u_{p,i}*u_{p,i}*L*-0.000019840846294843$
$+u_{p,i}*u_{p,i}*u_{p,i}*h*0.0220903408397669+u_{p,i}*u_{p,i}*u_{p,i}*\beta*$
$-0.0258750142274593+u_{p,i}*u_{p,i}*u_{p,i}*\omega_{p,i}*-0.00109912843315489+u_{p,i}*u_{p,i}$
$*u_{p,i}*T_{p,i}*-0.0000787025241198871+\omega_{p,i}*T_{p,i}*-0.015760444615435+\omega_{p,i}*\omega_{p,i}$
$*apN*0.0024807933969279+\omega_{p,i}*\omega_{p,i}*L*-0.000012182063546398+\omega_{p,i}*$
$\omega_{p,i}*h*0.00365889152940052+\omega_{p,i}*\omega_{p,i}*\beta*-0.0763607967171228+\omega_{p,i}$
$*\omega_{p,i}*u_{p,i}*0.00403329678258349+\omega_{p,i}*\omega_{p,i}*T_{p,i}*0.0000932383151206998+\omega_{p,i}$
$*\omega_{p,i}*\omega_{p,i}*apN*-0.0000486383499172527+\omega_{p,i}*\omega_{p,i}*\omega_{p,i}*L*$
$0.000000150656098624+\omega_{p,i}*\omega_{p,i}*\omega_{p,i}*h*-0.0000315889930601375+\omega_{p,i}*$
$\omega_{p,i}*\omega_{p,i}*\beta*0.00111113793845296+\omega_{p,i}*\omega_{p,i}*\omega_{p,i}*u_{p,i}*$
$-0.0000418054619755312+\omega_{p,i}*\omega_{p,i}*\omega_{p,i}*T_{p,i}*0.000000966831304977+T_{p,i}*$
$T_{p,i}*apN*-0.000504723223070479+T_{p,i}*T_{p,i}*L*0.0000010180190827979+T_{p,i}$
$*T_{p,i}*h*0.000723316741074582+T_{p,i}*T_{p,i}*\beta*0.0204038064101104$
$+T_{p,i}*T_{p,i}*u_{p,i}*0.000782140241588969+T_{p,i}*T_{p,i}*\omega_{p,i}*0.000170251657773102$
$+T_{p,i}*T_{p,i}*T_{p,i}*apN*0.0000035402497501088+T_{p,i}*T_{p,i}*T_{p,i}*L*$
$-0.0000000092162227419+T_{p,i}*T_{p,i}*T_{p,i}*h*-0.0000074210198852928+T_{p,i}$
$*T_{p,i}*T_{p,i}*\beta*-0.000135153958437068+T_{p,i}*T_{p,i}*T_{p,i}*u_{p,i}*$
$-0.000007695912204799+T_{p,i}*T_{p,i}*T_{p,i}*\omega_{p,i}*-0.0000010608248630349$

CC$=135.983069095451-11.4437241407163*apN+apN*apN*2.11571360373019+$
$apN*apN*apN*-0.134986606085959-0.119956534036814*L+L*L*$
$0.0000453643890071034+L*L*L*-0.000000089006181678+$
$-26.3718831768113*h+h*h*3.84742599782003+h*h*h$
$*-0.221480716567831-126.017436731067*\beta+\beta*\beta*273.597886714211$
$+\beta*\beta*\beta*-159.313025907036-30.8605561358713*u_{p,i}+u_{p,i}*u_{p,i}$
$*2.6595730214868+u_{p,i}*u_{p,i}*u_{p,i}*-0.161378623734618+4.54852243399671*\omega_{p,i}$
$+\omega_{p,i}*\omega_{p,i}*-0.0393992524830007+\omega_{p,i}*\omega_{p,i}*\omega_{p,i}*0.000844551487810428+$
$-6.42618354192812*T_{p,i}+T_{p,i}*T_{p,i}*0.040469818557101+T_{p,i}*T_{p,i}*T_{p,i}*$
$-0.000287047607594629+apN*L*-0.00472301843495183+apN*h*$
$-1.44006645470019+apN*\beta*41.0859018331365+apN*u_{p,i}*$
$-0.45541473086025+apN*\omega_{p,i}*0.434148420007268+apN*T_{p,i}*$
$-0.241011041115928+apN*apN*L*0.000567680903951317+apN*apN*$
$h*-0.246777651446156+apN*apN*\beta*-4.05060228053139+apN*$
$apN*u_{p,i}*-0.0515792729867582+apN*apN*\omega_{p,i}*-0.0809047889583812+$
$apN*apN*T_{p,i}*0.0379879148970516+apN*apN*apN*L*$
$-0.0000404216061505871+apN*apN*apN*h*0.01549681941202+$
$apN*apN*apN*\beta*0.307607375802651+apN*apN*apN*u_{p,i}*$
$0.0038148590064062+apN*apN*apN*\omega_{p,i}*0.00694522199803378+apN$
$*apN*apN*T_{p,i}*-0.00341416688351718+L*h*0.00984931288424607$
$+L*\beta*0.163198836215213+L*u_{p,i}*0.0182987938157266+L*\omega_{p,i}*$

-0.00276697953090838+L*$T_{p,i}$*0.0021464806155037+L*L*apN*
0.0000005754925256134+L*L*h*-0.0000027777210161656+L*L*
β*-0.0000017043623158952+L*L*$u_{p,i}$*-0.0000106162480429209+L*
L*$\omega_{p,i}$*0.0000010139655769165+L*L*$T_{p,i}$*-0.0000011852575333264+L
*L*L*apN*2.53661281395548e-11+L*L*L*h*
3.0360201555791e-10+L*L*L*β*3.25253801875052e-11+L*L
L$u_{p,i}$*0.0000000024127257529+L*L*L*$\omega_{p,i}$*
-1.91026145181862e-10+L*L*L*$T_{p,i}$*2.33252805866084e-10+h*
β*-1.33051389848905+h*$u_{p,i}$*8.88206507500713+h*$\omega_{p,i}$*
-1.06036686092297+h*$T_{p,i}$*1.06410014831751+h*h*apN*
0.661326454854306+h*h*L*0.0000102865647794653+h*h*
β*-5.21699081638025+h*h*$u_{p,i}$*-1.00850489349719+h*
h*$\omega_{p,i}$*0.143134860416603+h*h*$T_{p,i}$*-0.145001729202352+h
*h*h*apN*-0.0468435102569255+h*h*h*L*
-0.0000071079236618439+h*h*h*β*0.396697330768494+
h*h*h*$u_{p,i}$*0.0506854809107257+h*h*h*$\omega_{p,i}$*
-0.00733823426120839+h*h*h*$T_{p,i}$*0.00667401427119927+β
*$u_{p,i}$*1.74860093485803+β*$\omega_{p,i}$*-13.0420334044153+β*$T_{p,i}$*
11.4789028554542+β*β*apN*-24.5557148441816+β*β*L
*-0.294496909346366+β*β*h*19.9671129077287+β*β
$u_{p,i}$-33.6320337250789+β*β*$\omega_{p,i}$*21.2224374047169+β*
β*$T_{p,i}$*-18.3202881633072+β*β*β*apN*6.21607285960789
+β*β*β*L*0.161891122534413+β*β*β*h
*-7.33453372584798+β*β*β*$u_{p,i}$*13.6453780735305+β*
β*β*$\omega_{p,i}$*-9.91181179479032+β*β*β*$T_{p,i}$*
9.98547424072337+$u_{p,i}$*$\omega_{p,i}$*-1.56229839115928+$u_{p,i}$*$T_{p,i}$*1.15778751407789
+$u_{p,i}$*$u_{p,i}$*apN*0.259599525413575+$u_{p,i}$*$u_{p,i}$*L*0.000991359018222994
+$u_{p,i}$*$u_{p,i}$*h*-0.963378442699022+$u_{p,i}$*$u_{p,i}$*β*1.50136749252599
+$u_{p,i}$*$u_{p,i}$*$\omega_{p,i}$*0.20704271620894+$u_{p,i}$*$u_{p,i}$*$T_{p,i}$*-0.186739239898771+$u_{p,i}$
*$u_{p,i}$*$u_{p,i}$*apN*-0.0243433062598928+$u_{p,i}$*$u_{p,i}$*$u_{p,i}$*L*
-0.000127268574275342+$u_{p,i}$*$u_{p,i}$*$u_{p,i}$*h*0.0815007150617399+$u_{p,i}$*$u_{p,i}$
*$u_{p,i}$*β*-0.123191008721734+$u_{p,i}$*$u_{p,i}$*$u_{p,i}$*$\omega_{p,i}$*-0.0165562605691717
+$u_{p,i}$*$u_{p,i}$*$u_{p,i}$*$T_{p,i}$*0.0136560659985251+$\omega_{p,i}$*$T_{p,i}$*0.0465157422880884
+$\omega_{p,i}$*$\omega_{p,i}$*apN*-0.00609415069185826+$\omega_{p,i}$*$\omega_{p,i}$*L*
0.0000127269720541135+$\omega_{p,i}$*$\omega_{p,i}$*h*0.00337744946017346+$\omega_{p,i}$*$\omega_{p,i}$*
β*0.111139789200621+$\omega_{p,i}$*$\omega_{p,i}$*$u_{p,i}$*0.0096841593029104+$\omega_{p,i}$*$\omega_{p,i}$*$T_{p,i}$
-0.00034429043931458+$\omega_{p,i}$ $\omega_{p,i}$*$\omega_{p,i}$*apN*0.000100959910573945+$\omega_{p,i}$*
$\omega_{p,i}$*$\omega_{p,i}$*L*0.0000001065732307429+$\omega_{p,i}$*$\omega_{p,i}$*$\omega_{p,i}$*h*
-0.0000949153709084053+$\omega_{p,i}$*$\omega_{p,i}$*$\omega_{p,i}$*β*-0.00182876803720217+$\omega_{p,i}$*
$\omega_{p,i}$*$\omega_{p,i}$*$u_{p,i}$*-0.000113372135119384+$\omega_{p,i}$*$\omega_{p,i}$*$\omega_{p,i}$*$T_{p,i}$*
0.000000677456271977+$T_{p,i}$*$T_{p,i}$*apN*0.00184321154954262+$T_{p,i}$*$T_{p,i}$*L
*0.0000113973884572634+$T_{p,i}$*$T_{p,i}$*h*0.000824365772886258+$T_{p,i}$*$T_{p,i}$*
β*-0.0994983563446244+$T_{p,i}$*$T_{p,i}$*$u_{p,i}$*0.00480853434851725+$T_{p,i}$*$T_{p,i}$*
$\omega_{p,i}$*-0.000251352118966825+$T_{p,i}$*$T_{p,i}$*$T_{p,i}$*apN*-0.0000097967918308047
+$T_{p,i}$*$T_{p,i}$*$T_{p,i}$*L*-0.0000001019182369036+$T_{p,i}$*$T_{p,i}$*$T_{p,i}$*h*
0.0000091923211643871+$T_{p,i}$*$T_{p,i}$*$T_{p,i}$*β*0.000566738842659953+$T_{p,i}$*
$T_{p,i}$*$T_{p,i}$*$u_{p,i}$*-0.0000104711570921414+$T_{p,i}$*$T_{p,i}$*$T_{p,i}$*$\omega_{p,i}$*
0.000000303704256802

WC=446.98698479378-33.0944047375167*apN+apN*apN*9.0777789856059+apN
*apN*apN*-0.896826128100973-0.114609386682022*L+L*L*
0.0000212111171047492+L*L*L*0.0000000039436700885+
-84.4384689287081*h+h*h*8.22811240194462+h*h*h
*-0.333496067939115-578.201346162065*β+β*β*595.532278630214
+β*β*β*-287.198691685378-104.074208094603*$u_{p,i}$+$u_{p,i}$*$u_{p,i}$

$*6.47486555816504+u_{p,i}*u_{p,i}*u_{p,i}*-0.302196286436216+12.8565250773074*\omega_{p,i}$
$+\omega_{p,i}*\omega_{p,i}*-0.0978626301357462+\omega_{p,i}*\omega_{p,i}*\omega_{p,i}*0.0010131992542848+$
$-14.1255958304219*T_{p,i}+T_{p,i}*T_{p,i}*-0.036260923418787+T_{p,i}*T_{p,i}*T_{p,i}*$
$0.000286225199867116+apN*L*0.000631016287244177+apN*h*$
$1.80393252476027+apN*\beta*44.582872918045+apN*u_{p,i}*1.16986646492992$
$+apN*\omega_{p,i}*0.237658595706643+apN*T_{p,i}*0.099896568189113+apN*apN$
$*L*-0.000186378829911406+apN*apN*h*-0.628993925204502+$
$apN*apN*\beta*-6.37851512803329+apN*apN*u_{p,i}*-0.74829300699188$
$+apN*apN*\omega_{p,i}*0.00202417642099407+apN*apN*T_{p,i}*$
$-0.0588772147305111+apN*apN*apN*L*0.0000274835410655669+apN$
$*apN*apN*h*0.059774911968242+apN*apN*apN*\beta*$
$0.550906165719487+apN*apN*apN*u_{p,i}*0.0799618110742281+apN*$
$apN*apN*\omega_{p,i}*-0.00204536741974563+apN*apN*apN*T_{p,i}*$
$0.00715386702804995+L*h*0.00402791836498242+L*\beta*$
$0.151422975498948+L*u_{p,i}*0.0216387185220702+L*\omega_{p,i}*$
$-0.00301820721552412+L*T_{p,i}*0.00209833053154042+L*L*apN*$
$-0.000002293798331934+L*L*h*0.0000029482072037929+L*L*$
$\beta*0.0000076574191528939+L*L*u_{p,i}*-0.000012144468542934+L*L$
$*\omega_{p,i}*0.0000010451723490495+L*L*T_{p,i}*-0.0000015651665240103+L*$
$L*L*apN*0.000000009486722358+L*L*L*h*$
$-0.000000019651704746+L*L*L*\beta*-0.000000049701449781+L$
$*L*L*u_{p,i}*0.000000022251114779+L*L*L*\omega_{p,i}*$
$-1.55869478200481e-10+L*L*L*T_{p,i}*2.74740350874696e-10+h*$
$\beta*20.2273761237916+h*u_{p,i}*20.5107485829788+h*\omega_{p,i}*$
$-2.51806765909614+h*T_{p,i}*2.25752172065978+h*h*apN*$
$0.0966802712696729+h*h*L*0.000642703997707936+h*h*$
$\beta*-1.97944520747425+h*h*u_{p,i}*-1.80194402128038+h*$
$h*\omega_{p,i}*0.229517599027507+h*h*T_{p,i}*-0.261325623274672+h$
$*h*h*apN*-0.00333180107144315+h*h*h*L*$
$-0.000039381089487479+h*h*h*\beta*0.0586299707525433+$
$h*h*h*u_{p,i}*0.0733573671591638+h*h*h*\omega_{p,i}*$
$-0.00894716537459704+h*h*h*T_{p,i}*0.00965647918795762+\beta$
$*u_{p,i}*76.1480459427643+\beta*\omega_{p,i}*-25.4108774464597+\beta*T_{p,i}*$
$23.2331105835018+\beta*\beta*apN*-20.3155087449505+\beta*\beta*L$
$*-0.269584026562018+\beta*\beta*h*17.6997827141809+\beta*\beta$
$*u_{p,i}*-73.0833052202091+\beta*\beta*\omega_{p,i}*26.386094270201+\beta*\beta$
$*T_{p,i}*-28.7068914921792+\beta*\beta*\beta*apN*4.33640777084607$
$+\beta*\beta*\beta*L*0.148149236559339+\beta*\beta*\beta*h*$
$-12.1825496479822+\beta*\beta*\beta*u_{p,i}*30.3558110431467+\beta*$
$\beta*\beta*\omega_{p,i}*-12.3137084392196+\beta*\beta*\beta*T_{p,i}*$
$15.1662342964786+u_{p,i}*\omega_{p,i}*-3.19129256303047+u_{p,i}*T_{p,i}*2.03609299615703$
$+u_{p,i}*u_{p,i}*apN*0.187189126048055+u_{p,i}*u_{p,i}*L*0.00198579493122874$
$+u_{p,i}*u_{p,i}*h*-1.44705125505382+u_{p,i}*u_{p,i}*\beta*0.426834423459613$
$+u_{p,i}*u_{p,i}*\omega_{p,i}*0.252197537495251+u_{p,i}*u_{p,i}*T_{p,i}*-0.269351124142113+u_{p,i}$
$*u_{p,i}*u_{p,i}*apN*-0.0090215265413692+u_{p,i}*u_{p,i}*u_{p,i}*L*$
$-0.000208337114355861+u_{p,i}*u_{p,i}*u_{p,i}*h*0.101708845720718+u_{p,i}*u_{p,i}$
$*u_{p,i}*\beta*-0.156162060769164+u_{p,i}*u_{p,i}*u_{p,i}*\omega_{p,i}*-0.0155286424026357$
$+u_{p,i}*u_{p,i}*u_{p,i}*T_{p,i}*0.0157733649510445+\omega_{p,i}*T_{p,i}*0.129776531245551$
$+\omega_{p,i}*\omega_{p,i}*apN*-0.00410538033675436+\omega_{p,i}*\omega_{p,i}*L*0.0000069222274842044$
$+\omega_{p,i}*\omega_{p,i}*h*0.00853952690832225+\omega_{p,i}*\omega_{p,i}*\beta*0.197341317429249$
$+\omega_{p,i}*\omega_{p,i}*u_{p,i}*0.0185828653165616+\omega_{p,i}*\omega_{p,i}*T_{p,i}*-0.000711316969778683$
$+\omega_{p,i}*\omega_{p,i}*\omega_{p,i}*apN*0.0000486186827415933+\omega_{p,i}*\omega_{p,i}*\omega_{p,i}*L*$
$0.0000002203919131024+\omega_{p,i}*\omega_{p,i}*\omega_{p,i}*h*-0.000124824253873574+\omega_{p,i}*$
$\omega_{p,i}*\omega_{p,i}*\beta*-0.0018459713830828+\omega_{p,i}*\omega_{p,i}*\omega_{p,i}*u_{p,i}*$
$-0.000175106165474496+\omega_{p,i}*\omega_{p,i}*\omega_{p,i}*T_{p,i}*0.0000059774196156437+T_{p,i}*$

$T_{p,i}*apN*-0.00180344542407871+T_{p,i}*T_{p,i}*L*0.0000382683475181503+T_{p,i}$
$*T_{p,i}*h*0.00958510746439007+T_{p,i}*T_{p,i}*\beta*-0.0635612789772108$
$+T_{p,i}*T_{p,i}*u_{p,i}*0.0237692013871247+T_{p,i}*T_{p,i}*\omega_{p,i}*-0.00100353471075894+$
$T_{p,i}*T_{p,i}*T_{p,i}*apN*0.0000228287974892259+T_{p,i}*T_{p,i}*T_{p,i}*L*$
$-0.0000003256030617287+T_{p,i}*T_{p,i}*T_{p,i}*h*-0.0000318174760863471+T_{p,i}$
$*T_{p,i}*T_{p,i}*\beta*0.00019448558566980\,8+T_{p,i}*T_{p,i}*T_{p,i}*u_{p,i}*$
$-0.00010590320154637\,5+T_{p,i}*T_{p,i}*T_{p,i}*\omega_{p,i}*0.0000040017721735077$

COP$=446.98698479378-33.0944047375167*apN+apN*apN*9.0777789856059+apN$
$*apN*apN*-0.896826128100973-0.114609386682022*L+L*L*$
$0.000021211171047492+L*L*L*0.000000039436700885+$
$-84.4384689287081*h+h*h*8.22811240194462+h*h*h$
$*-0.333496067939115-578.201346162065*\beta+\beta*\beta*595.532278630214$
$+\beta*\beta*\beta*-287.198691685378-104.074208094603*u_{p,i}+u_{p,i}*u_{p,i}$
$*6.47486555816504+u_{p,i}*u_{p,i}*u_{p,i}*-0.302196286436216+12.8565250773074*\omega_{p,i}$
$+\omega_{p,i}*\omega_{p,i}*-0.0978626301357462+\omega_{p,i}*\omega_{p,i}*\omega_{p,i}*0.0010131992542848+$
$-14.1255958304219*T_{p,i}+T_{p,i}*T_{p,i}*-0.036260923418787+T_{p,i}*T_{p,i}*T_{p,i}*$
$0.000286225199867116+apN*L*0.000631016287244177+apN*h*$
$1.80393252476027+apN*\beta*44.582872918045+apN*u_{p,i}*1.16986646492992$
$+apN*\omega_{p,i}*0.237658595706643+apN*T_{p,i}*0.099896568189113+apN*apN$
$*L*-0.000186378829911406+apN*apN*h*-0.628993925204502+$
$apN*apN*\beta*-6.37851512803329+apN*apN*u_{p,i}*-0.74829300699188$
$+apN*apN*\omega_{p,i}*0.00202417642099407+apN*apN*T_{p,i}*$
$-0.0588772147305111+apN*apN*apN*L*0.0000274835410655669+apN$
$*apN*apN*h*0.059774911968242+apN*apN*apN*\beta*$
$0.550906165719487+apN*apN*apN*u_{p,i}*0.0799618110742281+apN*$
$apN*apN*\omega_{p,i}*-0.00204536741974563+apN*apN*apN*T_{p,i}*$
$0.00715386702804995+L*h*0.00402791836498242+L*\beta*$
$0.151422975498948+L*u_{p,i}*0.0216387185220702+L*\omega_{p,i}*$
$-0.00301820721552412+L*T_{p,i}*0.00209833053154042+L*L*apN*$
$-0.000002293798331934+L*L*h*0.0000029482072037929+L*L*$
$\beta*0.0000076574191528939+L*L*u_{p,i}*-0.000012144468542934+L*L$
$*\omega_{p,i}*0.0000010451723490495+L*L*T_{p,i}*-0.0000015651665240103+L*$
$L*L*apN*0.0000000009486722358+L*L*L*h*$
$-0.0000000019651704746+L*L*L*\beta*-0.0000000049701449781+L$
$*L*L*u_{p,i}*0.0000000022251114779+L*L*L*\omega_{p,i}*$
$-1.55869478200481e-10+L*L*L*T_{p,i}*2.74740350874696e-10+h*$
$\beta*20.2273761237916+h*u_{p,i}*20.5107485829788+h*\omega_{p,i}*$
$-2.51806765909614+h*T_{p,i}*2.25752172065978+h*h*apN*$
$0.0966802712696729+h*h*L*0.000642703997707936+h*h*$
$\beta*-1.97944520747425+h*h*u_{p,i}*-1.80194402128038+h*$
$h*\omega_{p,i}*0.229517599027507+h*h*T_{p,i}*-0.261325623274672+h$
$*h*h*apN*-0.0033318010714431\,5+h*h*h*L*$
$-0.0000393810894874 79+h*h*h*\beta*0.0586299707525433+$
$h*h*h*u_{p,i}*0.0733573671591638+h*h*h*\omega_{p,i}*$
$-0.00894716537459704+h*h*h*T_{p,i}*0.00965647918795762+\beta$
$*u_{p,i}*76.1480459427643+\beta*\omega_{p,i}*-25.4108774464597+\beta*T_{p,i}*$
$23.2331105835018+\beta*\beta*apN*-20.3155087449505+\beta*\beta*L$
$*-0.269584026562018+\beta*\beta*h*17.6997827141809+\beta*\beta$
$*u_{p,i}*-73.0833052202091+\beta*\beta*\omega_{p,i}*26.386094270201+\beta*\beta$
$*T_{p,i}*-28.7068914921792+\beta*\beta*\beta*apN*4.33640777084607$
$+\beta*\beta*\beta*L*0.148149236559339+\beta*\beta*\beta*h*$
$-12.1825496479822+\beta*\beta*\beta*u_{p,i}*30.3558110431467+\beta*$
$\beta*\beta*\omega_{p,i}*-12.3137084392196+\beta*\beta*\beta*T_{p,i}*$
$15.1662342964786+u_{p,i}*\omega_{p,i}*-3.19129256303047+u_{p,i}*T_{p,i}*2.03609299615703$

$+u_{p,i}*u_{p,i}*apN*0.187189126048055+u_{p,i}*u_{p,i}*L*0.00198579493122874$
$+u_{p,i}*u_{p,i}*h*-1.44705125505382+u_{p,i}*u_{p,i}*\beta*0.426834423459613$
$+u_{p,i}*u_{p,i}*\omega_{p,i}*0.252197537495251+u_{p,i}*u_{p,i}*T_{p,i}*-0.269351124142113+u_{p,i}$
$*u_{p,i}*u_{p,i}*apN*-0.0090215265413692+u_{p,i}*u_{p,i}*u_{p,i}*L*$
$-0.000208337114355861+u_{p,i}*u_{p,i}*u_{p,i}*h*0.101708845720718+u_{p,i}*u_{p,i}$
$*u_{p,i}*\beta*-0.156162060769164+u_{p,i}*u_{p,i}*u_{p,i}*\omega_{p,i}*-0.0155286424026357$
$+u_{p,i}*u_{p,i}*u_{p,i}*T_{p,i}*0.0157733649510445+\omega_{p,i}*T_{p,i}*0.129776531245551$
$+\omega_{p,i}*\omega_{p,i}*apN*-0.00410538033675436+\omega_{p,i}*\omega_{p,i}*L*0.0000069222274842044$
$+\omega_{p,i}*\omega_{p,i}*h*0.00853952690832225+\omega_{p,i}*\omega_{p,i}*\beta*0.197341317429249$
$+\omega_{p,i}*\omega_{p,i}*u_{p,i}*0.0185828653165616+\omega_{p,i}*\omega_{p,i}*T_{p,i}*-0.000711316969778683$
$+\omega_{p,i}*\omega_{p,i}*\omega_{p,i}*apN*0.0000486186827415933+\omega_{p,i}*\omega_{p,i}*\omega_{p,i}*L*$
$0.0000002203919131024+\omega_{p,i}*\omega_{p,i}*\omega_{p,i}*h*-0.000124824253873574+\omega_{p,i}*$
$\omega_{p,i}*\omega_{p,i}*\beta*-0.0018459713830828+\omega_{p,i}*\omega_{p,i}*\omega_{p,i}*u_{p,i}*$
$-0.000175106165474496+\omega_{p,i}*\omega_{p,i}*\omega_{p,i}*T_{p,i}*0.0000059774196156437+T_{p,i}*$
$T_{p,i}*apN*-0.00180344542407871+T_{p,i}*T_{p,i}*L*0.0000382683475181503+T_{p,i}$
$*T_{p,i}*h*0.00958510746439007+T_{p,i}*T_{p,i}*\beta*-0.0635612789772108$
$+T_{p,i}*T_{p,i}*u_{p,i}*0.0237692013871247+T_{p,i}*T_{p,i}*\omega_{p,i}*-0.00100353471075894+$
$T_{p,i}*T_{p,i}*T_{p,i}*apN*0.0000228287974892259+T_{p,i}*T_{p,i}*T_{p,i}*L*$
$-0.0000003256030617287+T_{p,i}*T_{p,i}*T_{p,i}*h*-0.0000318174760863471+T_{p,i}$
$*T_{p,i}*T_{p,i}*\beta*0.00019448558566980 8+T_{p,i}*T_{p,i}*T_{p,i}*u_{p,i}*$
$-0.000105903201546375+T_{p,i}*T_{p,i}*T_{p,i}*\omega_{p,i}*0.0000040017721735077$

MLR-7 (Response Surface)

$\boldsymbol{\varepsilon_{dp}}$=-0.206948209500542-0.124047912173297*apN+0.0000995986166286987*L
+0.0210396910736227*h+2.20931897679685*β-0.00851895572861097*$u_{p,i}$
+0.0356486509325435*$\omega_{p,i}$+0.011977878600295*$T_{p,i}$+apN*apN*
0.000222212659475384+apN*L*-0.000017509542454 5967+L*L*
-0.0000001193805777993+apN*h*0.0116958462107096+L*h*
0.0000395986776546671+h*h*-0.0046476821369252 2+apN*β*
0.108817718852266+L*β*0.000221321923667053+h*β*
-0.125851856267273+β*β*-1.03897749169037+apN*$u_{p,i}$*
0.00744354257108033+L*$u_{p,i}$*0.0000346899865926767+h*$u_{p,i}$*
-0.0224303619984146+β*$u_{p,i}$*-0.098079520120642+$u_{p,i}$*$u_{p,i}$*
0.00627746026695895+apN*$\omega_{p,i}$*0.000202637881905837+L*$\omega_{p,i}$*
0.0000007584775947712+h*$\omega_{p,i}$*-0.00038341174985102+β*$\omega_{p,i}$*
-0.00852028132042205+$u_{p,i}$*$\omega_{p,i}$*-0.000495699061830108+$\omega_{p,i}$*$\omega_{p,i}$*
-0.000589080993478658+apN*$T_{p,i}$*0.000044183845676983+L*$T_{p,i}$*
0.0000001407227861256+h*$T_{p,i}$*-0.0000926001574328187+β*$T_{p,i}$*
-0.0081995713045 6772+$u_{p,i}$*$T_{p,i}$*0.0000026243699981153+$\omega_{p,i}$*$T_{p,i}$*
-0.00011137651080 6237+$T_{p,i}$*$T_{p,i}$*-0.0000530388733072813

$\mathbf{T_{p,o}}$=7.41705311040083+1.88372713834906*apN+0.00124950216098368*L+
-1.50910133946997*h-26.8778581044436*β-1.06601864209459*$u_{p,i}$
+1.23058541476244*$\omega_{p,i}$+0.313745298992947*$T_{p,i}$+apN*apN*
-0.00682959798484982+apN*L*0.000282711636871511+L*L*
0.0000019035515190675+apN*h*-0.18921879982451 8+L*h*
-0.000610211381639638+h*h*0.0679867896986611+apN*β*
-1.72656270262026+L*β*-0.00380923643985799+h*β*
2.11613840437751+β*β*15.8861033322491+apN*$u_{p,i}$*
-0.119960335678395+L*$u_{p,i}$*-0.000533907603525854+h*$u_{p,i}$*
0.353448435877231+β*$u_{p,i}$*1.69696400250495+$u_{p,i}$*$u_{p,i}$*-0.108934122738293
+apN*$\omega_{p,i}$*-0.0159002657165608+L*$\omega_{p,i}$*0.000244731782518096+h*$\omega_{p,i}$
-0.0984024996266835+β$\omega_{p,i}$*0.914747689185008+$u_{p,i}$*$\omega_{p,i}$*
-0.0969998914984557+$\omega_{p,i}$*$\omega_{p,i}$*-0.0105556485398018+apN*$T_{p,i}$*
0.00797217855222032+L*$T_{p,i}$*-0.000188080532966665+h*$T_{p,i}$*
0.0773206309381266+β*$T_{p,i}$*-0.420585896621012+$u_{p,i}$*$T_{p,i}$*
0.0762641558733348+$\omega_{p,i}$*$T_{p,i}$*-0.0054312873145063+$T_{p,i}$*$T_{p,i}$*
-0.0025566564908196

CC=-33.1084932010087-6.24940983298023*apN-0.0210217230841739*L
+7.22061873247902*h+220.395044761496*β+1.87223179501704*$u_{p,i}$+
-1.14094291668312*$\omega_{p,i}$-0.889835026367884*$T_{p,i}$+apN*apN*
0.00403466388824133+apN*L*-0.00123784489557593+L*L*
-0.0000068010038550805+apN*h*0.606344242121633+L*h*
0.00452083710076622+h*h*-1.19067637078596+apN*β*
7.53328697850611+L*β*-0.00330863098046842+h*β*
-9.53499826974466+β*β*-112.48350445979+apN*$u_{p,i}$*
0.176176676787348+L*$u_{p,i}$*0.00621029143275363+h*$u_{p,i}$*
-0.19850289074231+β*$u_{p,i}$*-15.2242483406478+$u_{p,i}$*$u_{p,i}$*-1.41573792163542
+apN*$\omega_{p,i}$*0.0587628987321059+L*$\omega_{p,i}$*-0.000894334230173599+h*$\omega_{p,i}$
-0.188286407151409+β$\omega_{p,i}$*1.72613136904734+$u_{p,i}$*$\omega_{p,i}$*
-0.690284423603707+$\omega_{p,i}$*$\omega_{p,i}$*0.0267862690290679+apN*$T_{p,i}$*
-0.0252700198878705+L*$T_{p,i}$*0.000822425559843047+h*$T_{p,i}$*
0.25161920418477+β*$T_{p,i}$*-3.36149762779299+$u_{p,i}$*$T_{p,i}$*0.784467892238654
+$\omega_{p,i}$*$T_{p,i}$*0.0231297425642108+$T_{p,i}$*$T_{p,i}$*0.0114063910466764
WC=196.817744446237-4.19825104177608*apN-0.0338864353769712*L+

$$-17.8592924519706*h-19.7080776291801*\beta-47.4465250769317*u_{p,i}$$
$$+3.48813494470006*\omega_{p,i}-9.67991102468241*T_{p,i}+apN*apN*-0.0773752092139415$$
$$+apN*L*-0.00122458625473019+L*L*-0.0000110863975071224+apN$$
$$*h*0.58241654447805+L*h*0.00661683525030883+h*h*$$
$$-1.59685317371264+apN*\beta*7.21429692752659+L*\beta*$$
$$0.000955485008759599+h*\beta*14.0945798876974+\beta*\beta*$$
$$-122.176312588868+apN*u_{p,i}*-0.0820008421562193+L*u_{p,i}*$$
$$0.008828405226506+h*u_{p,i}*3.62077761346388+\beta*u_{p,i}*27.6930332440104$$
$$+u_{p,i}*u_{p,i}*-1.80373624830699+apN*\omega_{p,i}*0.106724544428499+L*\omega_{p,i}*$$
$$-0.00103459946031885+h*\omega_{p,i}*-0.84984748197748+\beta*\omega_{p,i}*$$
$$-5.40408238785881+u_{p,i}*\omega_{p,i}*-1.88636612083254+\omega_{p,i}*\omega_{p,i}*0.0424127793175484$$
$$+apN*T_{p,i}*-0.070917032405131+L*T_{p,i}*0.00112414054180114+h*T_{p,i}$$
$$*1.00918171102782+\beta*T_{p,i}*3.3956103989444+u_{p,i}*T_{p,i}*2.21631207110613$$
$$+\omega_{p,i}*T_{p,i}*0.0630066235671088+T_{p,i}*T_{p,i}*0.0367585962874094$$

COP$=-160.978490820725-33.747766239797*apN-0.486745977862845*L$
$$+275.429095442044*h+477.616228066425*\beta-409.958897291708*u_{p,i}+$$
$$-67.3371598837319*\omega_{p,i}+57.1648244899914*T_{p,i}+apN*apN*10.2410288241416$$
$$+apN*L*-0.015536354402217+L*L*0.000511848614651339+apN*h$$
$$*2.17596982131878+L*h*0.0088135793213269+h*h*$$
$$-12.3943913359371+apN*\beta*4.32034532757997+L*\beta*$$
$$0.462501736468652+h*\beta*-232.963503201532+\beta*\beta*$$
$$-363.19286502393+apN*u_{p,i}*-17.7173466185482+L*u_{p,i}*0.0947120232466514$$
$$+h*u_{p,i}*-36.4649556462682+\beta*u_{p,i}*388.266647649489+u_{p,i}*u_{p,i}*$$
$$84.1635828081483+apN*\omega_{p,i}*-2.09844023401637+L*\omega_{p,i}*0.00708690018551151$$
$$+h*\omega_{p,i}*-2.05066956607308+\beta*\omega_{p,i}*38.0650940764617+u_{p,i}*\omega_{p,i}*$$
$$11.6375736720377+\omega_{p,i}*\omega_{p,i}*0.194829023006492+apN*T_{p,i}*2.41344211503836$$
$$+L*T_{p,i}*-0.0087601487170410 9+h*T_{p,i}*2.65958314837086+\beta*T_{p,i}*$$
$$-52.5551765016077+u_{p,i}*T_{p,i}*-12.0107342077085+\omega_{p,i}*T_{p,i}*0.173806582162005$$
$$+T_{p,i}*T_{p,i}*0.0689899618532057$$